SPECTRAL DISTRIBUTION OF SOLAR RADIATION IMPACTS ON PV IN SOUTHEASTHERN BRAZILIAN SITES

Guilherme Marques Neves

Doctorate Thesis of the Graduate Course in Space Engineering and Technology / Science and Technology of Material and Sensors, guided by Drs. Enio Bueno Pereira, Waldeir Amaral Vilela, and Gustavo Nofuentes Garrido, approved in April 26, 2022.

URL of the original document:
<http://urlib.net/8JMKD3MGP3W34T/47A5LAE>

INPE

São José dos Campos

2022

SPECTRAL DISTRIBUTION OF SOLAR RADIATION IMPACTS ON PV IN SOUTHEASTHERN BRAZILIAN SITES

Guilherme Marques Neves

Doctorate Thesis of the Graduate Course in Space Engineering and Technology / Science and Technology of Material and Sensors, guided by Drs. Enio Bueno Pereira, Waldeir Amaral Vilela, and Gustavo Nofuentes Garrido, approved in April 26, 2022.

URL of the original document:
<http://urlib.net/8JMKD3MGP3W34T/47A5LAE>

INPE

São José dos Campos

2022

INSTITUTO NACIONAL DE PESQUISAS ESPACIAIS

DEFESA FINAL DE TESE DO GUILHERME MARQUES NEVES
BANCA N° 087/2022, REGISTRO 130486/2016.

No dia 26 de abril de 2022, as 14h00, Videoconferência, o(a) aluno(a) mencionado(a) acima defendeu seu trabalho final (apresentação oral seguida de arguição) perante uma Banca Examinadora, cujos membros estão listados abaixo. O(A) aluno(a) foi **APROVADO(A)** pela Banca Examinadora, por unanimidade, em cumprimento ao requisito exigido para obtenção do Título de Doutor em Engenharia e Tecnologia Espaciais/Ciência e Tecnologia de Materiais e Sensores. O trabalho não precisa de correções.

Título: "**Spectral distribution of solar radiation impacts on PV in Southeasthern Brazilian sites.**"

Membros da Banca

Dr. Enio Bueno Pereira - **Presidente** e Orientador – INPE / CCST

Dr. Waldeir Amaral Vilela – Orientador – INPE/COPDT

Dr. Gustavo Nofuentes Garrido – Orientador – UJA / IDEA - (Assinatura da aprovação do membro estrangeiro está em anexo)

Dr. Luiz Angelo Berni – Membro Interno – INPE / COPDT

Dr. André Rodrigues Gonçalves – Membro Interno - INPE / CCST

Dra. Simone Marilene Sievert Da Costa Coelho – Membro Interno - INPE / DISSM

Dr. Roberto Zilles – Membro Externo – USP / IEE

Dra. Marcia Yamasoe – Membro Externo – USP / IAG

Dr. Rafael Haag – Membro Externo – UERGS / ProPPG

Documento assinado eletronicamente por **Luiz Ângelo Berni**, **Pesquisador Titular**, em 16/05/2022, às 15:27 (horário oficial de Brasília), com fundamento no § 3º do art. 4º do Decreto nº 10.543, de 13 de novembro de 2020.

Documento assinado eletronicamente por **Marcia Akemi Yamasoe (E)**, **Usuário Externo**, em 16/05/2022, às 16:57 (horário oficial de Brasília), com fundamento no § 3º do art. 4º do Decreto nº 10.543, de 13 de novembro de 2020.

Documento assinado eletronicamente por **Roberto zilles (E)**, **Usuário Externo**, em 16/05/2022, às 17:12 (horário oficial de Brasília), com fundamento no § 3º do art. 4º do Decreto nº 10.543, de 13 de novembro de 2020.

Documento assinado eletronicamente por **Rafael Haag (E)**, **Usuário Externo**, em 16/05/2022, às 18:06 (horário oficial de Brasília), com fundamento no § 3º do art. 4º do Decreto nº 10.543, de 13 de novembro de 2020.

Documento assinado eletronicamente por **Simone Marilene Sievert da Costa Coelho**, **Pesquisador**, em 17/05/2022, às 18:55 (horário oficial de Brasília), com fundamento no § 3º do art. 4º do Decreto nº 10.543, de 13 de novembro de 2020.

Documento assinado eletronicamente por **Enio Bueno Pereira**, **Pesquisador Titular**, em 19/05/2022, às 10:41 (horário oficial de Brasília), com fundamento no § 3º do art. 4º do Decreto nº 10.543, de 13 de novembro de 2020.

Documento assinado eletronicamente por **Waldeir Amaral Vilela**, **Tecnologista**, em 31/05/2022, às 16:07 (horário oficial de Brasília), com fundamento no § 3º do art. 4º do Decreto nº 10.543, de 13 de novembro de 2020.

A autenticidade deste documento pode ser conferida no site http://sei.mctic.gov.br/verifica.html, informando o código verificador **9657258** e o código CRC **E8515B07**.

Referência: Processo nº 01340.002605/2022-61   SEI nº 9657258

I dedicate this thesis to all teachers, professors, and advisors I have had in my life.

Thank you all for teaching me everything I know.

ABSTRACT

Solar radiation spectral distribution variation and its impacts on different PV materials -single crystalline (sc-Si), multi crystalline (mc-Si) and amorphous Silicon (a-Si), CdTe, CIGS, and Perovskite- were analyzed in three nearby cities in the state of São Paulo. Data recorded over a whole year in São Paulo, São José dos Campos, and Cachoeira Paulista through state-of-the-art and self-developed spectroradiometers were analyzed on an instantaneous, monthly, and annual basis. In such analysis, the average photon energy and the spectral mismatch factor obtained for all PV technologies were adopted. The results indicate that a blue-biased solar spectrum prevails in the three sites along the year, with a similar seasonal behavior. Large band gap materials (i.e., a-Si, Perovskite and CdTe) are the most benefited, reaching annual spectral gains of up to around 6%, 4% and 2%, respectively. In contrast, lower band gap technologies do not exhibit remarkable spectral effects on an annual basis, as their annual spectral mismatch factor ranges between 0.9 and 1.1. The findings are very similar for the three sites and agree reasonably well with previous studies also carried out in low-latitude and sub-tropical or tropical locations with simulations or experimental campaigns. In this sense, the spectral effects probably have a regional behavior and should not be ignored when the energy produced outdoors by large band gap devices is to be predicted. It was also found that the monthly average photon energy has a quasi-linear relationship with the monthly spectral mismatch factor for all PV technologies analyzed, which agrees with previous papers.

Keywords: Solar Energy. Solar Spectrum. Spectral effects.

x

IMPACTOS DA DISTRIBUIÇÃO ESPECTRAL DA RADIAÇÃO SOLAR EM MÓDULOS FOTOVOLTIACOS NA REGIÃO SUDESTE DO BRASIL

RESUMO

A variação da distribuição espectral da radiação solar e seus impactos em diferentes tecnologias de materiais fotovoltaicos -Silício mono (sc-Si) e poli cristalino (mc-Si), Silício amorfo (a-Si), CdTe, CIGS, e Perovskita- foram analizados em três cidades próximas entre sí do estado de São Paulo. Dados coletados ao longo de 12 meses em São Paulo, São José dos Campos e Cachoeira Paulista através de espectrorradiômetros tidos como referência e desenvolvidos em laboratório foram analizados em uma base instantânea, mensal e anual de tempo. Em tal análise, a energia media dos fótons e o fator de descasamento espectral obtidas para todas as tecnologias fotovoltaicas foram adotados. Os resultados indicam que um espectro solar mais azulado prevalece nas três cidades ao longo do ano, com um comportamento sazonal similar. Materiais com energia de gap maiores (i.e., a-Si, Perovskite and CdTe) são os mais beneficiados, chegando a ganhos espectrais anuais de até 6%, 4% e 2%, respectivamente. Por outro lado, tecnologias com menores energias de gap não apresentam ganhos consideráveis, já que seus fatores de descasamento espectral variam entre 0.9 e 1.1. Os resultados dos três locais avaliados são muito similares entre si e são muito próximos aos encontrados por estudos também conduzidos em localidades de baixa latitude e com clima subtropical e tropical através de simulação ou experimentos. Assim, provavelmente os efeitos espectrais apresentam uma característica regional e não podem ser ignorados ao se realizar a previsão do comportamento em campo de módulos com elevadas energias de gap. A energia media dos fótons mensal apresenta uma relação quase linear com o factor de descasamento espectral mensal para toda as tecnologias fotovolticas analizadas, concordando com trabalhos prévios a esse.

Palavras-chave: Energia Solar. Espectro Solar. Efeitos Espectrais.

FIGURE LIST

TABLE LIST

LIST OF ACRONYMS AND ABBREVIATIONS

AC	Alternating current
AERONET	Aerosol Robotic Network
a-Si	Amorphous silicon
ASTM	American Society for Testing and Materials
BC	Black Carbon
BOS	Balance of System
BrC	Brown Carbon
CAGR	Compound annual growth rate
CCN	Cloud condensation nuclei
CdTe	Cadmium Telluride
CE	Cloud enhancement
Cfa	Humid subtropical climate
Cfb	Temperate oceanic climate
CG	Centralized generation
CIGS	Copper Indium Gallium Diselenide
COMIT/INPE	Design and Mechanical Fabrication Department of Manufacturing, Assembly, Integration and Testing Coordination at INPE (*Coordenação de Manufatura, Montagem, Integração e Teste do INPE*)
COP25	Climate Ambition Alliance
CPA	Cachoeira Paulista
c-Si	Crystalline-Silicon
CSP	Concentrating solar power
DC	Direct current
EPE	Brazilian Energy Research Office ()
F_0	Filter 0
F_1	Filter 1
F_2	Filter 2
F_{MM}	Filter *MM*
GDF	Photovoltaic devices group (*Grupo de dispositivos fotovoltaicos*)
IEC	International Electrotechnical Commission
IN	Ice nuclei
INPE	Brazilian National Institute for Space Research (*Instituto Nacional de Pesquisas Espaciais*)
IPCC	Intercontinental Panel for Climate Changes

IR	Infrared
ISO	International Standards Organization
LABREN	Laboratory of Modeling and Studies on Renewable Energy Resources (*Laboratório de Modelagem e Estudos de Recursos Renováveis de Energia*)
LCOE	Levelized Cost of Energy
LER	Reserve Energy Auction (*Leilões de Energia Reserva'*)
LIM	Meteorological Instrumentation Laboratory
mc-Si	Multi-Crystalline Sillicon
MD	Mineral Dust
MIR	Mid infrared
MMDG	Micro and mini distributed generation
MODTRAN	Moderate Resolution Atmospheric Transmission
MPPT	Maximum power point tracking
NASA	National Aeronautics and Space Administration
NIR	Near Infrared
NIST	National Institute of Standards and Technology
NOAA	National Oceanic and Atmospheric Administration
OI1	Optical Interface 1
OI2	Optical Interface 2
PAR	Photosynthetically active radiation
POA	Plane of the array
PPA	Power Purchase Agreement
PTFE	Polytetrafluoroethylene
PVGCS	PV grid-connected systems
PVGIS-SARAH	Photovoltaic Geographical Information System
QTH	Quartz Tungsten Halogen
RE	Renewable energy
SACZ	South Atlantic Convergence Zone
SAMS	South American Monsoon System
sc-Si	Single-Crystalline Sillicon
SJC	São José dos Campos
SMARTS2	Simple Model of the Atmospheric Radiative Transfer of Sunshine
SONDA	*Sistema de Organização Nacional de Dados Ambientais*
SORCE	Solar Radiation and Climate Experiment
SPA	São Paulo
SPG	Serviço de Pós-Graduação

SPMM	macro metropolitan complex of São Paulo
STC	Standard Test Conditions
TDI	Teses e Dissertações Internas
USP	University of São Paulo (*Universidade de São Paulo*)
UV	Ultraviolet
UV-B	Ultraviolet B
UV-C	Ultraviolet C
VIS	Visible

SYMBOLS LIST

$\overline{H_i}$	The average monthly global horizontal irradiation of the *i*-th month, $Wh{\cdot}m^{-2}$
χ	PV panel tilted at an angle, °
τ	extinction coefficient, dimensionless
β	Angstrom's turbidity coefficient, dimensionless
α	Angstrom' exponent, dimensionless
$\beta_S(\lambda, z)$	Linear scattering coefficient, m^{-1}
$\beta_A(\lambda, z)$	Linear absorption coefficient, m^{-1}
$\phi_{PH}(\lambda)$	photon flux at a given wavelength, $m^{-2}{\cdot}s^{-1}$
η	Efficiency, %
λ_{EGAP}	Wavelength equivalent to the bandgap energy related to the solar cell, nm
a	Lower limit of integration, nm
Ac	Area of the solar cell, cm^2
AM	Relative optical air mass or simply air mass, dimensionless
AM'	Relative optical air mass or simply air mass, dimensionless
AOD	Aerosol Optical Depth, dimensionless
$AOD_{500nm\ DA}$	Daily average of Aerosol Optical Depth at 500nm
$AOD_{500nm\ MA}$	Monthly average of Aerosol Optical Depth at 500 nm
AOI	Angle of incidence, °
APE	Average Photon Energy, eV
APE_{AW}	Annual weighted average photon energy, eV
APE_{DW}	Daily weighted average photon energy, eV
APE_i	*APE* corresponding to the *i*-th spectral irradiance, eV
APE_{MW}	Monthly weighted average photon energy, eV
APE_{MWi}	Monthly weighted *APE* of the *i*-th month, eV
b	Upper limit of integration, nm
BF	Blue Fraction, dimensionless
c	speed of light in vacuum, $299792458\ m \cdot s^{-1}$
DHI	Diffuse horizontal irradiance, $W{\cdot}m^{-2}$
DNI	Direct normal irradiance, $W{\cdot}m^{-2}$
E	Electric field, $V{\cdot}m^{-1}$
E(λ)	Spectral irradiance, $W{\cdot}m^{-2}{\cdot}nm^{-1}$
E_{GAP}	Bandgap energy, eV

EHI	Extraterrestrial Horizontal Irradiance, $W \cdot m^{-2}$
E_i	The *i*-th spectral irradiance, $W \cdot m^{-2}$
$E_R(\lambda)$	Spectral irradiance of the reference device, A/W
FF	Fill Factor, dimensionless
FOF	Field Output Factor, dimensionless
GHI	Global horizontal irradiance, $W \cdot m^{-2}$
GHI_i	global horizontal irradiance corresponding the *i*-th spectral irradiance, $W \cdot m^{-2}$
h	Planck constant, $6.62607 \cdot 10^{-34} m^2 \cdot kg \cdot s^{-1}$
H	Global horizontal irradiation, $Wh \cdot m^{-2}$
I	Current, A
I_0	Diode saturation current, A
I_{MP}	Current at maximum power, A
I_{PH}	Photogenerated current, A
I_{SC}	Short circuit current, A
I_{SC-STC}	Short circuit current generated by the PV device under the reference solar spectrum, A
J_{PH}	Photogenerated current density, $A \cdot cm^{-2}$
k	Boltzmann constant, $1.38065 \cdot 10^{-23} m^2 \cdot kg \cdot s^{-2} \cdot K^{-1}$
K_T	Clearness index, dimensionless
MM	Spectral Mismatch Factor, dimensionless
MM_{MW}	Monthly weighted spectral mismatch factor, dimensionless
MM_{MWi}	Monthly weighted spectral mismatch factor of the *i*-th month, dimensionless
N	diode ideality factor, dimensionless
n	total amount of data in each day or month, days or months
P_{MP}	Maximum power output, W
$P_{MP@STC}$	Maximum power output measured under the standard test conditions (STC), W
PR	Performance Ratio, %
PW	Precipitable water, cm^{-1}
PW_{MA}	Monthly averages of precipitable water, cm^{-1}
q	electronic charge, C
QE	Quantum efficiency, %
R^2	Coefficient of determination, dimensionless
R_S	Series resistance, Ω
R_{SH}	Shunt resistance, Ω
SF	Spectral Factor, dimensionless

SR	Spectral Response, A/W
$SR_{PV}(\lambda)$	Spectral response of the PV cell, A/W
SR_r	Relative spectral responses, dimensionless
$SR_R(\lambda)$	Spectral response of the reference device, A/W
SSA	Single Scattering Albedo, dimensionless
T	Temperature, K
TSI	*Total Solar Irradiance,* W·m^{-2}
UF	Useful Fraction
v	Voltage, V
V_{MP}	Voltage at the maximum power, V
V_{OC}	Open circuit voltage, V
λ	Wavelenght, nm
ρ	Pearson's correlation coefficient, dimensionless
θ_Z	Zenithal angle, radians

SUMMARY

1 INTRODUCTION

The commercialization of Photovoltaic (PV) modules is based on their power rated in laboratories under the Standard Test Conditions (STC), namely cell temperature 25°C, incident irradiance of 1000 W·m^{-2} and the AM1.5G spectrum (defined in standard IEC 60904-3 or ASTM G-173-03) (IEC, 2016; ASTM, 2012). Despite enabling the standardization of PV modules power ratings, the STC rarely occurs in the field, especially altogether at the same time. The conditions indoors are under control, differently from outdoors where various environmental, physical, and atmospheric factors (i.e., wind, rain, pollution, etc.) constantly change the conditions in PV surroundings. Thus, the power delivered by these devices during their lifetime rarely matches that which is rated indoors under controlled conditions, even with the importance of accurate predictions to maximize the return on investment. In this sense, more realistic ratings have been studied and proposed by scientists and solar engineers in order to improve PV performance prediction, increasing the bankability and competitiveness of solar energy projects (HULD et. al, 2013; DIRNBERGER; MULLER; REISE, 2015). These ratings require an in-depth knowledge of the PV behavior outdoors and the factors that may impact the performance of such devices.

Various factors can influence the outdoor performance of PV modules. While both incident irradiance and operating temperature are the most important, angular responses, low light levels, soiling, and spectral distribution of the irradiance (spectral irradiance, in short) must also be of chief concern. Apart from incident irradiance and temperature, solar spectral irradiance may cause the largest contribution to variations in output for PV devices (DUCK; FELL, 2015). Thus, disregarding such contribution may lead to errors of up to 10% during the simulation of some PV electrical parameters such as the short-circuit current of single junction PV devices with large band gap (GOTTSCHALG et al., 2005). Despite noticeable effects, the impact of the varying spectrum on PV materials is far from being fully understood when compared to the influence exerted by the remaining parameters previously described (DIRNBERGER et al., 2015;

NOFUENTES et al., 2013; NOFUENTES et al., 2017; CHANTANA et al., 2020). Thus, in order to improve the understanding of such impacts, studies carried out with ground-based measurements or simulations through data retrieved from satellites have been conducted all over the world. Regardless of the different instruments, methodologies, and protocols applied in each work, such contributions show that the solar spectral influence on the PV performance is dependent on the optical properties of the solar cells (like absorption coefficient, band gap energy, etc.) and on the local atmospheric and geographic characteristics of the installation site (such as climate, albedo, etc.) (CORNARO; ANDREOTTI, 2013; ISHII et al., 2013; DIRNBERGER et al., 2015; NOFUENTES et al., 2017; GOTTSCHALG et al., 2005; CHANTANA et al., 2020; YE et al., 2014; BRAGA et al., 2020; CONDE et al., 2021).

For various reasons, most of the work was carried out in mid-latitude sites with temperate climates (CORNARO; ANDREOTTI, 2013; ISHII et al., 2013; DIRNBERGER et al., 2015; NOFUENTES et al., 2017; GOTTSCHALG et al., 2005; CHANTANA et al., 2020), which leads to the conclusion that in general the prominent seasonality of the spectral impact on PV is partially cancelled when an annual scale of integration is considered. On the other hand, low-latitude locations with tropical to sub-tropical climates lack knowledge of how the solar spectral irradiance variations affect PV materials. So far, few studies have been conducted under these conditions, as those carried out in South Brazil (BRAGA et al., 2020), Singapore (YE et al., 2014), Thailand (SIRISAMPHANWONG; KETJOY, 2014) and Peru (CONDE et al., 2021). In general, these studies show that spectra shifted to shorter wavelengths prevail all over the year, which means that PV performance can be significantly influenced by the spectral irradiance on an annual basis. Thus, further research using spectral instances recorded with spectroradiometers in different places and under different climatic conditions are required to fill this knowledge gap. Besides, such contribution is key not only in itself but it may also help the development and/or validation of computational models used to assess the impact of the spectrum on PV behavior in tropical and sub-tropical regions, especially closer to big cities where urban pollution impacts the air quality.

Therefore, this work aims at broadening the knowledge of solar spectral effects exhibited by PV materials in sub-tropical areas by using 12-month ground-measured data recorded in São Paulo (SP), São José dos Campos (SJC) and Cachoeira Paulista (CPA), a big, medium sized, and small city, respectively. In São Paulo and São José dos Campos, the spectral global horizontal irradiance was measured by means of weatherproof grating spectroradiometers. In Cachoeira Paulista, the measurements were conducted with an optical fiber spectroradiometer coupled with an optical interface developed at INPE's laboratories especially for this application. Such apparatus was designed and developed to collect the solar spectrum with maximum efficiency along 400 to 1700 nm from 2π sr and to resist weather effects. The whole set was calibrated with a FEL NIST standard lamp. The results obtained in this work are analyzed and compared to previously published experimental and modelled spectral impacts on PV behavior results collected in low-latitude areas. The reliability of a parameter developed to describe the influence of the spectrum on PV devices was also investigated.

We present a literature review in Section 2. We describe the technical characteristics of the measuring facilities employed in conjunction with the parameters and methods used for the data analysis in Section 3. We present the characterization of the solar spectrum in São Paulo, São José dos Campos and Cachoeira Paulista, followed by the spectral impact computed for various PV technologies on instantaneous, monthly and annual timescales in all cities in Section 4. Then, we compare the latest results with findings of previous experimental and simulated studies. We also discuss the outcomes related to the investigation on the reliability of a given spectral parameter as a spectral indicator. Finally, we present the conclusions of this work in Section 5.

2 OBJECTIVES

The present work aims at investigating the effects caused by spectral distribution variation on the solar resource of three Southeastern Brazilian sites in different PV materials. In this regard, two state-of-the-art spectra data acquisition systems were employed in conjunction with a system developed in this work designed and configured for each observation site. The objectives of this thesis are listed below:

i. To develop a reliable and low-cost solar spectral data acquisition system for outdoor measurements.

ii. To characterize the solar spectrum in three Brazilian cities: São Paulo, São José dos Campos and Cachoeira Paulista, comparing the results with those found in mid-latitude sites acquired through ground-based measurements and simulations.

iii. To investigate how local atmosphere is affecting the solar spectrum on daily, monthly, and seasonal timescales, aiming to determine which atmospheric compounds are causing such impacts.

iv. To investigate the spectral effects on six PV technologies from different solar cell generations on an instantaneous, monthly and annual basis.

v. To verify the reliability of a spectral parameter widely used for the analysis of solar spectra as an indicator of spectral effects.

3 LITERATURE REVIEW

3.1 Photovoltaic solar energy overview

Increasing amounts of energy have been required over the last decades in order to promote social and economic development. Since approximately the mid-19th Century, such demand has been met mostly through fossil fuels (coal, oil, and gas) combustion, emitting greenhouse gases species (such as CO_2, CH_4, N_2O, etc.) and particulates (anthropogenic aerosols) into the atmosphere. At the same time, Earth's surface temperatures have increased at an unprecedented rate in last decades. As outlined by the Intercontinental Panel for Climate Changes (IPCC) (2021a), the observed rise in the Earth's average temperature is driven by human activities, showing strong evidence that there is a near-linear relationship between cumulative anthropogenic CO_2 emissions and global warming. Changes in the world's climate induced by human activities are already affecting many regions across the globe, increasing the frequency and intensity of hot extremes, marine heat waves, heavy precipitation, droughts, etc. The IPCC last report *'Global Warming of 1.5°C'* (IPCC, 2018) is categorical in stating that such events will become increasingly common and dangerous, causing social, environmental, and economic damage. Therefore, limiting and preventing greenhouse gas emissions on a global scale together with adaption initiatives are crucial to avoid or at least minimize harmful climate impacts (IPCC, 2014).

In view of the above, international conferences aiming to promote climate change mitigation policies have been conducted worldwide. In 2019, during the United Nation's Climate Change Conference COP25, 77 countries joined the Climate Ambition Alliance (COP25) committing to achieving net-zero CO_2 emission by 2050 (COP25, 2021). A more sustainable development is coming true, but there is still a long way to go. As displayed by Figure 3.1, in 2020, renewable energy (RE) sources (i.e., hydropower, wind, solar, geothermal, biomass, wave, and tidal) comprised around 27% of global electricity generation and around 11% of global total energy generation (electricity, transport, and heat) (BP, 2020; IEA, 2021a). Adding RE's share to nuclear, one can say that around one-third of global electricity is derived from low-carbon sources, differently from the global total

energy generation mix. Hence, reaching long-term climate targets requires more effective actions to be taken globally by all nations to promote a transition of fossil fuel to a more efficient cost-effective renewable energetic matrix (IRENA, 2021a; IEA, 2021b).

Figure 3.1 - Global electricity (top) and total energy generation (bottom) mix in 2020. Other renewable sources include geothermal, biomass, wave and tidal.
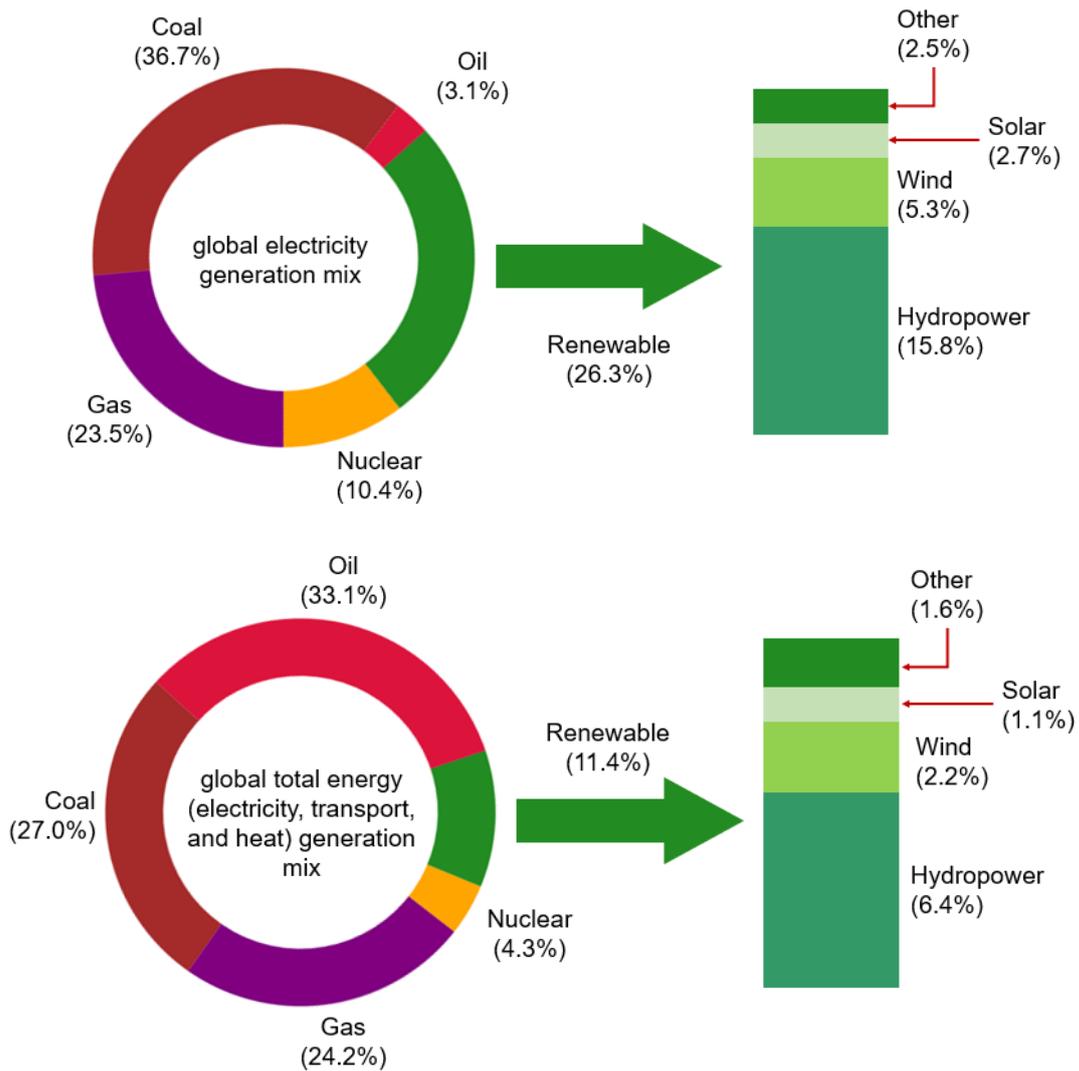
Source: Adapted from BP (2020) and IEA (2021a).

Regardless of the current small share of total energy generation, sustainable sources have been on the rise and receiving the biggest investments in the energy segment in the last decade (BP, 2020; IEA, 2021c). Figure 3.2 depicts the

evolution along the last ten years of the main electricity sources, where a rising of the mentioned sustainable source adoption can be seen. Moreover, some of RE technologies are going through a very significant growth, including over the 19-covid pandemic (REN21, 2021). During 2020, the primary energy consumption decreased by 4.5%, thus implying a reduction of around 6% in CO_2 emissions (BP, 2021). While oil, coal, and natural gas decreased in this period, renewable energy experienced an annual capacity addition increase of 45%, with almost 280 GW installed capacity. A major part of this amount corresponds to the installation of new wind and solar plants, which expanded 238 GW, a fraction 50% larger than that of   any other time in history (BP, 2021; IEA, 2021e). Furthermore, renewable sources are set to provide more than half of the increase in global electricity supply in 2021, with solar PV and wind contributing with two-thirds of such growth (IEA, 2021d). Cost reductions, faster learning, and developments, in conjunction with support policies have driven such growth (REN21, 2021; BP, 2021). However, continuous innovation, securing strategic political support, and increasing technology efficiency, will be required to meet long-term environmental goals.

Figure 3.2 - Global electricity generation mix evolution over the last decade.
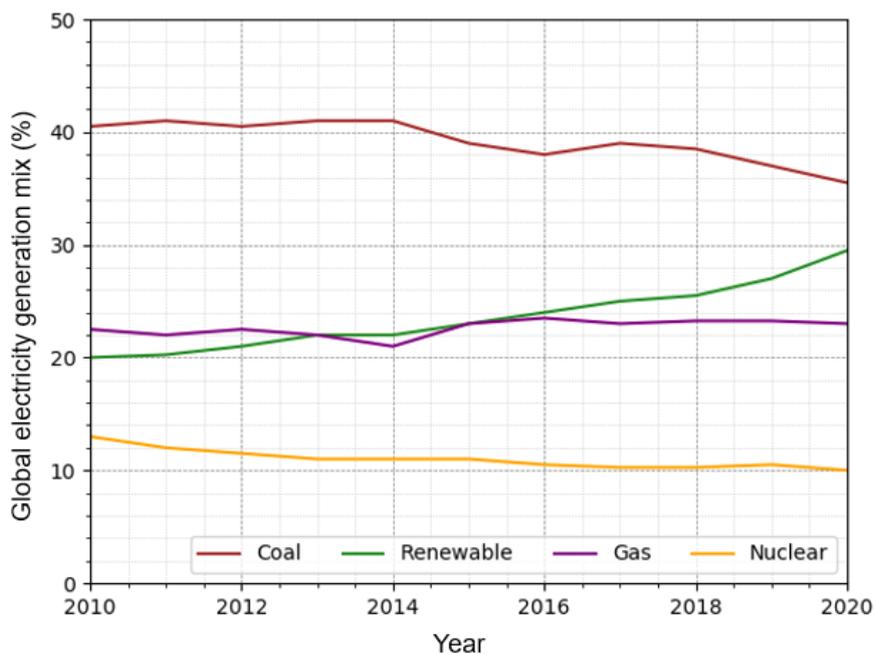
Source: Adapted from IEA (2021a).

3.1.1 Photovoltaic solar energy

According to Luque and Hegedus (2002), photovoltaic (PV) solar energy is the technology that converts sunlight into direct current (DC) electrical power through semiconducting devices called solar cells. Due to the use of solar radiation for electricity generation, this source has low pollution levels during its useful lifetime. In this sense, PV production is an affordable and sustainable energy that can help to mitigate global warming. Moreover, such energy source has other advantages that have also contributed to its popularity and expansion such as the easy assembly of power generation systems with a wide range of output power in a centralized or distributed configuration, its easy integration to other structures (buildings, roofs, etc.), and its low operating costs, etc. On the other hand, it also has disadvantages that limit its expansion as solar intermittence. For a better understanding, PV energy pros and cons are listed in Table 3.1.

Table 3.1 - Advantages and disadvantages of solar PV energy.

Advantages	Disadvantages
Practically infinite and free source	Sunlight is a relatively low-density energy source
High availability	Lack of economical efficient energy storage.
Low operation and maintenance costs	Non-dispatchable resource
Easy integration to pre-installed structures (buildings, roofs, etc.)	High initial cost
Operation at ambient temperature	Lower capacity factor than fossil-fired and nuclear electricity generation techniques
Generators (PV modules) with long lifetime (higher than 25 years)	
Can be built with a vast range of power output (from smaller to bigger power plants)	
Potential to help with the reduction of greenhouse gases emissions	

Source: Adapted from Luque and Hegedus (2002) and Sampaio and Gonzáles (2017).

Solar PV energy has been one of the fastest growing markets in the renewable energy sector. According to the Fraunhofer Institute for Solar Energy Systems (2021), between 2010 and 2020 the compound annual growth rate (CAGR) of cumulative PV installations was 34%. In the same period, the total cumulative capacity installed worldwide expanded from 40 GW to 708 GW (BP, 2021; IRENA, 2021b). Figure 3.3 displays this evolution specifically for each region of the world. Only in 2020, 139 GW of new PV capacity were installed worldwide, avoiding the emission of 877 Mt of CO_2. It is the largest growth in capacity installation ever seen in a single year even with the economic impacts of COVID-19 pandemic, with Asian countries on the lead for the eighth consecutive year. As depicted by the chart shown in Figure 3.4, together with some countries from the Pacific, Asia accounted for nearly 61% of global PV market in 2020. Such growth was led by China, which experienced an increase of almost 60% on its PV market in 2020 in part because of changes in its feed-in tariffs, reaching 253.4 GW of PV capacity. The same happened to Japan, Korea, Taiwan, and Malaysia, while India went through a contraction due to pandemic-related lockdowns and labor shortages. The Americas was the second biggest global PV market in 2020 with a share of 18%, mainly because of the United States of America, which ranked as the second globally for new installations and total capacity (19.2 GW were added and 93 GW were reached). In this sense, it is worth noting that Brazil, Chile and Argentina also contributed towards such expansion, adding almost 5 GW put together followed by Europe, with more than 22 GW added in a single year totalizing 162.7 GW. Germany was on the lead with 4.9 GW added, followed by The Netherlands (3 GW), Spain (2.8 GW), Poland (2.6 GW) and Belgium (1 GW). In the Middle East and Africa 4 GW were implemented as a whole, with Turkey and South Africa installing 1 GW of capacity each. In the South Pacific, Australia still has the largest market, being the seventh for new installed additions and total capacity in the global ranking (REN21, 2020; IEA-PVPS, 2021b).

Figure 3.3 - Solar PV global capacity over the last decade by region.
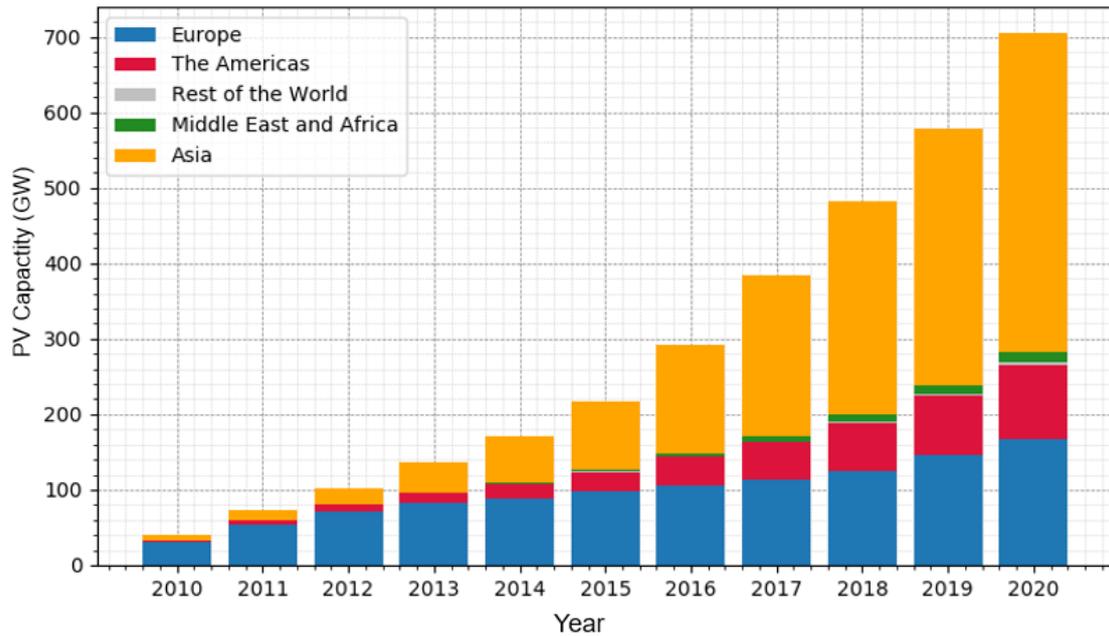
Figure 3.4 - Global PV market in 2020 shares by region.
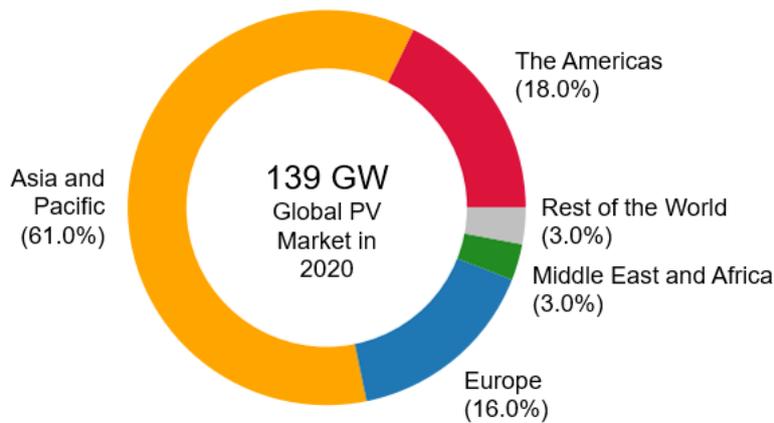
Nowadays, China, the United States, Japan, Germany, India, Italy, Australia, Vietnam, Republic of Korea, and United Kingdom are at the top globally for solar PV installations, comprising more than 70% of the world's total capacity - their share are depicted by Figure 3.5. Despite being concentrated in these countries, PV solar source already has a significant share in the electricity mix of several nations (REN21, 2021; JAEGER-WALDAU, 2019; AJADI et al., 2020), expected

to keep expanding in the short-term, i.e., within one to two years (IEA, 2021e). Driven by falling costs, effective policies, market competitiveness, and huge investments, PV is already the most competitive option for electricity generation in many countries, principally those with favorable policies and high availability of solar resource (IEA, 2021e). As an example, Figure 3.6 depicts the historical averages of the Levelized Cost of Energy Comparison (LCOE) of utility-scale generation techniques in the United States of America. As one can see, PV was the most competitive technique in 2020. This has helped to enable the insertion of countries with low PV fraction of their energetic matrix into the top ten PV national markets in the last decade, as Vietnam and Brazil, which added 11.1 and 3.1 GW, respectively in 2020 (REN21, 2021). Figure 3.7 displays the PV capacity added by the top ten countries in the same year.

Figure 3.5 - Top 10 countries for PV installations additions in 2020.
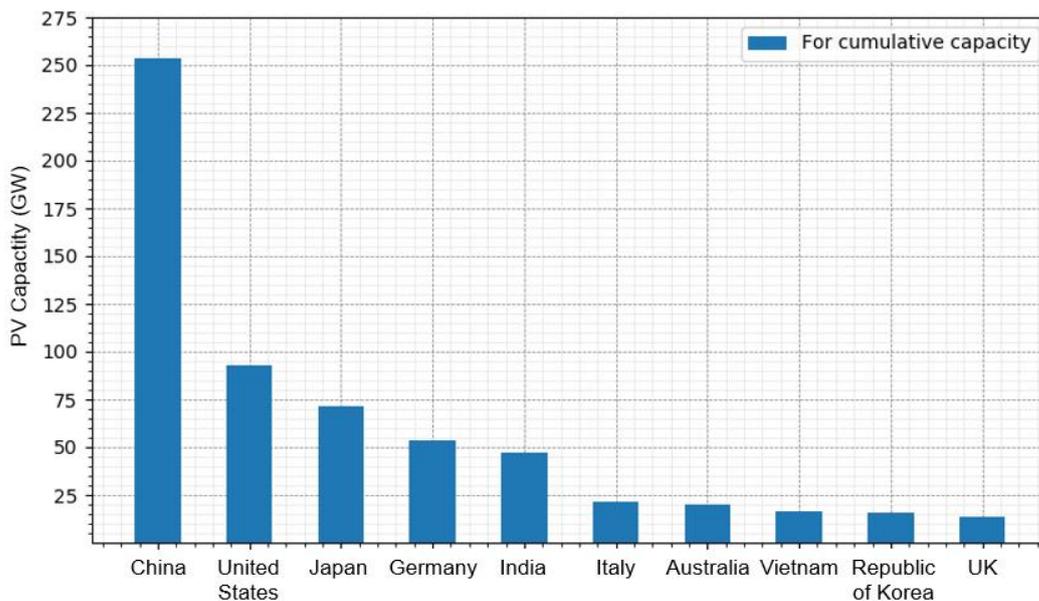
Source: Adapted from IEA-PVPS (2021).

Figure 3.6 - Historical unsubsidized LCOE for some utility-scale generation techniques in USA.
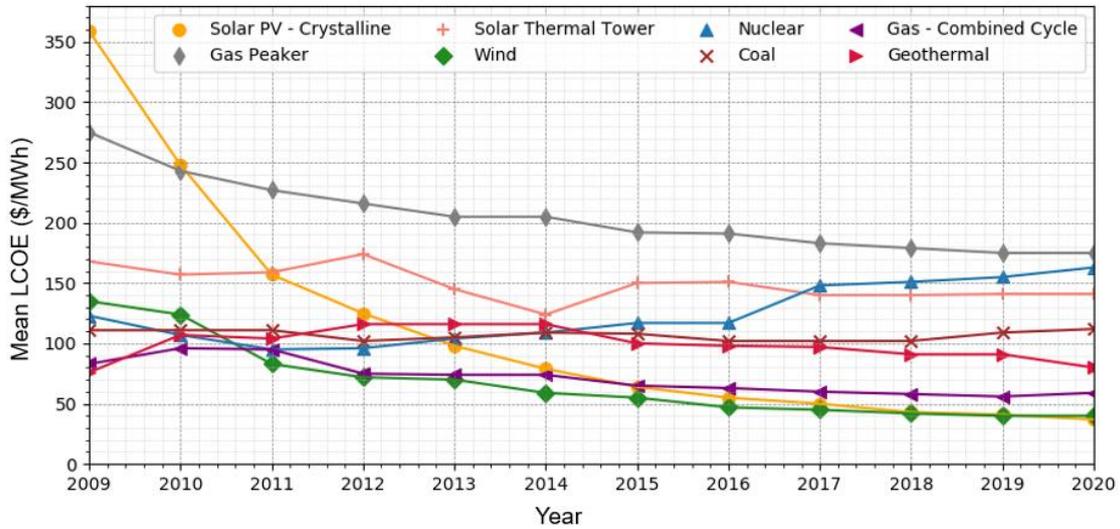
Source: Adapted from Lazard (2021).

Figure 3.7 - Top 10 countries for total installed capacity in 2020.
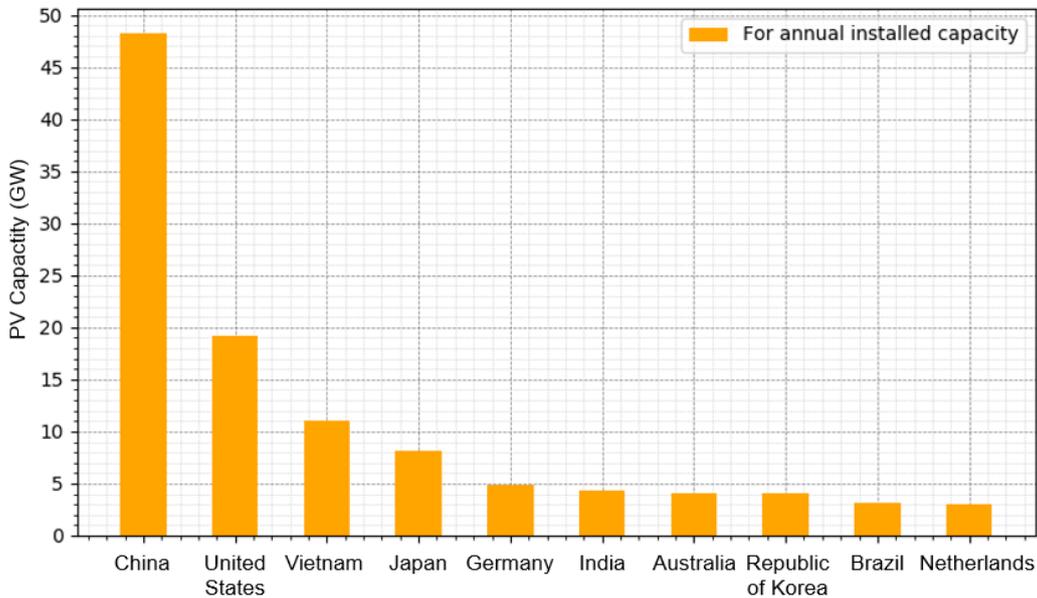
Source: Adapted from IEA-PVPS (2021)

After a huge solar installation expansion in 2019, Vietnam added around 11 GW, rising to the third place in global PV additions. The rapid Vietnamese growth in solar generation largely aims at meeting rising electricity demand as well as ensuring energy security and reducing carbon emissions (REN21, 2021). Thus,

since 2014 some Chinese companies have been making investments to increase the production capacities not only in Vietnam, but also in other countries such as Malaysia or Thailand. As costs plummet, more and more PV markets are emerging in different areas, many of them located in tropical and sunny regions of the world with a promising growing potential for this technology (REN21, 2020; IEA-PVPS, 2021b). Bearing in mind that almost 70% of the projected increase in global energy demand in the short-term will take place in emerging markets and developing economies (IEA, 2021d), and that PV solar can help supplying such demand, it is crucially important to include these technologies when developing specific energy strategies and broadening knowledge for these nations.

3.1.2 Photovoltaic solar energy in Brazil

Brazil is a South American country with continental dimensions, with the Atlantic Ocean to the east and crossed by the Equator in the north and the Tropic of Capricorn in the southeast. Almost 90% of its territory is within the tropical zone and is in a fraction of the globe that receives considerable high amounts of solar radiation. For a better understanding, Figure 3.8 shows the annual averages of solar resources in the five geopolitical Brazilian regions. Their solar resources range between annual average horizontal irradiation values of 1600— 2200 $kWh \cdot m^{-2}$ and are comparable or even higher than those of countries with a well-consolidated solar energy market, such as Germany (900 to 1250 $kWh \cdot m^2$) and Spain (1200 to 1850 $kWh \cdot m^2$) (PEREIRA et al., 2017). Brazil's vast territory as well as its environmental characteristics and high availability of solar resource make solar PV energy a promising alternative for electricity supply.

Figure 3.8 - Values of annual average daily horizontal irradiation in the five Brazilian geographic regions.
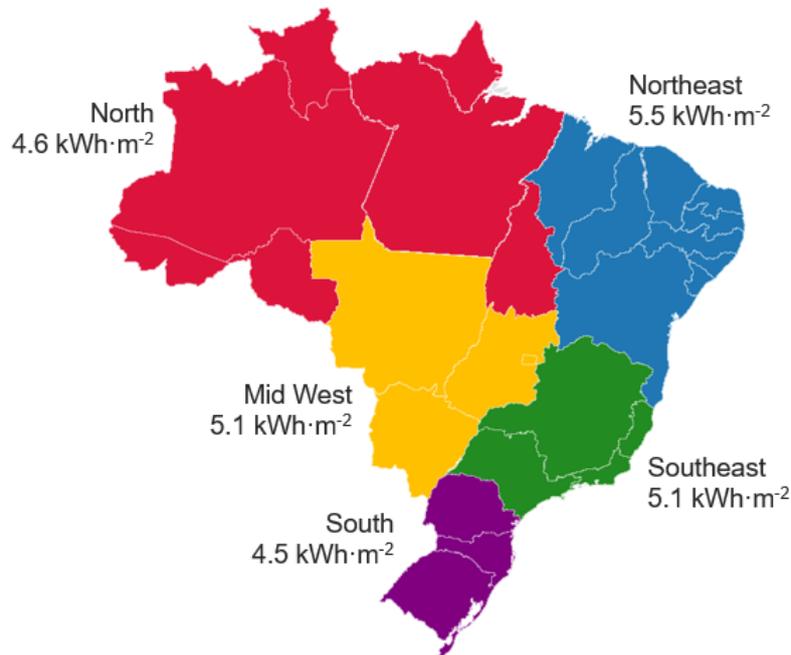
Source: Adapted from Pereira et al. (2017).

Brazilian electricity mix is composed of renewable energy whose share reached as much as 84.8% in 2020 (EPE, 2021). According to the Energy Research Office (*'Empresa de Pesquisa Energética'*, EPE) (2021), the biggest contributor to the RE's share is the hydropower as depicted by the chart shown in Figure 3.9. Despite being the highest contribution to electricity generation in Brazil, such source has lost space, declining from 79.1% in 2010 of total electricity generation to 65.2% in 2020 (EPE, 2011; 2020). On the other hand, sources such as solar, wind, and biomass had their combined fraction elevated from 5.3% to 19.6% in the same period. The decrease in the use of power generated by water is due to the lack of investment in new hydropower plants and to the necessity of energetic matrix diversification. Another reason is related to the risks of climate change, in view of the long droughts that have plagued the country in the last decade (QUEIROZ, 2019).

Figure 3.9 - Brazilian electricity generation mix in 2020.
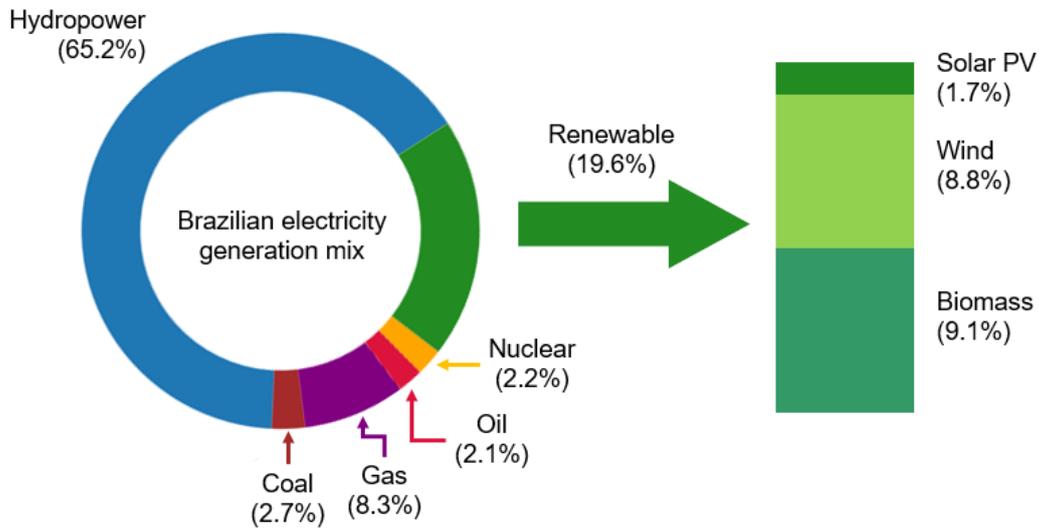
Source: Adapted from EPE (2021).

This scenario of solar resource abundance, tropical weather, the drought that affected the Brazilian hydroelectric plants in 2013 – 2015 (BARRUCHO, 2021), and the future insecurity caused by global warming, has prompted the fast growth of the Brazilian solar market during the last few years. Driven by increasing energy demand, decreasing PV costs (FRAUNHOFER ISE, 2021), a national net metering regulation, and electricity prices rising above inflation rates (REN 21, 2021), 3.1 GW of solar PV were installed –an amount almost 68% higher than that of the previous year-2020, reaching almost 7.8 GW of cumulative PV capacity in the same year. Figure 3.10 shows the evolution of the Brazilian PV installed capacity with generation mode -centralized or distributed- highlighted. In this chart, a significant rising in installation additions can be observed from 2017 till now. Such growth has partly been driven by the technology-specific auctions promoted by the Brazilian government since 2014 to expand renewable-based electricity capacity. Thus, during the first Reserve Energy Auction (*'Leilões de Energia Reserva'*, *LER*, in Portuguese) held in 2014, 31 projects to provide around 1048 MWp were established (EPE, 2014) and 1050 solar projects have been registered for 41.852 MW capacity (ANEEL/ABSOLAR, 2021) in the last

auction, which took place in July 2021. Such increase in energy supply indicates how Brazilian solar PV market may grow in the coming years.

Figure 3.10 - Brazilian PV capacity growth over the last years.
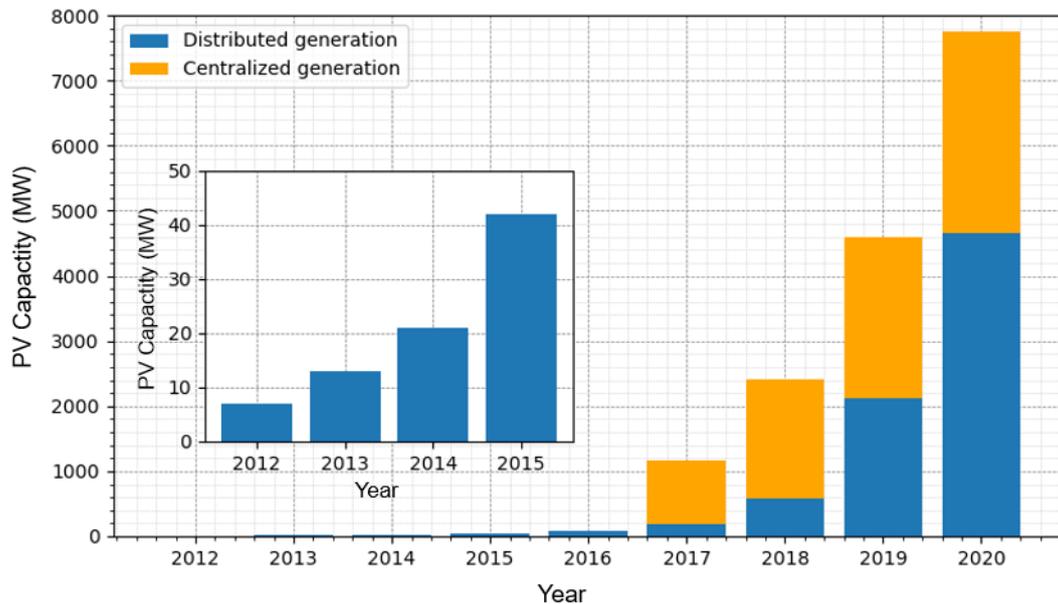
Source: ANEEL/ABSOLAR (2021).

Figure 3.10 also shows that, for the second uninterrupted year, the majority of installed PV capacity falls into the distributed generation market. With an increase of 137% of 2020 over 2019 (EPE, 2021), micro and mini distributed generation (MMDG) is a segment in expansion and in the former year it represented 60% of the total Brazilian PV installed capacity (ANEEL/ABSOLAR, 2021). Such current growth is motivated by the easier commercialization, higher number of consumers, and more independency from government intermediation. Nowadays, most of the centralized generation (CG) projects are still dependent on the previously mentioned government auctions. On the other hand, because of the lower output power, MMDG has been purchased for domestic and commercial energy supply (ANEEL/ABSOLAR, 2021). In this sense, the latter happens with lower bureaucracy and faster returns on investment, contributing to a higher market share. Minas Gerais and São Paulo are the two federals units leading the growth of distributed energy generation as shown in the MMDG ranking displayed in Figure 3.11. The high energy fees and taxes, low cloudiness,

and their low level of hydropower generation (LUNA, et al., 2019) explain their high positions in the rank. Minas Gerais also has the highest fraction of CG installations, with around 6600 MW of PV capacity installed, under implementation and to be installed in the short-term (ANEEL/ABSOLAR, 2021).

Figure 3.11 - Top 5 Brazilian federal units for distributed PV cumulative capacity.
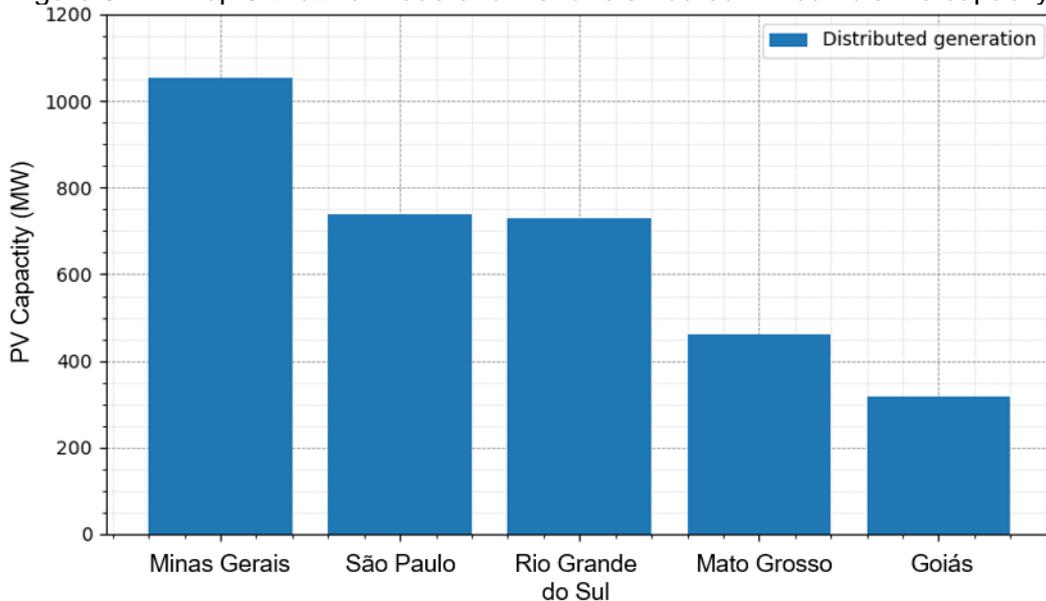
Source: Aneel/Absolar (2021).

3.2 Solar radiation

The sun is the center of our Solar System and the most important energy source for life on Earth. It is basically an ionized gas sphere whose radius and mass equal 6.9626 ($\pm$ 0.0007) x 10^8 m and 1.9891 ($\pm$ 0.0012) x 10^{30} kg, respectively (YAMASOE, CORREA, 2016). It is mainly composed of hydrogen and helium and has traces of heavier elements such as oxygen, carbon, nitrogen, iron, etc. Because of thermonuclear reactions converting four atoms of hydrogen into one of helium in its interior, the Sun emits electromagnetic radiation to its surroundings similarly to a blackbody at the same temperature of its photosphere. The Sun's temperature decreases from 5 x 10^6 K in its core to around 5800 K on its surface (also called photosphere) (LIOU, 2002). A comparison between both spectral radiation is shown in Figure 3.12. However, the extraterrestrial solar spectrum differs from the blackbody's spectral radiation curve due to the radiation emitted by some gases in the solar outermost regions.

17

Figure 3.12 - Spectral distribution of extraterrestrial solar radiation and radiation emitted by a blackbody at 5800 K.
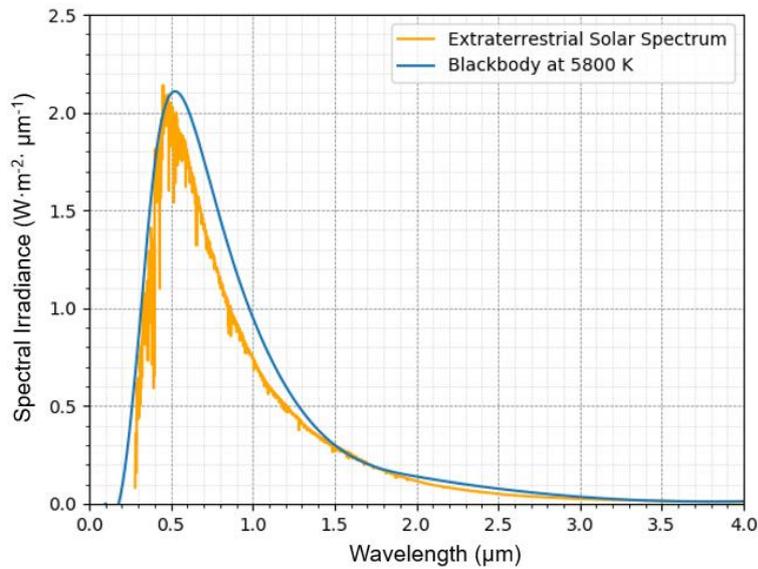
The amount of energy reaching the top of the Earth's atmosphere has been measured by different techniques and instruments such as aircrafts and satellites since the early 1970s (IQBAL, 1983; LIOU, 2002). The rate of solar energy integrated over the electromagnetic spectrum per unit area perpendicular to the direction of the Sun considering the average distance between the star and the planet is known as the *Total Solar Irradiance* (*TSI*, in W·m^{-2}), also known as *Solar Constant*. However, values of *TSI* depend on the methodology used in the measurements. Thus, different institutions around the world adopt different values for such parameter. The American Society for Testing and Materials (ASTM) stated in ASTM E490-00a (ASTM, 2019) a standard value for *TSI* 1366.1 $\pm$ 2.5 W·m^{-2}. This value was obtained through the mean of daily average of data collected with absolute cavity radiometers installed in six different satellites between 1978 and 1998.

The *Total Solar Irradiance* varies as consequence of internal physical processes on the Sun and of astronomical relations between the star and the Earth. Solar activity increases and decreases in a time interval of around 11 years as magnetic field flux erupts, evolves, and decays at different rates generating sunspots that

modulate total and spectral solar radiative outputs (LIOU, 2002; HATHAWAY, 2010). According to Solanki (2003) sunspots are magnetic structures visible in the solar photosphere that have lower temperatures and therefore darker coloration than the rest of the photosphere. During the 11-year cycle, the number of sunspots increases and decreases, and this variation is related to the variation of the Solar Constant, as shown in Figure 3.13.

Figure 3.13 - Daily total solar irradiance obtained by the Solar Radiation and Climate Experiment (SORCE) by NASA for the period from 2003 to 2020.
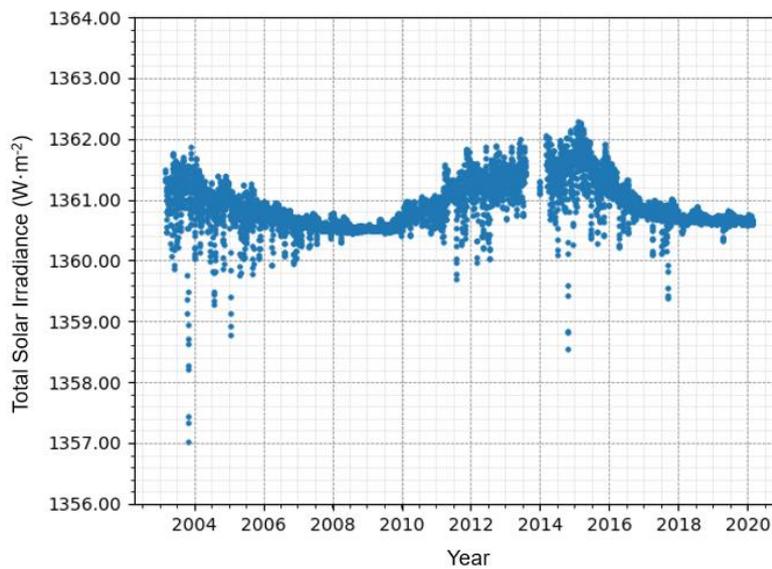
Source: Adapted from LASP (2021).

3.3 Atmospheric effects on solar radiation

At the top of terrestrial atmosphere, solar radiation varies as function of the Earth-Sun astronomical relations and processes happening inside the Sun (as the rising and the vanishing of sunspots). Once solar electromagnetic waves enter the atmosphere, they interact with atoms, molecules, and particulates which attenuate the incident radiation before reaching the Earth's surface in terms of magnitude and spectral distribution. The attenuation (or extinction) is a consequence of absorption and scattering of the incoming radiation. Absorption is the physical process in which photons are absorbed by molecules (such as O_2) or particles (such as soot) and transformed into thermal or kinetic energy.

Scattering is a process in which the photons are scattered out of their original direction into different possible directions (RUIZ-ARIAS; GUEYMARD, 2015). Because of such effects, the spectral distribution of solar irradiance is distorted as shown in Figure 3.14, which compares these curves at the top of the atmosphere with an example of the Earth's surface.

Figure 3.14 - Spectral solar irradiance at the top of the atmosphere versus on the Earth's surface.
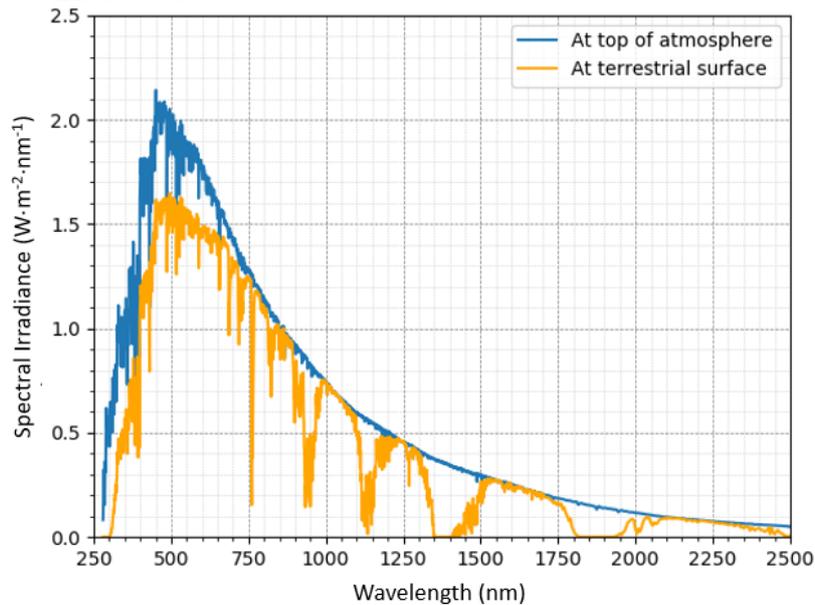
Source: Adapted from Iqbal (1983).

As a result of these interactions, the decomposition of the incident sunlight beam is divided into different components. For an observer (as a radiometer, for example) on a horizontal plane on the Earth's surface as illustrated by Figure 3.15 (a), the fraction of solar radiation arriving in a straight line without being deviated by the atmosphere is called direct radiation. Another fraction is scattered throughout the atmosphere, which in part returns to space and in part reaches the ground. The scattered radiation coming from all directions in the sky, apart from the sun's disk, is called diffuse radiation. The sum of the direct and diffuse irradiances arriving at a horizontal plane is called global radiation (IQBAL, 1983; LUQUE; HEGEDUS, 2002). For the PV panel tilted at an angle X [°] relative to the horizon illustrated in Figure 3.15 (b), the total radiance incident is the sum of the direct, diffuse, and reflected radiation by the ground, known as albedo

(HARBELIN, 2012). The spectral distribution of the global, direct, and diffuse solar radiation is plotted on Figure 3.16. In practical terms, the following definitions were adopted hereafter in accordance with the terminology presented in ASTM E772 (2015) standard to describe the solar radiation's fraction discussed previously:

i. Direct normal irradiance (*DNI*, in W·m⁻²): solar irradiance arriving from the solid angle of the sun's disk (generally around 6°) to a plane perpendicular to sunlight rays.

ii. Diffuse horizontal irradiance (*DHI*, in W·m⁻²): solar irradiance received on a horizontal surface from a hemispherical field of view, apart from a solid angle within 5° concentric to the sun's disk.

iii. Global horizontal irradiance (*GHI*, in W·m⁻²): solar irradiance arriving at location from all directions within a hemispherical solid angle (i.e., 2π stereoradians). *GHI* comprises the direct and diffuse solar radiation as follows:

$$GHI = DHI + DNI \cdot cos(\theta_Z) \qquad (3.1)$$

Where θ_Z [rad] is the zenithal angle.

iv. Global tilted irradiance (*GTI*, in W·m⁻²): solar irradiance incident on a non-horizontal stationary surface under a hemispherical solid angle.

Figure 3.15 - Solar radiation's components for an observer at Earth's surface on (a) a horizontal plane and (b) a tilted plane.
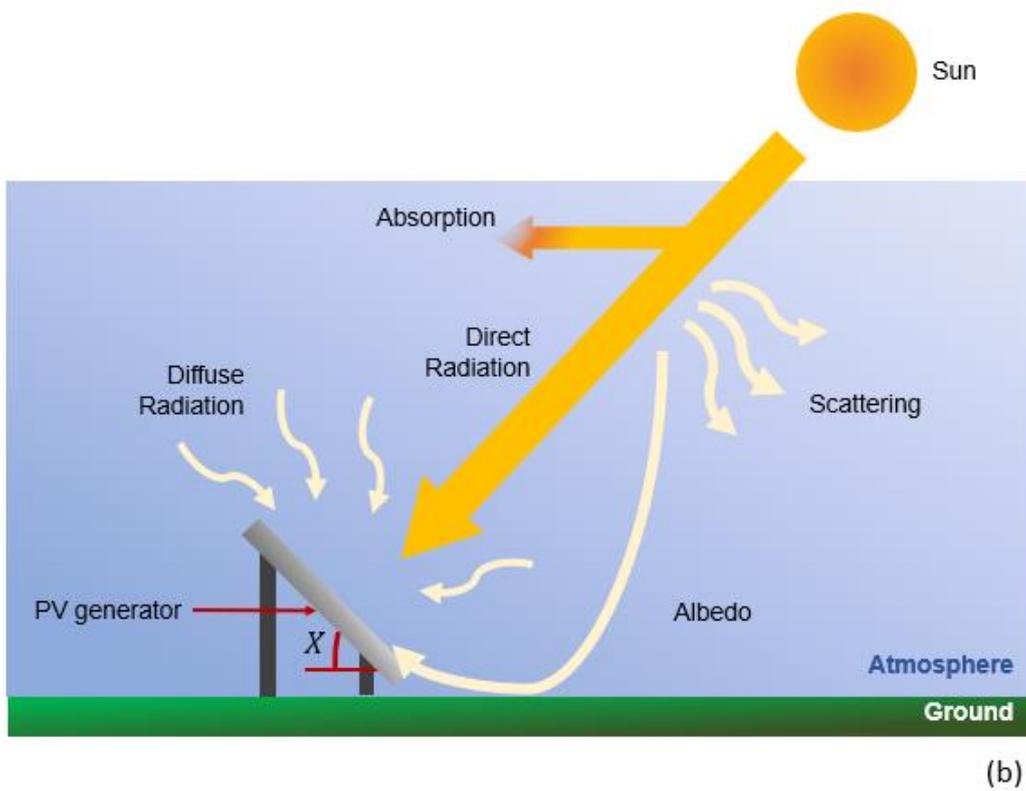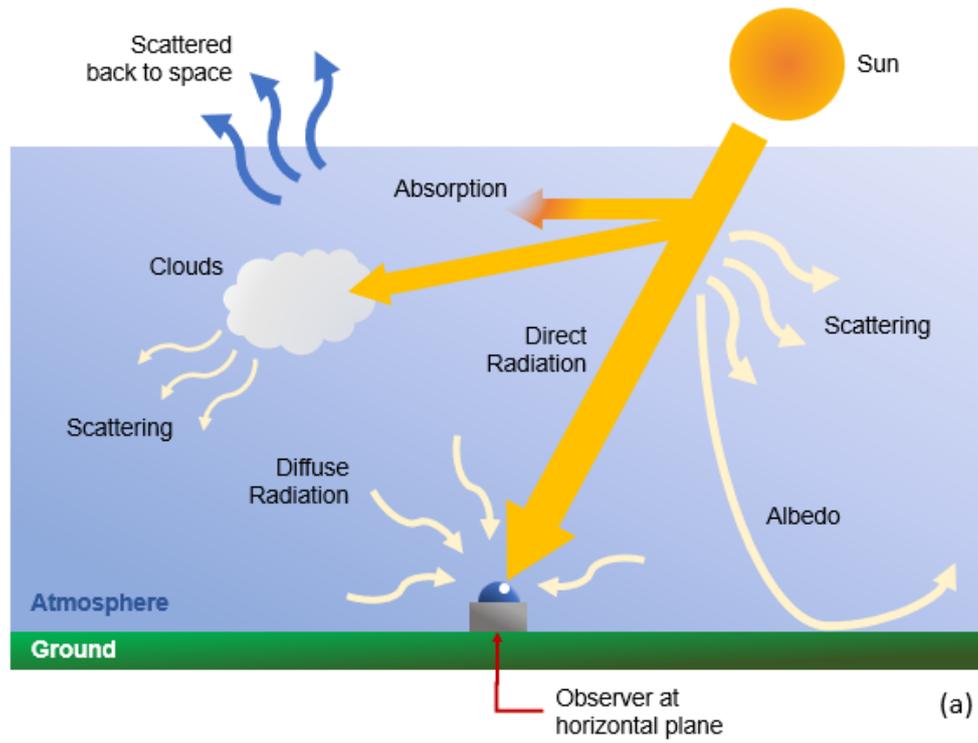
Source: Adapted from Iqbal (1983).

Figure 3.16 - Spectral distribution of solar global horizontal irradiance; direct normal irradiance; and diffuse horizontal irradiance.
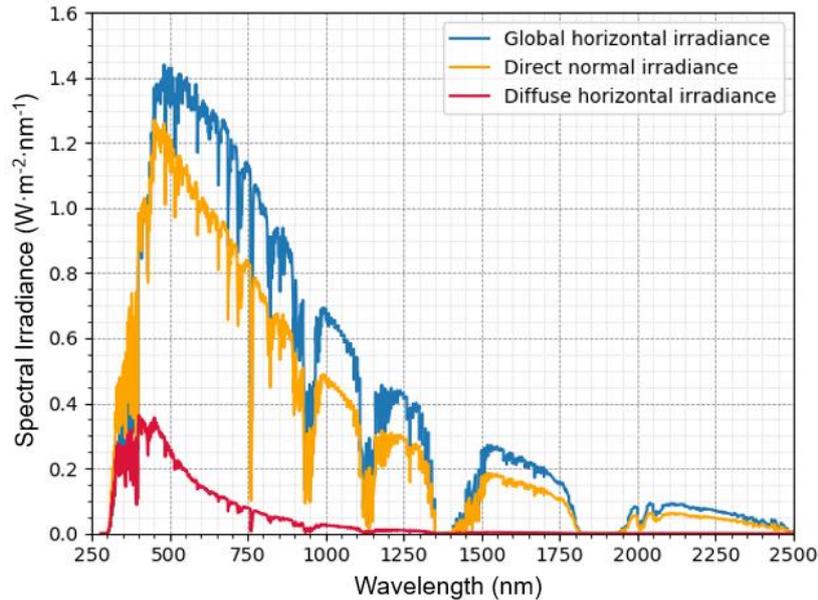
Curves generated with *SMARTS2* radiative transfer code (GUEYMARD, 1995;2001) for the U.S. Standard Atmosphere (NOAA, 1976), Rural aerosol profile proposed by Shettle and Fenn (1976), on an inclined surface with 37°.
Source: Author.

Solar resource impinging on Earth's surface can be measured or estimated through three different techniques: ground observation, numerical modelling, or satellite remote sensing. Ground observations are carried out through optoelectronic sensors installed in situ, that directly measure the solar radiation properties. Pyranometers are the most reliable way of measuring the solar resource at a specific site if high-quality calibrated sensors are employed (HUANG et al., 2019). On the other hand, this method is more difficult to be carried out in remote areas and does not have a large area coverage. Numerical modelling combines available observations with atmospheric models to produce solar data over time and space on regional or global scales. In this sense, they can produce complete and consistent databases, being very important for long-term climate monitoring and analysis (DECKER, 2012; HUANG et al., 2019). Lastly, satellite remote sensing estimates solar radiation by computation through different algorithms (e.g., physical and/or statistical radiative transfer models, machine learning, etc.) with cloud, aerosol, surface variables and other atmospheric parameters as input (TAN et al., 2016; HUANG et al., 2019; LIAN et

al., 2019). These parameters are measured with narrow or broadband radiometers onboard satellites (DEWITTE; CLERBAUX, 2017). As numerical modelling, such technique also has a large geographical coverage with different scales and resolutions. Furthermore, as the spatial distribution and evolution of clouds are easily measured by satellites, this technique is considered the best way to estimate the components of solar radiation on regional and global scales (HUANG et al., 2019).

3.3.1 Atmospheric composition

The atmosphere is a set of layers made of a fluid and composed of a mix of gases, aerosols and clouds that surround the Earth, held in place by gravity. Because of its interactions with solar radiation, the Earth's surface and its inner processes, suffer physical and chemical property variations as a function of space and time (KILLINGER; CHURNSIDE; ROTHMAN, 1995; RUIZ-ARIAS; GUEYMARD, 2015).

3.3.1.1 Gases

The atmosphere is composed in its majority of O_2 and N_2, which together comprise more than 98% of its volume. Together with other gases listed on Table 3.2, these gases are classified as permanent, once their volume ratio is virtually constant up to 60 km of altitude (LIOU, 2002). In contrast, CO_2, CH_4, and NO_2 concentrations have increased since pre-industrial times due to human activities (IPCC, 2013). Therefore, these gases are not homogeneously distributed throughout the atmosphere, such as those termed as variable constituents listed on Table 3.2 (IQBAL, 1983; LIOU, 2002). Their concentrations vary owing to anthropogenic activities and general atmospheric dynamics (IQBAL, 1983). Even though they account for a minor fraction, variable constituents exert an important impact on radiative energy budget of atmosphere, especially those termed as *greenhouse* gases (YAMASOE; CORREA, 2016). The atmospheric gases contribute to the extinction of solar radiation through molecular scattering in a continuum process along wavelengths (λ, in μm or nm) and some of them (as oxygen, ozone, methane, water vapor, etc.) absorb radiation in different parts of the solar spectrum, known as absorbing bands (IQBAL, 1983; LIOU, 2002).

Table 3.2 - Atmospheric composition of sea-level dry air.

Permanent constituents		Variable constituents	
Gas species	% by volume	Gas species	% by volume
N_2	78.0840	H_2O	from 0 to 0.04
O_2	20.9476	O_3	from 0 to 0.12 $\times 10^{-4}$
Ar	0.9340	SO_2	0.001×10^{-4}
CO_2	0.0314	NO_2	0.001×10^{-4}
Ne	18.18×10^{-4}	NH_3	0.004×10^{-4}
He	5.24×10^{-4}	NO	0.0005×10^{-4}
Kr	1.14×10^{-4}	H_2S	0.00005×10^{-4}
Xe	0.089×10^{-4}	HNO_3	trace
CH_4	1.7×10^{-4}	Chlorofluorocarbons ($CFCl_3$, CF_2Cl_2, CH_3CCl_3, CCl_4, etc.)	trace
N_2O	0.3×10^{-4}		
CO	0.08×10^{-4}		
H_2	0.5×10^{-4}		

Source: Adapted from NOAA (1976) and Liou (2002).

All gases previously mentioned are considered as part of a mix called '*clean dry air*' (IQBAL, 1983). When water in gaseous state (i.e., water vapor) is added to such mixture, it becomes '*moist air*'. Water is the most influent substance in atmospheric dynamics (JACOB, 2001; SCHENEIDER; GORMAN; LEVINE, 2010). It can be found in nature in gaseous, liquid, or solid state as water vapor, water droplets and ice crystals in clouds or hydrometeors (rain, snow, etc.), interchanging between them in space and time depending on local hydrological cycles (LIOU, 2002). Because of this variability in addition to large-scale transport processes, water can heat up and cool down the air in its surroundings affecting

atmospheric circulation (JACOB, 2001; SCHNEIDER; GORMAN; LEVINE, 2010). To evaluate the amount of water vapor in atmosphere, a parameter called precipitable water (PW, cm^{-1}) is adopted. According to Iqbal (1983) it can be defined as the total amount of water vapor that could condensate in a unit cross-sectional area extending between the Earth's surface and the top of the atmosphere in the zenith direction (IQBAL, 1983).

3.3.1.2 Aerosols

Aerosols are solid and/or liquid particulates ranging in size from approximately 10^{-4} to around 20 µm suspended in the atmosphere from days to weeks (IQBAL, 1983; LIOU, 2002; YAMASOE; CORREA, 2016). In contrast to permanent gases, their concentration, size, chemical composition, form, etc. vary considerably in space and time and depend on their source and/or on the 'aging' process they may undergo while suspended in the air (YAMASOE; CORREA, 2016). Concerning their sources, they can have a natural or anthropogenic origin. Examples of natural aerosols include volcanic emissions, smoke, and soot from wildfires, dust and sand dragged by wind blows from deserts, biological materials (microorganisms, pollen, etc.), and particles from sea spray (LIOU, 2002; POSCHL, 2005; RUIZ-ARIAS; GUEYMARD, 2015). Particles emitted by fossil fuel combustion, industrial activity, biomass burning, and dust from street pavement suspension are examples of anthropogenic aerosols (YAMASOE; CORREA, 2016). On the other hand, there are species of aerosols (e.g., sulphates, secondary organics) that are not directly emitted, but produced through chemical reactions that occur between some gaseous and aerosol species. They are called secondary aerosols. Main aerosols found in the troposphere around the world are shown in Table 3.3.

Table 3.3 - Main aerosol species in the troposphere.

Aerosol Species	Main Sources	Tropospheric Lifetime
Sulphate	Emitted by marine (through phytoplankton) or volcanic sources. Anthropogenic sources can also create this specie. They are produced by oxidation of SO_2 and S (aging).	~ 1 week
Nitrate	Injected in atmosphere by soil, lighting, or combustion emissions. Produced through the oxidation of NO_2 (aging).	~ 1 week
Black Carbon	Combustion of fossil fuels, biofuels, and biomass.	1 week to 10 days
Organic aerosols	Combustion of fossil fuel, biofuel, and biomass. Continental and marine ecosystems. Some anthropogenic and biogenic non-combustion sources	~ 1 week
Brown Carbon	Combustion of biofuels and biomass. Natural humid- as substances from the biosphere	~ 1 week
Mineral Dust	Wind erosion, soil resuspension. Some agricultural practices and industrial activities (cement)	1 day to 1 week depending on size
Sea Spray	Wave breaking and wind erosion.	1 day to 1 week depending on size

Source: Adapted from IPCC (2013).

Despite the clear distinction into separate aerosol categories shown in Table 3.3, generally mixings of aerosol species are observed in nature (SAMSET et al., 2018). Some studies, therefore, categorize aerosols in general groups consisting of a mix of different species according to type and location where they were found (LIOU, 2002). Some important aerosol groups are listed in Table 3.4.

Table 3.4 - Aerosol's main groups.

Aerosol group	Details	Origin
Rural	Aerosol species of continental areas not affected by urban and/or industrial aerosols sources (Shettle and Fenn, 1976).	Produced in part by reactions between various atmospheric gases and dust particles picked up from the surface (Shettle and Fenn, 1976).
Biomass burning	Comprised by black carbon, organic aerosols, sulphates, nitrates, etc. Generally found in rural areas suffering forest and grassland fires (Dubovick, et al., 2001;).	Produced by burning of forests, savanna, and agricultural waste or by emissions generated by substances burned for fuel (wood, dung, and peat) (IPCC, 2013).
Urban/Industrial	In urban areas the rural aerosol background gets modified by the addition of aerosols from combustion products and industrial sources. It is a mixture of the rural aerosol with carbonaceous aerosols (Shettle and Fenn, 1976).	Fossil fuel combustion in populated regions and industrial activities (Dubovick, et al., 2001).
Desert dust	Found in regions with easily erodible dry soils, little vegetation and strong winds (Mahowald, et al., 2014).	The desert aerosol model has a sand component consisting of quartz particles. Desert dust blown into the atmosphere by wind (Dubovick, et al., 2001).
Marine	Aerosol of marine origin.	The maritime aerosol component is due to salt particles which are caused by the evaporation of seaspray droplets (Shettle and Fenn, 1976).

Source: Author.

Once injected into the atmosphere, aerosols can be transported over long distances causing many different impacts on climate, human health, etc. A region containing aerosols can be called turbid or hazy and they are mostly restricted to the lower atmosphere (IQBAL, 1983; RUIZ-ARIAS; GUEYMARD, 2015). During their lifetime, aerosols can suffer physical or chemical transformation, termed as *aging*, when they change their physical, chemical, and optical properties (YAMASOE; CORREA, 2016; FUZZI et al., 2006). Aerosols are removed from the atmosphere through dry or wet deposition. The former happens through diffusion and adhesion to the Earth's surface and the latter by means of

rainfall, being the main sink of atmospheric aerosol particles. Depending on aerosols properties and meteorological conditions, the period of aerosols' atmospheric suspension range from hours to weeks (POLSCH, 2005; YAMASOE; CORREA, 2016).

Aerosols cause direct and indirect significant impacts on the radiative budget of the Earth on both global and local scales. The direct effects are the scattering and absorption of short and long-wave radiation, which leads to the cooling or heating of the air in its surroundings. By indirect effects, aerosols in the lower atmosphere act like cloud condensation nuclei. In this case, they enhance the liquid water content in clouds, favor an increase in cloud duration and change their optical properties such as reflection and absorption of sunlight (KOMMALAPATI; VALSARAJ; 2009; ROELOFS; 2012; YAMASOE; CORREA, 2016).

3.3.1.3 Clouds

Clouds are water particles in liquid (droplet) and/or solid (crystals) state suspended in the atmosphere. They are formed when moist air is cooled down or moistened until saturation to create condensation or freezing nuclei. If the droplets and crystals become large enough, they become heavier and fall from the cloud as precipitation, such as rain or snow. Depending on where they are formed and on their appearance in the atmosphere, they can be classified into *cirrus* clouds for those with base heights of about 6 km above ground at midlatitude sites; *stratus* and *cumulus* for the ones below around 2 Km; *altocumulus* and *altostratus* if they have a height between 2 Km and 6 Km; and cumulonimbus for those which have a significant vertical development (Liou, 2002). A hazy atmosphere can impact cloud formation as aerosols can serve as cloud condensation nuclei (CCN) or ice nuclei (IN) providing a surface in which water condensates favoring cloud formation (LIOU, 2002; KOMMALAPATI; VALSARAJ, 2009; IPCC, 2013).

Clouds are globally distributed, and their covering depends on different factors. For an easy characterization of the sky condition in terms of cloud cover during

solar radiation measurements, the clearness index K_T (dimensionless) has been adopted (IQBAL, 1983). K_T can be estimated at a given location and time through:

$$K_T = \frac{GHI}{EHI} \qquad (3.2)$$

Where EHI [W·m^{-2}] is the Extraterrestrial Horizontal Irradiance. As explained by Iqbal (1983), according to the clearness index, the sky can be classified into clear, partly cloudy, or cloudy. In Brazil, Escobedo et al. (2009) conducted a study concerning the investigation of ultraviolet, photosynthetically active and near infrared (NIR) parts of solar energy in Botucatu (Southeast Brazil, 22°53'S, 48°26'W, 920 m) and proposed the following categories to objectively classify the sky conditions based on four different intervals of K_T:

i.   Cloudy sky ($K_T \leq 0.35$): global radiation dominated by diffuse radiation.
ii.   Partly cloudy sky with predominance of diffuse component of the solar radiation ($0.35 < K_T \leq 0.55$):
iii.   Partly cloudy sky with predominance of direct component of the solar radiation ($0.55 < K_T \leq 0.65$):
iv.   Sunny sky ($K_T > 0.65$): global radiance composed by direct and diffuse radiation, but the contribution of the latter fraction is small compared to the former.

Figure 3.17 illustrates the relation between the global, direct, and diffuse components of the hourly solar radiation for the different categories of sky's cloud cover.

Figure 3.17 - Hourly average values of global, diffuse and direct components of solar radiation, on the surface, in terms of clearness index intervals.
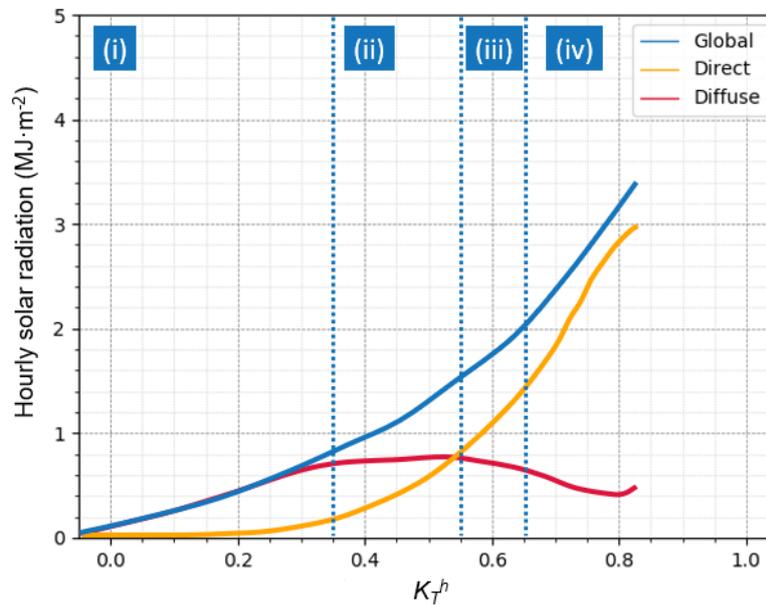
Vertical dashed lines define regions of K_T values associated to sky condition and identified by i (cloudy sky), ii (partially cloudy with predominance of diffuse component of the solar radiation), iii (partially cloudy with predominance of direct component of the solar radiation) and iv (clear sky).
Source: Adapted from Escobedo et al. (2009).

3.3.2 Atmospheric scattering

When solar photons traverse the atmosphere, they can strike gases, molecules, or particulates. The collision deviates solar photons from their original path to different directions without changing their wavelength or frequency in a phenomenon called scattering. Eventually, the scattered photons can strike other particles during their path and be scattered again, a process called multiple scattering (IQBAL, 1983; YAMASOE; CORREA, 2016). Depending on the particle size, different mathematical formulations can be applied to describe the scattering process as illustrated by the graph in Figure 3.18. When the particle is spherical and much smaller than the wavelength of incident radiation, the *Rayleigh's theory* is applied. In case of particles with size of the same magnitude as the incident radiation's wavelength, the *Mie's theory* is applied. For larger particles, the *Geometric Optics* is considered (IQBAL, 1983).

Figure 3.18 - Different scattering regimes as function of particles' radius and incident radiation's wavelength.
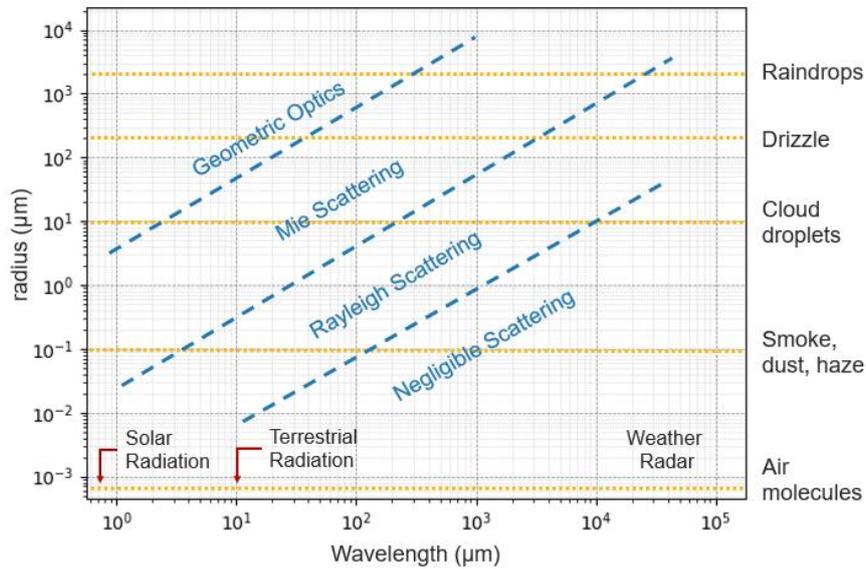
Source: Adapted from Wallace and Hobbs (2006).

The English physicist and mathematician John William Strutt (1842-1919), also known as Lord Rayleigh, proposed Rayleigh's mathematical formulation in 1871. It assumes homogeneous, isotropic, and spherical, particles, with a diameter lower than around 0.1λ, and that they scatter radiation independently of one another (IQBAL, 1983; YAMASOE; CORREA, 2016). According to this theory, the monochromatic transmittance coefficient is approximately proportional to λ^{-4}, which makes the scattering in ultraviolet more intense than that of infrared (IR) regions of solar spectrum. Figure 3.19 shows the spectral transmittance due to Rayleigh scattering caused by the mix of atmospheric gases. The color of the sky can be explained considering such theory. As shown in Figure 3.14 the largest portion of energy received by the Earth from the Sun is contained in the visible (VIS), between the colors blue and red. As the blue light ($\lambda \approx 425$ nm) has a shorter wavelength than that of the red light ($\lambda \approx 650$ nm) its scattering is about 5.5 times more intense than that of the red light. So, in this sense, the sky appears blue because of the more efficient radiation scattering taking place at this wavelength. For higher zeniths (at sunset or sunrise), most part of the visible fraction has already been scattered in a way that the solar spectrum becomes

richer with reddish-colored photons. The more reddish colored photons present in the solar spectrum, the more efficiently scattered they are turning the sky red (LIOU, 2002). Air molecules and smaller aerosols scatter the solar radiation following Rayleigh's theory.

Figure 3.19 - Atmospheric transmittance due to Rayleigh's scattering process and rural aerosols scattering (Mie scattering).
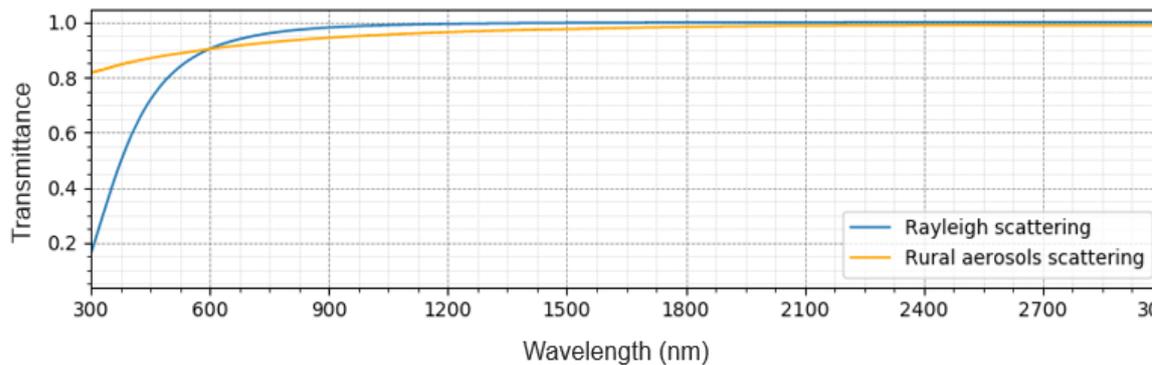
Curve simulated through *SMARTS2* radiative transfer code (Gueymard, 1995;2001) for the U.S. Standard Atmosphere (NOAA, 1976), Rural aerosol profile proposed by Shettle and Fenn (1976), on an inclined surface with 37°.
Source: Author.

For particles with size comparable to the wavelength of the light, as aerosols particles, water droplets and ice crystals, the scattering events can be mathematically described by Mie theory. In this case, the scattered intensity is less dependent on photon's wavelength and is primarily dependent on particle size. As a result, clouds have a white color and non-absorbing aerosols produce the white glare around the Sun (LIOU, 2002). Figure 3.19 shows the transmittance due to rural aerosols. Another difference from Rayleigh scattering is the mode in which photons are spread when they interact with the particles. As shown in Figure 3.20, in the Rayleigh mode the scattering process is maximum for both forward and backward directions and minimum for perpendicular ones to the angle of incidence. In Mie scattering case, photons are more scattered forward compared to the backward direction. Additionally, forward scattering becomes stronger as the particle size increases (IQBAL, 1983).

Figure 3.20 - Different scattering regimes. (a) Rayleigh scattering; (b) and (c) Mie scattering.
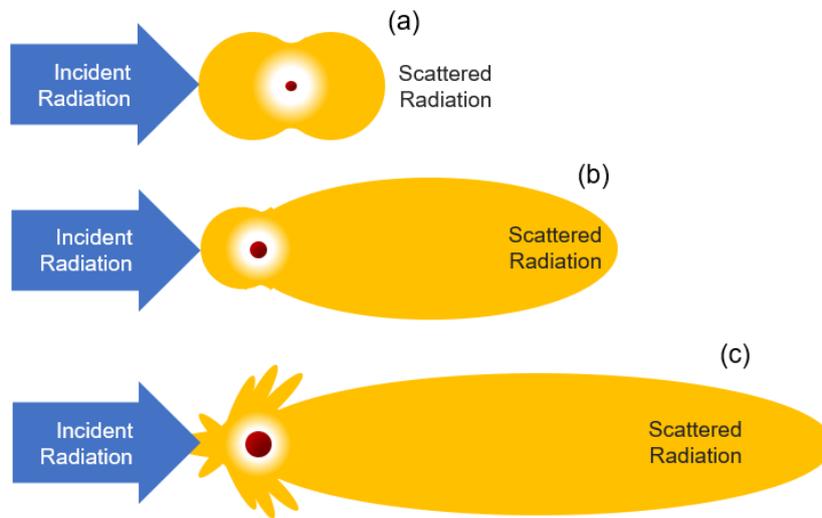
Source: Adapted from Iqbal (1983) and Wallace and Hobbs (2006).

3.3.3 Atmospheric absorption

In addition to the scattering process, the atmospheric components can also absorb part of the incident solar radiation. Differently from the former, the latter process transforms the electromagnetic energy into kinetic and/or thermal energy. As far as gases are concerned, radiation is absorbed only if the photons have energy to promote transitions among the allowed quantized rotational, vibrational, or electronic energy states of the molecules. This process occurs for specific and discrete wavelengths and is called selective absorption. When the absorption lines happen for several different wavelengths very close to each other, they overlap forming an absorption band. In this sense, the radiation absorption by gases is not continuous but happens as isolated or overlapping spectral bands along the solar spectrum. To gain a better understanding of this fact, the atmospheric transmittances due to absorption bands of mixed gases (O_2, CH_4, CO_2, N_2O), O_3 and H_2O are shown in Figure 3.21 for the waveband between 300 and 3000 nm (KILLINGER; CHURNSIDE; ROTHMAN, 1995; IQBAL, 1983; LIOU, 2002).

Figure 3.21 - Atmospheric absorption transmittance due to (a) mixed gases, (b) ozone and (c) water vapor.
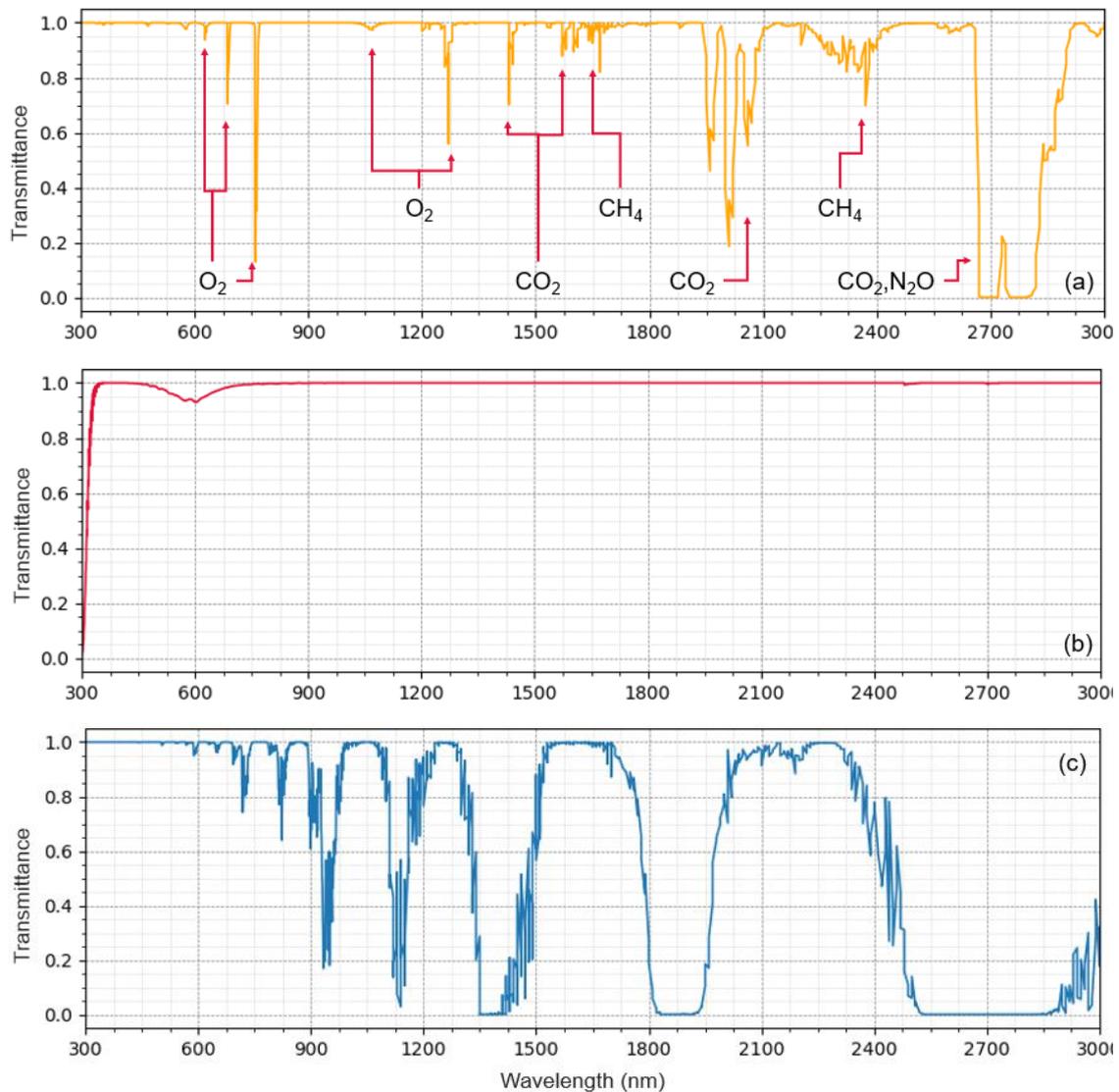
Curves generated with *SMARTS2* radiative transfer code (Gueymard, 1995;2001) for the U.S. Standard Atmosphere (NOAA, 1976), Rural aerosol profile proposed by Shettle and Fenn (1976), on an inclined surface with 37°.
Source: Author.

Different gas species absorb radiation in different regions of the solar spectrum. In the ultraviolet and visible range of the solar spectrum there are five principal absorbing gases: Diatomic Oxygen (O_2); Nitrogen (N_2); Atomic Oxygen (O); Nitrogen (N); and Ozone (O_3). Below 200 nm, atomic and diatomic oxygen together with nitrogen absorb solar radiation in several bands, which prevents that radiation below such wavelength from reaching the surface of the Earth.

From 200 nm to 300 nm and from 300 nm to 360 nm, ozone absorbs the ultraviolet B and C (UV-B and UV-C, respectively) radiation through the Hartley's and Huggins' bands, respectively. In the visible, there is the ozone's less pronounced Chappui band that extends from 450 nm to 770 nm. The spectral transmittance of O_3 is shown in Figure 3.21 (b). Diatomic oxygen also has three absorption bands in the visible spectrum centered at 630 nm (γ band), 690 nm (B band), and 760 nm (A band) (IQBAL, 1983; MCCLUNEY, 1983; LIOU, 2002).

In visible and infrared wavebands, the main absorber is water vapor with bands centered at 720, 820, 940, 1100, 1380, 1870, 2700, 3200, and 6300 nm. The effects caused by water vapor absorption on the solar spectrum are shown in Figure 3.21 (c). Such graph elucidates how much energy water vapor can absorb as opposed to other gases discussed here. Another important absorber gas in infrared is the CO_2 with bands at 1450, 1600, 2000, 2700, 4300, 4800, and 5200 nm (LIOU, 2002; MCCLUNEY,1983). Due to the small concentration of N_2O, CO, and CH_4 in the atmosphere, their total effect on the solar radiation is minimal (IQBAL, 1983).

Despite acting as scatterers, some species of aerosols also absorb solar radiation (SAMSET et al., 2018). Unlike gases, such process is a continuous function of wavelength without selective bands or lines (IQBAL, 1983). This absorption affects the atmosphere by reducing the radiation reaching the surface as well as increasing the temperature aloft, altering cloud properties, atmospheric stability and the water cycle (BERGSTRONG et al., 2007, SAMSET et al., 2018). The main light-absorbing species are the black carbon (BC), mineral dust (MD), and brown carbon (BrC) (MOOSMULLER; CHAKRABATTY; ARNOTT, 2009). Black carbon is pure carbon emitted by high-temperature incomplete combustion of fossil fuels, forest fires etc. while brown carbon is emitted mainly by biomass combustion. Black carbon absorbs solar radiation across all ranges, from ultraviolet to infrared with an approximate λ^{-1} dependence (BERGSTROM et al., 2002; KIRCHSTETTER; NOVAKOV, 2004; LASKIN; LASKIN; KIZKORODOV, 2015; SAMSET, 2018). On the other hand, brown carbon absorbs more efficiently UV and VIS with strong spectral dependence because its absorption coefficient has a dependence ranging from λ^{-2} to λ^{-6} (LASKIN; LASKIN; KIZKORODOV,

2015; PARK; YU, 2019; SAMSET et al., 2018). Mineral dust, also known as solid dust, is a group of aerosols in the form of aggregates made of a wide variety of mixed minerals, including quartz, clay minerals (as kaolinite, hillite, and montmorillonite), hematite, etc., produced by the suspension of minerals constituting the soil. Its optical properties vary widely with the relative abundance of each mineral and how they mix. Quartz is a good absorber in the infrared but a weak one at UV and VIS wavebands. On the other hand, Hematite proved to have the strongest absorption at ultraviolet and visible wavelengths. Clay minerals are strong absorbers from UV to IR wavelengths. (MOOSMULLER; CHAKRABATTY; ARNOTT, 2009; SAMSET et al., 2018).

The radiative effects of aerosols can be determined by a parameter called Aerosol Optical Depth (*AOD*, dimensionless) or extinction coefficient (τ, dimensionless), which describes the attenuation of incoming solar radiation through the atmosphere caused by these particles. The extinction can be obtained through Angstrom's turbidity formula (ANGSTROM, 1929):

$$\tau(\lambda) = \beta(\lambda)^{-\alpha} \tag{3.3}$$

Where β [dimensionless] is Angstrom's turbidity coefficient, λ [µm] is the wavelength, and α [dimensionless] is the Angstrom' exponent. Angstrom's exponent is closely related to the size distribution of the aerosols, varying between 0 for large particles and around 4 for very small aerosols (i.e., the order of air molecules). Angstrom's turbidity coefficient, on the other hand, describes the concentration of aerosols present in atmosphere. The higher the β, the more turbid the atmosphere will be. According to Holben et al. (2001), the aerosol optical depth is the most suitable parameter for remote evaluation of aerosols load which has been considered in local studies for aerosols characterizations, pollution investigation, etc. The American governmental agency NASA in collaboration with different agencies, institutes, universities, individual scientists, and partners worldwide support a project called Aerosol Robotic Network (AERONET) which measures *AOD*, precipitable water and other atmospheric

parameters through ground-based sunphotometers installed all over the word (HOLBEN et al., 1998).

As aerosols can scatter and absorb radiation, a parameter became necessary to describe the fraction of extinct radiation that was scattered. Such parameter is called Single Scattering Albedo (*SSA*, dimensionless) and is defined as (YAMASOE; CORREA, 2016):

$$SSA(\lambda, z) = \frac{\beta_S(\lambda, z)}{\beta_S(\lambda, z) + \beta_A(\lambda, z)}$$

(3.4)

Where $\beta_S(\lambda, z)$ [m⁻¹] is the linear scattering coefficient, and $\beta_A(\lambda, z)$ [m⁻¹] is the linear absorption coefficient. A *SSA (λ, z)* in the vicinity of the unit means that the scattering process dominates the radiation extinction. In contrast, the more the parameter decreases, the higher the absorption becomes. Some examples of the spectral *SSA* for different sites grouped by the type of predominant aerosols according to Dubovick et al. (2001) analysis is shown in Figure 3.22. As portrayed in these graphs, each kind of aerosol has a specific absorption/scattering proportion as function of wavelength. As portrayed in Figure 3.22 (a) and (b) the *SSA* decreases with wavelength for urban pollution and biomass burning aerosols. On the other hand, Figure 3.22 (c) shows that this factor tends to increase with wavelength for dust aerosols. Mixed and maritime aerosols follow the same behavior as urban and biomass burning aerosols. According to Bergtrom et al. (2007) larger particles such as dust scatter radiation fairly independently from *λ*, which makes *SSA* match the decrease in absorption with wavelength. For smaller particles such as urban pollution, the scattering generally decreases faster than the absorption with the increasing wavelength. Hence, the single scattering albedo reduces with wavelength.

Figure 3.22 - The averaged *SSA* of different types of tropospheric aerosol retrieved from the worldwide AERONET network for (a) Urban–industrial (reddish curves) and Mixed (black curve); (b) biomass burning (greenish curves); and (c) desert dust (brownish curves) and oceanic (blueish curves) aerosols species.
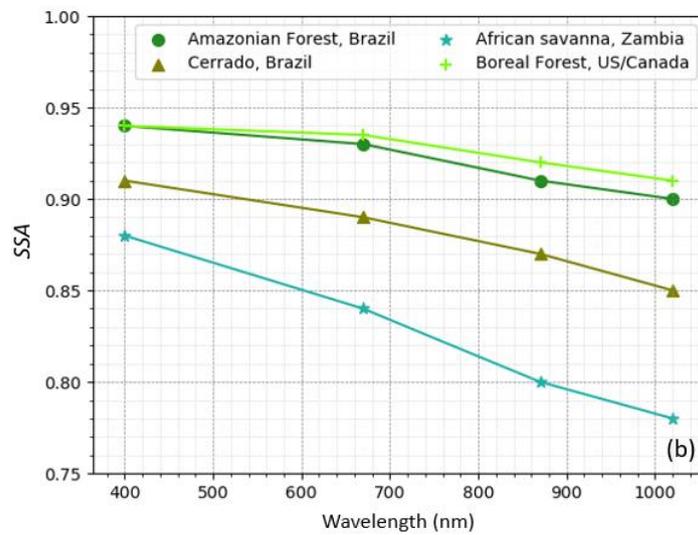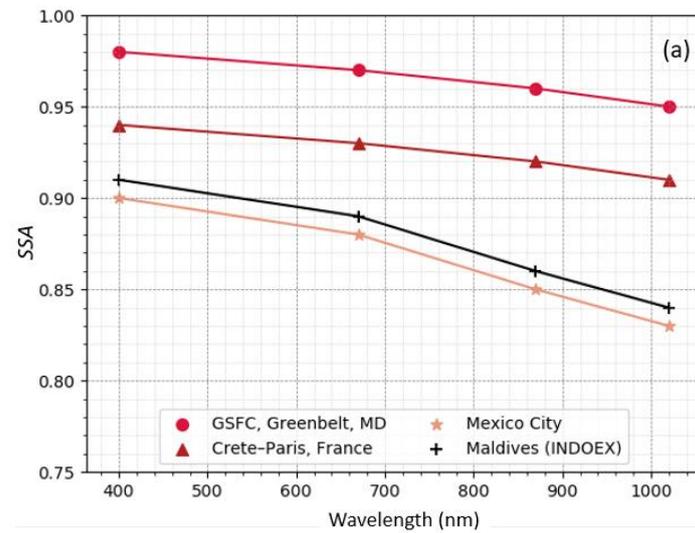
Figure 3.22 – Conclusion.
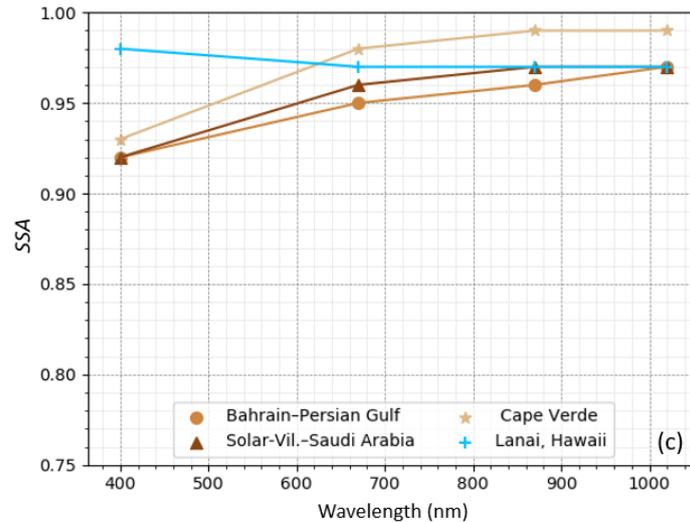
Source: Adapted from Dubovick et al. (2001).

3.3.4 Solar radiation path on the atmosphere

The magnitude of attenuation of solar radiation is proportional to the type and number of atmospheric compounds in the sunlight path. As shown in Figure 3.23 (a), the longer the path, the more molecules, and more solar ray particulates strike, increasing the probability of interaction among them. Bearing this in mind, a convenient way to describe the path-length travelled by sunlight in the atmosphere is through the relative optical air mass or simply air mass (*AM*, dimensionless) (IQBAL, 1983; LIOU, 2002). According to Ruiz-Arias and Gueymard (2015), such quantity accounts for the increased number of atmospheric compounds that is traversed by solar radiation with respect to a trajectory in zenith's direction directly to the sea level. Assuming a plane-parallel, nonrefractive and homogeneous atmosphere as the illustration of Figure 3.23 (b), *AM* can be approximated by (LUQUE; HEGEDUS, 2002)

40

Figure 3.23 - Earth-Atmosphere scheme in which: (a) different path-lengths relative to different Sun positions are shown. More interaction radiation-matter is expected to happen for path-length 1 compared to 2 because it is longer; and (b) *AM* and *AM'* and its relationship with θ_z is illustrated. The continuous thick lines show the bending of the sunlight path due to atmospheric refraction.
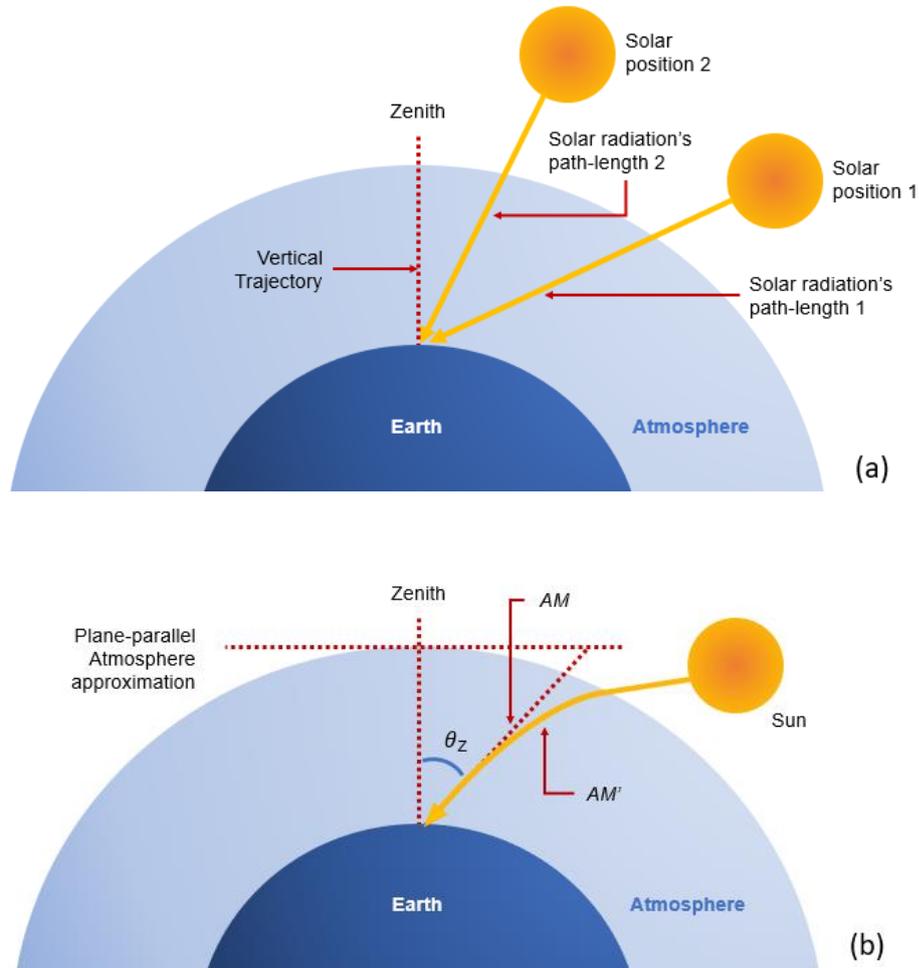
$$AM = \frac{1}{cos(\theta_Z)} \tag{3.5}$$

Even though Equation 3.5 is very convenient and a good approximation for lower values of θ_Z, it is not a good approach for larger angles of radiation incidence (IQBAL, 1983). So, some empirical formulae were developed to consider the

Earth 's sphericity, as the one proposed in Gueymard (2003) and Ruiz-Arias and Gueymard (2015) described by *AM'* below:

$$AM' = \frac{1}{cos(\theta_Z) + 0.48353 \cdot \theta_Z^{0.095846} \cdot (96.7412 - \theta_Z)^{-1.754}} \quad (3.6)$$

Some *AM* conditions are used as reference by standards and research in Solar Energy. For example, the *AM0* refers to the top of atmospheric conditions, *AM1* is related to the path travelled by radiation in a trajectory perpendicular to the Earth's surface, while *AM1.5* represents the distance in which solar rays impinge with θ_Z equals 48.236° (ASTM, 2012). Figure 3.24 shows a draw with such *AM* conditions.

Figure 3.24 - *AM* values used as reference by standards and research in Solar Energy.
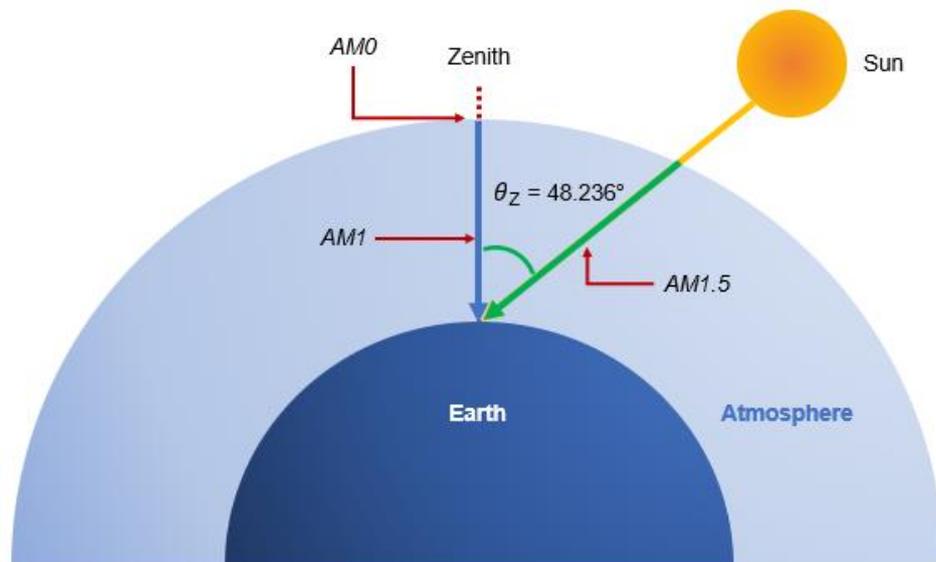
Source: Adapted from Iqbal (1983).

3.3.5 The ASTM 1.5G solar spectrum

As discussed earlier, the astronomical relationships between the Earth and the Sun, in addition to atmospheric effects, have a major impact on the solar radiation incident on the surface. Consequently, the spectral distribution of solar irradiance

can vary both in space and in time. Bearing this in mind, some standard organizations have recommended standardized solar spectra for different applications. In PV, the standards aim to enable the comparison of the relative optical performance of different spectrally sensitive devices (such as radiometers and solar cells) from different manufacturers to be installed around the world (ASTM, 2012). The American Association for Testing and Materials proposed two solar spectra to be considered as references for terrestrial applications in ASTM G173-03 standard (ASTM, 2012). One of them is a global solar spectrum called ASTM AM1.5G. It was designed for flat plate module analysis and has an integrated power density of 1000 $W \cdot m^2$. The other one was initially designed for concentrating solar power (*CSP*), called ASTM AM1.5 Direct (AM1.5D) spectrum. Aside from the direct beam, it includes the circumsolar component in a disk of 2.5° around Sun. In this case, its irradiance equals 900 $W \cdot m^2$. The International Standards Organization (ISO) and International Electrotechnical Commission (IEC) also recommend including these spectra into the standards ISO 9845-1 (1992) and IEC 60904-3 (2019).

Both modeled spectra were generated on version 2.9.2 of the Simple Model of the Atmospheric Radiative Transfer of Sunshine (*SMARTS2*) atmospheric radiative transfer code (GUEYMARD, 1995; 2001); for the 1976 U.S. Standard Atmosphere (NOAA, 1976); and the Shettle and Fenn Rural Aerosol profile (SHETTLE; FENN, 1976). The input data were based on the average atmospheric conditions obtained for the 48 contiguous states of the United States of America (U.S.A.) over a year. They are listed in Table 3.5 for appreciation. The standard spectrum was generated for an inclined plane at 37° tilt towards the equator. This value represents the average latitude for the contiguous U.S.A states already mentioned.

Table 3.5 - Atmospheric conditions considered for the ASTM AM 1.5G standard solar spectrum simulation.

Parameter	Adopted value
Absolute Air Mass	1.5
Zenithal angle	48.236°
Total column water vapor	1.42 cm
Total column ozone	0.34 cm
Angstrom turbidity at 500 nm	0.084

Source: Adapted from ASTM (2012).

In Gueymard (1995; 2001; 2002), 'validations' of the modeled standard spectra were conducted through other radiative transfer codes as the Moderate Resolution Atmospheric Transmission (MODTRAN) and spectral data measured under 'known' atmospheric conditions and AM 1.5. The findings agree with the standards within the uncertainties of the spectral instrumentation calibration and measurement uncertainties. Despite standardizing the solar spectrum, the *AM 1.5G* standard disagrees with solar spectral data collected around the world under different conditions from those presented in Table 3.5. It can introduce errors on PV performance rating, energy predictions, etc. In this sense, analysis on impact of solar spectrum variations on spectrally selective devices must be made to improve the results of PV performance analysis.

3.3.6 Parameters for solar spectra analysis

Studies aiming to evaluate the impacts caused by variations of the spectral distribution of solar irradiance (in short, spectral irradiance) over time for a specific location on PV must deal with some difficulties. The first issue is the format of these data. Spectral data are tables in which the amount of monochromatic irradiance depends on the analyzed wavelength interval and on the optical resolution of the spectroradiometer. All these points require a huge computational capacity for data processing at a high frequency due to integrations in 2D domains (wavelength and time). The second issue concerns the possibility of comparing solar spectra with environmental and atmospheric

parameters described by a single number in addition to the need for a parameter that can be easily employed in PV engineering calculations. As raised by Jardine et al. (2012), the description through a single number of how 'rich' solar spectrum can be, in a specific waveband, enables the correlation between spectral data and other parameters as temperature, for example.

Bearing this in mind, some researchers proposed different parameters to represent the solar spectrum by means of a single number. Jardine et al. (2012) introduced the concept of Average Photon Energy (*APE*, in eV), a parameter aimed to compute the average energy of photons from a given spectrum distribution. It can be obtained as follows:

$$APE = \frac{\int_a^b E(\lambda)d\lambda}{q\int_a^b \phi_{PH}(\lambda)d\lambda}$$
(3.7)

Where $E(\lambda)$ [W·m^{-2}·nm^{-1}] is the spectral irradiance, a and b [nm] are the lower and upper limits of integration, q is the electron charge [1.602×10^{-19}] and $\phi_{PH}(\lambda)$ [m^{-2}·s^{-1}] is the photon flux at a given wavelength which in turn can be computed through:

$$\phi_{PH}(\lambda) = \frac{\lambda E(\lambda)}{hc}$$
(3.8)

Where h [$6.62607 \cdot 10^{-34}$ m^2·kg·s^{-1}] is the Planck constant and c [299792458 m·s^{-1}] is the speed of light in vacuum. *APE* is one of the most widely adopted parameters to describe the solar radiation spectral distribution. It qualitatively characterizes the shape of solar spectra and indicates spectral asymmetries, generally referred to as "color". Higher values of *APE* mean that the solar spectrum is richer in photons from shortwave radiation, called *'blue shifted'*. If *APE* has lower values, the spectrum is called *'red shifted'* because photons from longer wavelengths prevail. The change in such parameter indicates how atmosphere and Sun-Earth geometry impacts the solar spectrum. For example,

Figure 3.25 shows some synthetic spectra with their respectively *APE* values for different situations discussed hereafter. Cornaro and Andreotti (2013), Nakada et al. (2010) and Magare et al. (2016), for instance, showed that higher values of *AM* are related to redder solar spectrums. In this situation, the longer paths in the atmosphere increase the Rayleigh scattering in the ultraviolet and visible spectral regions caused by gases, diminishing the number of higher energy photons of a single solar spectrum as shown in Figure 3.25 (a). Conversely, lower values of *AM* are conducive to higher values of *APE* because of the shorter paths traveled by radiation in the atmosphere, which decrease the scattering effect.

Figure 3.25 - Effect of (a) air mass; (b) precipitable water and (c) aerosol optical depth variation on the solar spectral irradiance while the remaining atmospheric parameters are held constant. Solar spectrum data simulated with *SMARTS2* radiative transfer code (Gueymard, 1995; 2001) for the U.S. Standard Atmosphere (NOAA, 1976), Rural aerosol profile proposed by Shettle and Fenn (1976), on an inclined surface with 37°.
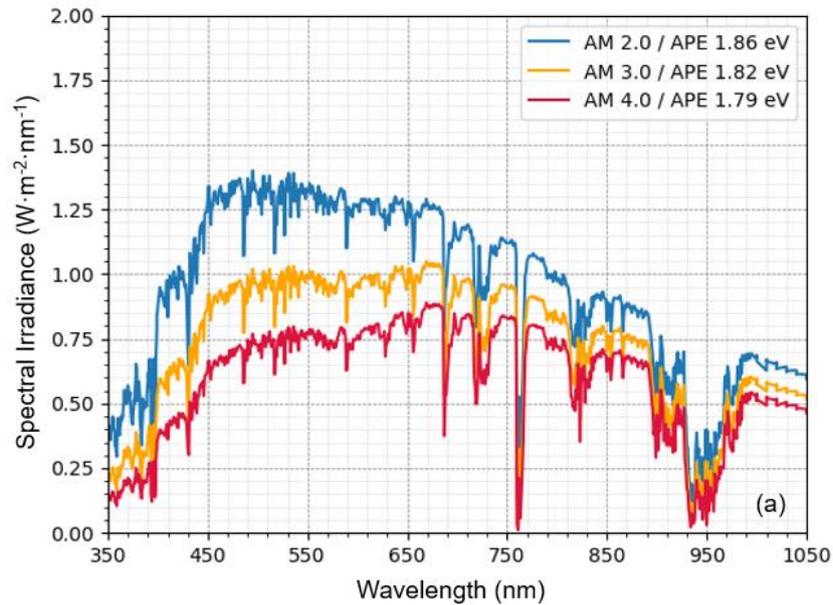
Figure 3.25 – Conclusion.
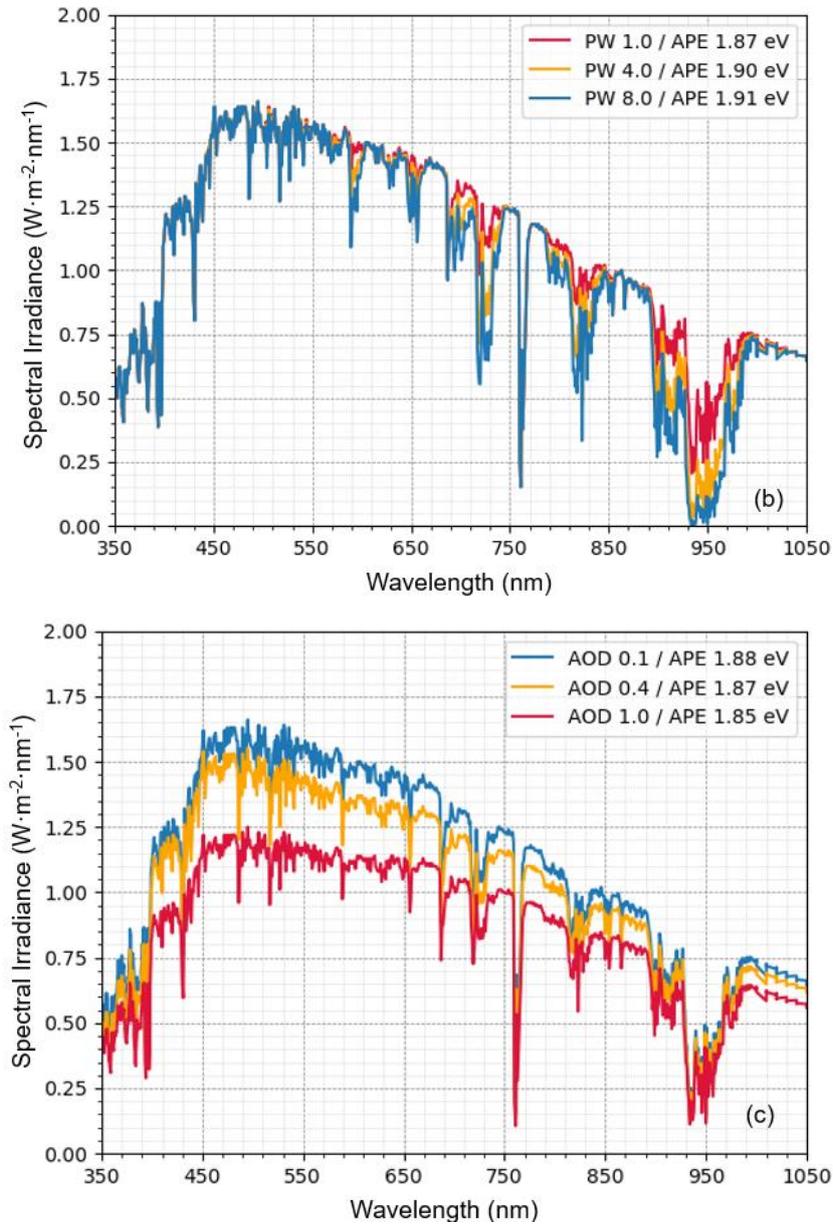
Source: Author.

It has also been reported that water vapor impacts *APE* (Figure 3.25 - b). According to Cornaro and Andreotti (2013), Ishii et al. (2013) and Chantana et al. (2017), for a wetter atmosphere, such as during cloudy days or rainy seasons, values of *APE* tend to be higher, whilst for drier climates, values of *APE* tend to be lower. This is due to the strong absorption bands water vapor has in the infrared region as illustrated by the *PW* variations and its influence on *APE* shown in Figure 3.25 (b) in conjunction with the Mie scattering by clouds (in case of

cloudy skies) which is less wavelength dependent. Aerosols also exert a significant influence on *APE* values, since their extinction decreases with increasing wavelength and therefore the effects on UV and VIS regions are more noticeable than those on IR. It attenuates the shorter wavelengths region of the spectrum, as discussed by Fernandez et al. (2016) and Braga et al. (2020). Such effect is also portrayed in Figure 3.25 (c), where it is clear that higher aerosol loads lead to lower *APE* values, biasing the solar spectrum to red.

The average photon energy also depends on the measured spectral range. Larger wavelength intervals lead to a reduction in this parameter in general. Table 3.6 shows how *APE* obtained for the ASTM AM 1.5G solar spectrum varies as function of wavelength range. In this sense, the 350-1050 nm waveband has been used to calculate *APE* in many papers (JARDINE et al., 2002; NOFUENTES et al., 2017a; NOFUENTES et al., 2014; FERNÁNDEZ et al., 2016; POLO et al., 2017; CABALLERO et al., 2018; YE et al., 2014). For this wavelength interval, *APE* for the ASTM AM 1.5G solar spectrum is 1.880 eV.

Table 3.6 - Average Photon Energy values computed for different wavelength intervals for the ASTM AM 1.5G standard solar spectrum.

Wavelength interval (nm)	APE (eV)
350 – 1050	1.880
350 – 1700	1.590
300 – 2500	1.480
300 – 4000	1.450

Source: Author.

Another parameter to describe the solar spectrum is the blue fraction (*BF*, dimensionless), proposed by Sutterlueti et al. (2011). It describes the fraction of solar irradiance included inside the considered 'blue fraction' of the whole spectrum (i.e., until 650 nm, the wavelength related to the blue color). It can be estimated through:

$$BF = \frac{\int_a^{650nm} E(\lambda)d\lambda}{\int_a^b E(\lambda)d\lambda} \qquad\qquad (3.9)$$

Where a [nm] is the lower integration limit and b [nm] is the higher integration limit. As *BF* gets higher, the energy of the spectral waveband comprised from blue color to far ultraviolet gets higher as it occurs with *APE*. As shown in Table 3.7, considering a 350-1050nm waveband, *BF* for the ASTM AM 1.5G standard spectrum equals 0.52. Other intervals are also shown. (RODRIGO et al., 2017). As *BF* aims to determine the 'blueness' of solar spectrum as *APE*, the atmospheric and astronomical parameters previously described for the latter have the same impacts on the former.

Table 3.7 - Blue Fraction values computed for different wavelength intervals for the ASTM AM 1.5G standard solar spectrum.

Wavelength interval (nm)	BF
350 - 1050	0.52
350 - 1700	0.43
300 - 2500	0.40
300 - 4000	0.39

Source: Author.

3.4 Photovoltaic solar energy

3.4.1 Solar cells

A solar cell is an electronic device specially designed to convert solar energy into electrical energy through the photovoltaic effect, which is basically the process of voltage and current generation that happens when a PV device is exposed to light (LUQUE; HEGEDUS, 2003). Nowadays, solar cells can be manufactured with different materials, structures, and architectures (AVRUTIN; IZYUMSKAYA, MORKOÇ, 2011; MIT, 2015; SINKE, 2019). Depending on their features, solar

cells work with different levels of efficiency during the energy conversion process as shown by Green et al. (2020).

3.4.1.1 Conventional solar cell operation

A conventional solar cell consists basically of two or more layers of semiconductor material fused together in structures called *junctions*, as '*pn-*junction', '*p-i-n*-junction', etc., metallic contacts and an antireflection coating as depicted in Figure 3.26. The junction is responsible for sunlight conversion and comprises semiconducting layers doped with different substances. Depending on the doping substance, an excess of negative or positive charge carriers (i.e., electrons and holes, respectively) is created on the material. The *n*-type side of the junction is doped to achieve higher amounts of electrons and the *p*-type is doped to create an excess of holes. As such layers are fused together, an electric field *E* is built on the interface between the two sides of the junction due to the diffusion of charges. The metallic contacts collect the charge carriers generated by the junction, conducting them to an external load. An antireflective coating is used to reduce the reflection of incident photons. The solar cell efficiency can be improved by contact optimization and antireflective coating (HU; WHITE, 1983; MIT, 2015).

Figure 3.26 - Basic conventional solar cell morphology.
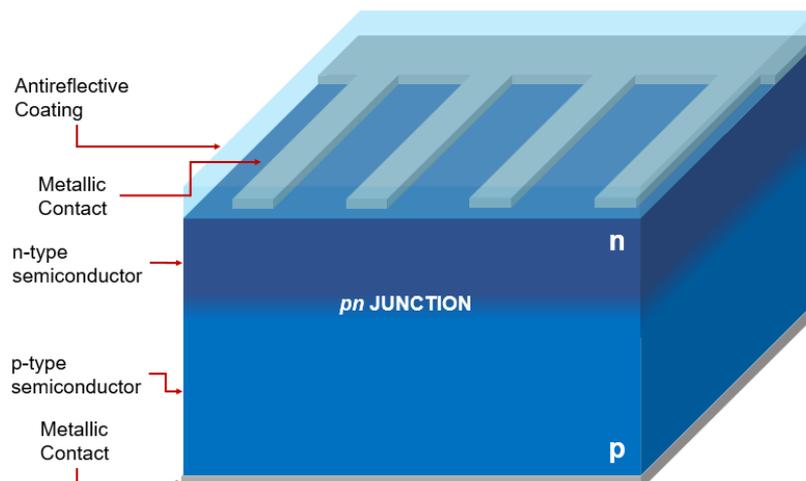
Source: Author.

A conventional solar cell operation is summarized in the four basic steps displayed in Figure 3.27. Firstly, the top of the solar cell is irradiated by the Sun and part of the incoming photons are transmitted through the antireflective coating and those with energy greater than the so-called Bandgap energy (E_{GAP}, in eV) of the cell interact with electrons in covalent bonds generating electron-hole pairs (step 1). The built-in electrical field (E, in V·m^{-1}) of the pn-junction separates the electron and the hole that diffuse through the cell toward the metallic contacts (step 2). Then, the electrons flow through the metallic contacts to the external circuit, giving rise to electric voltage and current in an external circuit (step 3). After that, the electrons return to the cell combining with holes, being annihilated (step 4) (MIT, 2015; FONASH, 2010; AVRUTIN, IZYUMSKAYA; MORKOÇ, 2011). The movement of these charges through long distances in atomic scales creates the so-called photogenerated current (I_{PH}, in A), which will be discussed in depth in the next section.

Figure 3.27 - Basic steps for energy generation in conventional solar cells.
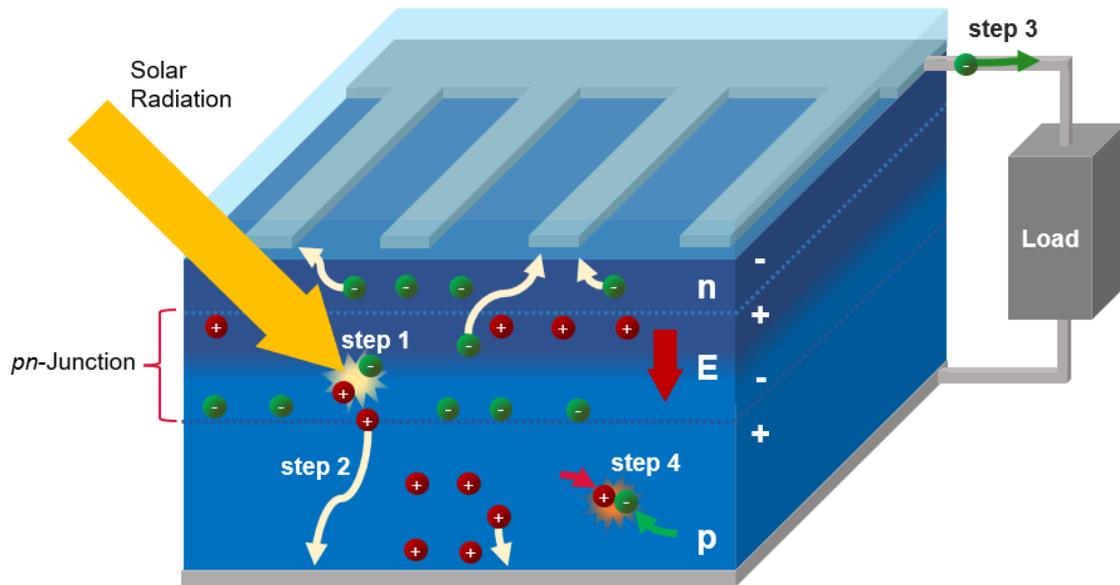
Source: Author.

The operation principle described above for ideal solar cells can be modeled by an equivalent circuit composed of a pn-junction diode connected in parallel with

a current source as shown in Figure 3.28. The former represents the solar cell functioning in the dark, which is basically a standard semiconductor diode, and the latter represents the photocurrent generated by the incoming sunlight (CHEN, 2011). McEvoy, Markvart and Castañer (2005) described the current and voltage generated by such circuit:

$$I = I_{PH} - I_0 \left[exp \left(\frac{qV}{NkT} - 1 \right) \right]$$

(3.10)

Where I_0 [A] is the diode saturation current, q [C] is the electronic charge, V [V] is the voltage generated by the solar cell, N [dimensionless] is the diode ideality factor, k [$1.38065 \cdot 10^{-23} m^2 \cdot kg \cdot s^{-2} \cdot K^{-1}$] is the Boltzmann constant, and T [K] is the solar cell temperature.

Figure 3.28 - Equivalent circuit of an ideal solar cell.
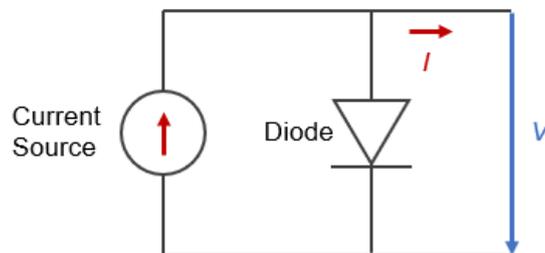
Source: Adapted from McEvoy, Markvart and Castañer (2005).

The relationship between current and voltage of a solar cell described by Equation 3.10 gives its main electrical characteristics, which can be easily seen when plotted on an *IV* curve. As an example, Figure 3.29 (a) depicts an *IV* curve of a generic solar cell and Figure 3.29 (b) shows the same graph with its relative power *versus* voltage curve. Important parameters can be derived from these curves. They are described below (PEARSALL, 2017; LUQUE; HEGEDUS, 2002):

i.   Short circuit current (I_{SC}, in A): generated under short-circuited condition, i.e., when the voltage across the solar cell is zero. This is the maximum current produced by a PV device and is identical to the photogenerated current for an ideal solar cell with moderate resistive loss mechanisms.

ii. Open circuit voltage (V_{OC}, in V): generated under open circuit condition, i.e., when solar cell terminals are not connected to any load. The V_{OC} is the maximum voltage available from a solar cell and can be obtained through:

$$V_{OC} = \frac{nkT}{q} ln \left(\frac{I_{PH}}{I_0} + 1 \right)$$

(3.11)

iii. Maximum power (P_{MP}, in W): as outlined hereafter, the current and voltage produced by a PV device varies as function of different factors. Therefore, there will be a point in the *I-V* curve where the product of such parameters will lead to the maximum power generated by the cell. At this point, the current and voltage are called I_{MP} [A] and V_{MP} [V], respectively, and the power is known as P_{MP} [W]. P_{MP} is obtained through:

$$P_{MP} = V_{MP} \cdot I_{MP}$$

(3.12)

iv. Fill Factor (*FF*): compares the real maximum power P_{MP} with the ideal maximum power generated by a PV device, i.e., the product of V_{OC} and I_{SC}, as:

$$FF = \frac{P_{MP}}{V_{OC} \cdot I_{SC}} = \frac{V_{MP} \cdot I_{MP}}{V_{OC} \cdot I_{SC}}$$

(3.13)

Graphically, it also gives the squareness of the *IV* curve as illustrated by the areas A_1 and A_2 in Figure 3.21. The squarer the curve, the greater the *FF* value and the more efficient the solar cell.

v.   Efficiency (η): gives the measurement of how efficiently the PV device converts solar energy into electricity. It can be obtained through:

$$\eta = \frac{P_{MP}}{G \cdot A_C} = \frac{V_{MP} \cdot I_{MP}}{G \cdot A_C}$$

<div align="right">(3.14)</div>

where A_c [m²] is the area of the solar cell.

Figure 3.29 - *IV* curves of a generic solar cell with (a) the areas $A_1 = V_{MP} \cdot I_{MP}$ and A_2 = $V_{OC} \cdot I_{SC}$ highlighted, being $FF = A_1 \cdot A_2^{-1}$ and (b) its respective *PV* curve.
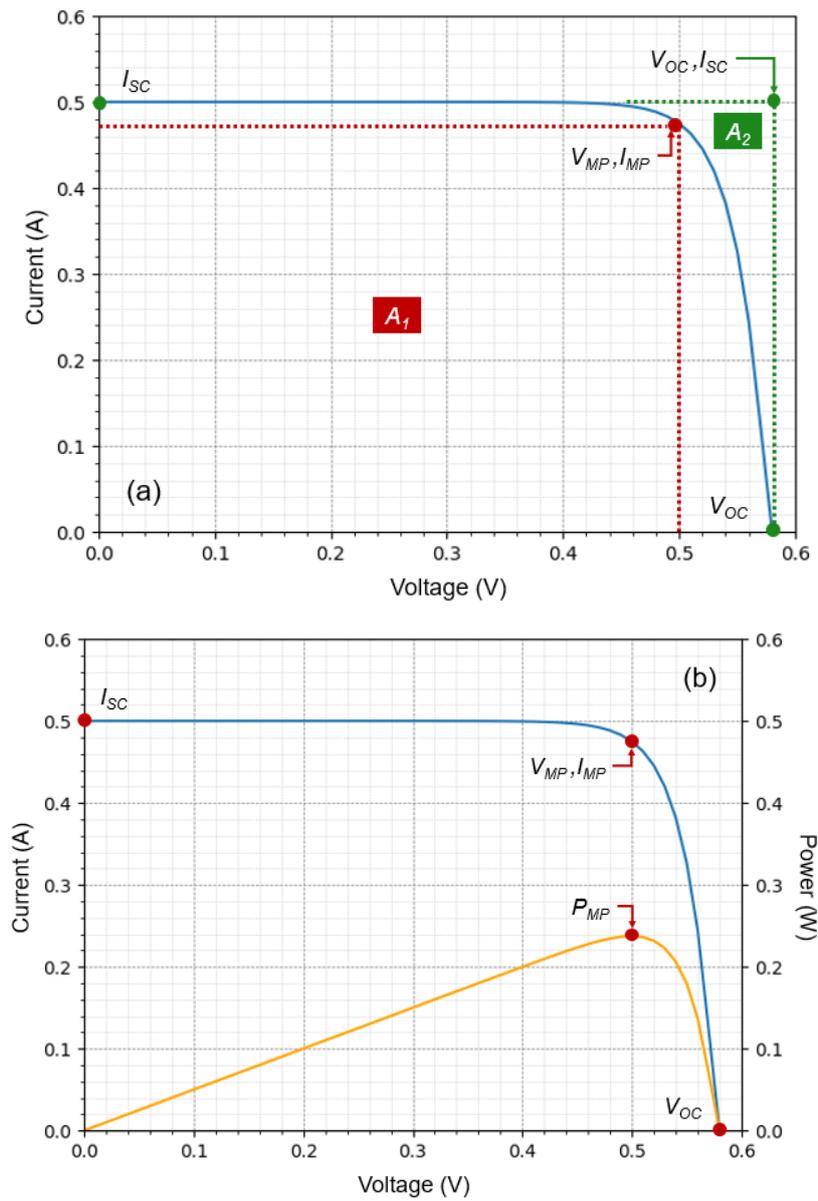
Source: Adapted from McEvoy, Markvart and Castañer (2005).

The equivalent circuit shown in Figure 3.28 represents idealized devices and neglects inner parasitic resistances typically associated with real solar cells. These resistances cause power dissipation lowering the device efficiency and can be classified as series (R_S, in Ω) and shunt (R_{SH}, in Ω) resistances. The former is caused by the resistance due to the current flowing in the semiconducting layer, metallic contacts, and in between them. The latter is caused by the formation of a secondary path in addition to that of the junction. Both resistance effects can be minimized by improving solar cell design and adopting good quality materials. The equivalent circuit of a PV cell considering R_S, and R_{SH} is displayed in Figure 3.30. Under these circumstances, a solar cell current can be computed by:

$$I = I_{PH} - I_0 \left\{ exp \left[\frac{q\,(V + IR_S)}{nkT} - 1 \right] \right\} - \frac{V + IR_S}{R_{SH}} \qquad (3.15)$$

Figure 3.30 - Equivalent circuit of a non-ideal solar cell.
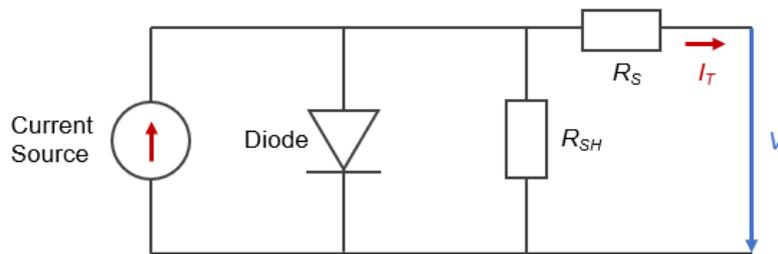
Source: Adapted from McEvoy, Markvart and Castañer (2005).

Due to the low power generated by a single solar cell, PV modules are manufactured by wiring a number of these devices to improve the converted energy. The number of associations and how they are done determine the voltage and current output of the array. The connections between solar cells can be in series or in parallel. PV cells wired in series have one of their positive terminals connected to the negative terminal of the next one, increasing output voltage without any change in the generated current. Figure 3.31 (a) depicts such connection and the *I-V* curve of this arrangement. In parallel connections, the positive terminals are wired together, as negative terminals are, which increases

only the current, as displayed by the circuit in Figure 3.31 (b) and its *IV* curve (PEARSALL, 2017; GERMAN ENERGY SOCIETY, 2008).

Figure 3.31 - Connection in (a) series and (b) parallel between two solar cells with the respective *IV* curves of the resultant assembly.
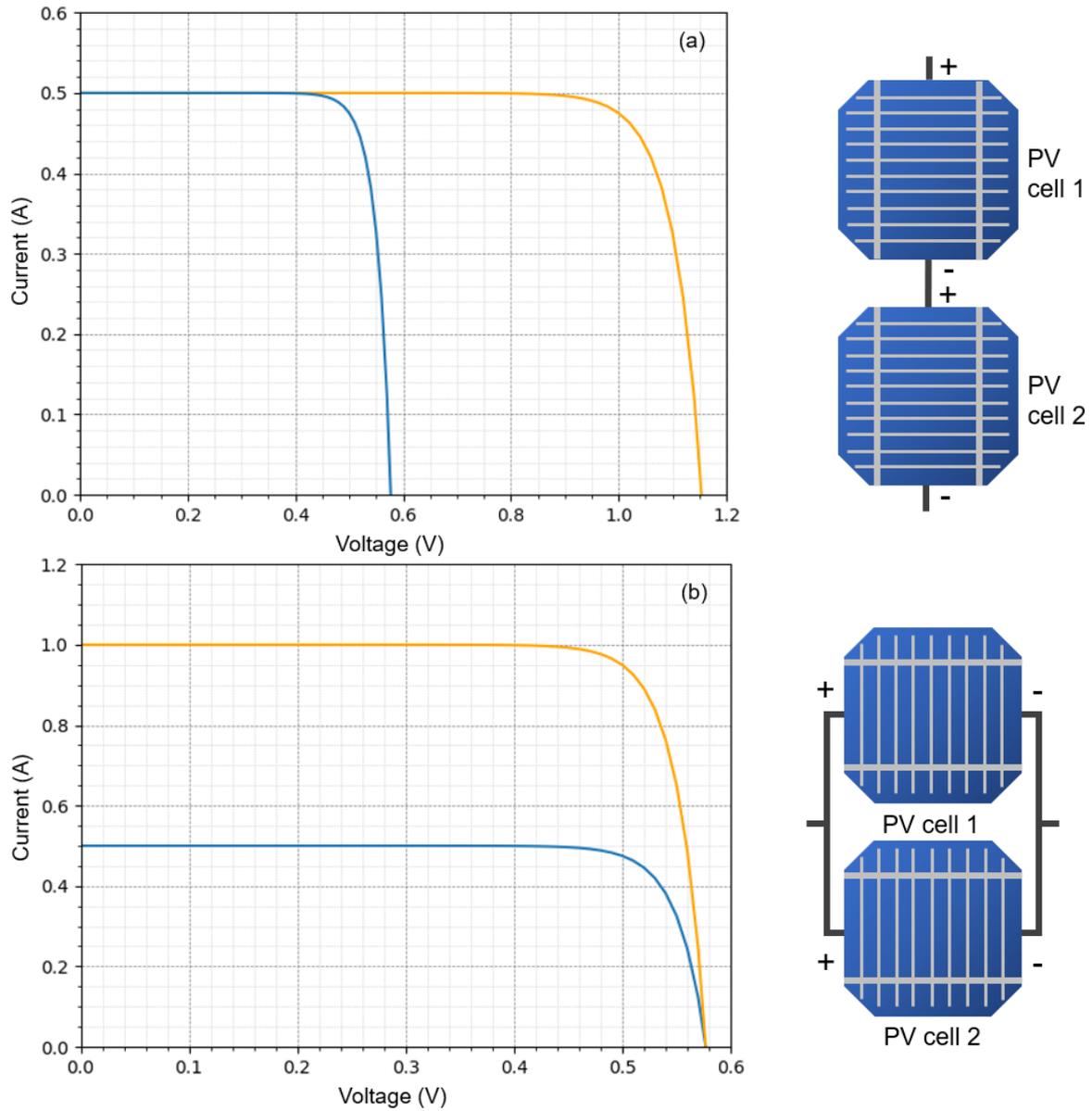
3.4.1.2 Solar cells optical properties

For the electron-hole pair generation, the incident solar photons must have energy higher or at least equal to the E_{GAP} of the PV cell semiconductor material.

The E_{GAP} is the energy required to break the covalent bonds between the electron and the atomic nuclei and promote the former from the valence to the conduction band, where it is free to move through the material. The band gap energy is dependent of the atomic properties of each semiconductor and is very important for solar cell characterization since it has influence on the cell's I_{SC} and V_{OC} values. Bearing this in mind, there will be an optimum band gap energy value for maximum PV power conversion depending on the incident solar spectra as depicted by Figure 3.32. According to these curves, for terrestrial application (AM1.5G spectrum), the optimum band gap is 1.34 eV. Cadmium Telluride (CdTe), Indium Phosphide (InP), and Gallium Arsenide (GaAs) have their E_{GAP} closest to the ideal. As discussed by Avrutin, Izyumskaya, and Morkoç (2011), semiconductors with E_{GAP} ranging between 1.0 and 1.7 eV are generally employed in solar generating devices. Table 3.8 shows some band gap energy for some PV materials.

Figure 3.32 - Power conversion efficiency as a function of semiconductor bandgap.
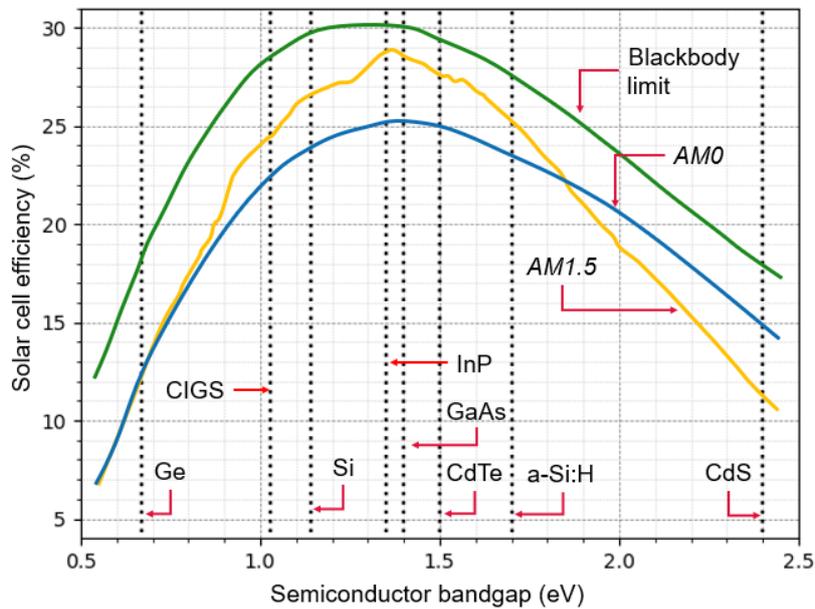
Source: Adapted from Avrutin, Izyumskaya and Morkoç (2011) and Harbelin (2012).

Table 3.8 - Bandgap energies of common PV materials at 25°C. Some of them have their E_{GAP} varying as function of their compounds, as CIGS.

Semiconducting Material	Chemical Formula	Bandgap Energy (eV)
Crystalline Silicon	c-Si	1.1
Amorphous Silicon	a-Si	1.7
Germanium	Ge	0.7
Cadmium Telluride	CdTe	1.5
Copper Indium Gallium Diselenide	CIGS	~1.0
Gallium Arsenide	GaAs	1.4
Indium Phosphide	InP	1.35
Cadmium Sulfide	CdS	2.4
III-V triple junction cells semiconductors	$In_{0.495}Ga_{0.505}P$ / $In_{0.01}Ga_{0.99}As$ / Ge	1.9 / 1.4 / 0.7
Methylammonium lead iodine (Perovskite solar cells)	$CH_3NH_3PbIn_3$	1.5 ~ 1.7

Source: Adapted from Avrutin, Izyumskaya and Morkoç (2011) and Khatun et al. (2020).

Each photon can generate only one electron-hole pair, independently of its energy. If the photon is more energetic than the band gap of the semiconductor material, the excess is dissipated as heat in the material through a process known as thermalization (HU; WHITE, 1983). On the other hand, photons with less energy than E_{GAP} cannot be absorbed and do not contribute to the electric current. In this sense, only a fraction of the incident solar spectrum can be absorbed and converted into electricity by PV cells. Figure 3.33 displays the ASTM AM1.5G standard spectrum in addition to the portion absorbed by a crystalline Silicon solar cell. Aiming to increase the conversion efficiency and diminish optical and thermalization losses, PV developers choose the best semiconductors for

terrestrial solar spectrum as previously discussed and look for better designs for these devices.

Figure 3.33 - Maximum fraction of ASTM AM 1.5G that may be absorbed by a single-crystalline Silicon solar cell. The reddish part is lost by thermalization, the blueish one is lost due to its low energy photons, and the orangish may be absorbed. The orangish curve was obtained through the product between the solar spectrum and the spectral response of the photovoltaic device.
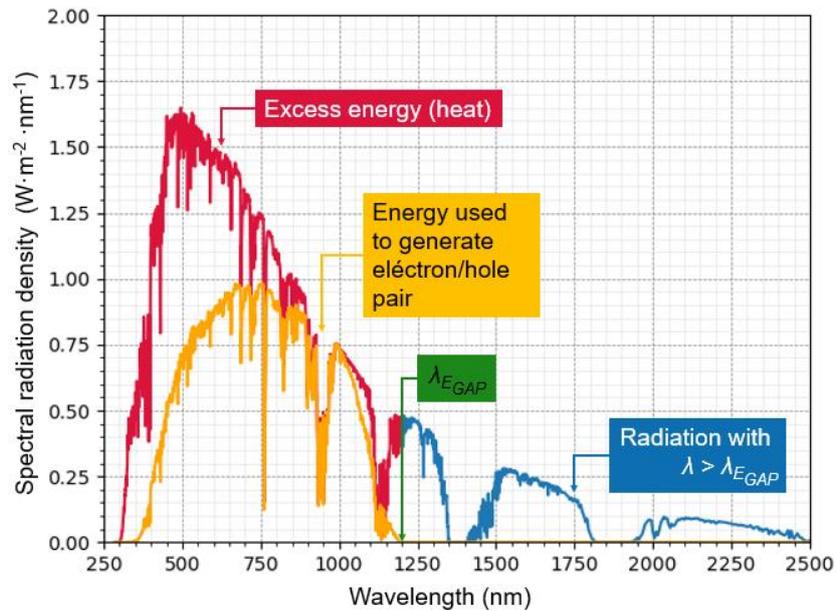
The number of charge carriers generated per number of incident photons in a solar cell is defined as the 'quantum efficiency' (QE, in %). Such characteristic defines the absorption efficiency, and which spectral regions can be converted by the cell. For real PV devices, QE is always lower than the unit due to reflection and charge carrier recombination. As the number of incident photons and generated carrier concentration are not easily measured, the PV community adopts, the Spectral Response instead of QE. Basically, the Spectral Response (SR, in A/W) determines the amount of current density generated per incident power density unit at a given wavelength along the absorption band of a PV device. As QE, SR also gives information regarding the fraction of the incident spectral radiation that can be absorbed and how efficiently the absorption happens. For comparison, Figure 3.34 depicts the QE and SR curves for a

crystalline silicon solar cell. Each solar cell technology has a different spectral response curve due to its optical semiconductor properties, architecture features, antireflective coating, etc.

Figure 3.34 - Quantum efficiency and the relative spectral response of a Si solar cell.
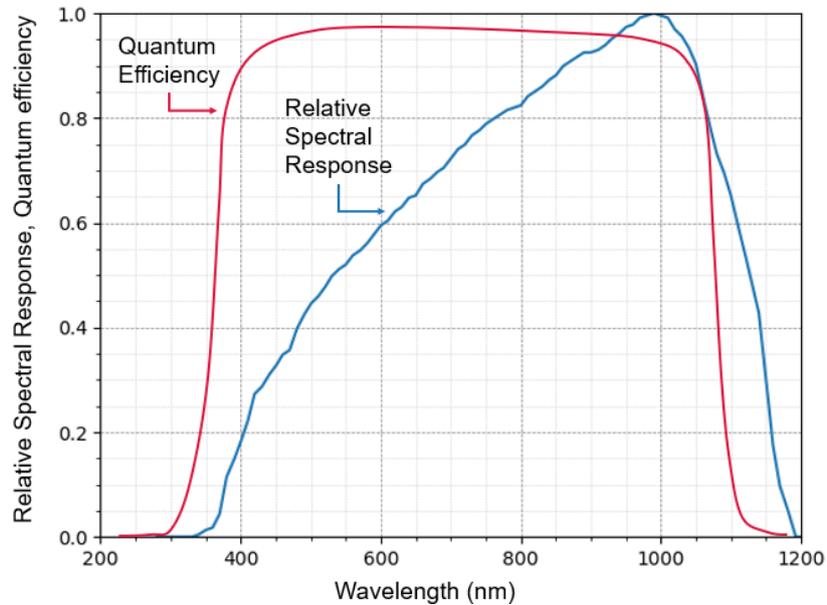
Source: Adapted from PV Education (2021).

The current generated by the separation and collection of the charge carriers produced by the incident photons (i.e., photogenerated current) is related to the spectral response and the incident solar spectrum through the following equation:

$$I_{PH} = q \cdot A_C \cdot J_{PH} = q \cdot A_C \cdot \int E(\lambda)SR(\lambda)d\lambda \qquad (3.16)$$

Where J_{PH} [A·cm^{-2}] is the photogenerated current density. It is worth mentioning that for solar cells with small resistive losses, I_{PH} can be considered approximately equal to I_{SC}. Considering that, as explained by Rodrigo et al. (2017), for most solar cells the maximum power changes in the same proportion as its short-circuit current only if irradiance and spectral effects are under scrutiny, so it can be said that Equation 3.16 indicates how solar spectrum affects the performance of solar cells.

3.4.2 Solar cell generations

Solar cells can be classified into four 'PV generations' according to the materials employed, PV technology, market maturity, levels of development, etc. (MIT, 2015). The first-generation solar cells are the oldest and most commercialized technology and are based on inorganic semiconductor wafers. Single-crystalline and multi-crystalline Silicon (sc-Si and mc-Si, respectively) are examples. The second generation is also based on inorganic compounds, but built in a flexible thin film architecture. Historically, this approach was meant to lower the costs of production as opposed to the previous generation. Cadmium Telluride (CdTe), Copper-Indium-Gallium Diselenide ($Cu(In_XGa_{1-X})Se_2$ or CIGS) and Amorphous Silicon (a-Si) are examples of these cells. The third generation refers to the advanced thin films or multijunction devices based on a variety of new materials, including nanomaterials, organic dyes, and polymer-based solar cells or tandem multijunction made with III-V semiconductors (RANABHAT et al., 2016). Lastly, the fourth generation refers to devices manufactured with composite materials. These cells combine previous technologies with nanomaterials as metallic nanoparticles, carbon nanotubes, graphene, and its derivatives (GREEN, 2001; SINKE, 2019; LUCEÑO-SÁNCHEZ; DÍEZ-PASCUAL; CAPILLA, 2019). Table 3.9 depicts all PV technologies grouped by generation and semiconductor families in addition to the best obtained efficiency of each.

Table 3.9 - Non-concentrator PV technologies from different generations with their best efficiencies obtained indoors under AM1.5G solar spectrum. Due to early development level, only some examples of fourth-generation solar cells are depicted.

Generation	Semiconductor family	PV Technology	Efficiency	Reference
First	Crystalline Silicon PV cells	Single crystalline	26.1%	(NREL, 2021)
		Multi crystalline	23.3%	(NREL, 2021)
		Heterostructures (HIT)	26.7%	(NREL, 2021)
		Bifacial	24.3% (front) / 23.4% (rear)	(ELECTROOPTICS, 2021)
	Single-Junction GaAs	GaAs	27.8%	(NREL, 2021)
Second	Commercial Thin-Films	CdTe	22.1%	(NREL, 2021)
		CIGS	23.4%	(NREL, 2021)
		Hydrogened Amorphous Silicon	10.2%	(GREEN, et al., 2021)
Third	Multijunction cells	Five-junction cell (bounded)	38.8%	(GREEN, et al., 2021)
		InGaP/GaAs/InGaAs	37.9%	(GREEN, et al., 2021)
	Emerging Thin-Films	Organic	18.2%	(GREEN, et al., 2021)
		Dye sensitized	12.25%	(GREEN, et al., 2021)
		Quantum dots	18.1%	(NREL, 2021)
		Perovskite	21.6%	(GREEN, et al., 2021)
		CZTS	11.0%	(GREEN, et al., 2021)
Fourth	Organic-inorganic hybrid solar cells	Semiconducting nanocrystals in polymeric matrix	13.1%[a]	(XIE, et al., 2020; BAEK, et al., 2019)
	Graphene-based materials applied in PV	Organic solar cell with graphene-based electrodes	7.1%[a]	(PARK, et al., 2014)
		Perovskite solar cell with graphene quantum dots	20.31%[a]	(XIE, et al., 2017)

Source: Author.

3.4.3 Factors affecting PV devices performance

The outdoor performance of PV devices is influenced by several factors. Some of them are internal, related to the module itself, as its design, materials and semiconductors and others are related to its location and environmental issues. These effects are discussed below.

3.4.3.1 Design and material effects on photovoltaic devices

a. **Degradation:** PV modules may suffer chemical, thermal, electrical, or mechanical degradation, which causes a reduction of efficiency during their lifetime. Generally, the performance decline is resultant from continuous and accumulative damages caused by long-term environmental factors. Thus, PV module manufacturers usually guarantee against this performance loss at 80% of nameplate power after 25 years whether in a stepped or linear fashion (JORDAN; KURTZ, 2016). Early degradation of PV modules may be due to poor design, bad quality materials or manufacturing issues.

b. **Parasitic resistances:** the series and shunt resistances can reduce a module efficiency due to their capacity to dissipate part of the solar cell generated power as heat. To illustrate such effects, Figure 3.35 depicts how I-V curves vary as a function of both resistances. To diminish their impacts, R_S must be as low as possible while R_{SH} must be as high as possible which can be fully guaranteed through the usage of good quality materials and optimized architectures on PV cells (VIDYANANDAN, 2017).

Figure 3.35 - Effects caused on PV cells' *IV* curves by the variation of (a) series resistance with $R_{S5} > R_{S4} > R_{S3} > R_{S2} > R_{S1}$ and (b) shunt resistances with $R_{SH5} < R_{SH4} < R_{SH3} < R_{SH2} < R_{SH1}$.
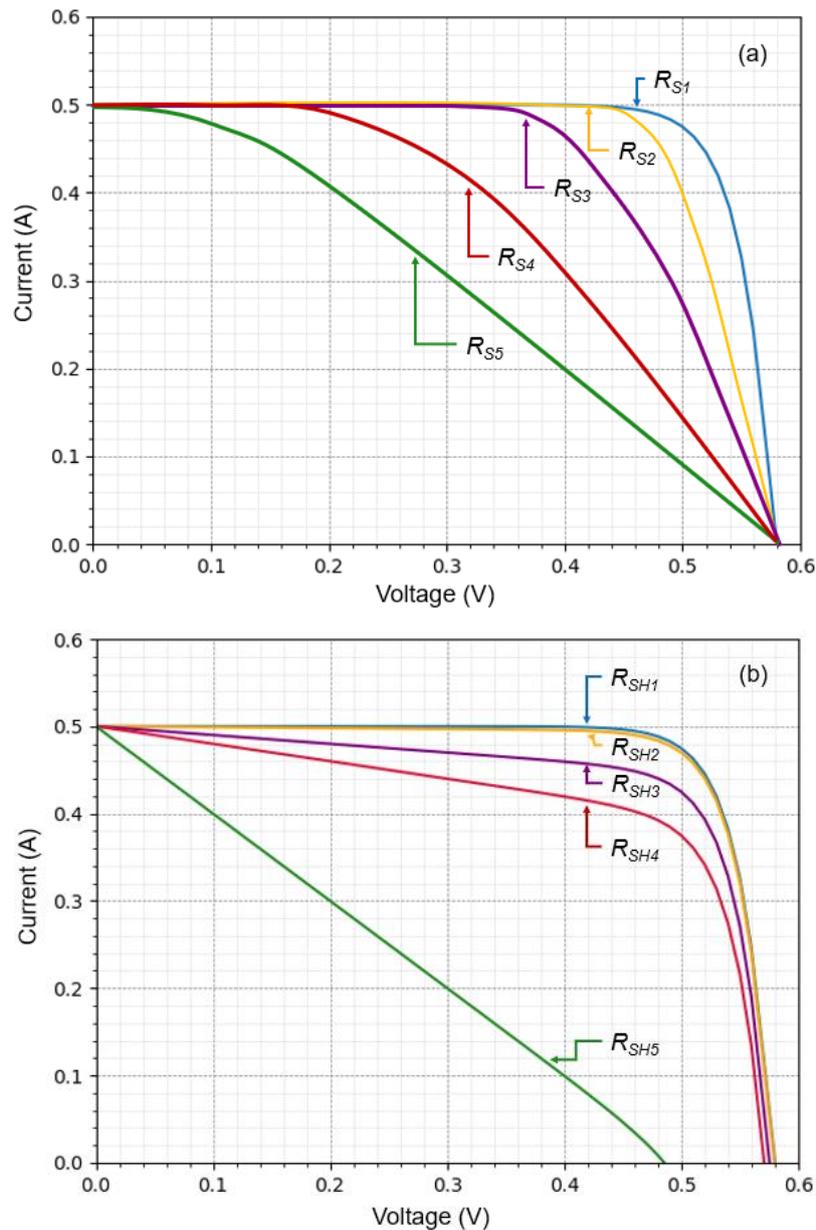
Source: Adapted by Vilela (2010).

c. **Optical losses:** PV modules are manufactured with different layers made with different materials. When sunlight traverses these layers towards the cells, they can absorb a portion of it. It reduces the available energy for absorption and conversion. Furthermore, they can also affect the heat balance of the PV cells (ALY; AHZI; BARTH, 2019).

d. **Mismatch losses:** these are losses caused by the interconnection of PV cells or modules with different operating parameters (V_{OC}, I_{SC}, etc.) or which are experiencing different operating conditions. In the first case, the maximum power point of the cells happens at different values of voltage and current. In the second case, the electrical parameters of one of the cells/modules have a considerable contrast with the remaining devices. Therefore, in both cases, the device with the lowest performance (PEARSALL, 2017) will determine the power output.

3.4.3.2 Environmental influence on photovoltaic device behavior

a. **Irradiance:** as defined in a previous section, irradiance describes the total rate of solar energy impinging on solar cells per area unit and per time unit. In this sense, the power produced by such devices is directly related to the incident irradiance, which has direct influence on I_{SC}, and second order influence on V_{OC}, *FF* and η. The higher the incoming solar energy, the higher the energy produced. Figure 3.36 shows the influence of irradiance on the *I-V* curve of a solar cell. As previously discussed, solar irradiance varies as function of the presence of clouds, hour, day of the year, weather, etc., and consequently the PV power delivered will vary according to these factors as well (FOUAD; SHIHATA; MORGAN, 2017; VIDYANANDAN, 2017).

Figure 3.36 - Effects of the incident irradiance on PV cell's *IV* curve.
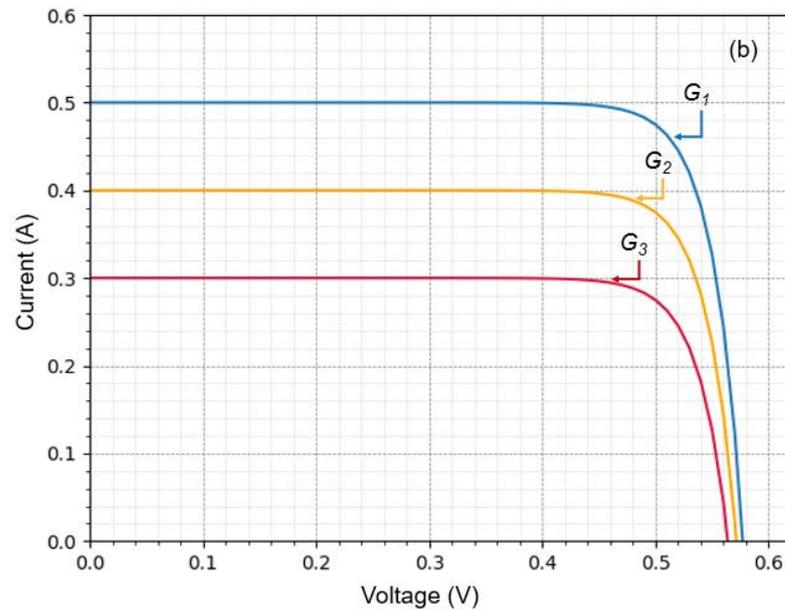
Regarding the irradiance values, $G_3 > G_2 > G_1$.
Source: Author.

b. **Module temperature:** PV cells are very sensitive to temperature variation. As working temperature increases, PV power output and efficiency decrease. Such loss can be better understood through the *I-V* curves plotted in Figure 3.37 in which shows that as *T* gets higher, the short circuit current slightly increases, while the open circuit voltage undergoes a significant reduction. As V_{OC} reduction is more pronounced than I_{SC} increment, the power and efficiency deteriorate. The PV device temperature is affected by several environmental factors, such as incident irradiance, weather, wind speed, etc. (FOUAD; SHIHATA; MORGAN, 2017; VIDYANANDAN, 2017).

Figure 3.37 - Effects of working temperature on PV cell's *I-V* curve.
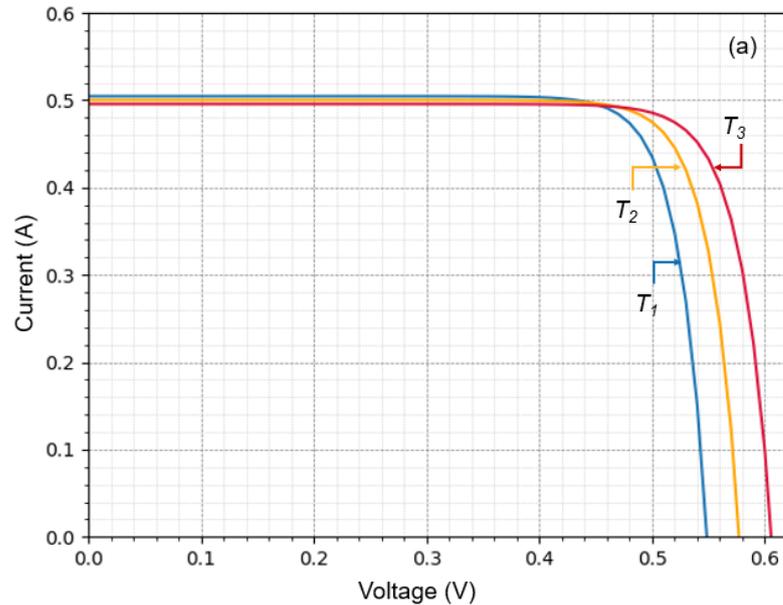
Regarding the temperature values, $T_1 > T_2 > T_3$.
Source: Drawn by Author.

c. **Angle of Incidence:** the irradiance impinging on the plane of the array (*POA*) is dependent of its angle of incidence (*AOI*, in degrees). As *AOI* increases, more light can be reflected from the PV surface and the path travelled by photons in the solar cell interior grows larger, thus reducing generated power. The magnitude of *AOI* effects is a function of the solar position throughout the day and year for the site in which the PVs are installed, its orientation regarding Earth's equator, and the module reflection characteristics (DIRNBERGER; MULLER; REISE, 2015; PEARSALL, 2017). Soiling also influences losses due to *AOI* effects.

d. **Soiling:** as defined by Vidyanandan (2017), soiling is resultant of the accumulation of particulates and other contaminants as dirt and dust on the PV module surface. The particles precipitate forming a thin film over the modules, which can shade some cells thus reducing the available light falling on the devices. These effects depend on climatic and weather conditions, module tilt angle, wind speed, and superficial properties of the

PV devices. The lower edge of a module is the most affected part, especially in PV arrays installed at low inclinations (FOUAD; SHIHATA; MORGAN, 2017; VIDYANANDAN, 2017; PEARSALL, 2017).

e. **Shading:** as the solar cells are interconnected in a PV module, the complete or even partial shading of a single cell can reduce the generated power of the whole device due to the reduced incoming solar energy and mismatch losses. Furthermore, the shaded cells can overheat and be damaged due to different currents generated by them as well as by the unshaded ones (known as the hot-spot phenomenon). Shadows happen for different reasons, as trees, buildings, etc., surrounding PV installations, as well as leaves, bird-droppings, etc. To minimize shading problems, bypass diodes are employed, and better PV interconnection schemes can be developed (FOUAD; SHIHATA; MORGAN, 2017; VIDYANANDAN, 2017; PEARSALL, 2017).

f. **Low light levels**: Under low light level conditions the fraction of the total current produced by the solar cell flowing through the shunt resistance increases. Consequently, power loss due to such resistance also increases. In this regard, PV cells with higher R_{SH} present better performance under low light levels than those with lower R_{SH} (BUNEA et al., 2006).

g. **Spectral effects:** PV cells are spectrally selective devices. Considering that the spectral distribution of solar irradiance varies as a function of atmospheric parameters like water vapor, aerosols, zenith angle, etc., such variations can cause impacts on PV performance. The spectral effects will be discussed in depth in the next sections.

3.4.4 PV systems

Photovoltaic systems are energy systems designed to supply a specific power level to an electric equipment or public electricity grid by means of PV devices (LUQUE; HEGEDUS, 2002). Basically, they are composed of the PV arrays and the balance of system (BOS). The PV arrays are an ensemble of several electrically connected solar panels designed to collect and convert sunlight into electricity. The BOS are all components employed for power conditioning, mounting and support, energy storage, wiring, etc. Table 3.10 depicts some examples of BOS components with their description and details. Depending on some PV system characteristics (such as whether the system is connected to grid or not, if it includes storage facilities, etc.), the BOS components may vary (PEARSALL, 2017).

Table 3.10 - Examples of BOS components and their description.

BOS component	Description
Inverters	PV devices generate DC power, that cannot be directly fed to the grid or consumed by AC domestic appliances. Thus, inverters are employed to convert the direct power (DC) from the PV array to alternating power (AC), that can be used by the electric network or AC loads at home.
Battery bank	Used to store the electrical energy.
Mounting structure	Metallic structure designed to fix the PV arrays at ground, rooftops or to integrate them to a building.
Wiring	Cables used to link PV system components.

Source: Fouad et al. (2017).

As it is easy to adjust the produced electric power by adjusting the number of photovoltaic modules, silent operation, lack of emissions, etc., PV systems have different applications, varying in size and configuration according to consumer needs. They can be installed on rooftops or be building-integrated with low production (household appliances) or used in a large utility-scale power station, delivering much higher amounts of electricity. In addition, they can be combined

with other energy sources as wind or hydro turbines to assure a continuous power supply, as there is no solar power production during the night (HERNÁNDEZ-CALLEJO; GALLADO-SAAVEDRA; ALONSO-GÓMEZ, 2019).

In general, PV systems are classified into stand-alone or grid-connected systems depending on whether they are tied or not to the local electricity grid. Stand-alone PV systems operate separately from the grid supply and are installed in not easily accessible areas or in applications in which they are cost-effective or desirable. Generally, they are designed and sized to have their yield matched to the energy demand, as for example, water pumping, telecommunications, ventilation fans, etc. Nevertheless, the energy generated is not usually (or infrequently) required at the same time as it is generated, so battery banks are usually employed to store electricity. A charge controller is also used for power management and protection of the batteries. In this sense, typical stand-alone PV systems are composed of PV arrays, battery bank, charge controller and the specified load. Such configuration is schematically displayed in Figure 3.38 (GERMAN ENERGY SOCIETY, 2005; HÄBERLIN, 2012; PEARSALL, 2017).

Figure 3.38 - Schematic of a stand-alone PV system providing electricity for both DC and AC loads.
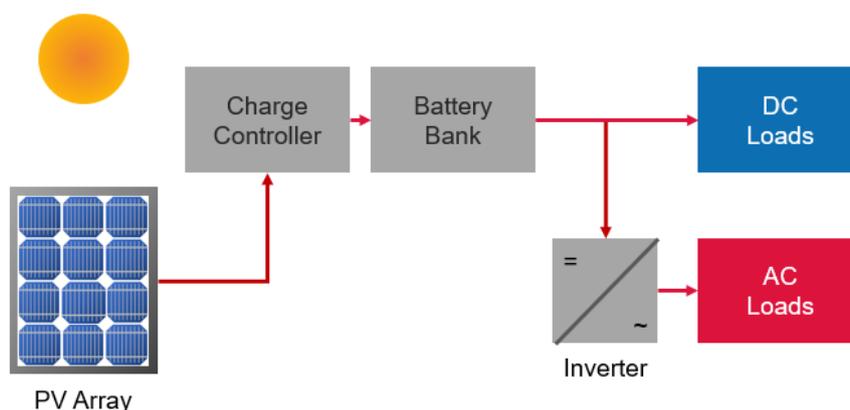
Source: Adapted from Pearsall (2017).

PV grid-connected systems (PVGCS) are those connected to the public electricity grid, which works as a kind of energy store (GERMAN ENERGY SOCIETY, 2005). They can be built for self-consumption or as a centralized utility-scale

plant. Regardless of their application, they are designed to always produce their maximum energy. PVGCS for self-consumption are developed to deliver their generation to a specific load on site. In case of shortfalls, the energy is supplied by the grid, Contrarily, in case of PV generation surplus, the excess is delivered to the grid. As battery banks are not required for grid-connected system operation, they are more cost-effective than the stand-alone systems. They also require less maintenance (PEARSALL, 2017). For these systems the PV array is connected to an inverter, which converts the DC output of the array into AC output matching the voltage and frequency of the local grid supply as shown in Figure 3.39. On the other hand, utility-scale solar plants are designed to deliver merchant power to local or regional electricity grid, supplying power at utility level as depicted in Figure 3.40. Generally, they have a Power Purchase Agreement (PPA), that is a primary contract between the parties (supplier and consumer) which guarantees a market for energy produced for a determined period. These systems have the advantage of providing electricity at a fixed price during periods when the demand peaks and the energy derived from fossil fuels is more expensive. Several utility-scale solar plants also include batteries for energy storage aiming to provide power to the grid when light level is low, increasing grid reliability and resiliency (GREEN TECH MEDIA, 2021; WORLD BANK, 2021). By the year of 2019, PVGCS accounted around 99.6% of Global Cumulative PV installation (ISE, 2020).

Figure 3.39 - Schematic diagram of a grid-connected PV system oriented to self-consumption.
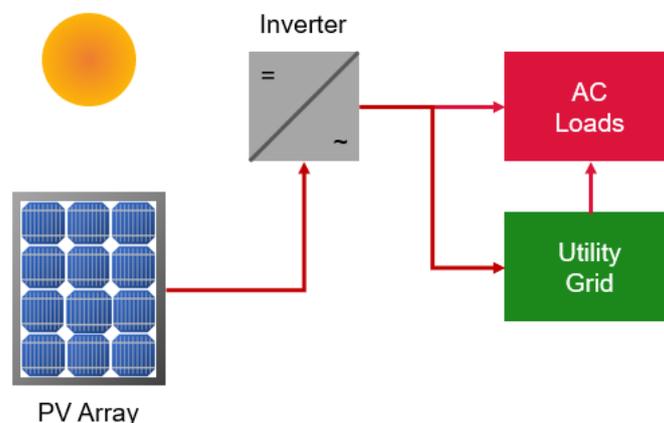
Source: Adapted from Pearsall (2017).

Figure 3.40 - Schematic diagram of a utility scale PVGCS.
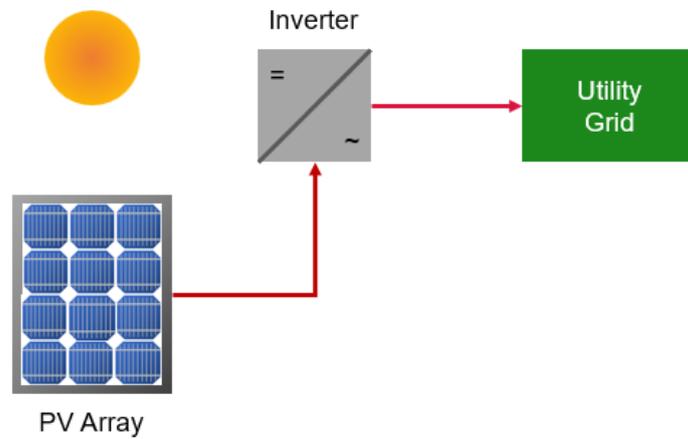
Source: Author.

Several factors impact the performance of the PV systems. Performance losses can happen in the PV arrays and in the BOS component operations, due to system configuration, climatic conditions, etc. Factors that may be detrimental to PV array efficiency have already been discussed. Losses caused in the BOS components or in the whole system are summarized in Table 3.11.

Table 3.11 - Examples of losses caused on the BOS components of a PV system.

Typical loss factor	PV system component	Description
MPP tracking losses	MPPT	Losses related to the time taken to reacquire the maximum power point of the PV modules when the operating conditions change.
Inverter efficiency	Inverter	Losses of efficiency related to inverter operation and its threshold.
Inverter clipping	Inverter	Losses caused by the inverter, as it limits the amount of PV electricity that may be drawn from the PV field because the device in question reaches its maximum capacity (Anderson and Perry, 2020).
Inverter shutdowns	Inverter	Happens when inverters shutdown and it prevents the energy delivery to the load.
Fuse losses	Fuses	Fuse losses are caused by: a) Power dissipation (Joule effect) when current flows through these components. Such losses are inevitable b) When fuses blow —due to a faulty operation of the PV field or a badly-sized design— the string current flow is interrupted. When not identified, these failures lead to efficiency decrease.
Cabling losses	Wiring	Cables used to link PV systems parts must withstand environmental and electrical conditions under which they work.

Source: Adapted from Pearsall (2017).

3.4.5 PV rating

The energy produced by PV devices depends on their operating circumstances. Considering that outdoor conditions are highly variable, a variety of PV performance indicators has been employed by the PV community to enable the commercialization of solar modules. Generally, they are rated and sold taking as reference their maximum power output $P_{MP@STC}$ [W] measured under the standard test conditions (STC). These procedures are so-called *'power rating'* (EMERY, 1999; HULD et al., 2013). Table 3.12 summarizes the standard test conditions. Power rating is very useful because it standardizes the measurement techniques and conditions, which can be easily recreated in laboratories around the world. In addition, it gives good comparison metrics among modules from the

same manufacturer and technology (EMERY, 1999; PEARSALL, 2017; IEA-PVP, 2021a). However, STC conditions are hardly met outdoors and are not representative for most regions around the world (PEARSALL et al., 2017). For example, in these conditions, the evaluation is conducted at 25°C, but PV modules typically run at 40°C to 70°C outdoors. Power rating does not give any information on how much energy is to be generated by the PV module in a long-term perspective either, which considers degradation and system losses (EMERY, 2011; CASTRO et. al, 2021; LUQUE; HEGEDUS, 2003).

Table 3.12 - Standard Test Conditions to evaluate PV performance.

Irradiance	Angle of Incidence	Spectrum	Temperature
(1000 ± 50) W·m^{-2}	(90 ± 50) °	AM 1.5G	(25 ± 2) °

Source: ASTM (2015).

While power rating under the STC is considered as a reference for PV commercialization, knowing the energy generated under realistic conditions over the lifetime or payback time of solar installations is crucial for estimating their return of investment (DIRNBERGER; MÜLLER; REISE, 2015). Moreover, the continuous assessment of PV electrical yield is very important for operation and maintenance issues (DURRANI et al, 2018). More realistic approaches were developed to rate PV modules according to their performance outdoors rather than STC power (DIRNBERGER et al., 2015; CASTRO et. al, 2021). Such approaches are known as *'energy rating'* and *'yield prediction'* and environmental data in conjunction with operating conditions are considered in addition to specific module characteristics to assess the predicted and/or expected energy production.

According to Huld et al. (2013) and Dirnberger et al. (2015), energy rating is a set of standardized calculation methods that consider optical, thermic, and electric PV characteristics in addition to weather standard data set to compare the performance of different PV modules under realistic conditions. The energy rating

74

procedures are described in IEC 61853 series of standards *"Photovoltaic (PV) module performance testing and energy rating"* and predicts the energy produced by a technology under standardized weather conditions, not being a site-specific prediction. On the other hand, yield prediction is an estimate of the total energy that a PV system may produce at a specific site. In this sense, it requires much more detailed site assessment and modeling (HULD et al., 2013), as long-term effects caused by PV system degradation and changes in availability of solar resource. Both ways to evaluate PV performance require weather data as well as module characteristics, such as irradiance and temperature dependency, angular and spectral responses, surface reflectance, etc. Simulation procedures are used to combine all data and to predict the energy yield (DIRNBERGER et al., 2015). The basic steps conducted in each energy prediction are depicted in Table 3.13.

Table 3.13 - Main parts of energy rating and yield prediction procedures for PV generating evaluation.

Step	Energy Rating	Yield Prediction
1	Measure PV module characteristics (e.g., irradiance and temperature dependency, spectral response, etc.) under STC.	Realize an assessment of the solar resource.
2	Measure weather data like irradiance, temperature, etc.	Estimate PV system performance using the meteorological data.
3	Combine the PV characteristics measured in step 1 with environmental data of step 2 to estimate the energy produced.	Simulate the long-term changes in energy yield over the expected lifetime of the PV system.

Source: Adapted from Dirnberger, Müller and Reise (2015) and Muller, et al. (2014).

3.4.6 Spectral impact on solar cells

As previously discussed, the outdoor performance of PV modules is influenced by various environmental factors. The PV community has studied the influence

exerted by the broadband irradiance and temperature for a long time, and there is a set of methods aimed at evaluating their influence on energy production with good accuracy. In addition, solar irradiance and temperature data with high quality are available with sufficient spatial and temporal resolution in different meteorological stations and solar resource databases around the world (DIRNBERGER et al., 2015; PEARSALL et al., 2017). With some exceptions, the solar resource measurement or estimation does not consider the spectral selectivity of PV devices, independently of the measurement technique employed, i.e., ground measurement, numerical modeling, or satellite remote sensing. In this sense, the available broadband irradiance data will not be the same as that absorbed by a PV module. Broadband irradiance data are measured at almost all wavelengths due to the optical properties of the thermopile pyranometers that show a flat response, in contrast with PV modules, which can only use irradiance from specific wavelength regions (DIRNBERGER et al., 2015). Figure 3.41 displays the relative spectral responses[1] (SR_r) curves of a thermopile pyranometer and that of a sc-Si solar cell for comparison. The same happens to numerical modeling and to data obtained through remote sensing. While irradiance computation in several spectral bands is available for both procedures, data used for PV forecasts are not generally concerned about spectral issues and only broadband irradiances are retrieved from these methods.

---

[1] Relative spectral response [dimensionless] is defined as the spectral response of a device normalized with respect to the highest *SR* point.

Figure 3.41 - Relative spectral responses of a sc-Si solar cell and a thermopile pyranometer. The solar spectrum is also shown for comparison of the fraction absorbed by both devices.
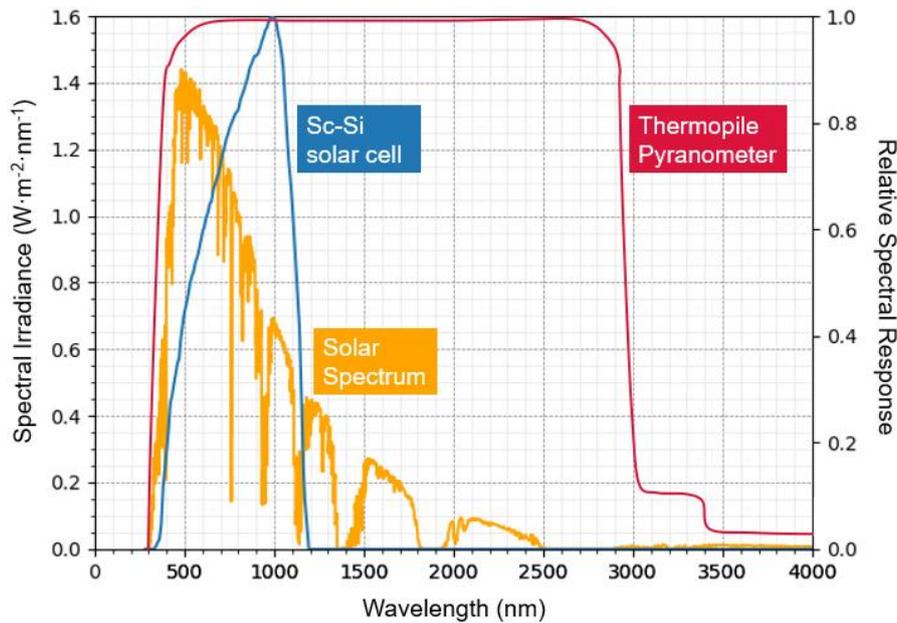
PV devices spectral sensitivity in comparison with scientific techniques employed for irradiance measurement in addition to the variability of the solar spectral irradiance lead to the spectral effects observed in different papers (DIRNBERGER; MÜLLER; REISE, 2015). In this sense, the spectral effects can be defined as the difference between the expected and the real performance exhibited by a PV device due to the difference between the actual and the standard solar spectra in addition to the difference between the spectral responses of the PV device and the equipment used for solar resource measurement. Neglecting such effects may cause errors of up to 10% when modelling parameters such as the short-circuit current of single junction large band gap PV devices on energy yield predicting (GOTTSCHALG et al., 2005) and up to 18% in PV modules performance modelling (LINDSAY et al., 2020). According to Duck and Fell (2015), following incident irradiance and temperature, the spectral irradiance may provide the largest contribution to variations in output of PV devices. It is worth mentioning that other effects (such as soiling, *AOI,* etc.) may also affect the influence exerted by solar spectra on PV.

In order to illustrate spectral effects, solar spectra were simulated using *SMARTS2* under the same conditions as the ASTM AM1.5G standard but varying only the atmospheric precipitable water amount from 1.42 cm to 12 cm and the air mass in the range of 1.5 – 7.5, separately. The photogenerated current of an amorphous silicon PV cell produced under each synthetic solar spectrum was computed through Equation 3.25 and then divided by the photogenerated current yielded by the same device under the ASTM AM1.5G. The results are plotted in Figure 3.42 (a) for *PW* and Figure 3.42 (b) for *AM* variations. For comparison, the same ratios were computed for a thermopile pyranometer[2] under the same conditions and are also shown in these graphs. In Figure 3.42 (a), the increasing water vapor amount deteriorates the infrared part of the solar spectrum. Such effect can be measured more precisely with the pyranometer, which can absorb solar radiation up to ~ 3000 nm. For this device, I_{PH} decreases more intensely than that of a-Si, which is sensitive to irradiance only up to around 780 nm. The latter device is less affected by spectral variations taking place in wavebands that cannot absorb. Therefore, their photogenerated current is higher than that produced by the thermopile pyranometer. If such equipment is used as a reference device for PV performance estimation, its measurements will result in an underestimation of the current generated by the aforementioned PV technologies. It can be defined as *'spectral gains'*, situations in which solar cells generate more energy than the predicted amount assuming that the incident broadband irradiance —measured with a reference device as discussed here — conforms to the shape of an AM1.5G distribution.

---

[2] From a technical point of view pyranometers do not have a short circuit current. For a better understanding of the spectral effects, signal generated by such devices in the present context is thought of as the short circuit current of a theoretical PV device with relative spectral response in the vicinity of the unit within the waveband from 200 nm to 3800 nm.

Figure 3.42 - $I_{PH}/I_{PH\ AM\ 1.5G}$ ratio versus incident irradiance obtained for an amorphous silicon solar cell and a thermopile pyranometer sensor under different (a) *PW* conditions and (b) *AM* conditions. For computations, solar spectra were simulated with *SMARTS2* radiative transfer code (Gueymard, 1995;2001) for the U.S. Standard Atmosphere (NOAA, 1976), Rural aerosol profile proposed by Shettle and Fenn (1976), on an inclined surface with 37°.
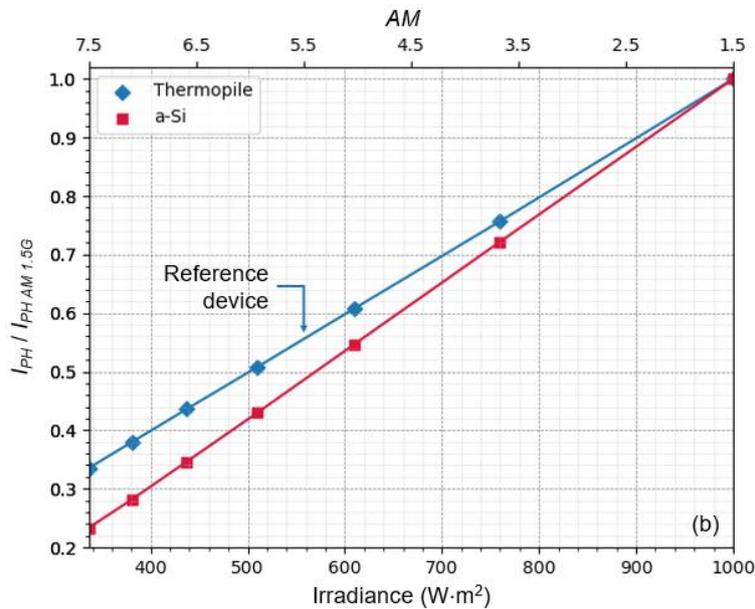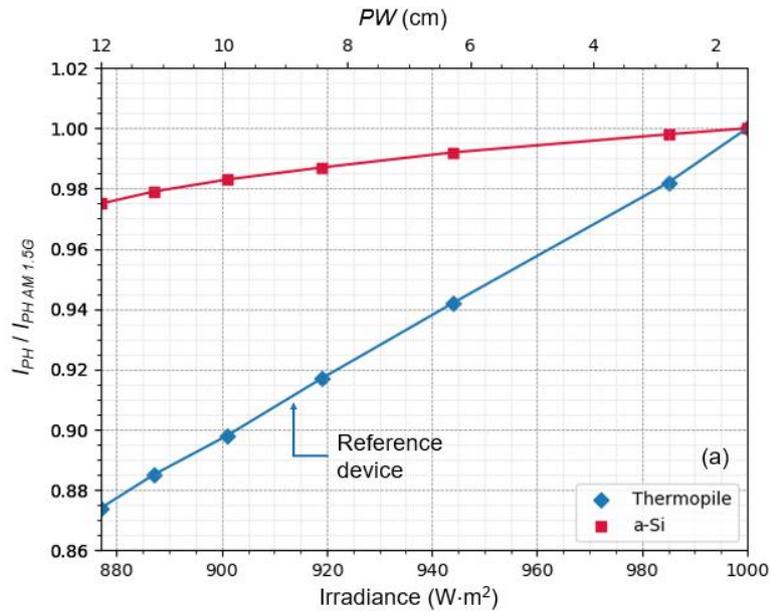
Source: Author.

Figure 3.42 (b) depicts the effects of the pathway traversed by the solar radiation on the atmosphere at irradiance level and the current generated by devices under concern. The degradation caused by the increasing *AM* in solar spectrum affects the a-Si solar cell more intensely in comparison with the thermopile pyranometer. As amorphous Silicon absorbs radiation over a narrower waveband, its signal is more affected by the Rayleigh scattering effects, which is more intense in lower wavelengths. The thermopile pyranometer, on the other hand, has a wider spectral response. Therefore, its output signal can be balanced with photons from the longwave fraction of the solar spectrum, which is less affected by *AM* increase. When PV cells produce lower energy than the predicted amount assuming that the incident broadband irradiance —measured with a reference device as discussed here— conforms to the shape of an AM1.5G distribution, a *'spectral loss'* situation takes place.

In view of the above, disregarding the spectral PV device selectivity and spectral variability during the assessing of PV performance might lead to errors. So, instead of the total broadband irradiance, the so-called *'effective irradiance'* should be considered for energy rating or yield prediction of PV. As defined by IEA (2017), the effective irradiance is the total irradiance arriving at the plane of the array (*POA*) adjusted with the soiling, reflection, shading, and spectral losses, i.e., the irradiance fraction that truly contributes to power generation by a PV device. Studies to improve the knowledge of the impacts caused by these PV factors have been conducted around the world in last decade.

3.4.6.1 Parameters for spectral impact evaluation

Spectral effects can be investigated and quantified through a variety of parameters. The most common are the Spectral Mismatch Factor (*MM,* dimensionless), the Spectral Factor (*SF,* dimensionless), and the Useful Fraction (*UF,* dimensionless). Other factors also exist and have been applied in different studies as outlined by Rodrigo et al. (2017). However, they are not as commonly adopted as the ones previously mentioned. The Spectral Mismatch Factor is defined in the IEC 60904-7 (IEC, 2019) standard as:

$$MM = \frac{\int E(\lambda)SR_{PV}(\lambda)d\lambda}{\int E_R(\lambda)SR_{PV}(\lambda)d\lambda} \cdot \frac{\int E(\lambda)_R SR_R(\lambda)d\lambda}{\int E(\lambda)SR_R(\lambda)d\lambda} \qquad (3.17)$$

Where $E_R(\lambda)$ [W·m^{-2}] is the spectral irradiance of reference, $SR_{PV}(\lambda)$ [A·W^{-1}·nm^{-1}] is the spectral response of the PV cell, and $SR_R(\lambda)$ [A·W^{-1}·nm^{-1}] is the spectral response of the reference device. *MM* can be used to estimate the impacts of solar spectrum variations in PV modules considering a pyranometer as a reference device with a flat spectral response (DIRNBERGER et al., 2015; NOFUENTES et al., 2017a). In this case, some authors name a mismatch factor as a Spectral Factor and it basically indicates how efficiently the PV material absorbs the actual incident solar spectrum compared to the AM1.5G reference spectrum absorption (RODRIGO et al., 2017). Consequently, when the value of this parameter is higher/lower than the unit, it is said that the PV material exhibits spectral gains/losses. Thus, considering a flat spectral response device – a pyranometer – reference, *MM* may be rewritten as:

$$MM = \frac{\int E(\lambda)SR_{PV}(\lambda)d\lambda}{\int E_R(\lambda)SR_{PV}(\lambda)d\lambda} \cdot \frac{\int E(\lambda)_R d\lambda}{\int E(\lambda)d\lambda} \qquad (3.18)$$

MM can also be obtained through an alternative way based on Equation 3.18 and is given by:

$$MM = \frac{I_{SC}}{I_{SC-STC}} \cdot \frac{G_{STC}}{G} \qquad (3.19)$$

Where I_{SC} [A] is the short circuit current generated by the PV device outdoors, and I_{SC-STC} [A] is the short circuit current generated by the PV device under the reference solar spectrum. In this sense, spectral effects may be estimated either by using outdoor measurements of the short circuit current generated by a given

PV device or by combining its spectral response with spectrally resolved measurements of irradiance recorded with spectroradiometers. The latter method is usually preferred to the former, given that the first one is difficult to implement over the course of a prolonged experimental campaign. Indeed, the short circuit at STC of thin film devices is often unstable, showing meta-stabilities along the year (SILVESTRE et al., 2016; NOFUENTES et al., 2017b). Moreover, the influence exerted by the device temperature, soiling, angular losses and degradation might mask the spectral effects (DIRNBERGER et al., 2015; NOFUENTES et al., 2017a). In any case, leaving aside such influences, the effective irradiance can be thus obtained through the product of the irradiance measured by a thermopile pyranometer and the *MM* (DIRNBERGER; MULLER; REISE, 2015).

Regarding the Useful Fraction, as defined by Gottschalg et al. (2003), this parameter can be obtained through:

$$UF = \frac{\int_a^{\lambda_{Egap}} E(\lambda)d(\lambda)}{\int_a^b E(\lambda)d(\lambda)}$$ (3.20)

Where λ_{EGAP} [nm] is the wavelength equivalent to the band gap energy related to the solar cell under concern. *UF* represents the fraction of the spectrum power available for the photovoltaic conversion. This index is easier to be obtained than *MM* because the spectral response of the device under scrutiny is not required for its computation. Instead, only the wavelength equivalent to the band gap energy related to solar cell semiconductor must be known, a value easily available in the literature (RODRIGO et al., 2017). As *UF* is device-dependent, it cannot be considered for comparison of spectral impacts among different PV technologies (BETTS, 2004). This parameter may also be used to investigate solar spectrum variation, just as *APE*. Betts (2004) demonstrated that both parameters correlate to CIGS, c-Si, a-Si, and to CdTe PV technologies.

3.4.6.2 Investigations of spectral impacts around the world

As raised by many authors (DIRNBERGER et al., 2015; NOFUENTES et al., 2013a; NOFUENTES et al., 2017a; CHANTANA et al., 2020) in comparison with the influence exerted by incident irradiance and temperature, the effects caused by the varying spectrum on PV materials are far from being fully understood. Hence, several research groups have carried out ground-based measurements in different regions of the world in order to improve the understanding of such impact. Some good contributions based on measurements taken from spectroradiometers are worthy of mention. In Loughborough (UK), Gottschalg and his research group studied the effects of solar spectrum for a maritime climate on solar cell performance of several technologies through different spectral indicators (as *UF*, *APE*, etc.) (JARDINE et al., 2002; GOTTSCHALG et al., 2002; GOTTSCHALG; INFIELD; KEARNEY, 2003; GOTTSCHALG et al., 2005). In Spain, some studies (NOFUENTES et al., 2017a; SILVESTRE et al., 2016; NOFUENTES et al., 2014; GARCIA et al., 2017) performed the spectral characterization of three different cities – Madrid, Málaga and Jaén – with *APE* and investigated the impact of the spectrum on various PV technologies by means of the *MM* on instantaneous, monthly, and annual basis. Dirnberger et al. (2015) in Freiburg im Breisgau (Germany) also analyzed the spectral influence on PV in different integration timescales considering the uncertainties related to the results. In addition, they also investigated if *APE* has a bijective relationship with the spectrum shape and concluded that it was not the case, which agrees with a subsequent work (NOFUENTES et al., 2017b). On the other hand, Chantana et al. (2020), Minemoto, Nagae and Takakura (2007) and Minemoto, et al. (2009b) hypothesized that each solar spectrum distribution has one and only respective *APE* value. Taking into account such hypothesis, this index was employed in conjunction with some other parameters to study spectral influences on the output of single-junction and multijunction solar devices in three Japanese sites: Kusatsu city, Tsukuba city and Miyazaki city. Cornaro and Andreotti (2013) investigated how solar spectrum variations collected in Rome (Italy) exerted influence on the Performance Ratio (*PR*, dimensionless) of multi crystalline and double junction amorphous silicon PV technologies.

Generally, the solar resource is measured by means of pyranometers when spectral information is not provided. Integrated irradiance is more common in comparison with the spectrally-resolved irradiance data because the latter is far more difficult and expensive to be measured on a temporally continuous basis. The cost and care required to record spectral instances can be prohibitive for research projects with limited resources. Thus, such data is uncommon and only found for few sites (POLO et al., 2020). In this sense, some researchers make use of synthetic spectra generated by atmospheric radiative transfer codes with atmospheric input data retrieved from meteorological data databases. Thus, the spectral effects on PV were investigated by Alonso-Abella et al. (2014) on different timescales through the SEDES2 spectral model and data retrieved by Meteonorm software for Stuttgart (Germany), Tamanrasset (Algeria), Madrid and Jaén. Following a similar procedure, Fernández et al. (2016) and Polo et al. (2020), simulated solar spectra with SMARTS2 software (GUEYMARD, 1995) and retrieved data from AERONET stations for many locations worldwide. Monthly and annual spectral gains of various PV technologies were obtained for all these sites. Amillo et al. (2015), resorted to satellite-based solar radiation-modelled data to study the annual average spectral mismatch in different European and African places. Their findings were validated through measurements obtained only for a CdTe module in Ispra (Italy). Despite the affordability in estimating spectral effects, simulation procedures have some advantages as the limitation on generating solar spectrum data for cloudy sky conditions (GUEYMARD; KAMBEZIDIS, 2004). In addition, Dirnberger et al. (2015), Nofuentes et al. (2017a) and Amillo et al. (2015) pointed out that spectral effect results derived from simulation and satellite-based data may deviate from those measured by ground installed spectroradiometers in European sites. In this sense, further research and subsequent empirical validation is required.

Nearly all studies presented above were carried out in mid latitude sites, where non-tropical climate prevails. In spite of different instruments, protocols, and methodology employed in their analysis, these contributions show that the spectral effects have a prominent seasonality in such sites which leads to their partial cancellation on an annual scale of integration. On the other hand, similar

studies for low-latitude sites with tropical climates are very scarce. Lack of knowledge on how PV materials are influenced by the solar spectrum in these sites still exists once just a few studies performed with ground-based experimental data are available in the literature for such locations. These contributions are discussed hereafter. Ye et al. (2014) and Chatchai et al. (2014) characterized the solar spectrum through the *APE* in Singapore and Thailand, respectively. Ye et al. (2014) studied the spectral impacts on the performance of PV modules with MM in conjunction with the Effective Irradiance Ratio (EIR, dimensionless) while Chatchai et al. (2014) adopted a parameter called Field Output Factor (*FOF*, dimensionless). In Latin America, Conde et al. (2021) investigated the spectral variations through *APE* and their effects on distinct PV technologies by means of *MM* in Lima (Peru). In Brazil, Braga, et al. (2020) studied the spectral irradiance in Florianopolis (South Brazil) and Assu (North Brazil) through the *BF* index and estimated the spectral effects on CdTe and multicrystalline PV modules by means of *MM*. Such findings indicate that in lower latitudes spectra shifting to shorter wavelengths predominates throughout the year. This feature can significantly impact PV performance. Nevertheless, due to a lack of knowledge on such issue, further research on ground-based spectral instances in different lower latitude sites are required. Indeed, besides contributing to the knowledge concerning spectral effects, such research may also help to design and/or validate the models employed on assessing the impacts caused by solar spectrum on PV in tropical regions.

4 MATERIALS AND METHODS

This study has been conducted in three south-eastern Brazilian sites: São Paulo (23°32'S, 46°38'W, 745 m - SPA), São José dos Campos (23°10'S, 45°53'W, 596 m - SJC) and Cachoeira Paulista (22°40'S, 44°59'W, 545 m - CPA). All cities are located in the macro metropolitan complex of São Paulo (SPMM), a populous urban conglomeration that emerged through the process of conurbation among metropolitan areas around São Paulo (SILVA; FONSECA, 2013; FONSECA et al.; 2020). The SPMM has around 33 million inhabitants and comprises 174 municipalities, being the richest and most industrialized region of the country (TORRES; RAMOS; POLLACHI, 2020; IBGE, 2018). São Paulo is the principal industrial center and the biggest and most populous city of Latin America and the 4th in the world with more than 21.6 million inhabitants considering its metropolitan area (IBGE, 2018). São José dos Campos is a smaller city around 93 km away from São Paulo, with lower levels of pollution and around 730,000 inhabitants (IBGE, 2018). Cachoeira Paulista is around 195 km and 110 km northeast from the former and the latter, respectively, with around 34,000 inhabitants, being the smallest and most unpolluted city studied in this work. Their location can be seen in Figure 4.1. Other sites are also highlighted in such figure for comparison.

Figure 4.1 - Map of Brazil with the three sites under scrutiny and other locations mentioned in this work for comparison.
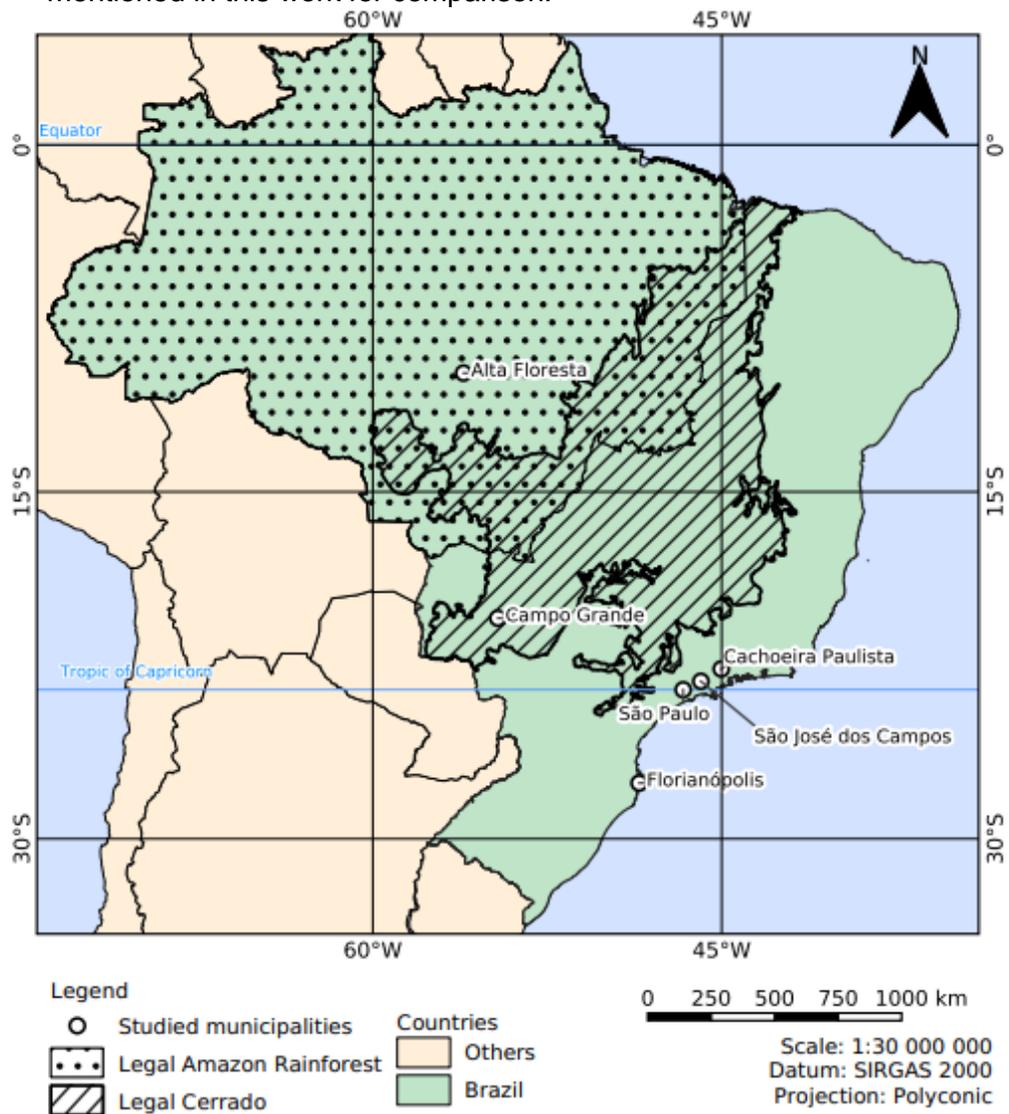
All cities studied in the present work are in the southeastern part of the country, a region with high levels of industrialization and crossed by the Capricorn Tropic, around 90 km far from the Atlantic Ocean. São Paulo and São José dos Campos have a humid subtropical climate (Cfa) according to the Koppen climate classification while Cachoeira Paulista has a temperate oceanic climate (Cfb). In general, their climate is characterized by a dry winter and a rainy summer which is influenced by the South American Monsoon System (SAMS) and by the South Atlantic Convergence Zone (SACZ), which increase the air humidity and

precipitation during the summer and spring months causing some heavy rainfall events (BRASILIENSE et al., 2018; ZILLI et al., 2019). A significant part of aerosol load over the local atmosphere, principally over the more densely populated areas is anthropogenic (HELD et al., 2012; CETESB, 2019). The aerosols are mainly produced by vehicle fuel combustion (as gasohol –a mixture of gasoline with ethanol– hydrated ethanol, and diesel), industrial activities, and resuspended urban soil dust (CASTANHO; ARTAXO, 2001; MARTINS et al., 2017, YAMASOE et al., 2017; CETESB, 2019; ALBUQUERQUE, 2012; ALMEIDA et al., 2013) observed that the most abundant aerosol species suspended in São Paulo city are brown carbon and black carbon, which are very light absorbents, especially in the shortwave wavelength range of the solar spectra (BERGSTRONG et al., 2002; DUBOVIK et al., 2002; BERGSTRONG et al., 2007; MOOSMULLER et al., 2009). Other substances are also injected into the urban atmosphere, but in lower rates, contributing in part to the varying of urban aerosols optical properties (CASTANHO; MARTINS; ARTAXO, 2008; ROSÁRIO, 2011; ALMEIDA et al., 2013; ALVIM et al., 2017). Lima and Rueda (2018) showed that the reduction of green areas, unplanned urbanization, air pollution, etc. have been causing climate changes in the metropolitan area of São Paulo such as an increase in frequency of moderate to extreme rainfall events and daily extreme temperatures.

According to Artaxo et al. (2002), Martin et al. (2010), and Rosário et al. (2011), during the dry season – from August to October– plumes derived from biomass burning associated to soil management (cattle raising and agriculture) in the Cerrado region (Midwest Brazil) along with deforestation fires in peripheries of the Amazon forest (North Brazil) are transported to all Latin America increasing aerosol load in different regions, including the state of São Paulo (LANDULFO et al., 2003; FREITAS et al., 2005; SOUZA et al., 2014; LOPES et al., 2012; MARTINS et al., 2018). Due to different sources, aging effects, etc., these aerosols have different optical characteristics from those found in the target regions of this study (CASTANHO; ARTAXO, 2001; ROSÁRIO, 2011).

4.1 Experimental setup

4.1.1 Experimental setup in São Paulo and São José dos Campos

In São Paulo city, the spectral distribution of solar radiation was measured by an EKO™ MS700 grating spectroradiometer installed on a horizontal plane on the roof of the Institute of Physics building at the University of São Paulo (*Universidade de São Paulo*, USP). Similarly, in São José dos Campos, spectral data were measured by the same instrument in addition to an EKO™ MS712 spectroradiometer both installed on a horizontal plane on the roof of the Spatial Technologies Centre building in the Brazilian National Institute for Space Research (*Instituto Nacional de Pesquisas Espaciais*, INPE). Figure 4.2 shows pictures of all spectroradiometers installed in each site. All instruments were calibrated by the manufacturer before the experimental campaign and their technical information is shown in Table 4.1.

Figure 4.2 - Pictures of EKO™ MS700 spectroradiometer installed in (a) São Paulo and (b) in São José dos Campos in addition to (C) EKO™ MS712 in the last city.
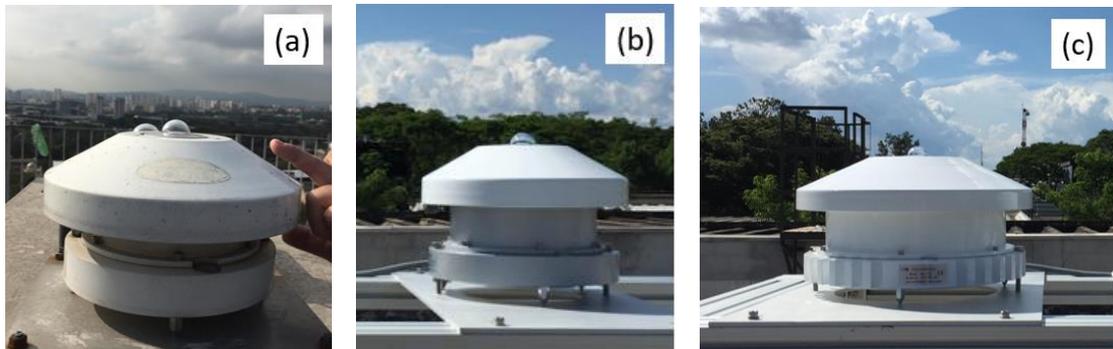
Source: Author.

Table 4.1 - Technical specifications of spectroradiometers installed in São Paulo and São José dos Campos.

Specification	EKO™ MS700	EKO™ MS712
Wavelength Range	350 to 1050 nm	900 to 1700 nm
Optical Resolution (FWHM)	< 10 nm	< 7 nm
Wavelength interval	~ 3 nm	~ 2 nm
*Wavelength accuracy	± 0.3 nm	± 0.2 nm
Temperature response	< 2% (from -10°C to + 50°C)	< 5% (from -10°C to + 50°C)
Operating temperature range	-10°C to + 40°C	-10°C to + 40°C

Source: Author.

The global horizontal irradiance measurements in São Paulo were carried out using a CMP11 pyranometer from Kipp & Zonen, installed near the spectroradiometer, also on a horizontal plane. The specifications of such instruments are in Table 4.2. On the other hand, there were no pyranometers during the spectra data acquisition period in São José dos Campos, so *GHI* was estimated through the integration between 300 nm and 4000 nm of solar spectra that were extrapolated following a procedure described in Section 4.2.3.

Table 4.2 - Technical specifications of radiometer installed in São Paulo.

Specification	CMP11
Wavelength Range	285 to 2800 nm
Sensitivity	7 to 14μV/W/m^2
Response time	< 5 s
Temperature dependence of sensitivity (-10°C to + 40°C)	< 1%
Operating temperature range	-10°C to + 80°C

Source: Author.

The experimental campaign was carried out from October 2013 to August 2015 in São Paulo city. Due to heavy rainfalls and experimental problems, data breaks

lasting a few months occurred. Therefore, a complete year sample was assembled with data collected during time intervals without interruption (or with small data breaks) of three different years. Such 'complete adjusted' year was built with three data periods, specifically those corresponding from January 2014 to February 2014, March 2015 to July 2015 and August 2013 to December 2013. Measurements were performed at every minute during the experimental campaign. In São José dos Campos, data was collected between January 2019 and December 2019 at 30-min intervals from January to the first half of August and every minute from the second half of August to the end of December. A data break that lasted 15 days occurred in September 2019.

4.1.2 Experimental setup in Cachoeira Paulista

In Cachoeira Paulista, the spectral irradiance was measured by a FLAME-S-XR1^{TM} and a FLAME-NIR^{TM} spectroradiometers manufactured by Ocean Optics, which when combined, measure radiation with wavelength ranging from 190 nm to 1650 nm (Figure 4.3). Their technical information is described in Table 4.3. Unlike EKO^{TM}, these spectroradiometers were developed to perform measurements indoors, coupled with an optical fiber and a cosine corrector depending on its application. Bearing this in mind, two apparatus were developed to adapt them for continuous outdoor exposure to collect solar radiation. One of them is a weatherproof equipment called 'Optical Interface' that collects sunlight from 2π steradians. The other one is a meteorological shelter that protects the spectroradiometers from environmental agents, such as rain, dust, etc. Basically, in this set, the optical interface collects sunlight, and the collected photons are transmitted through a bifurcated optical fiber to the spectroradiometers that are kept inside the meteorological shelter as illustrated in Figure 4.4. A computer is required to measure and store spectral data.

Figure 4.3 - Spectroradiometers (a) Flame – S – XR1 and (b) Flame – NIR from Ocean Optics installed in Cachoeira Paulista.
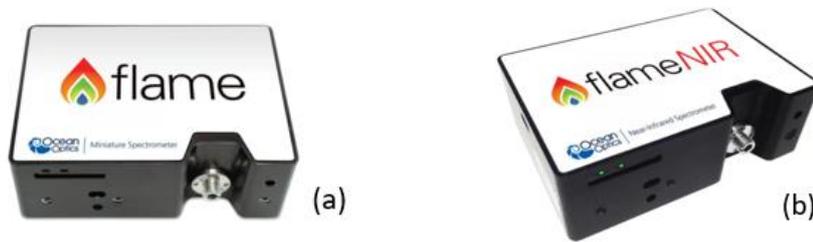
Source: Ocean Optics (2022).

Table 4.3 - Technical specifications of spectroradiometers installed in Cachoeira Paulista.

Specification	Ocean Optics ™ FLAME-S-XR	Ocean Optics ™ FLAME-NIR
Wavelength Range	200 to 1025 nm	970 to 1700 nm
Wavelength interval	~ 0.4 nm	~ 6 nm
Optical Resolution (FWHM)	~ 2 nm	~ 10 nm
Wavelength accuracy	± 0.3 nm	± 0.2 nm
Thermal stability	0.02 nm/°C for 650 nm range	0.08 nm/°C for 670 nm range
Operating temperature range	-30°C to + 70°C	-30°C to + 70°C

Source: Author.

Figure 4.4 – Layout of the automatic acquisition system installed at Cachoeira Paulista.
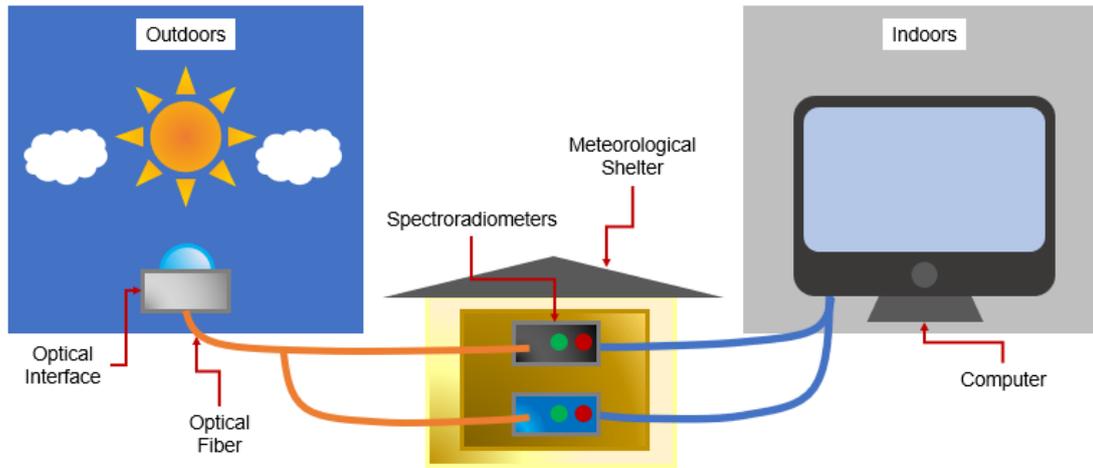
Source: Author.

The entire set, except the computer, was installed at the roof of the Meteorological Instrumentation Laboratory (Laboratório de Instrumentação Meteorológica - LIM) at INPE's campus in Cachoeira Paulista on the horizontal plane. Spectral data was collected every 1-minute from August 2020 until July 2021 and only one major data break occurred in this interval. On October 2020, INPE campus in CPA suffered intense fires as a result of an extreme drought. . In order to avoid serious damages to the system and to data measurement influenced by fire smoke, the system was turned off for 15 days. Smaller data breaks also happened, but they lasted less than two days.

In this site, the global horizontal irradiance data was retrieved from SONDA's station (*Sistema de Organização Nacional de Dados Ambientais*) installed in Cachoeira Paulista. SONDA project is a network of ground-based environmental sensors established by INPE Laboratory of Modeling and Studies on Renewable Energy Resources (LABREN). It is comprised by several meteorological stations installed all over Brazil and maintained by collaborators from universities, institutes, scientists, and partners. This project has been providing long-term continuous and public domain database of wind and solar resource in Brazil for more than 15 years. From the available data, *GHI*, *DHI*, photosynthetically active radiation (PAR), air temperature, air pressure, air relative humidity, etc. can be

cited. At Cachoeira Paulista station, *GHI* and *DHI* data were retrieved from SONDA station also installed at LIM/INPE.

It is worth mentioning that the same system was installed at the Institute of Physics at USP (SP), but due to communication problems between the spectroradiometers and the computer, the continuous data process acquisition was seriously hampered. For unknown reasons, the devices were taking a long time to respond to the computer. Different cables in conjunction with different communication standards and time intervals were applied without good results. Thus, measurements over long time intervals could not be made with this system in São Paulo. The same failure also happened to the system installed in Cachoeira Paulista, but the communication problems were fixed, and the measurements were carried out. In both cases, a 20m long USB cable was employed. In CPA such solution worked, whereas in SP the same was not true. These communication issues   must be upgraded in future studies.

4.1.2.1 Optical interface

Optical Interfaces were developed on the Design and Mechanical Fabrication Department of Manufacturing, Assembly, Integration and Testing Coordination at INPE (*Coordenação de Manufatura, Montagem, Integração e Teste do INPE –* COMIT/INPE) to collect sunlight for the spectroradiometers as they are fragile devices and can be damaged if exposed to dust, heat, rain, etc. An illustration of the entire optical interfaces with their parts is shown in Figure 4.5 (a). The optical interfaces are composed of a head, which works as radiation collector, and of a body, that supports the head. The head has a Polytetrafluoroethylene (PTFE) diffuser as optical entrance of solar radiation protected by a quartz dome fixed to a weatherproof aluminum body as shown in Figure 4.5 (b). The body has a drying cavity equipped with a drying cartridge where replaceable silica can be stored to reduce the humidity on the inside, avoiding water precipitation on the quartz dome. One end of the optical fiber is attached to the body, just below the diffuser and the other end is attached to the spectroradiometers. Screwed to the body, there is an aluminum base with four legs made of the same metal to fix the interface to the ground or to a measuring table which also serve as support for

the optical fiber. Adjustable levelling feet with a built-in bubble level are also installed on the body for horizontal position regulation. Photos of the Optical Interfaces can be seen in Figure 4.6.

Figure 4.5 – Scheme of the Optical Interface's (a) body and (b) head.
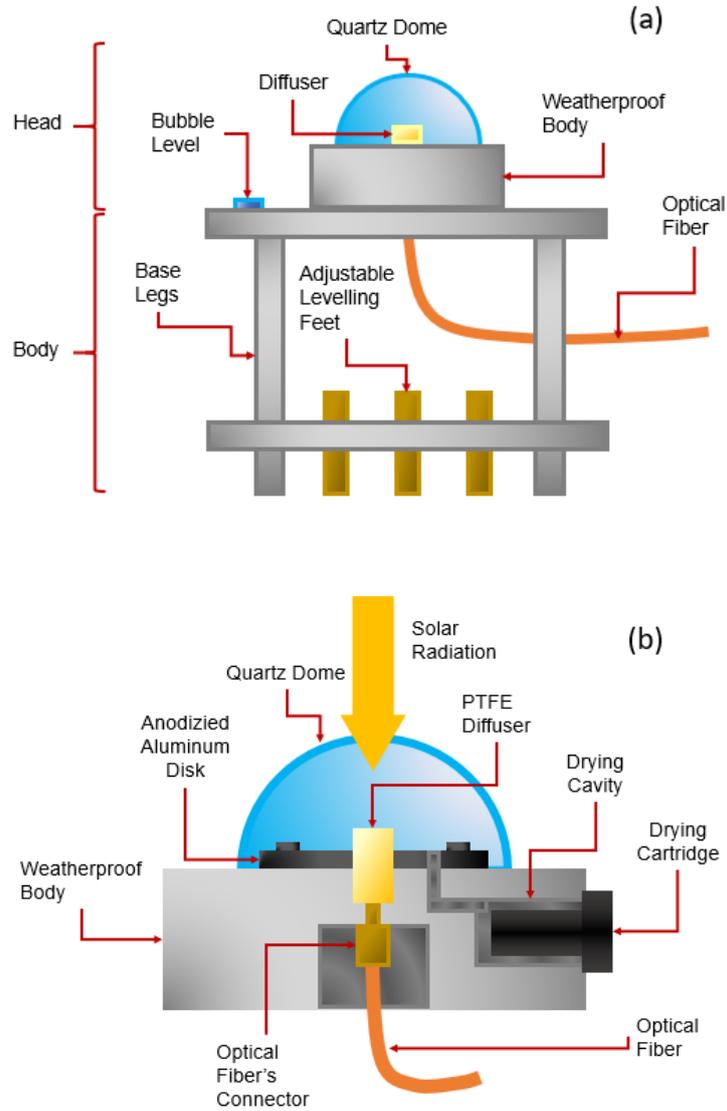
Source: Author.

Figure 4.6 - Pictures of the Optical Interfaces installed in (a) Cachoeira Paulista and (b) São Paulo.
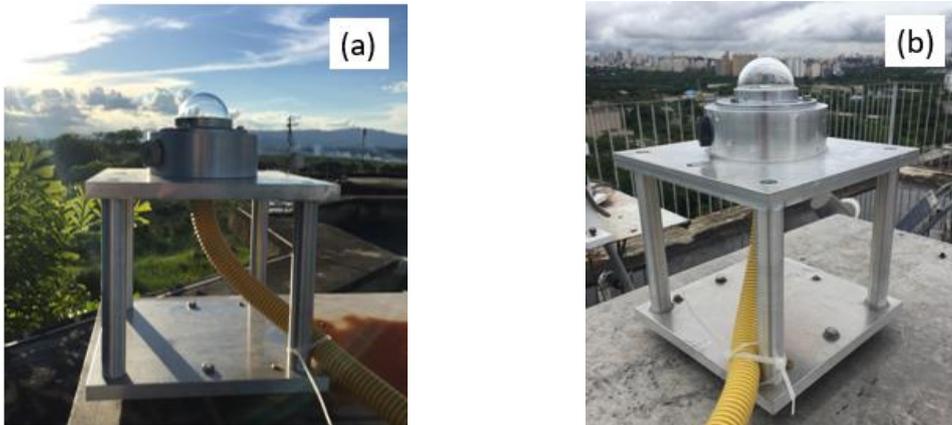
Source: Author.

When the interface is illuminated, photons are firstly transmitted through the dome and then through the diffuser, where they spread in all directions inside it in a way that the luminous output is homogeneous in all directions, thus avoiding effects caused by the solar radiation incidence angle. PTFE was chosen for the manufacturing of the diffuser because of its good properties as discussed by Tsai et al. (2008) and Vilela (2010). Besides that, this material also has an almost linear spectral transmittance between 250 and 850 nm as shown in Figure 4.7. Such property was measured with a U-3501 spectrophotometer from Hitachi installed in the Spatial Technologies Centre at INPE. After leaving the diffuser, the luminous signal is collected by the bifurcated optical fiber and conducted to the spectroradiometers. The optical fiber was also ordered from Ocean Optics ™ and designed to match the measurement waveband of spectroradiometers. Its technical specifications are in Table 4.4.

Figure 4.7 - Absolute Spectral Transmittance of the Teflon used to manufacture the Optical Interface diffuser.
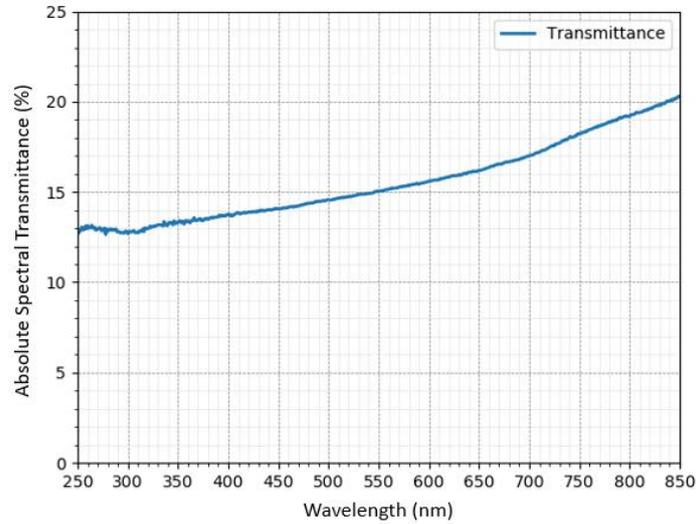
Source: Author.

Table 4.4 - Technical specifications of optical fiber used in conjunction with Ocean Optics [TM] spectroradiometers.

Specification	Description
Model	BIF200-VIS-NIR
Wavelength range	400 to 2100 nm
Fiber core size	200 μm
Length	2 m
Operating temperature range	-65°C to + 300°C
Aperture number	0.22

Source: Author.

The set composed of the optical interface and the bifurcated optical fiber was developed to meet the law of cosines. The error to the cosine response is plotted in Figure 4.8 (a) for the Optical Interface 1 (OI1) and (b) for the Optical Interface 2 (OI2). Such characteristic was measured in three different positions around its central axis as illustrated in Figure 4.9. For OI1 an error lower than ±5% up to

AOI around 65°, 70° and 72° was obtained for positions 1, 2 and 3, respectively. In OI2 case, the error was lower than ±5% in *AOI* around 58° for position 1, 62° for position 2 and 66° for position 3. For comparison, the same graph is plotted for the EKO^{TM} MS700 spectroradiometer in Figure 4.10 in four different sides illustrated in Figure 4.11 with data provided by the manufacturer. The error was lower than ±5% between 0° and 80° for all directions of measurements with the highest differences to the cosine response happening for 70° and 80° of radiation incidence. Comparing the results of Figure 4.8 and 4.10, it is clear that the 'state-of-the-art' spectroradiometers (the one manufactured by EKO) has a better response to the cosine law. But the equipment developed at INPE also has good cosine behavior on lower *AOI* angles, which means that they can perform measurements with low errors in such situations.

Figure 4.8 - Relative error to the cosine response in three positions (0°, 120° and 240°)
of the (a) Optical Interface 1 and (b) Optical Interface 2.
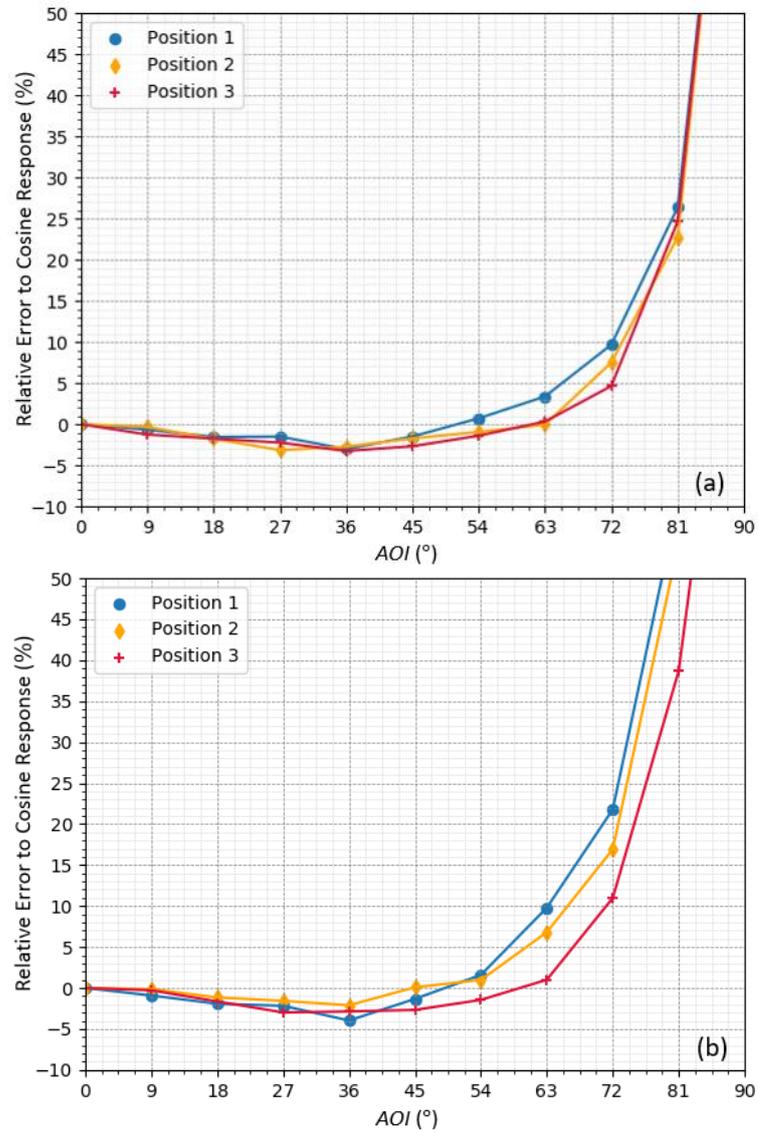
Source: Author.

Figure 4.9 - Positions in which the error to the cosine law of the Optical Interfaces were measured. The Optical Interface were rotated around its central axis every 120° to be measured at (a) position 1 at 0°, (b) position 2 at 120° and (c) position 3 at 240°.
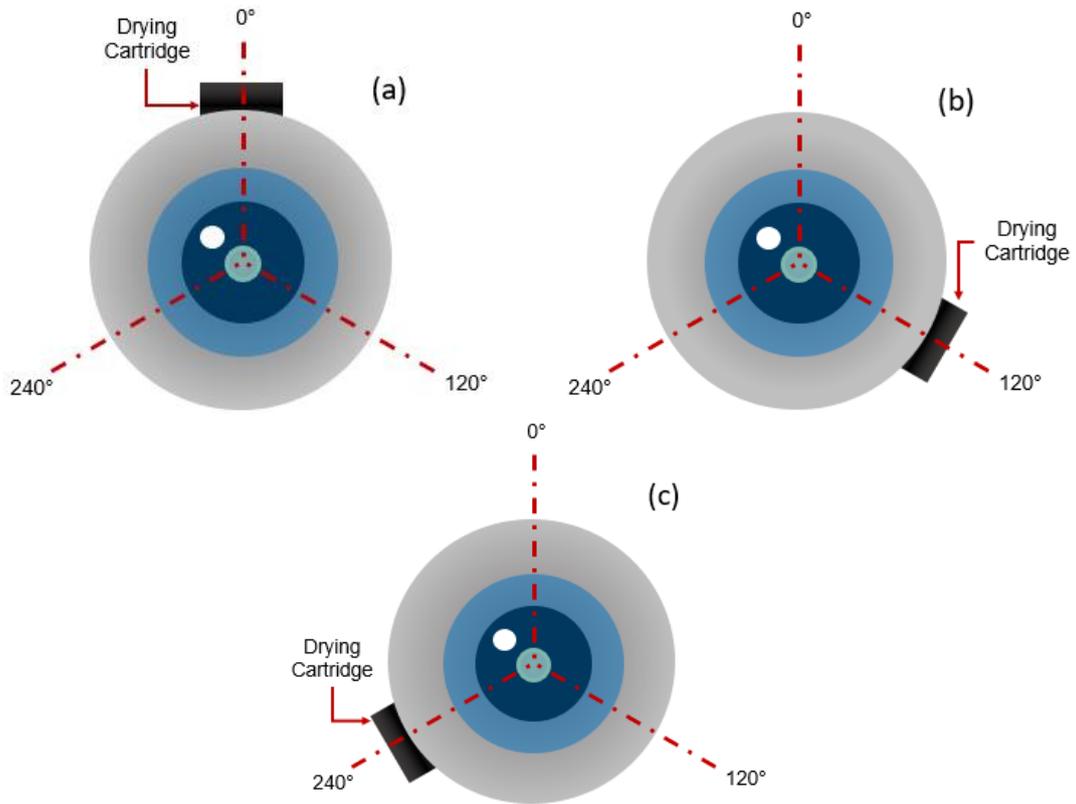
Image from the top.
Source: Author.

Figure 4.10 - Relative error to the cosine response in three positions (South, North, East, and West side) of the EKO^{TM} MS700 spectroradiometer. Data provided by the manufacturer.
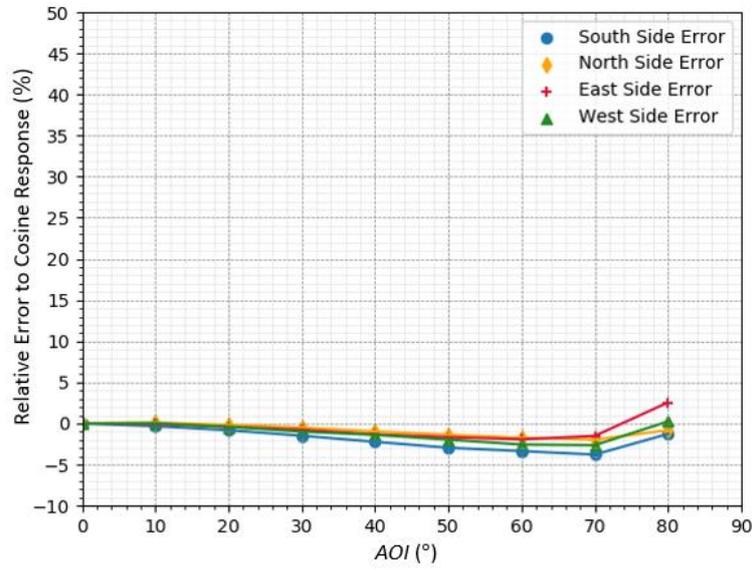
Source: Author.

Figure 4.11 - Positions in which the error to the cosine law of the EKO^{TM} MS700 spectroradiometer was measured. Data provided by the manufacturer.
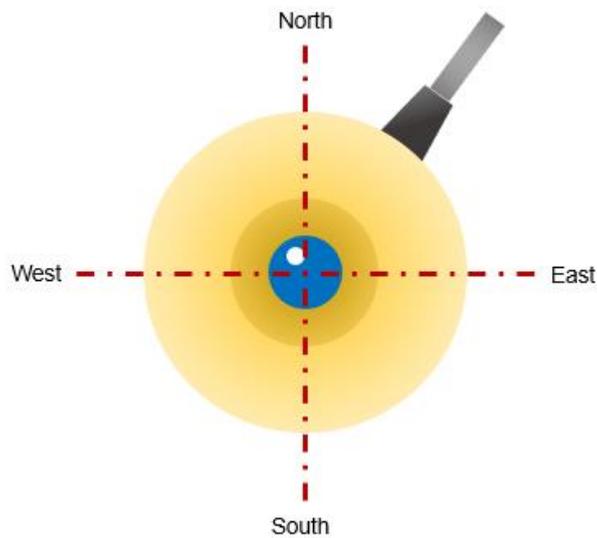
Image from the top.

Source: Author.

The spectral error to the response cosine was also investigated and is shown in Figure 4.12. According to these results, for lower angles (*AOI* ≤ 45°) the spectral error is almost linear for all wavelengths analyzed. For higher levels of incidence, the error is slightly higher for long wave radiation, reaching a maximum difference of 0.05% between 550 nm and 1000 nm for an angle of incidence of 72°. As the error to the cosine law is bigger in such situations, the difference is scarcely significant, as it does not vary as much as *AOI*. So, no variations on transmittance are expected to happen during the optical interface lifetime.

Figure 4.12 - Absolute Spectral Transmittance of the Teflon used to manufacture the Optical Interface's diffuser

Source: Author.
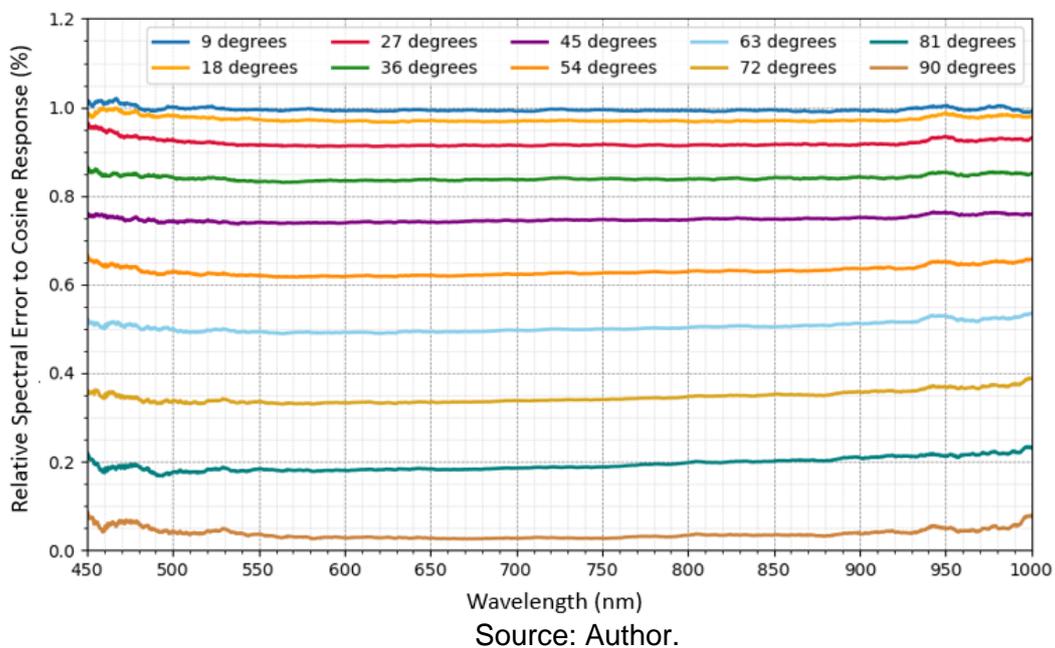
The scheme in Figure 4.13 illustrates the cosine response measurements conducted with a system assembled on an optical table at GDF's laboratory. A Newport Quartz Tungsten Halogen (QTH) Lamp Number 6315 was used in this system to irradiate light through three collimation tubes (3 m length and 40 cm diameter) and two aluminum first surface mirrors to illuminate the optical interface. The optical interface is attached to a holder which is rotated by a step motor around an axis perpendicular to the table in a way that the *AOI* of incident radiation varies between -90° and +90° as demonstrated in Figures 4.14 (a), (b) and (c). The diffuser is illuminated during all rotational movement. A Newport

photodiode Number 818 UV-DB, an NI USB-6211 data logger from National Instruments and a computer were used to measure the luminous signal collected by the optical interface.

Figure 4.13 - View from the top of the optical table where the set used to measure the response to cosine law of Optical Interface is assembled.
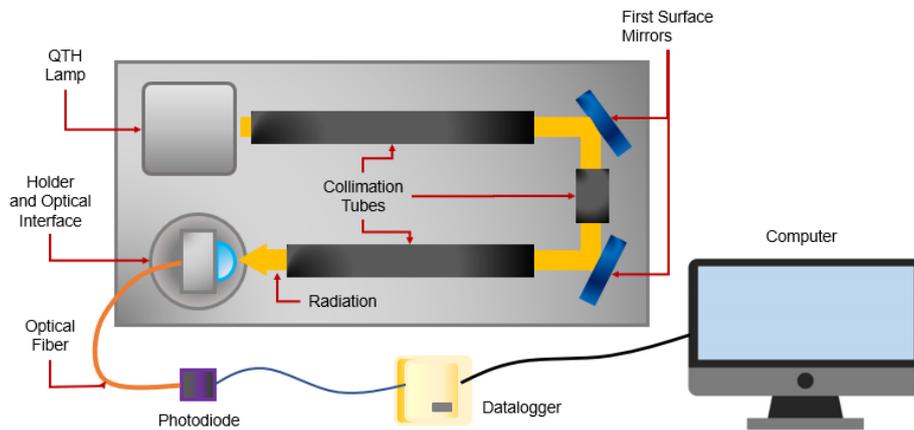
Source: Author.

Figure 4.14 - View from the top of the optical interface fixed on the holder while it turns around an axis perpendicular to this page during cosine's law response measurements.
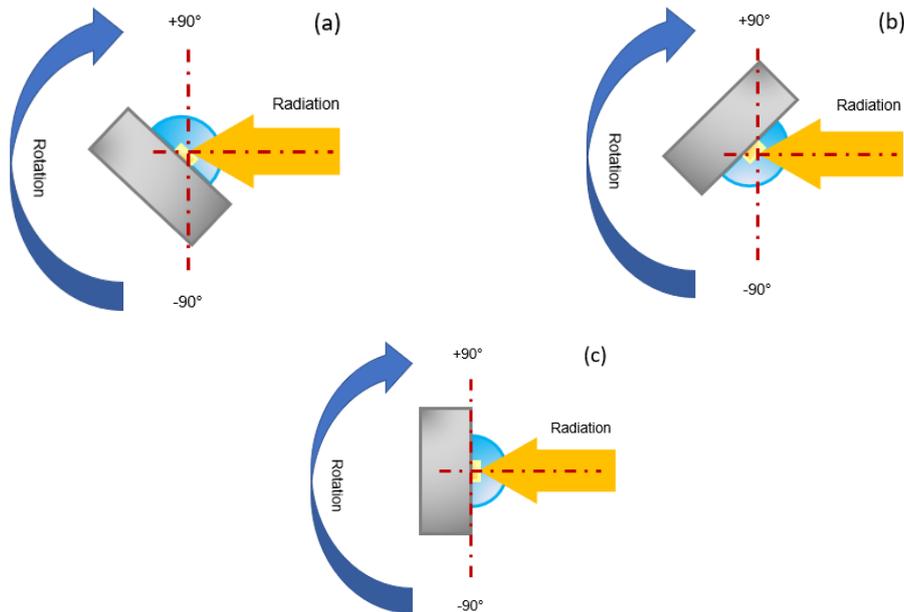
The holder turns in a way that the diffuser is illuminated all along the rotational movement. Please note that the AOI incident radiation varies between -90° and +90°.
Source: Author.

4.1.2.2 Meteorological Shelter

The meteorological shelters were developed to protect the spectroradiometers from weather enabling the usage of such devices outdoors. It is a shelter made of marine plywood painted with white oil-based paint with four cast iron legs, galvanized steel roof and, two front doors as shown in the illustrations of Figure 4.15. Ventilation grids are installed in the front and the back of the meteorological shelters, and two cooling fans are fastened inside them to enable air circulation. In one of the lateral walls there is a passage for the optical fiber. A refrigerator has also been used inside the shelters to maintain the spectroradiometers temperature around 20°C. A picture of shelters installed in Cachoeira Paulista and São Paulo is shown in Figure 4.16.

Figure 4.15 - Meteorological shelter front view illustration with (a) the front doors closed and (b) open.
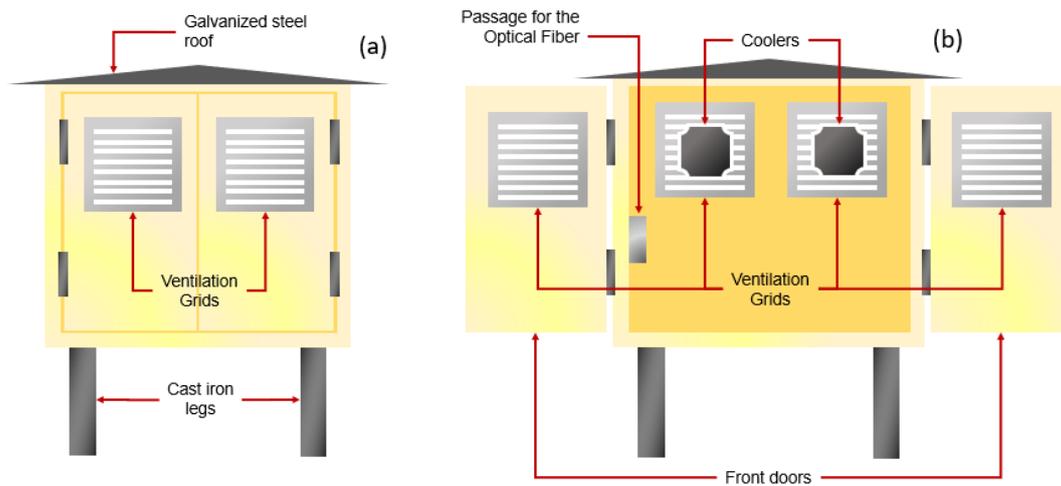
Source: Author.

Figure 4.16 - Meteorological shelters installed in (a) Cachoeira Paulista and (b) São Paulo.
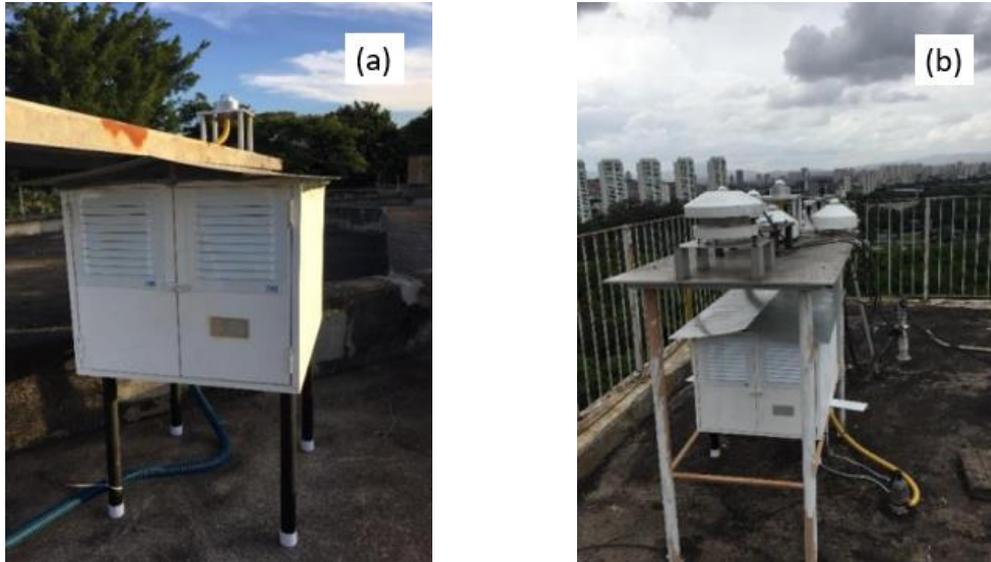
4.1.2.3 Spectroradiometer spectral calibration constant

As the optical apparatus was developed to enable spectroradiometers application, new spectral constants for solar radiation measurement for the spectroradiometers were obtained. The two sets composed of optical interface, a bifurcated optical fiber and two spectroradiometers had their spectral calibration constant measured at INPE's laboratories through the radiometric set up illustrated in Figure 4.17 following the US National Institute of Standards and Technology (NIST) (YOON; GIBSON, 2021) recommendations. As shown in the illustration, the set up was constituted by an optical table, a holder for the optical interface, a spectral irradiance standard and its DC current source. The spectral irradiance standard was the OL FEL IR lamp by Gooch and Housego, whose specifications are described in Table 4.5. Such lamp is a 1000 W FEL lamp with a tungsten coiled-coil filament enclosed in a small quartz envelope and a bipolar adjustment plug. It was calibrated by comparison to a standard that was calibrated directly against a NIST standard (2021). To ensure the accuracy of the luminous signal generated by the lamp, an OL 83A programmable DC current

source was used to supply energy to the lamp. It is a highly stable current source, and its specifications are shown in Table 4.6.

Figure 4.17 - Radiometric set up used to determine the spectral calibration constant of spectroradiometers.
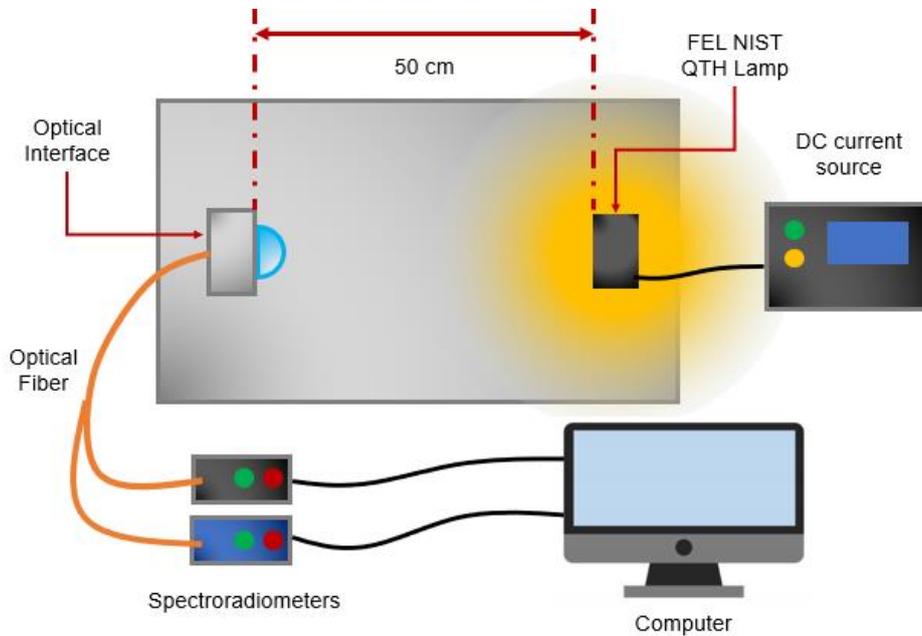
Source: Author.

Table 4.5 - Technical specifications of OL FEL IR lamp by Gooch and Housego.

Specification	Description
Manufacturer	Gooch and Housego
Wavelength range	250 to 4500 nm
Spectral irradiance (nominal)	0.03 μW/cm^{2}nm at 250 nm 25 μW/cm^{2}nm at 1000 nm
Total irradiance (nominal)	32 mW/cm^2
Long term stability	< 0.06% / hour
Operating current	8 A DC

Source: Gooch and Housego (2021).

Table 4.6 - Technical specifications of the OL 83A programmable DC current source.

Specification	Description
Manufacturer	Gooch and Housego
Power output	10 to 1000 W
Voltage output (maximum)	120 V DC
Current output (maximum)	8.4 A DC
Current resolution	0.001 A
Voltage resolution	0.01 V
Wattage resolution	0.1 W
Long term stability	< 0.06% / hour
Stability	±10 ppm after 20 minutes
Current error	< ±0.01% at 8 A

Source: Gooch and Housego (2022).

The radiometric set up was aligned in conjunction with the optical interfaces using lasers to line up the OL FEL IR filament with the center of the interface diffuser. As illustrated in Figure 4.18, the optical interface was placed at 90° in relation to the ground and the lamp had six dimensional variables of its holder indicated in Figure 4.19 and adjusted to minimize errors. The alignment was conducted using lasers and first surface mirrors. Following recommendations, the diffuser was 50 cm away from the lamp filament, where its radiation spectra is standardized and provided by the manufacturer. Such spectrum is plotted in Figure 4.19.

Figure 4.18 - OL FEL IR's adjustable holder mount with the six-dimensional variables to control the physical positioning of the lamp indicated.
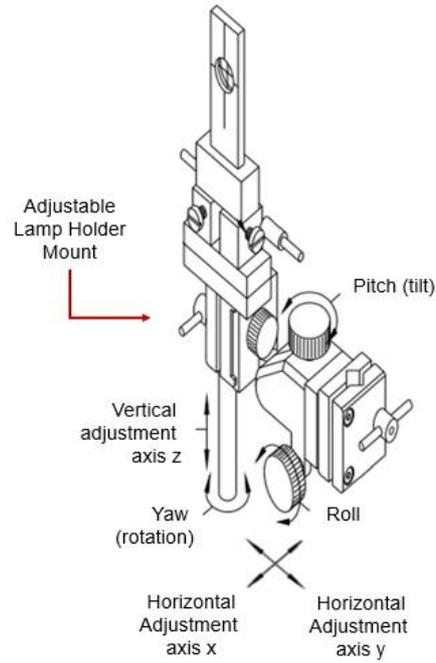
The variables are the spatial coordinates x, y and z in addition to the yaw (rotation around z axis), roll (rotation around x axis) and pitch (rotation around y axis)

Source: Adapted from Gooch and Housego (2022).

Figure 4.19 - Electromagnetic spectrum generated by OL FEL IR lamp at 50 cm from its filament.
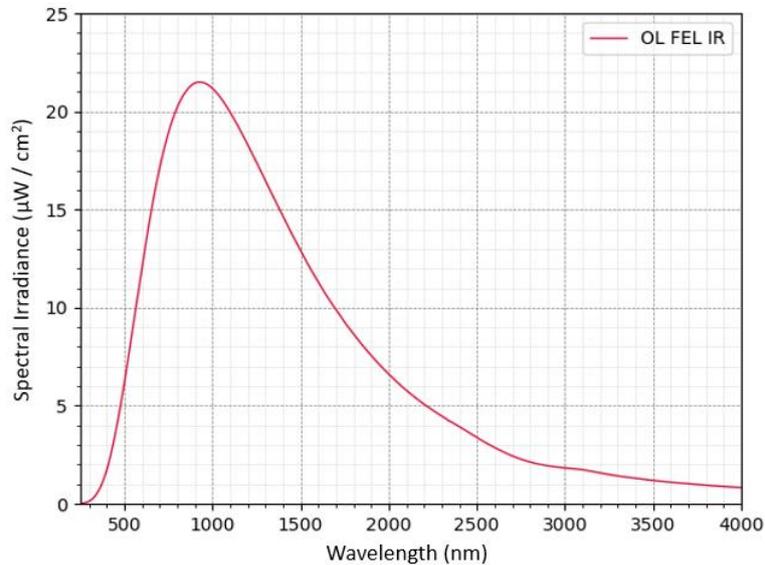
Source: Gooch and Housego (2022).

The determination of the spectral calibration constant process was conducted through the measurement of the radiation spectrum irradiated by the spectral irradiance standard at 50 cm from it by the spectroradiometer equipped with the optical interface and bifurcated optical fiber in counts units. Such measurement was then compared with the lamp spectral irradiance curve shown in Figure 4.19 by the spectroradiometer software generating the spectral calibration constants for both sets in radiometric units plotted in Figure 4.20. During the process, the dark signal is also measured and stored in the computer to be downloaded to the spectroradiometer whenever measurements with the developed set are conducted. It is worth mentioning that with the constant curves, all optical issues of all apparatus used to measure radiation are corrected. In order to avoid reflection and stray light, the laboratory walls were covered with black cloth.

Figure 4.20 - Spectral calibration constant of (a) FLAME-S and (b) FLAME-NIR spectroradiometers.
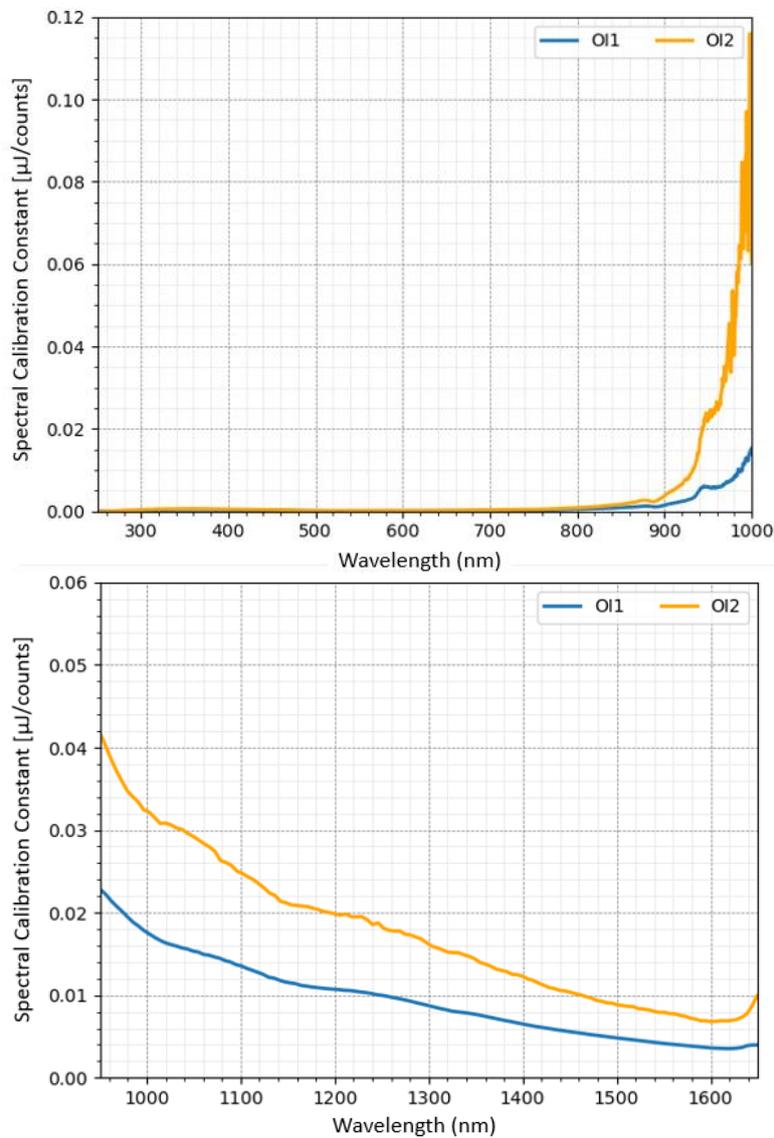
Source: Author.

4.1.3 PV materials

The impacts caused by solar radiation spectral variations were evaluated in six different PV materials. Two of them are classified as technologies from the first solar cell generation (sc-Si and mc-Si); three of them belonging to the second generation (a-Si, CdTe and CIGS), and one to the third generation (Perovskite). Their relative spectral responses were measured indoors at Fraunhoffer ISE

using an A+/A+/A+ solar simulator and 29 bandpass filters. The SR data was sourced from Dirnberger et al. (2015), and are shown in Figure 4.21.

Figure 4.21 - Relative spectral responses of PV modules representative of different technologies.
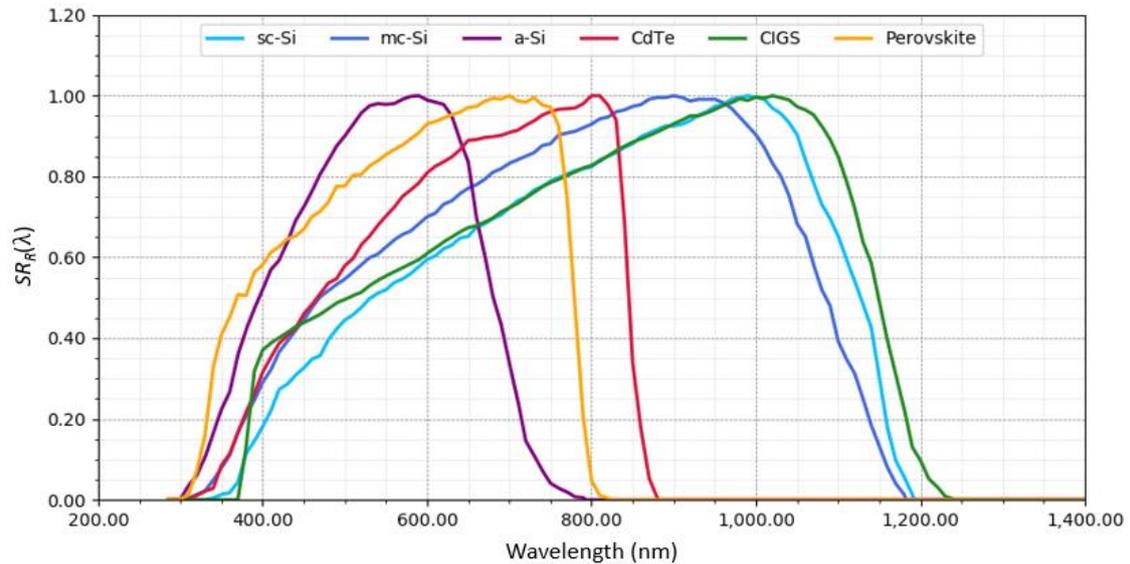
Source: Author.

4.2 Methodology

4.2.1 Spectral data filtering

Due to the huge amount of spectral data, a filtering process was implemented in order to remove corrupted and noisy files and measurements carried out outside the ideal conditions of time and zenith angle. All filters used in this work are described in Table 4.7. The F_0 was used to disregard corrupted measurement files during their generation or transfer from a computer to another. Generally, such files may have lost some characters which make their interpretation or computation impossible to be done. For similar reasons, the F_1 was also implemented. For unknown reasons, the spectroradiometers may not always use the ideal integration time to perform measurements. This leads to sensor saturation and consequently to the deformation of the generated spectral curve. Another error is caused by high temperatures of the spectroradiometer CCD which increases signal noise on longwave radiation. Measurements with low intensity also have a high noise/signal ratio. In this sense, the F_2 filter was

implemented as well in order to discard data collected in the early morning or at the end of the day.

Table 4.7 – Filters applied in this work to select data.

Filter	Description
F_0	Disregard corrupted files.
F_1	Disregard spectral data with noisy infrared regions.
F_2	Select only data collected between 7:00 and 17:00.
F_{MM}	Select only data collected with θ_z lower than 60° and *GHI* higher than 200 Wm^{-2}.

Source: Author.

The filter F_{MM} was adopted aiming to isolate spectral effects from angle-of-incidence effects on PV modules. Such filter was applied only for spectral effects on PV analysis so that spectral data collected with values of *AOI* higher than 60° were not considered. As in the present work the spectroradiometers were installed on horizontal plane, the *AOI* coincides with the zenith angle. With this filter, spectral data collected with *GHI* lower than 200 W·m^{-2} were also disregarded to reduce the uncertainty. Under low light conditions, PV modules undergo efficiency loss and inverters experience smaller efficiency, which make measurements unreliable. Additionally, only around 4% of the annual incident irradiation was collected below 200 W·m^{-2} and therefore, leaving these measurements out should not lead to significant errors in our calculations.

4.2.2 Merging procedure

In São José dos Campos and Cachoeira Paulista the solar spectra were measured by two spectroradiometers in different wavebands. As their software was not able to combine data collected with both devices, the merging approach described by Cornaro and Andreotti (2012) was followed to obtain only one solar spectrum from 350 to 1700 nm. In this approach, the merging procedure was applied on waveband between 900 nm and 950 nm. Because of the lower precision, the wavelengths of UV/VIS/NIR spectroradiometers were lined to

obtain the spectral irradiance at the same point of the NIR spectroradiometers. Then linear interpolation was used to calculate the spectral irradiance at these wavelengths. Thereby data of both spectroradiometers were combined by weighting, considering that the weighting of data for MS700N/FLAME-S-XR1 was 100% at 900 nm and 0% at 950 nm and 0% at 900 nm and 100% at 950 nm for the MS712/FLAME-NIR spectroradiometers. As an example, Figure 4.22 (a) shows a solar spectrum collected on July 1st at 12:00 pm in São José dos Campos separately and Figure 4.22 (b) shows the curves merged after applying such procedure.

Figure 4.22 - Solar spectrums measured on 1st July 2019 at 12:00 pm in São José dos Campos by (a) EKO™ MS700 and MS712 separately and (b) merged by the procedure described here.
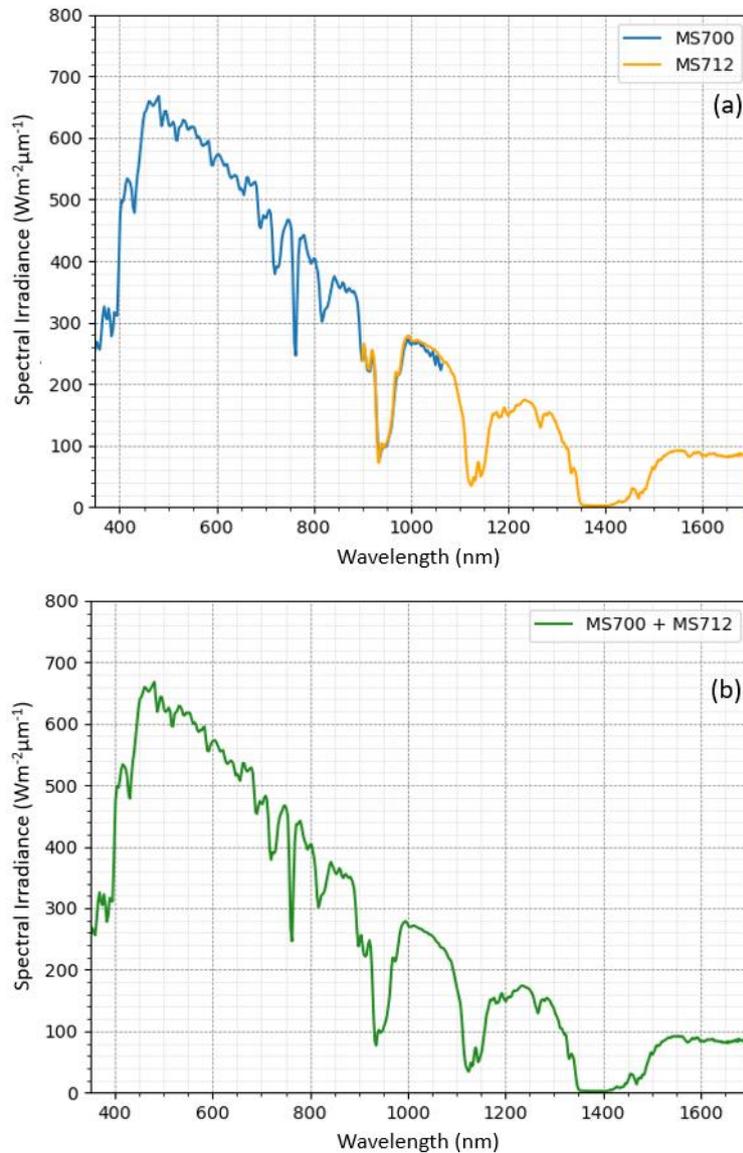
Source: Author.

4.2.3 Spectral extrapolation

In the experimental facilities installed in São José dos Campos there were no pyranometers available to perform broadband global irradiance measurements over the course of the experimental campaign. Hence, spectra measured by the spectroradiometers were first extrapolated to 280 – 4000 nm waveband and then integrated to obtain *GHI* values. Thus, the method described by Martin and Ruiz

(1999) was applied here for the near and mid infrared (NIR and MIR, respectively) radiation. In this extrapolation method, the atmospheric extinction that takes place in the interval of 700 to 1100 nm was chosen to represent the extinction occurring in the infrared (IR) portion of the solar spectrum not measured by the spectroradiometers. Therefore, the ratio between the irradiance integrated over mentioned wavelength interval of each measured spectrum and the irradiance in the same waveband of the AM1.5G standard was obtained. The spectral fraction that is lacking in the data measured by the spectroradiometers of the standard ASTM AM1.5 G was multiplied by this ratio and assumed as a part of the measured spectrum. Nofuentes et al. (2014), Nofuentes et al. (2017a) and Caballero et al. (2018), successfully followed this approach.

On the other hand, the lower limit in which EKO[TM] spectroradiometers measure the solar spectrum is 350 nm and Ocean Optics[TM] is 400 nm (because of the optical fiber equipped with it). Therefore, it was also necessary to extrapolate the spectrum to the wavelength interval of 280 - 350 nm for the former and 280 to 400 nm for the latter. Considering that in the ultraviolet (UV), Rayleigh scattering occurs due to gases, aerosols, and absorption by molecular Oxygen (O_2) and Ozone (O_3) (GOODY; YOUNG, 1989), the same principle considered for NIR and MIR region was followed for UV in this work. In this case, for EKO[TM] spectroradiometers, the ratio between irradiance integrated over 350 and 400 nm of the measured solar spectrum and the integrated irradiance in the same interval of the standard AM1.5G solar spectrum was obtained. The reference spectrum within 280 - 350 nm waveband was multiplied by this ratio and also assumed as a part of the measured spectrum. The same procedure was applied for the Ocean Optics[TM] spectroradiometers case but considering the waveband between 400 to 450 nm as reference for the extrapolation. Figure 4.23 shows the solar spectrum plotted in Figure 4.22 after the extrapolation described here.

Figure 4.23 - Example of a solar spectrum measured by EKO™ MS700 and MS712 extrapolated from its original wavelength interval of 350 to 1700 nm to 285 to 4000 nm with the procedure described here.
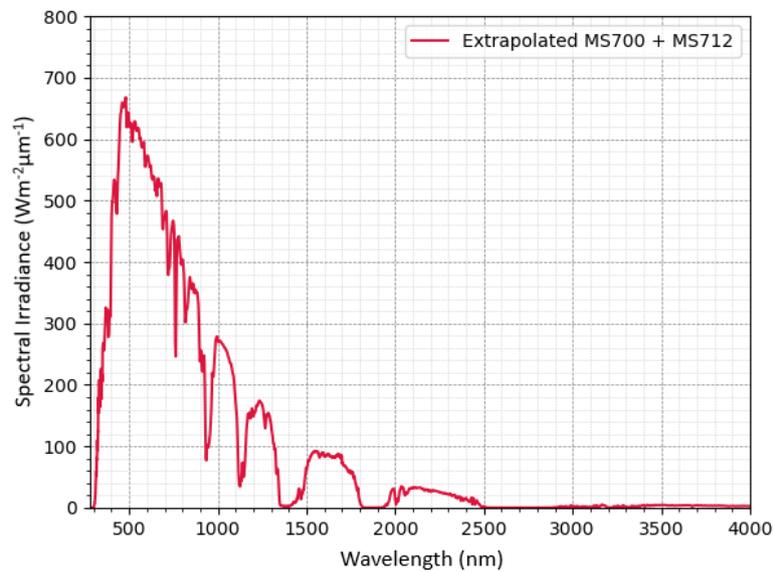
Source: Author.

4.2.4 Analysis parameters

4.2.4.1 Instantaneous spectral variations and impacts on PV materials

The instantaneous solar spectrum variation over time was studied here through the Average Photon Energy (*APE*) parameter described previously by Equation 3.7. Following the same methodology adopted in previous papers (JARDINE et al., 2002; NOFUENTES et al., 2014; NOFUENTES et al., 2017A; FERNANDEZ et al., 2016; POLO et al., 2020; CABALLERO et al., 2018; YE et al., 2014) to facilitate comparisons, the waveband of 350 to 1050 nm was considered to calculate such parameter in the present work. For such waveband, the value of *APE* of the ASTM AM 1.5G solar spectrum equals 1.880 eV. The instantaneous impacts caused by solar spectrum variations on PV materials were assessed by the Mismatch Factor (*MM*) described previously by Equation 3.18.

4.2.4.2 Daily, monthly, and annual spectral effects on PV materials

In previous sections the presented parameters considered to describe the spectrum variations and their impact on PV materials were defined in an instantaneous time scale. However, results obtained in such period cannot be very convenient for PV developers when planning their designs or for PV engineers during the monitoring of the PV modules performance (NOFUENTES; ALMONACID, 1999; LUQUE; HEGEDUS, 2002). In addition, other time scales can be useful to investigate effects of atmospheric components on solar spectrum. Therefore, *APE* and *MM* values were computed on a daily, monthly and annual basis. The daily and monthly weighted *APE* (APE_{DW} and APE_{MW}, respectively, both in eV) were obtained by:

$$APE_{DW} = \frac{\sum_{i=1}^{n} APE_i \cdot GHI_i}{\sum_{i=1}^{n} GHI_i} \tag{4.1}$$

$$APE_{MW} = \frac{\sum_{i=1}^{n} APE_i \cdot GHI_i}{\sum_{i=1}^{n} GHI_i} \tag{4.2}$$

where APE_i [eV] is the value of *APE* corresponding to the *i*-th spectral irradiance, GHI_i [W·m^{-2}] is the global horizontal irradiance corresponding to the *i*-th spectral irradiance and *n* to the total amount of data in each day or month. The values of GHI_i were computed by integrating the measured and extrapolated spectra for São José dos Campos or measured by a pyranometer for São Paulo and Cachoeira Paulista.

As previously described, in São José dos Campos the spectral data was collected at different time intervals during the experimental campaign. Therefore, the data sample size collected from January to July 2019 is smaller than that measured from August until the end of the same year. This was not the case for São Paulo, where spectral instances were logged at 1-min intervals to assemble a complete whole year. However, a few data breaks were identified in some of the 12 months under investigation in the latter site. Since distinct data sampling periods and breaks in the data series affect the annual weighted average photon energy

(APE_{AW}, in eV), a procedure similar to that followed by Dirnberger et al. (2015) was adopted to obtain the APE_{AW}, as follows:

$$APE_{AW} = \frac{\sum_{i=1}^{12} APE_{MWi} \cdot \overline{H_i}}{\sum_{i=1}^{12} \overline{H_i}}$$

(4.3)

where $\overline{H_i}$ is the average monthly global horizontal irradiation of the i-th month and APE_{MWi} is the monthly weighted APE of the i-th month, according to Equation 4.2. The values of $\overline{H_i}$ in São José dos Campos, São Paulo and Cachoeira Paulista were obtained by averaging values of monthly horizontal irradiation gleaned from the PVGIS-SARAH (Photovoltaic Geographical Information System) (PHOTOVOLTAIC GEOGRAPHICAL INFORMATION SYSTEM PHOTOVOLTAIC GEOGRAPHICAL INFORMATION SYSTEM, 2020) solar radiation database. Specifically, monthly horizontal irradiation values for each month sourced from the period 2012 and 2016 were used, as this was the most recent 5-year data period available for the sites under scrutiny.

The monthly weighted spectral mismatch factor (MM_{MW}, dimensionless) was obtained by:

$$MM_{MW} = \frac{\int E_{REF}(\lambda)d\lambda \cdot \sum_{i=1}^{n} \int E_i(\lambda) SR_R(\lambda)d\lambda}{\int E_{REF}(\lambda) SR_R(\lambda)d\lambda \cdot \sum_{i=1}^{n} \int E_i(\lambda)d\lambda}$$

(4.4)

where E_i (W·m-2·nm⁻¹) is the i-th spectral irradiance. As discussed earlier, both different recording data intervals and data breaks might bias the value of APE_{AW}. This undesired bias could also happen to the annual weighted spectral mismatch factor (MM_{AW}, dimensionless) values. Therefore, a similar procedure to that described by Dirnberger et al. (2015) for the calculation of spectral impact on an annual basis was also followed:

$$MM_{AW} = \frac{\sum_{i=1}^{12} MM_{MWi} \cdot \overline{H_i}}{\sum_{i=1}^{12} \overline{H_i}}$$

(4.5)

where MM_{MWi} (dimensionless) is the monthly weighted spectral mismatch factor for the PV technology under investigation corresponding to the *i*-th month.

4.2.4.3 Atmospheric parameters

Some atmospheric compounds were analyzed to investigate how they can impact solar spectrum in Southeast Brazil. The parameters are the Air Mass, Precipitable Water, Aerosol Optical Depth and Single Scattering Albedo. The first one was obtained through the Equation 4.6 while the remaining parameters were retrieved from ground-based sunphotometers of NASA's AERONET[3] (Aerosol Robotic Network) (HOLBEN et al., 1998) stations of São Paulo (installed at Institute of Physics/USP) and Cachoeira Paulista (installed at LIM/INPE). The chosen time interval considered for data analysis was defined by the availability of AERONET database for the mentioned sites. It is noteworthy that data retrieved from AERONET are available in the following levels of processing: level 1.0 (raw data), level 1.5 (automated cloud tracking data), and level 2.0 (data with guaranteed quality). In this work, data classified as level 2.0 and level 1.5 were retrieved according to the availability for São Paulo and Cachoeira Paulista, respectively.

$$AM = \left\{ cos(\theta_Z) + 0.48353 \cdot \left[\frac{\theta_Z^{0.095846}}{(96.7412 - \theta_Z)^{1.754}} \right] \right\}^{-1} \qquad (4.6)$$

---

[3] The AERONET program is a federation of ground-based sunphotometers established by the National Aeronautics and Space Administration (NASA), which started in the early 1990s (Holben, et al., 1998).

5 RESULTS

5.1 Site spectral characterization

To characterize the solar spectrum in São Paulo, São José dos Campos and Cachoeira Paulista, *APE* histograms of the cumulative percentage of global horizontal irradiation (*H*, in Wh·m^{-2}) collected in each site over one year are plotted for the three sites in Figures 5.1 (a), (b) and (c), respectively. The *APE* values are distributed from 1.84 eV to 2.04 eV and grouped into ten 0.02-eV bins. The results show that more than 95% of solar energy incidents on all sites during a year were measured with values of *APE* higher than 1.880 eV (*APE* corresponding to the ASTM AM1.5G solar spectrum). This percentage is high when compared to results obtained for mid-latitude sites. Minemoto, et al. (2007, 2009) conducted a similar analysis for Kusatsu city (Japan, latitude 34°58'N, longitude 135°47'W) and concluded that around 92.5% of the annual global tilted irradiation generated on a plane facing south with a tilt angle of 15.3° had *APE* values higher than 1.880 eV. In Rome (Italy, latitude 41°53'N, longitude 12°29'E), Cornaro and Andreotti (2012), found 60% for the same fraction on a horizontal plane. In the Spanish cities of Madrid (Spain, latitude 40°4' N, longitude 3°44' W), Jaén (Spain, latitude 37°49' N, longitude 3°48' W) and Málaga (Spain, latitude 36°43' N longitude 4°25' W), Nofuentes et al. (2013, 2014) concluded that 52%, 35%, and 70%, respectively, of irradiation measured on a 30°-tilted plane facing South was collected with spectral distributions in which *APE* was higher than the parameter calculated for the ASTM standard.

Figure 5.1 - Percentage cumulative distribution of the annual global horizontal irradiation collected from (a) January 2014 to February 2014, March 2015 to July 2015, and August 2013 to December 2013 as a function of *APE* (class width = 0.02 eV) in São Paulo; (b) from January 2019 to December 2019 as a function of APE (class width = 0.02 eV) in São José dos Campos; and (c) from August 2020 to July 2021 as a function of *APE* (class width = 0.02 eV) in Cachoeira Paulista.
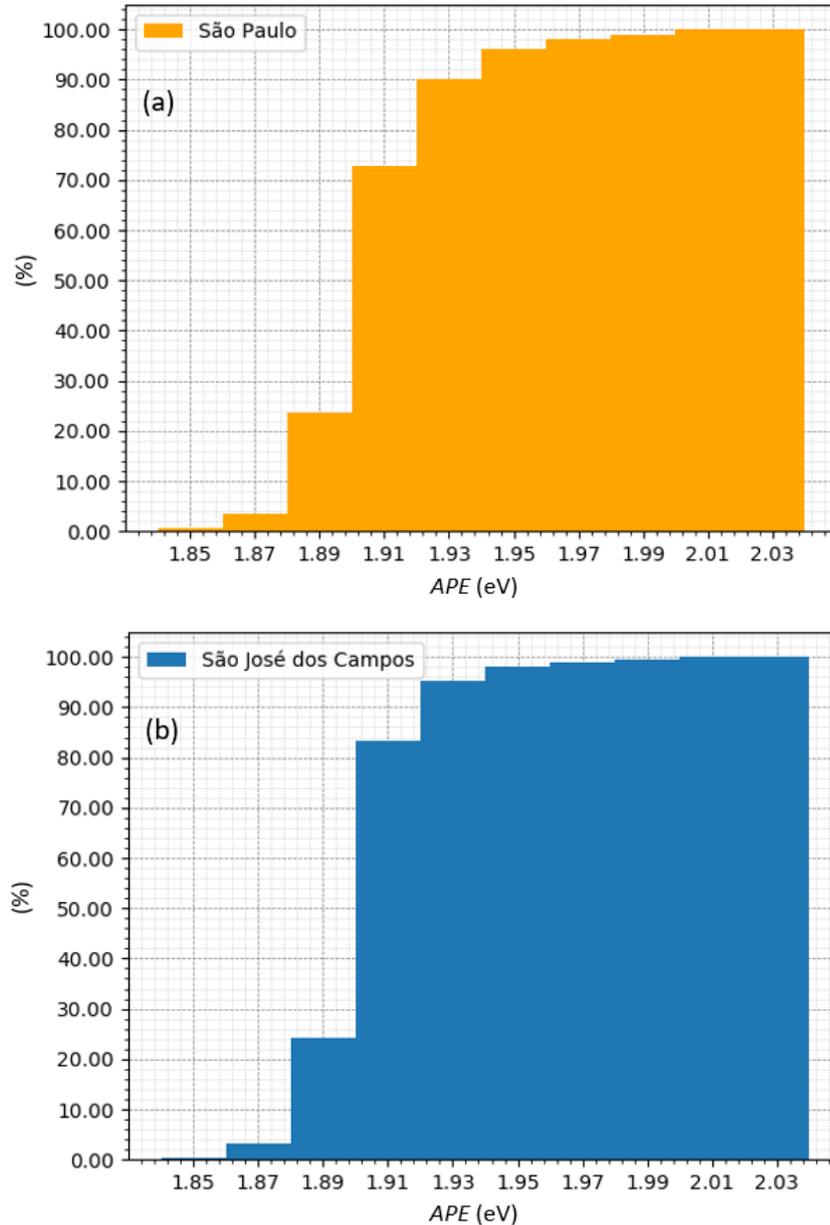
Figure 5.1 – Conclusion.
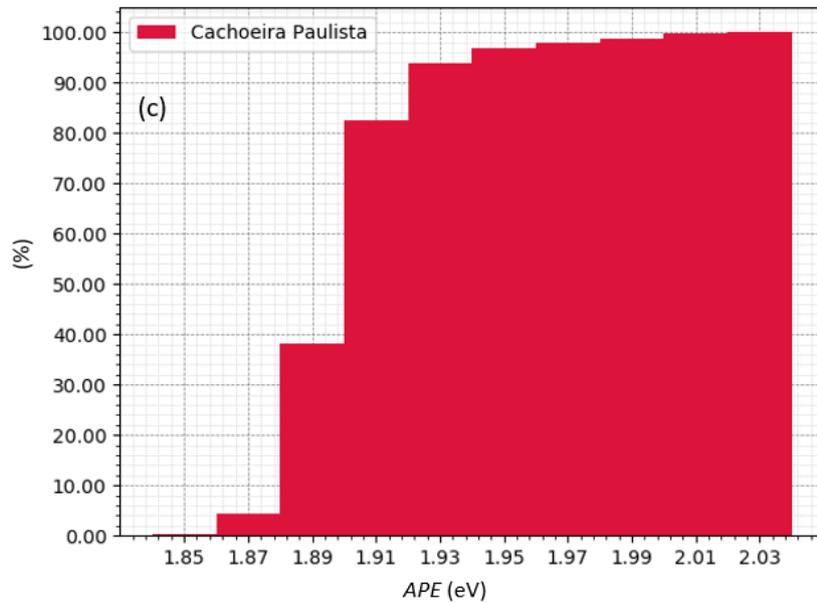
Source: Author.

On the other hand, studies of the blueness of annual solar resources conducted in low-latitude sites obtained similar results to those gleaned in Southeast Brazil. Sirisamphanwong and Ketjoy (2012) showed that the major fraction of annual total irradiation in Phitsanoluk[4] (Thailand, latitude 16°49' N, longitude 100°15' E) was related to solar spectra with *APE* ranging between 1.90 eV and 1.92 eV. In South America, Conde et al. (2021) demonstrated that for Lima (Peru, latitude 12°4' S, longitude 77°4' W) 40% of annual global tilted irradiance was measured with *APE* varying between 1.91 eV and 1.93 eV. These results agree in a qualitative way with those shown in Figure 5.1 since the higher cumulative percentage of *H* was generated for the 1.90 – 1.92 eV *APE* bins for the three Brazilian sites under scrutiny. In this sense, it indicates the blueness of solar resources of low-latitude sites compared to mid-latitude sites.

Unlike the Brazilian sites under scrutiny, in the Spanish, Japanese, and Peruvian studies, the annual global irradiation was collected on a tilted plane. In these cases, the proportion of direct irradiation is greater than that of the horizontal

---

[4] The orientation of the equipments were not described in such work.

spectrum, which leads to a higher red-light content than that of mid-latitude locations. Therefore, it might well be expected that *H* values in such locations have somewhat higher values of *APE* than those reported in the present work. In any case, comparisons with findings of Cornaro and Andreotti (2012) in Rome lead us to conclude that shorter wavelengths are enhanced in the spectral distributions of annual global horizontal irradiation in São Paulo, São José dos Campos and Cachoeira Paulista in relation to the previously discussed sites.

5.1.1 Instantaneous variations of solar spectrum

The fraction of annual horizontal irradiation with spectra characterized by high average photon energy (approximately bins with *APE* > 1.98 eV) was collected under low *GHI* levels and partly or completely overcast sky conditions as depicted in Figure 5.2. This graph is an example of the instantaneous *APE* plotted versus the irradiance grouped according to the sky condition during measurement for São Paulo. Solar spectra collected on cloudy days are dominated by diffuse radiation and impacted by clouds. Clouds have intense absorption wavebands in infrared and scatter light according to Mie scattering phenomena applied to water droplets. Considering that for water droplets the Mie scattering is wavelength-independent and photons from NIR are absorbed, in cloudy skies, the solar spectrum is biased to blue (NEVES, 2016). As proposed by Seckmeyer, Erb e Albold (1996) and explained by Kylling, Albold e Seckmeyer (1997), the spectral transmittance of clouds is also higher in lower wavelengths which can partially explain the highest *APE* during cloudy days.

Figure 5.2 - Instantaneous *APE* vs *GHI* plotted according to the sky condition during data measurement in São Paulo. Data were binned according to clearness index in cloudy sky for $0.3 < K_T$, partly cloudy sky for $0.3 < K_T < 0.65$, sunny sky for $0.65 < K_T < 1.0$ and cloud enhancement for $K_T > 1.0$.
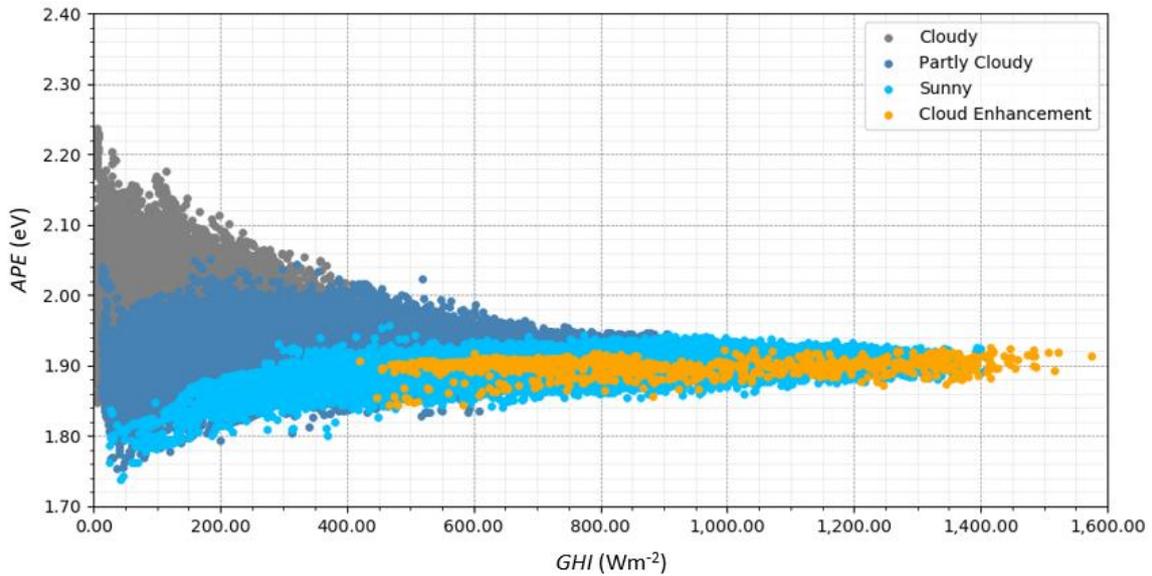
Source: Author.

On the other hand, bins in the low end of *APE* values are related to low *GHI* collected under partly cloudy or sunny skies and with a high zenith angle, as depicted in Figure 5.3. In this graph, only *APE* values measured under sunny skies were plotted and classified by the *AM* value at the time when the spectral irradiance was collected. Values of *APE* related to low irradiances were collected at dawn and sunset, when solar radiation travels a longer path in the atmosphere and as such interacts more with gases and aerosols. As Rayleigh scattering is dominant in clear skies, the spectra are biased to red, thus decreasing *APE*.

Figure 5.3 - Instantaneous *APE* vs *GHI* plotted according to their corresponding *AM* value for São Paulo.
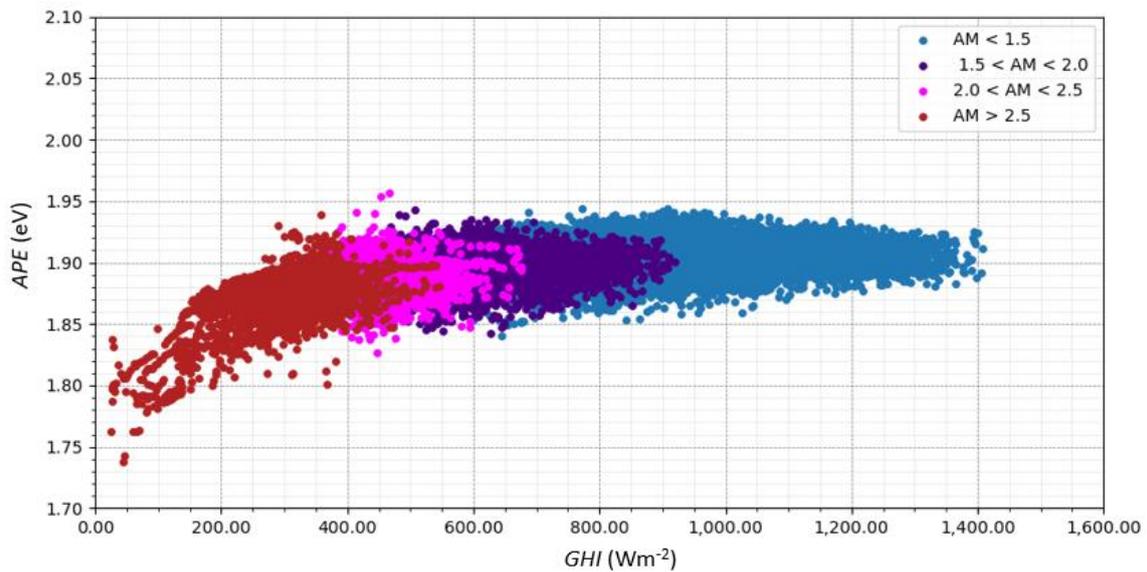
Source: Author.

Bins with *APE* ranging between 1.880 eV and 1.940 eV were mostly measured under a sunny sky and lower zenith angle conditions as shown in Figures 5.2 and 5.3. It means that the largest fraction of solar resource was obtained in such circumstances and has a bluer spectrum than that of standard ASTM. Despite being blue-biased or red-biased compared to the aforementioned bins, the fraction of *H* measured under cloudy skies or high *AM* values have a lower impact on the solar resource spectral characterization for the three sites. Therefore, their impact on timescales other than instantaneous (monthly and annual) is supposed to be small as well.

5.1.2 Cloud enhancement events

It is also worth mentioning that some *APE* values were obtained under exceedingly high levels of *GHI* as exhibited in Figure 5.2. These high *GHI* values were observed under special conditions in which clouds are distributed around the sun disk thus boosting the solar irradiance intensity in a way that can exceed the extraterrestrial irradiance (YORDANOV, 2013). This phenomenon occurs under partly cloudy sky conditions and is called in the literature over irradiance,

cloud lensing, irradiance enhancement, or cloud enhancement (*CE*) (JARVELA et al., 2020). Such events have been observed all over the world (GUEYMARD, 2017; JARVELA et al, 2020). Zilles et al. (2014) carried out an in-depth analysis of extreme enhancement events in São Paulo in which values of *GHI* up to 1590 Wm^{-2} were found and around 10% of all readings were measured with irradiance levels above 1 kWm^{-2}. In the present work, assuming K_T is higher than the unit (PIEDEHIERRO et al., 2014; GUEYMARD, 2017), around 0.50%, 0.15% and 0.38% of the total spectral measurements were measured under *CE* events in São Paulo, São José dos Campos and Cachoeira Paulista respectively. As explained by Yordanov et al. (2013b), because of the shorter Sun-Earth distances and lower levels of zenith angle during the summer, tropical regions with higher topography in the Southern Hemisphere near or north of the Tropic of Capricorn may be more affected by intense *CE* episodes.

Some examples of *CE* events measured in Cachoeira Paulista are shown in Figure 5.4, where *GHI*, *DNI* and *DHI* recorded with 1-min resolution measurement over a partially cloudy day conducted by SONDA station in addition to the *EHI* are plotted. The latter parameter was computed employing Equation 3.9. It is possible to notice *DNI* peaking, possibly attributed to *CE*, with *GHI* above *EHI*. Photographs of the sky collected with 1-min resolution by 4 megapixels, 2π field of view co-located Sky Camera (manufactured by Schreder GmbH) installed at the same side of moments next to the *GHI* peak of 12:30 are exhibited in Figure 5.5. An increase in the Sun brightness can be noticed in the Sky Camera pictures.

Figure 5.4 - Global horizontal irradiance, diffuse horizontal irradiance, direct normal irradiance, and extraterrestrial horizontal irradiance over time measured by SONDA's station in Cachoeira Paulista on 5th December 2020.
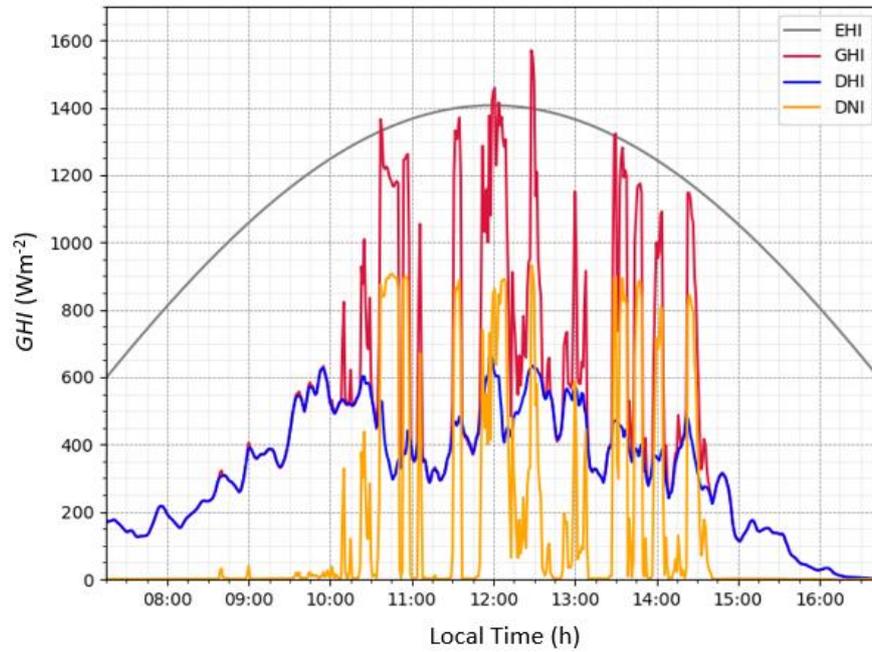
Source: Author.

Figure 5.5 - Images from the sky taken next to the *GHI* peak at 12:30 in Cachoeira Paulista on 5th December 2020.
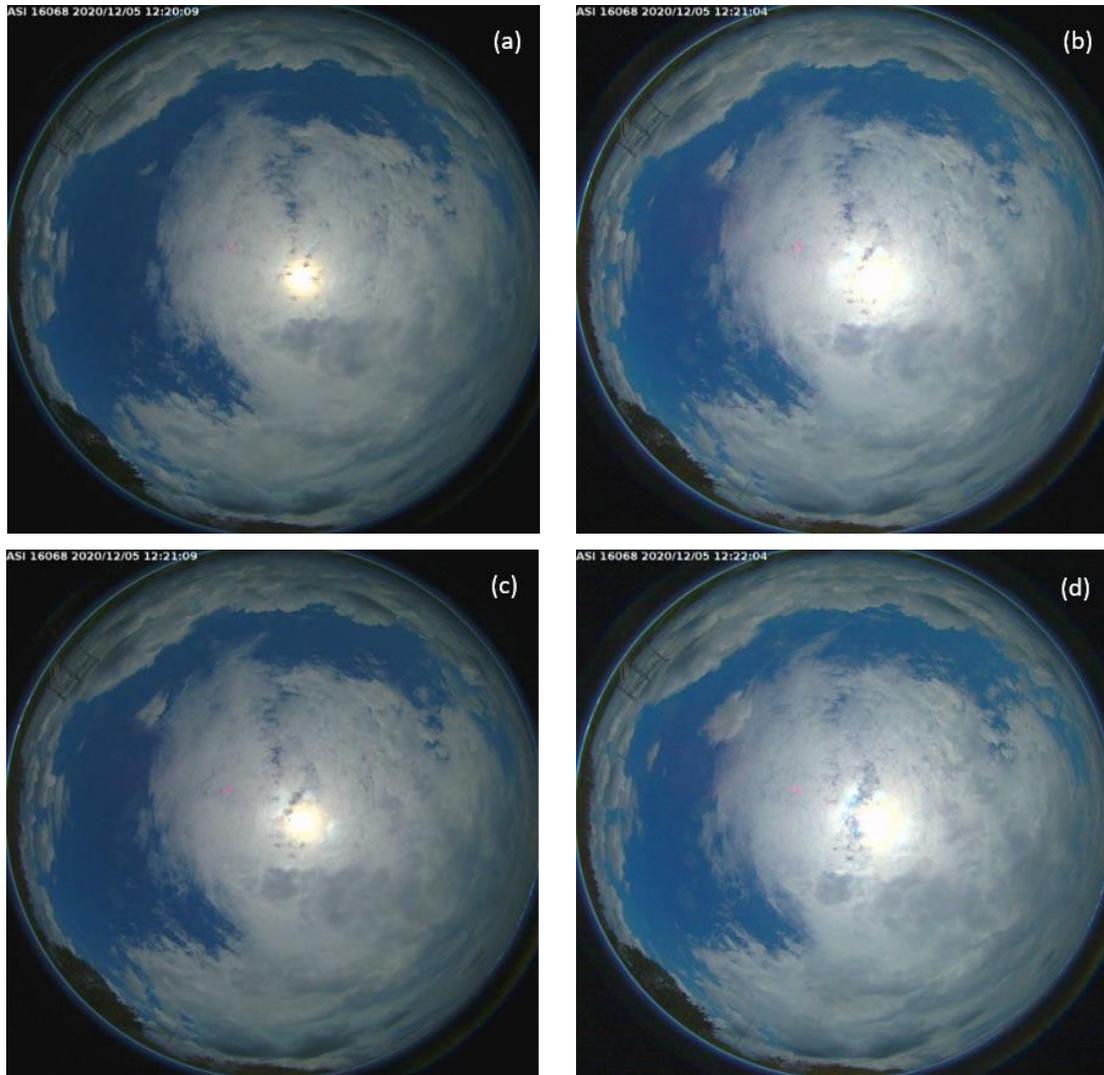
According to Figure 5.2, *APE* values obtained during *CE* events are remarkably close to those obtained for sunny skies which indicates that this phenomenon may not depend on wavelength and agrees with the physical explanation by Yordanov (2013a, 2013b) and Gueymard (2017). Once the irradiance level is enhanced by the forward scattering described by Mie theory, which is weakly dependent on wavelength in the water droplets case, the shape of the solar spectrum was not supposed to change. This can be proven by the similarity of *APE* values for *CE* events and clear sky conditions.

5.1.3 Seasonal variations of the solar spectrum

The predominance of blue-biased solar resource depicted in Figure 5.1 for the three cities is a consequence of the humid subtropical climate of Southeast Brazil and low latitude where all experimental campaigns were conducted. Such influences can be understood by means of Figure 5.6, where the monthly weighted *APE* is plotted over the year for the three data collection sites. Thus, APE_{MW} presents a similar seasonal variation in the three sites, reaching higher values in meridional summer months (21st December to 21st March) and lower values in meridional winter months (21st June to 22nd September). In São Paulo, such parameter peaks in December 2013 (1.922 eV), in São José dos Campos it happens in February 2019 (1.918 eV), and during December 2020 in Cachoeira Paulista (1.921 eV). On the other hand, APE_{MW} drops to a minimum in August 2013 (1.898 eV), July 2019 (1.888 eV), and August 2020 (1.892 eV), in São Paulo, São José dos Campos and Cachoeira Paulista, respectively. Despite the clear seasonality, APE_{MW} stays above 1.880 eV throughout the year for the three sites, which characterizes a predominance of blue-shifted spectra in all stations. A high monthly average result for *APE* was found for June 2021 in Cachoeira Paulista. Such result must be analyzed further in conjunction with other environmental data to verify if this value of APE_{MW} corresponds to an uncommon period in this site.

Figure 5.6 - Monthly weighted *APE* for São Paulo, São José dos Campos, and Cachoeira Paulista.
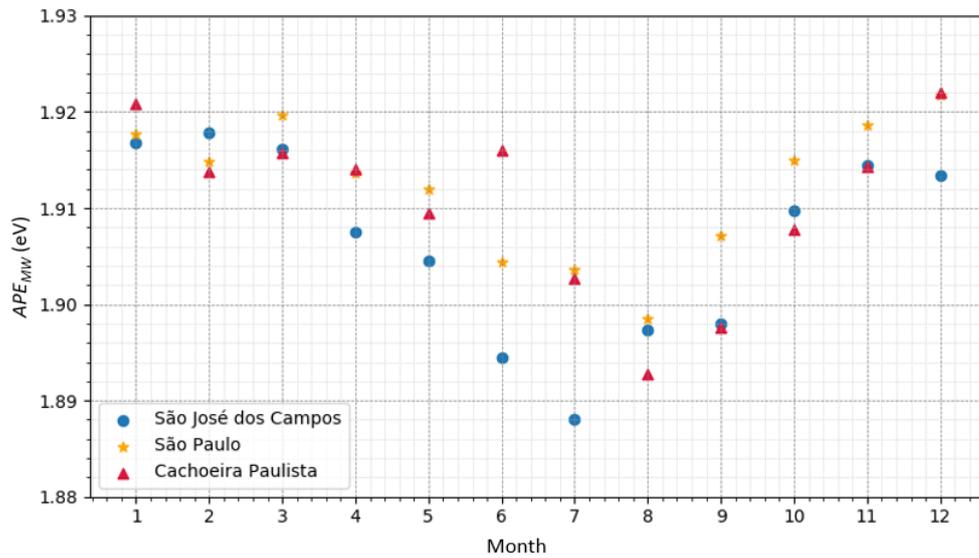
Source: Author.

The seasonal behavior of APE_{MW} can be understood by analyzing the water vapor content in the atmosphere and air mass values over the year. Monthly averages of precipitable water (PW_{MA}, in cm^{-1}) retrieved from AERONET for São Paulo station between 2009 and 2019 in addition to *AM* values calculated through Equation 4.6 for noon are shown in Figure 5.7. The same graph was plotted for Cachoeira Paulista with *PW* also retrieved from AERONET between 2019 and 2020 in conjunction with *AM* values obtained with Etion 4.6 for noon time in Figure 5.8. According to these graphs, the atmosphere is more humid during summer compared to winter in both cities for all analyzed years. At the same time, in the same season, the solar radiation travels smaller distances in the atmosphere to reach the ground as *AM* is lower in this period. The higher amount of water vapor in conjunction with lower zenith angles bias the solar spectrum to blue as water vapor absorbs photons from NIR and less radiation from UV and VIS is scattered by atmospheric gases. Therefore, shorter solar spectrum wavelengths are enhanced, thereby shifting it to blue and increasing APE_{MW} value.

Figure 5.7 - *PW* monthly averages for São Paulo (symbols) depicted from AERONET for the available years between 2009 and 2019. *AM* values for 12:00 am (blue line) are also plotted.
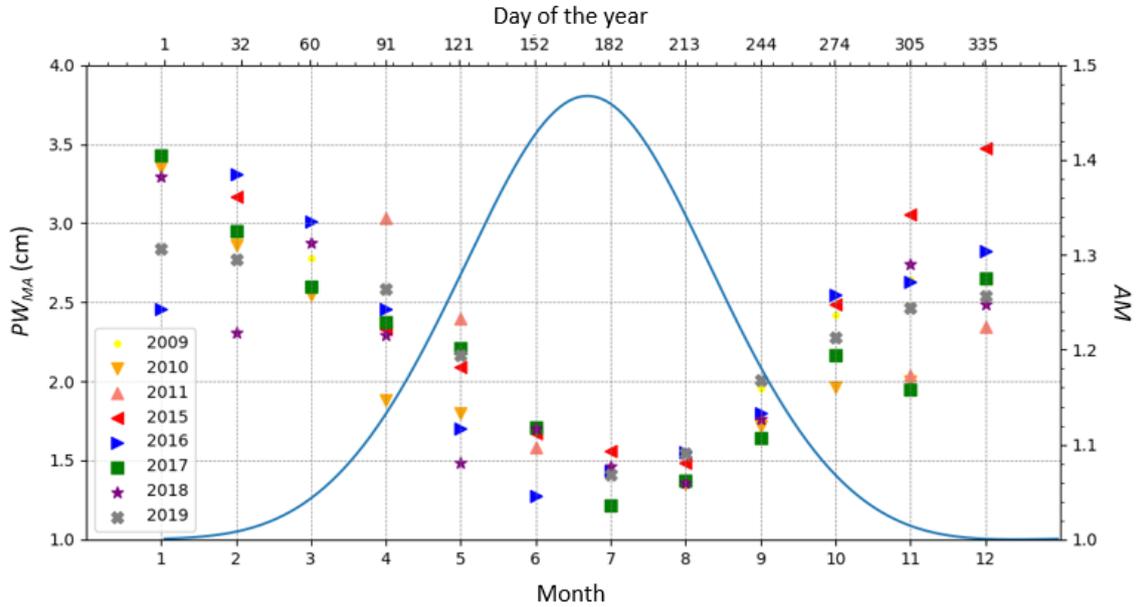
Source: Author.

Figure 5.8 - *PW* monthly averages for Cachoeira Paulista (symbols) depicted from AERONET for 2019 and 2020. *AM* values for 12:00 am (blue line) are also plotted.
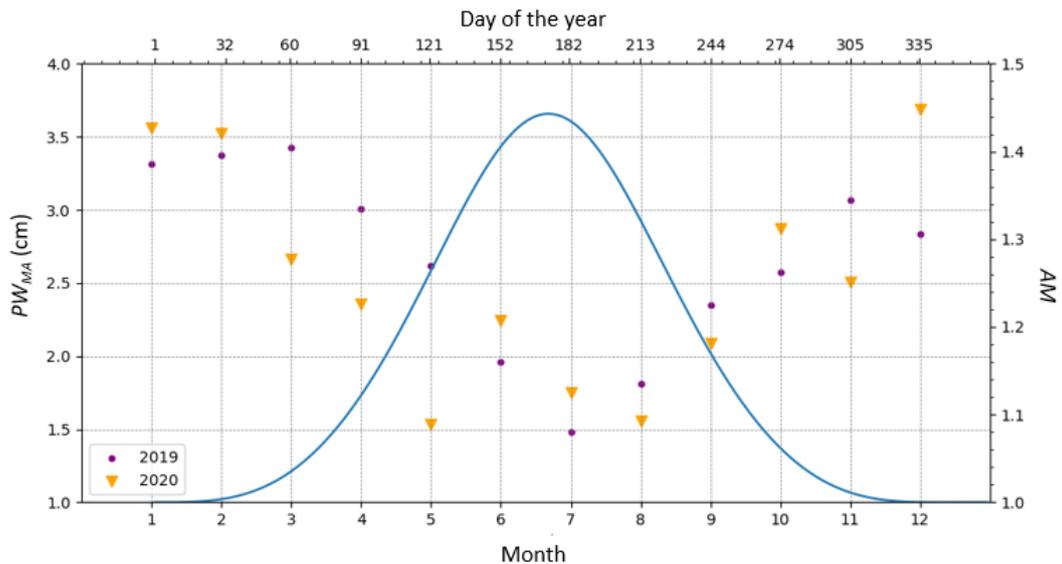
Source: Author.

Conversely, in winter, the path taken by radiation is higher because of the increase in the zenith angle, and the decrease in the amount of water vapor. These effects enhance the longer wavelengths in the solar spectrum and bias the radiation to red, thus decreasing APE_{MW}. To illustrate the differences between the spectral irradiance recorded in summer and winter, Figure 5.9 shows normalized spectral irradiance measured at solar noon of both a summer and a winter day in São Paulo, São José dos Campos and Cachoeira Paulista. The *AM*1.5G spectrum is also plotted for comparison. The solar spectra shown in Figure 5.9 are normalized following the same procedure described in Minemoto et al. (2009) and Cornaro and Andreotti (2012) in which the spectral irradiance of all wavelengths is divided by that measured at 560 nm. As reported in these studies, at this wavelength the scattering and absorption effects are less intense compared to those of other regions of the solar radiation spectral distribution.

Figure 5.9 - Normalized spectral distribution of solar radiation with different *APE* values measured at noon in (a) São Paulo, (b) São José dos Campos and (c) Cachoeira Paulista. The normalized ASTM AM 1.5G standard solar spectrum is interpolated to each spectroradiometer wavelength interval and plotted for comparison (greenish lines).
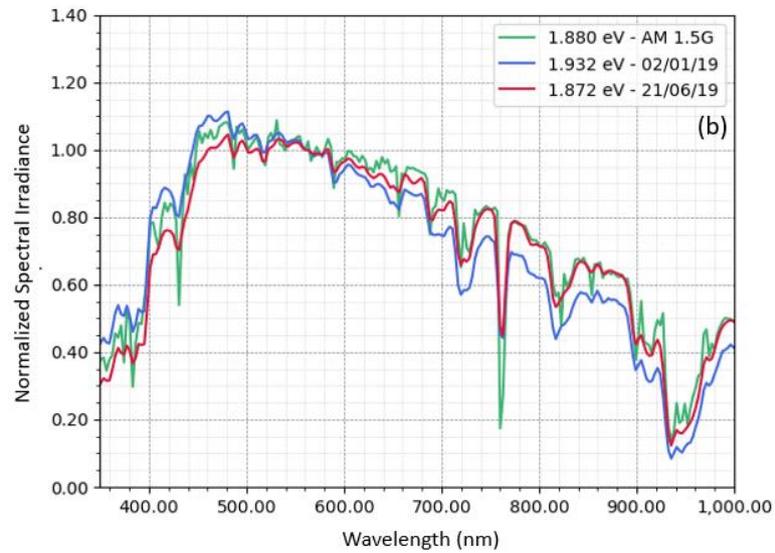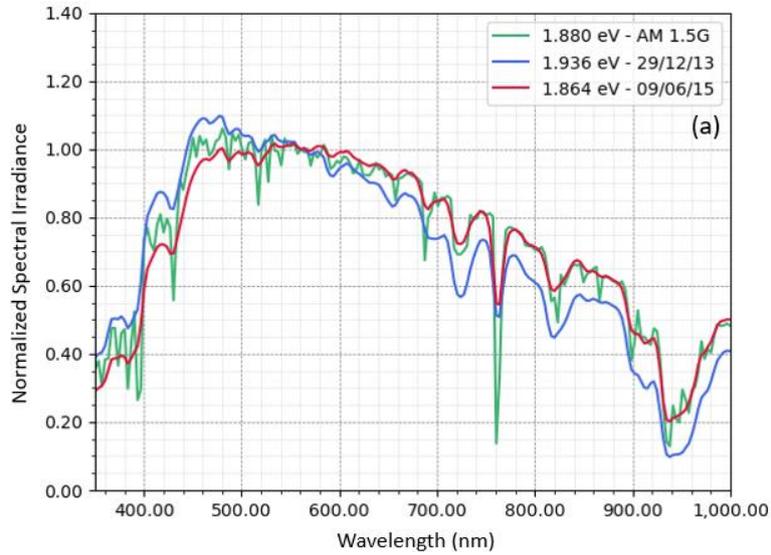
Figure 5.9 – Conclusion.
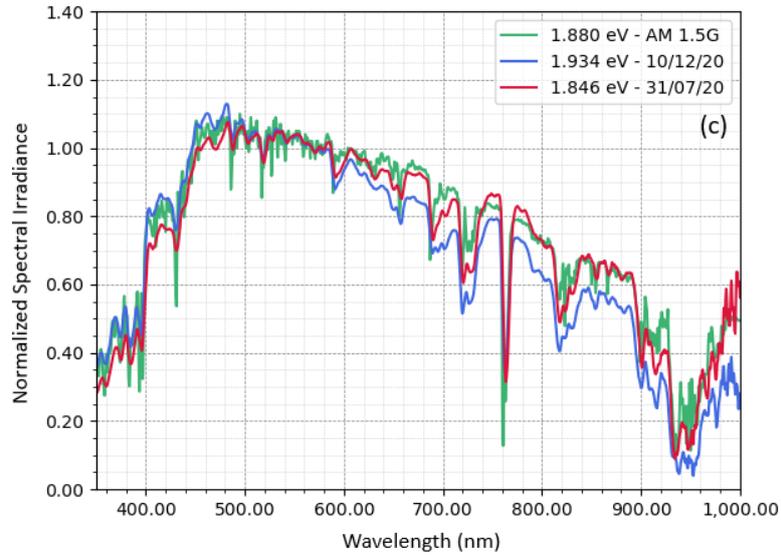
Source: Author.

5.1.4 Impact of aerosols on solar spectral radiation

The particulate variability load over São Paulo and Cachoeira Paulista can be observed in Figure 5.10 (a) and (b), respectively, through the *AOD* parameter. These figures show the monthly average of *AOD* at 500 nm ($AOD_{500nm\ MA}$, dimensionless) along ten years for the former and two years for the latter. In São Paulo, $AOD_{500nm\ MA}$ ranges between 0.1 and 0.3 with noticeable variability from January to July along the years, meanwhile such parameter reaches values higher than 0.3 in September and October. As discussed in Yamasoe, et al. (2017), the period of the year with the lower $AOD_{500nm\ MA}$ is when local urban pollution predominates and the higher values of such parameter during the dry season is attributed to the transported aerosols from the Amazonian basin and Cerrado biomass burnings. In Cachoeira Paulista, $AOD_{500nm\ MA}$ levels range around 0.15 in the humid period of the year indicating a clearer atmosphere compared to that over the city of São Paulo. During the dry season, this parameter also peaks higher than 0.3 showing that Cachoeira Paulista is also affected by biomass burning aerosols brought from Northern and Central parts of the country as expected.

Figure 5.10 - $AOD_{500nm\ MA}$ during the years of (a) 2009, 2010, 2011, 2015, 2016, 2017, 2018 and 2019 in São Paulo and (b) 2019 and 2020 in Cachoeira Paulista. Data retrieved from AERONET.
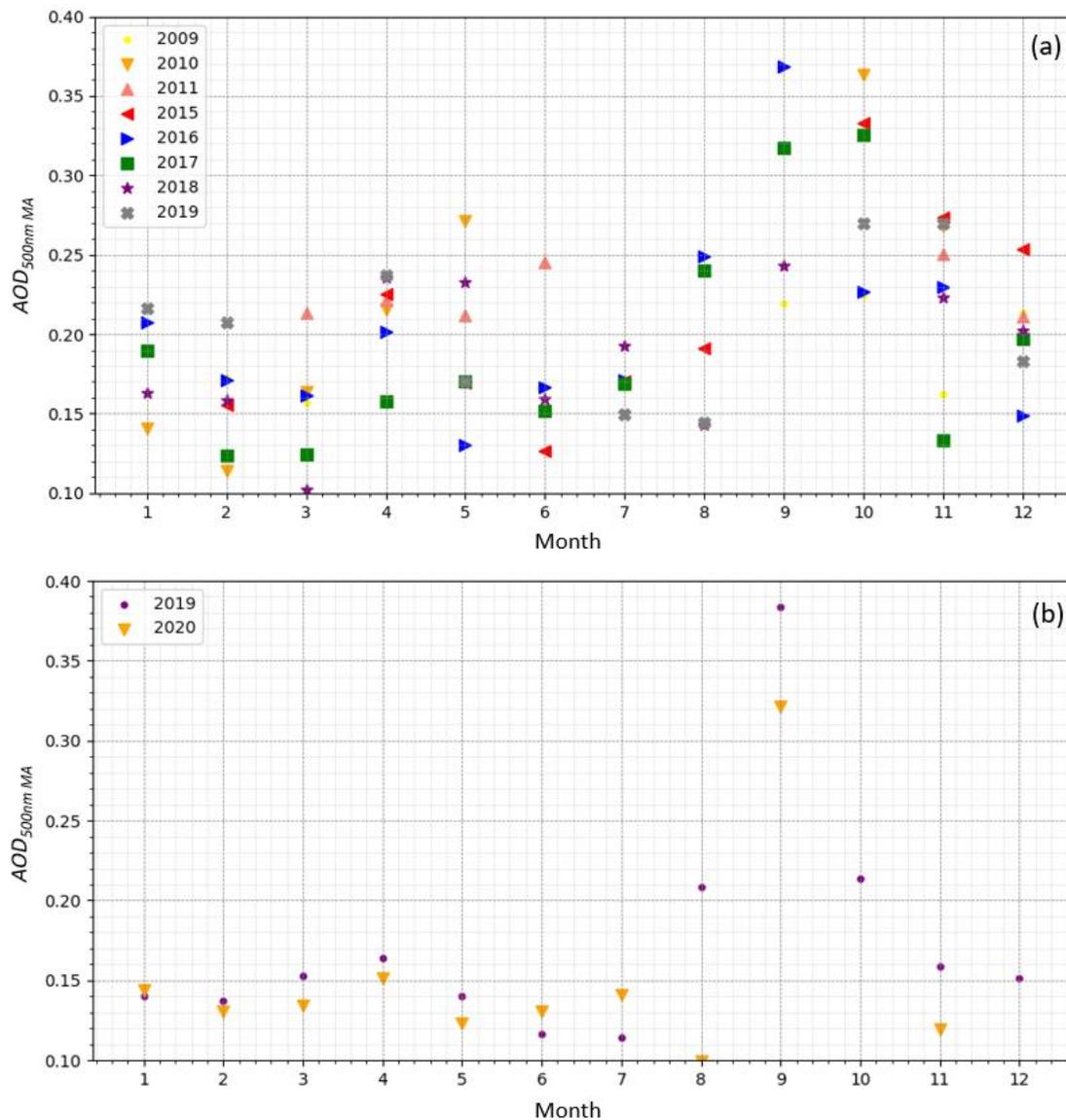
Source: AERONET (2022).

To analyze the effects caused by local and transported aerosols in the solar spectral radiation collected in São Paulo and Cachoeira Paulista, the spectral data measured under clear skies in addition to aerosol properties were studied separately for wet and dry seasons. As aerosol properties can change very quickly in the atmosphere, the studies were conducted on a daily basis, with data

135

collected in 2015 in São Paulo and in 2020/2021 in Cachoeira Paulista[5]. Basically, the relationship between daily weighted *APE* (*APE$_{DW}$*, in eV) and daily averaged *AOD* at 500 nm are investigated through Pearson's correlation coefficient (*ρ*, dimensionless) for each month. The results obtained for São Paulo are shown in Table 5.1 and for Cachoeira Paulista in Table 5.2. They reveal that for some months, especially September, October, and November, the mentioned parameters have a moderate to strong negative correlation in both cities (TAYLOR, 1990). The same happens for some months in São Paulo, such as during April and December, when *ρ* reaches values in the vicinity of -0.5 –weak to moderate correlation. In other months, the variation of aerosols does not appear to be related to the solar spectrum variation, as *ρ* is lower or closer to 0.3. As São Paulo is a polluted city, depending on some atmospheric factors, the weather conditions can be unfavorable for aerosol dispersion (CASTANHO; ARTAXO, 2001), which can lead to higher loads of pollution suspended over the city. For Cachoeira Paulista, no relevant relation was obtained outside the dry season. This can be a consequence of the less polluted atmosphere compared to São Paulo.

---

[5] The period under concern was chosen according to the availability of data from AERONET database.

Table 5.1 - Pearson correlation coefficient for the relations between APE_{DW} and $AOD_{500nmDA}$ on different months on the cities studied in this work.

Month	Pearson Correlation Coefficient (ρ)
April	-0.495
May	-0.293
June	-0.359
July	-0.183
August	-0.072
October	-0.610
November	-0.563
December	-0.509

Source: Author.

Table 5.2 - Pearson correlation coefficient for the relations between APE_{DW} and $AOD_{500nmDA}$ on different months on the cities studied in this work.

Month	Pearson Correlation Coefficient
February 2021	-0.032
March 2021	0.063
April 2021	-0.245
May 2021	-0.107
June 2021	-0.112
July 2021	-0.050
August 2020	0.066
September 2020	-0.599
December 2020	-0.201

Source: Author.

APE$_{DW}$ values are plotted versus *AOD*$_{500nm\ DA}$ values in conjunction with regression lines and 95% prediction and confidence intervals for October 2015 for São Paulo and September 2020 for Cachoeira Paulista in Figure 5.11. The same graph, but with data collected in April 2015 in the former site is shown in Figure 5.12. The graphs show that there is an inverse relationship between *APE*$_{DW}$ and *AOD*$_{500nm\ DA}$ for the months under concern. These results in addition to those from Tables 5.1 and 5.2 indicate that higher loads of urban and biomass burning aerosols seem to be related to redder solar spectra. The shifting to red of solar radiation can be better understood through the spectral *AOD* shown in Figure 5.13. In these graphs, the *AOD* gleaned for different wavelengths (*AOD* (*λ*)) are plotted for a month of the humid and dry season in São Paulo and in Cachoeira Paulista. They show higher extinctions for lower wavelengths, independently of the period of the year, and more pronounced effects during September and October. According to these results, the ultraviolet and visible are extinguished more efficiently than infrared by plumes and pollution particulates which decreases solar spectrum average photon energy as raised by (FERNANDEZ et al., 2014).

Figure 5.11 - Values of daily weighted *APE* versus daily averages of AOD_{500nm} for (a) October 2015 in São Paulo and (b) September 2020 in Cachoeira Paulista. Only solar spectra collected under sunny skies were considered for *APE* computation.
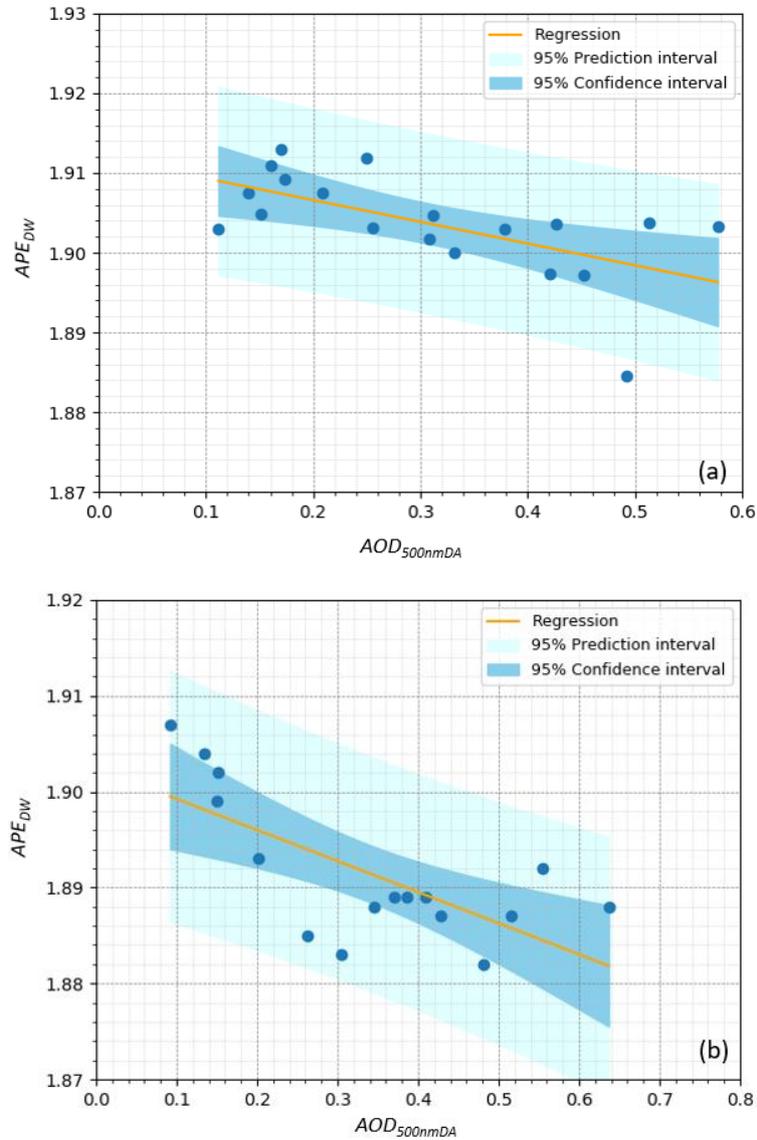
Source: Author.

Figure 5.12 - Values of daily weighted *APE* versus daily averages of AOD_{500nm} for April 2015 in São Paulo. Only solar spectra collected under sunny sky were considered for *APE* computation.
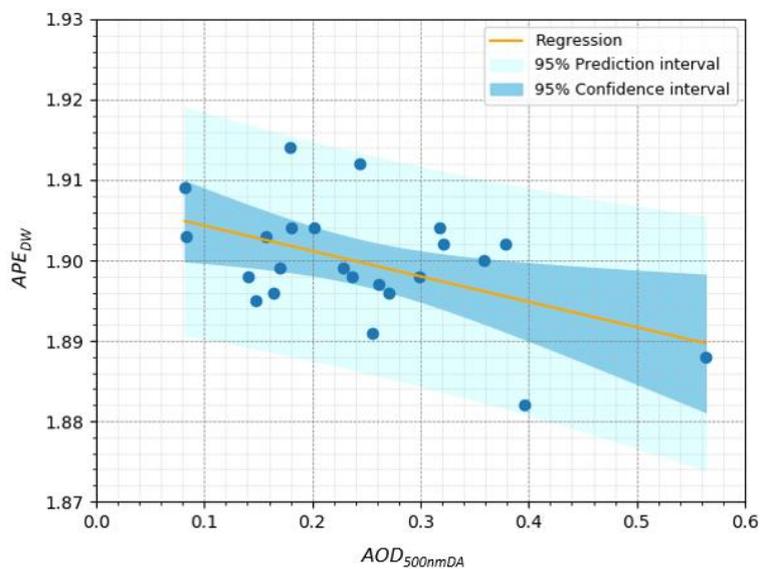
Source: Author.

Figure 5.13 - Monthly averages of *AOD* measured at different wavelengths for a month of the humid season and dry season in (a) São Paulo and (b) Cachoeira Paulista. Data retrieved from AERONET.
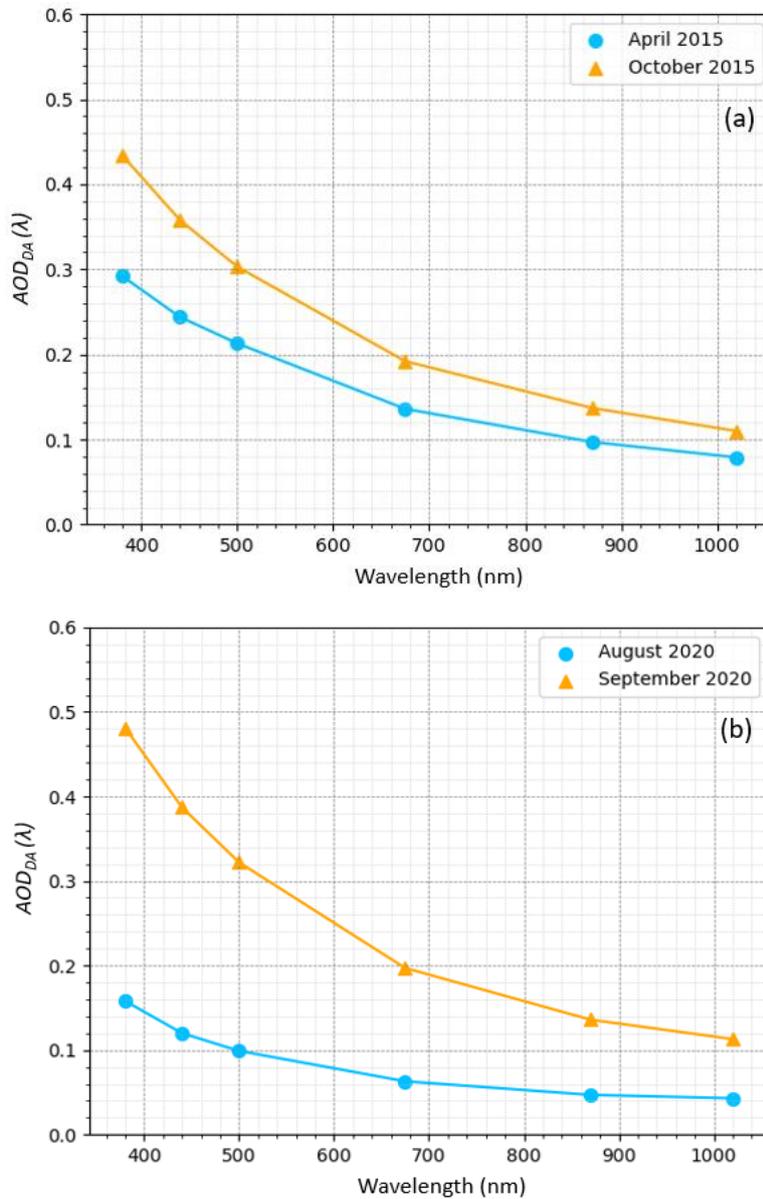
Source: Author.

Bearing in mind that aerosols from different sources have different properties, the monthly average of spectral single scattering albedo (*SSA*, dimensionless) measured over April and October 2015 and August and September 2020 for both sites analyzed here were plotted in Figure 5.14. Analyzing the spectral *SSA* curves, one can notice that such parameter is higher when biomass burning

aerosols are present over the studied cities. As analyzed in previous works (CASTANHO; ARTAXO, 2001; CASTANHO; MARTINS; ARTAXO, 2008) and explained by Rosário (2011), particles generated by fires in the Amazon and Cerrado regions are less absorbent and scatter radiation more efficiently because of their physical and chemical properties. On the other hand, urban aerosols found in São Paulo absorb more radiation in part because of their composition (ROSÁRIO, 2011; ALMEIDA et al., 2013). Considering that absorbed radiation is removed from the atmosphere and part of the scattered radiation can reach the Earth's surface as diffuse radiation (OLIVEIRA et al., 2007; MOOSMULLER, 2009), extinguishing caused by local aerosols is expected to be more efficient in shifting the spectrum towards the red than towards biomass burning aerosols. The intensity of such effects is proportional to the aerosol load suspended in the atmosphere, so despite being less absorbent, biomass burning particulates transported to the state of São Paulo have a higher impact on the solar spectrum.

Figure 5.14 - Monthly Averages of *SSA* measured in different wavelengths for a month of the humid season and dry season in (a) São Paulo and (b) Cachoeira Paulista.
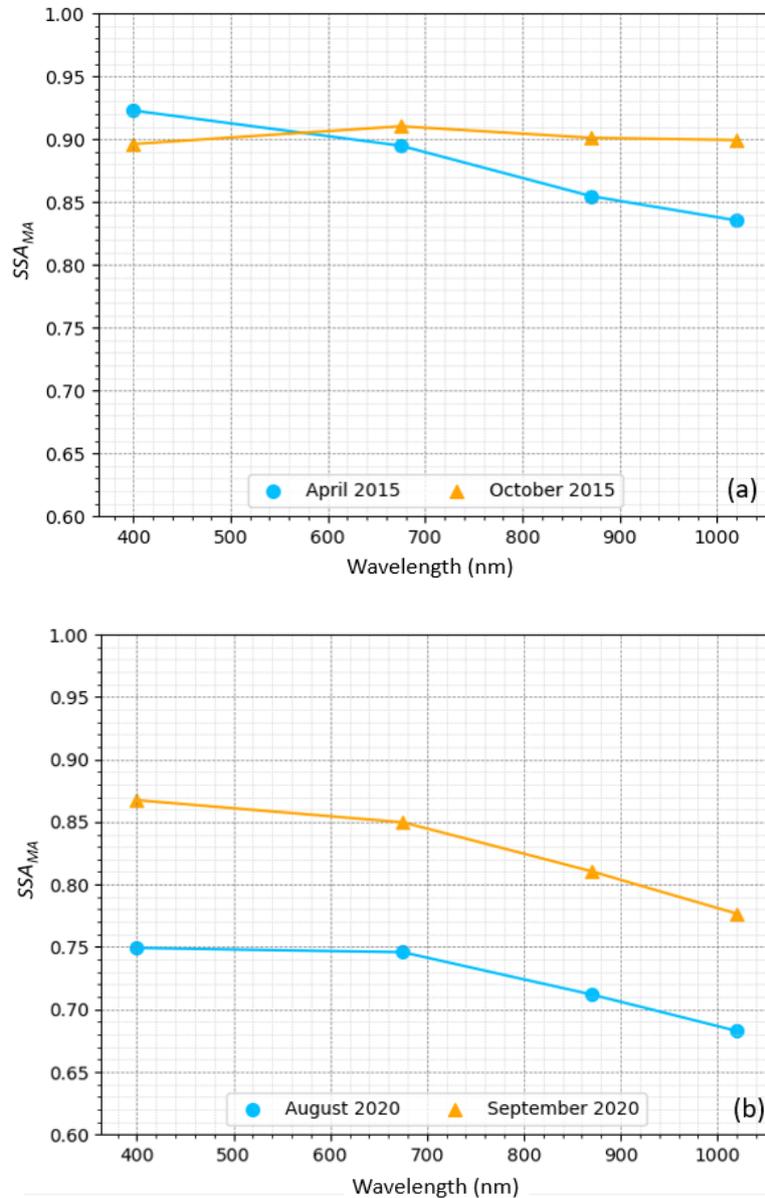
Source: Author.

Therefore, it is evident that plumes produced by burning biomass in the north and central parts of the country should impact the solar resource in the Southeast Brazil mainly during the dry season. Concerning the urban aerosols over São Paulo, they seem to influence the solar spectrum depending on the month of the year, in contrast with Cachoeira Paulista, which is a city with lower levels of

pollution. Due to the complexity of aerosols properties, further studies are required in order to gain a better understanding of how the different species of such components influence the *APE* and the whole solar spectrum.

5.1.5 Site spectral characterization using *APE* on an annual timescale

The annual value of *APE* for São Paulo, São José dos Campos, and Cachoeira Paulista are 1.913 eV, 1.908 eV and 1.909 eV, respectively. Such values are remarkably similar and indicate that the solar spectrum may exhibit similar features in these nearby sites, which can make APE_{AW} a regional parameter. Therefore, the similarity of these findings coupled with the results obtained for Lima by Conde et al. (2021), of 1.923 eV support the hypothesis that blue-biased spectra tend to prevail in low-latitude and tropical regions (YE et al., 2014).

5.2 Spectral effects exhibited by various PV materials at different timescales

5.2.1 Instantaneous spectral impact on various PV materials

The instantaneous impact caused by the spectral variations of solar radiation on different PV technologies are shown in Figure 5.15 for sc-Si and mc-Si, Figure 5.16 for a-Si and CdTe, and Figure 5.17 for Perovskite and CIGS in the three sites under scrutiny. In general, under high levels of *GHI,* the spectral impact is similar for all technologies, with *MM* lying in the vicinity of the unit with little scatter. For low incident irradiances, the spectral impact show more variability and depend on the optical characteristics of the semiconductors in which each technology is based. PV devices with smaller band gap energies (sc-Si, mc-Si, and CIGS) can suffer spectral losses under such conditions, also exhibiting less pronounced spectral gains within around 500-900 Wm^{-2}. By contrast, PV materials with large band gaps (a-Si, CdTe, and Perovskite) may exhibit remarkable spectral gains under low light conditions – e.g.: a-Si reaches gains of up to around 30%. The varying magnitudes of spectral impact at low levels of *GHI* are caused by different sky conditions and time of the day when the spectra were logged, as highlighted in Figures 5.2 and 5.3.

Figure 5.15 - *MM* versus global horizontal irradiance for sc-Si in (a) CPA, (b) SJC and
(c) SPA, and mc-Si in (d) CPA, (e) SJC and (f) SPA.
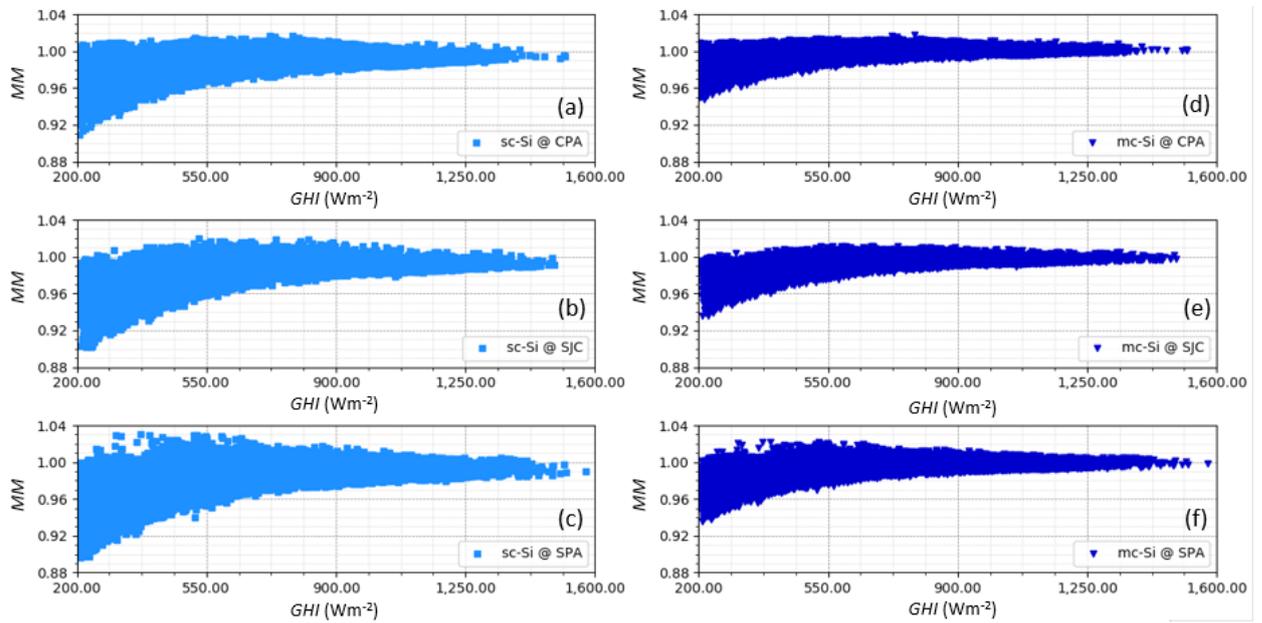
Source: Author.

Figure 5.16 - *MM* versus global horizontal irradiance for a-Si in (a) CPA, (b) SJC and (c)
SPA, and CdTe in (d) CPA, (e) SJC and (f) SPA.

Source: Author.

145
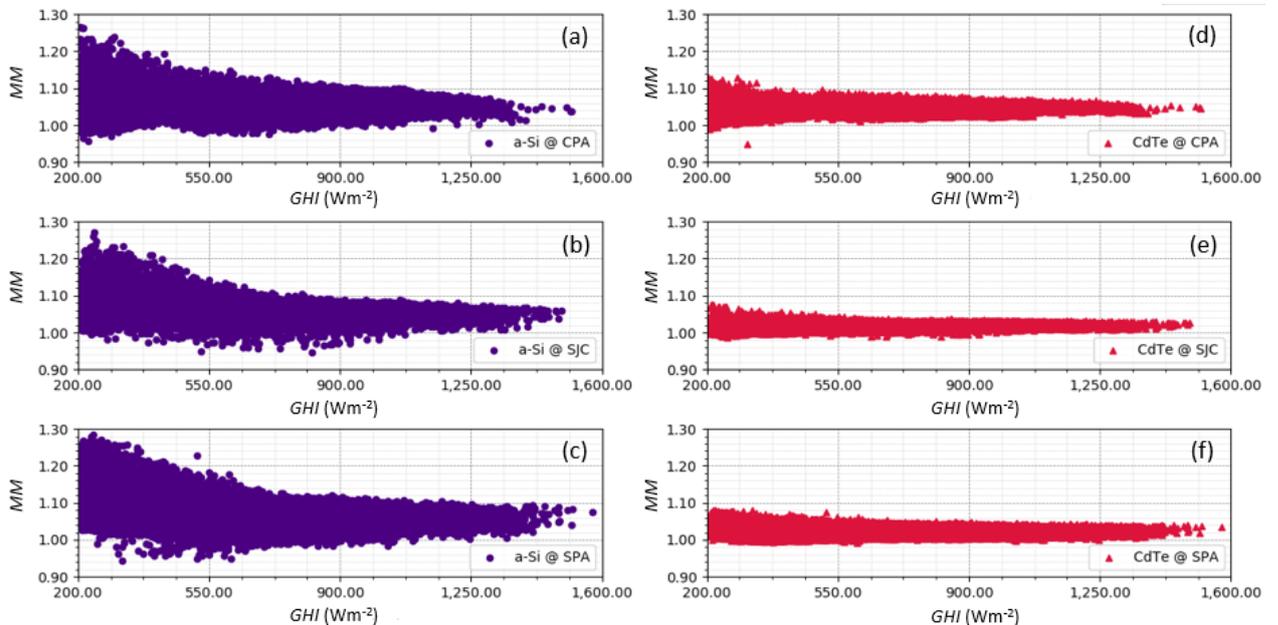
Figure 5.17 - *MM* versus global horizontal irradiance for CIGS in (a) CPA, (b) SJC and (c) SP, and Perovskite in (d) CPA, (e) SJC and (f) SP.
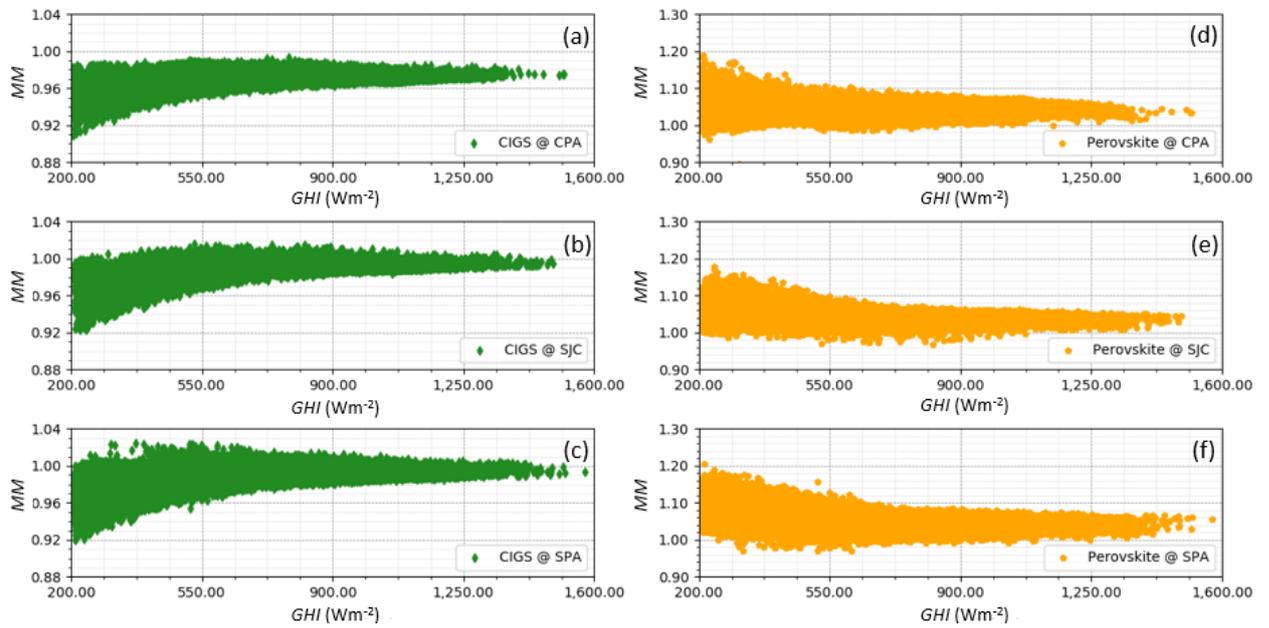
Source: Author.

The variance of *MM* and the significant impact caused on PV materials by low light intensities raise the importance of considering the spectral impact on PV when analyzing instantaneous PV module performance as concluded by Dirnberger et al. (2015). It is also worth mentioning that *MM* values for levels of *GHI* classified as cloud enhancement in accordance with Figure 5.2 are quite the same as those obtained for sunny skies. It corroborates the argument that the solar spectrum does not change very much with the boost experienced by global irradiance, indicating that spectral impact in such conditions is similar to those exhibited over irradiance events and under clear skies. More studies are required to gain a better understanding of how cloud enhancement events spectrally impact PV systems.

5.2.2 Monthly spectral impact on various PV materials

On a monthly basis, the analysis of the spectral impact on each PV material studied in this work was carried out through the monthly weighted *MM* for a complete year. The results for São Paulo, São José dos Campos and Cachoeira

146

Paulista are shown in Figure 5.18. A similar seasonal spectral effect can be observed for all PV technologies in the three sites. The aforementioned seasonal variation depends on the optical characteristics of the PV materials, being more pronounced for the large band gap ones. The highest seasonality was found for a-Si, which has MM_{MW} ranging between 1.047 (August 2013) and 1.077 (December 2013) in São Paulo, 1.027 (July 2019), and 1.068 (January 2019) in São José dos Campos and 1.036 (August 2020) and 1.073 (January 2021) in Cachoeira Paulista. Following amorphous Silicon, Perovskite is the second most affected technology with the highest impacts taking place in December 2013 (1.055) in São Paulo, January 2019 (1.049) in São José dos Campos and January 2021 (1.053) in Cachoeira Paulista, while the lowest impacts occur in August 2013 (1.033), July 2019 (1.019), and August (1.025), respectively. CdTe exhibited a similar however less pronounced seasonality. In this case, the values of MM_{MW} go down to 1.018 during August in São Paulo, to 1.010 in July in São José dos Campos, and to 1.013 during August in Cachoeira Paulista. This parameter peaks up to 1.030 during March, up to1.026 in January, and up to 1.035 in June for the respective mentioned sites.

Figure 5.18 - MM_{MW} for various PV technologies in (a) São Paulo, (b) São José dos Campos and (c) Cachoeira Paulista.
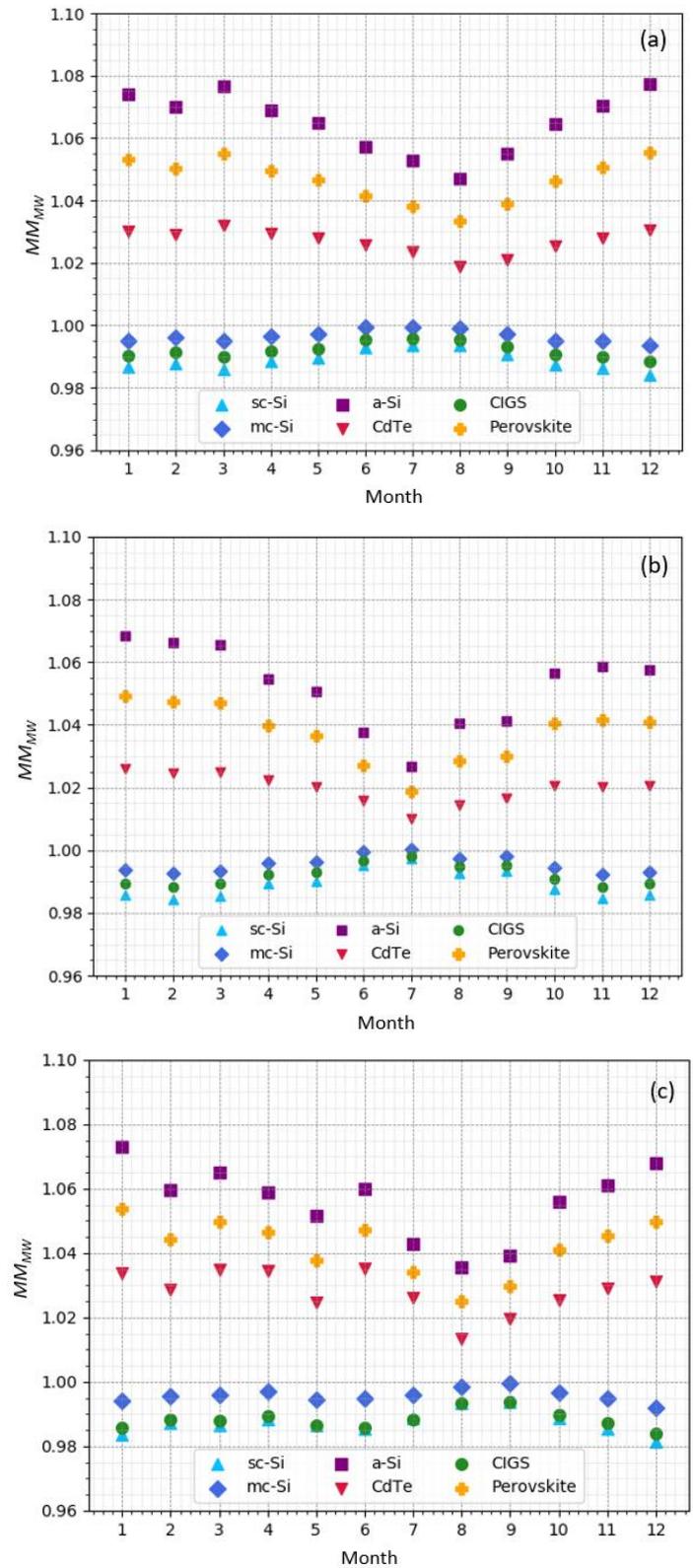
Unlike the aforementioned PV technologies, sc-Si, mc-Si and CIGS show an inverse trend over the seasons. These technologies are less influenced on a monthly basis by the solar spectrum as opposed to PV materials with larger band gaps as their values of MM_{MW} have remained close to the unit throughout the year, particularly during wintertime. In fact, such shorter band gap PV technologies exhibit neither high monthly spectral gains nor losses since the MM_{MW} values peak close to unit in winter while the lowest values occur in summer, when the values of this parameter lie in the vicinity of 0.985 for the three sites under investigation.

The different seasonal behavior of the influence exerted by the spectrum on PV materials with different energy gaps can be understood at least in part by the variation of solar spectrum along the year, as illustrated by APE_{MW} in Figure 5.6. Tropical, blue-biased spectra are beneficial to large band gap PV materials as also found in Singapore (YE et al., 2014) and Lima (CONDE et al., 2021), thus making them exhibit year-round spectral gains on a monthly timescale. That happens even in the presence of urban aerosols throughout the year and the impact caused by fire plumes in the dry season, which shifts the solar spectrum to red. On the other hand, the other PV technologies are less affected by solar spectrum variations. The *offset effect* –that occurs under high irradiance level conditions– discussed by Ishii et al. (2013) and, Nofuentes et al. (2014) can partly explain the reason for the lower impact results obtained for these materials.

The pattern of variation presented by the monthly spectral impact on PV throughout the year discussed above agrees with those found in mid-latitude sites by Ishii et al. (2011), Ishii et al. (2013), Dirnberger et al. (2015), and Nofuentes et al. (2017). According to such contributions, MM_{MW} also exhibits a seasonal behavior in each corresponding studied site depending on the PV technology. As pointed out in these studies, the MM_{MW} values for larger band gap PV materials generally present a broader variation with the highest values occurring in summer and the lowest values during winter – when they stay above the unity. Despite the seasonality also exhibited in Southeast Brazil, with the maximum in summertime and minimum over winter, the monthly spectral impact for a-Si, CdTe, and Perovskite remains above the unity throughout the year.

In addition to the mid-latitude cases, the findings of Figure 5.18 are reasonably well aligned with the simulated results computed by Fernández et al. (2016) for Alta Floresta (Midwestern Brazil, latitude 9°20'S, longitude 56°06' W), despite some differences identified and discussed hereafter. In the latter work, atmospheric data retrieved from AERONET served as input to model synthetic solar spectra per SMARTS2, which were analyzed and combined with relative spectral responses of PV materials very similar to those used here for spectral impact computation. The orientation or tilt angle of the surface considered in this study is not reported. Their findings show how a-Si, followed by CdTe, experience the highest spectral gains during summer months with a deviation of around ±0.01 in comparison with values of MM_{MW} found for the three sites studied in this work. The lowest spectral gains can be observed in winter, the season in which the differences between the simulated and experimental results presented here reach up to 0.11 and 0.04 for a-Si and CdTe, respectively. Differently from Southeast Brazil –which shows spectral gains throughout the year as discussed earlier– in Alta Floresta, such technologies experience spectral losses. This different spectral behavior is probably a consequence of the different load of plumes suspended in the atmosphere during the dry season caused by fires and deforestation of the Amazonian Forest and Cerrado, as discussed previously. The high amount of aerosol from burning biomass in Alta Floresta compared to that of São Paulo (ALVIM et al., 2017), and consequently to that of São José dos Campos and Cachoeira Paulista, biases the solar spectra more intensely to red, which may explain the difference in the results (LIU et al., 2014). The similarity to the other months probably indicates that the impact of urban aerosols on such PV technologies cannot be noticed on the timescale considered for analysis.

Conversely, aerosols from burning biomass events do not have a significant impact on monthly results of mismatch factor for small band gap materials in Alta Floresta, once the findings simulated for sc-Si and CIGS show differences of MM_{MW} around ±0.01 over the entire year with a similar trend to the ones presented in this work. No noticeable seasonality was found for mc-Si technology in Alta Floresta, although the values of MM_{MW} stay around ±0.01 of those found

for the same PV material in São Paulo, São José dos Campos and Cachoeira Paulista.

5.2.3 Annual spectral impact on various PV materials

The results of the annual analysis for the spectral effects on PV technologies are shown in Table 5.3. As expected, PV materials with larger band gaps exhibit a noticeable spectral impact in all sites studied in the present work. Higher spectral gains slightly less than 7% are found for a-Si, followed by Perovskite with approximately 5%, and close to 3% for CdTe technology. By contrast, sc-Si, mc-Si, and CIGS modules show less sensitivity to solar spectrum variations at an annual timescale as their MM_{AW} values remain around the unit. These results are well in line with those shown in Figures 5.14, 5.15, 5.16, and 5.17, thus showing that prevailing climate on studied sites influence PV behavior. All findings agree with the fact that large band gap materials are the most sensitive to solar spectral variations under all timescales analyzed here.

Table 5.3 - Annual spectral impact for various PV technologies in Southeas Brazil.

Site	MM_{AW}					
	sc-Si	mc-Si	a-Si	CdTe	CIGS	Perovskite
São Paulo	0.988	0.996	1.067	1.027	0.991	1.048
São José dos Campos	0.989	0.995	1.054	1.020	0.992	1.039
Cachoeira Paulista	0.987	0.995	1.056	1.029	0.988	1.042

Source: Author.

To gain a better perspective on the matter, results of MM_{AW} found for other low latitude and tropical sites with experimental and simulated spectral data are depicted in Table 5.4 for comparison. Although not all these results were obtained on a horizontal plane, when specified, the tilted angle is small and can be approximated. Comparing the results obtained for Southeast Brazil with those found in Florianópolis (South Brazil, latitude 27°35' S, longitude 48°32' W) (BRAGA et a., 2019), Lima (Peru, latitude 12°4' S, longitude 77°4' W) (CONDE et al., 2021) and Singapore (Singapore, latitude 1°17' N, longitude 103°51' E) (YE et al., 2014) one can note that they are in good agreement. The similarity among the results obtained for all the studies mentioned indicates that, in general, sites

closer to the Equator have climates that benefit from a spectral point of view of large bandgap PV technologies such as a-Si.

Table 5.4 - Annual spectral impact for various PV technologies in low-latitude sites.

Site	Country	PV technology						Source
		sc-Si	mc-Si	a-Si	CdTe	CIGS/CIS	Perovskite	
Alta Floresta (sim.) [a]	Brazil	0.99	0.99	1.05	1.03	0.99	na	(FERNÁNDEZ, et al., 2016)
Campo Grande (sim.) [b]	Brazil	0.99-1.00	0.99-1.00	1.02-1.03	1.01-1.02	0.99-1.00	na	(POLO, et al., 2017)
Florianópolis [c]	Brazil	na	0.97	Na	1.02	na	na	(BRAGA, et al., 2019)
Lima [d]	Peru	0.977	0.986	1.068	1.021	0.982/0.991	1.048	(CONDE, et al., 2021)
Singapore [e]	Singapore	na	Na	1.07	1.03	1.00	na	(YE, et al., 2014)

[a] No information regarding the orientation and tilt angle of the surface available.

[b] Equator-facing surface with inclination given by the site latitude.

[c] Horizontal surface.

[d] Equator-facing 20º-tilted surface.

[e] Equator-facing 10º-tilted surface.

Source: Author.

The empirical results obtained in this work also match reasonably well those achieved by using simulation as the ones computed by Polo et al. (2017) through SMARTS2 in conjunction with atmospheric data retrieved from AERONET for Campo Grande (Midwestern Brazil, latitude 20°26' S, longitude 54°38' W) and those found by Fernández et al. (2016) in Alta Floresta. Note that simulated values of MM_{AW} in the former site are somewhat smaller than those found in this work for São Paulo, São José dos Campos and Cachoeira Paulista. In Alta Floresta (FERNÁNDEZ et al., 2016), despite the differences caused in MM_{MW} by the biomass burning in Northern and Midwestern Brazil during the dry season,

the similarity between MM_{AW} values indicates that the effects caused by anthropogenic activity on PV are not noticeable from an annual perspective. In this sense, considering the agreement of the results discussed above, simulating with SMARTS2 and AERONET may be a reliable approach to predict the influence of the spectrum on PV behavior in Southeastern Brazil.

5.3 *APE* as a spectral impact parameter

To verify if *APE* and *MM* correlate in tropical sites, the same procedure described in Ishii et al. (2013) and Dirnberger et al. (2015) was applied here. As PV developers are interested in spectral effects assessed using monthly and annual results, the analysis was conducted considering these timescales. Scatterplots of MM_{MW} versus APE_{MW} are depicted in Figures 5.18 for São Paulo, São José dos Campos and Cachoeira Paulista. The results show that both parameters have a quasi-linear relationship at an increasing rate for a-Si, Perovskite, and CdTe while it is also quasi-linear at a decreasing rate for sc-Si, mc-Si, and CIGS. Such findings match very closely those found in Lima by Conde et al. (2021) in all PV technology cases, indicating that the spectral behavior can be very similar under similar spectral conditions. Although APE_{MW} has been computed in the 335-1700 nm waveband, in the mid-latitude site of Freiburg im Breisgau (DIRNBERGER et al., 2015), the correlation between this parameter and MM_{MW} largely agrees qualitatively with the results presented here. Results found by Chantana et al. (2020) are also well aligned in a qualitative way with the ones shown in Figure 5.19.

Figure 5.19 - Monthly weighted MM vs monthly weighted APE for various PV technologies in (a) São Paulo, (b) São José dos Campos and (c) Cachoeira Paulista.
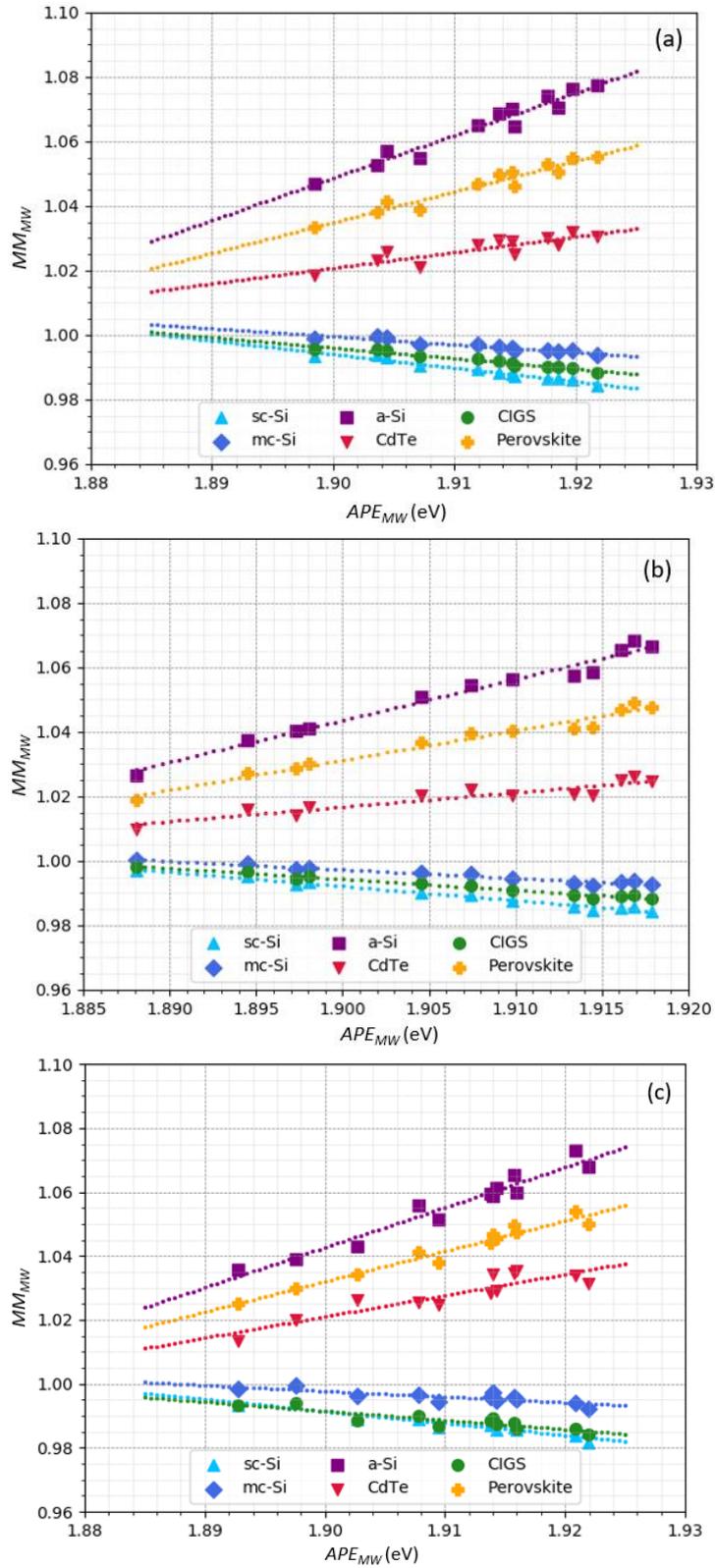
Source: Author.

As a quasi-linear relationship was obtained between MM_{MW} and APE_{MW} as shown in Figure 5.19, regression lines could be estimated to describe how the former varies as a function of the latter. The equations that describe the lines together with their coefficient of determination (R^2) computed for São Paulo, São José dos Campos and Cachoeira Paulista are gathered in Table 5.5, Table 5.6, and Table 5.7, respectively. To validate such equations, the annual mismatch factor for each PV technology was calculated, introducing the values of APE_{AW} obtained for all cities, i.e.: 1.913 eV for São Paulo, 1.908 eV for São José dos Campos and 1.909 eV in Cachoeira Paulista. The computed value of MM_{AW} for each case is also shown in the mentioned tables.

Table 5.5 - Regression line equations and the values of their coefficient of determination for different PV technologies in São Paulo. The values of MM_{AW} were obtained using these equations in conjunction with the values of APE_{AW}.

PV Technology	Regression Line Equation	MM_{AW}	R^2
sc-Si	1.796 – 0.422 (APE)	0.988	0.956
mc-Si	1.470 – 0.248 (APE)	0.996	0.901
a-Si	-1.452 + 1.316 (APE)	1.066	0.949
CdTe	0.100 + 0.485 (APE)	1.027	0.764
CIGS	1.615 – 0.326 (APE)	0.992	0.948
Perovskite	-0.771 + 0.950 (APE)	1.047	0.937

Source: Author.

Table 5.6 - Regression line equations and the values of their coefficient of determination for different PV technologies in São José dos Campos. The values of MM_{AW} were obtained using these equations in conjunction with the values of APE_{AW}.

PV Technology	Regression Line Equation	MM_{AW}	R^2
sc-Si	1.823 – 0.437 (APE)	0.989	0.983
mc-Si	1.496 – 0.262 (APE)	0.995	0.945
a-Si	-1.401 + 1.287 (APE)	1.054	0.977
CdTe	0.167 + 0.447 (APE)	1.020	0.870
CIGS	1.639 – 0.340 (APE)	0.992	0.980
Perovskite	-0.718 + 0.921 (APE)	1.038	0.968

Source: Author.

Table 5.7 - Regression line equations and the values of their coefficient of determination for different PV technologies in Cachoeira Paulista. The values of MM_{AW} were obtained using these equations in conjunction with the values of APE_{AW}.

PV Technology	Regression Line Equation	MM_{AW}	R^2
sc-Si	1.703 – 0.374 (*APE*)	0.988	0.877
mc-Si	1.342 – 0.181 (*APE*)	0.996	0.662
a-Si	-1.338 + 1.253 (*APE*)	1.053	0.948
CdTe	-0.241 + 0.664 (*APE*)	1.027	0.809
CIGS	1.536 - 0.287 (*APE*)	0.989	0.781
Perovskite	-0.776 + 0.951 (*APE*)	1.040	0.958

Source: Author.

Comparing the computed MM_{AW} results with those shown in Table 5.1, one can note a very close matching for all sites and PV materials. Hence, monthly weighted *APE* proves to be a suitable parameter to predict both the monthly and annual spectral impact on PV. Therefore, if the monthly or annual value of *APE* and the location and technology-specific function to describe its relationship with *MM* are known, the spectral impact can be determined. This conclusion is important and holds for the three subtropical and low-latitude sites investigated here. It should be kept in mind that this fact was already demonstrated for locations with medium latitude analyzed in Ishii et al. (2013) and Dirnberger et al. (2015) papers.

Furthermore, the expressions of MM_{MW} as a function of APE_{MW} for each PV material are very similar among the three sites. Taking it into account the determination coefficients, monthly and annually weighted *APE* may be considered as parameters to accurately derive the monthly and annual weighted *MM* for all technologies studied, which means that this can be a good approach. Therefore, potential PV developers could presumably consider the aforementioned regression lines for spectral impact predictions over an area near the three sites, inasmuch as differences on the solar spectrum caused by airmass, aerosols, and weather are considered small enough within them. More studies are required to estimate the regional limits within these expressions hold.

6 CONCLUSIONS

Solar resource spectral distribution impinging on a portion of Southeast Brazil and its impact on the performance of different PV materials has been investigated in São Paulo, São José dos Campos, and Cachoeira Paulista. Spectral data was recorded over 12 months for the three sites by weatherproof spectroradiometers in the first and second sites mentioned above and by spectroradiometers equipped with a weatherproof optical interface and housing for installation outdoors developed and calibrated specifically for the purpose of this work in the third site. Such developments took place due to the high costs of a spectrally resolved ground-based irradiance sensor designed for outdoor operations. A continuous acquisition data process was successfully performed at a lower cost (approximately half of its total cost) and with high reliability compared to the state-of- the-art devices. With the spectral instances, the average photon energy and spectral mismatch factor were obtained at instantaneous, monthly, and annual timescales. The results were then analyzed.

According to the results obtained, blue-biased solar spectra prevail throughout the year in the three sites analyzed. This observation was due in part to the humid subtropical climate that prevails in this region in addition to its low latitudes. The yearly *APE* histograms of the cumulative percentage of global horizontal irradiation point out that less than 5% of the solar energy impinging on the sites were measured with *APE* under 1.880 eV (*APE* corresponding to the AM1.5G standard spectrum), a far smaller share than those reported in the literature for mid-latitude sites. In addition, the monthly weighted *APE* remained above this value along all seasons in the three locations studied, which resulted in a higher annual weighted *APE*. The measured values were 1913 eV, 1908 eV and 1909 eV for São Paulo, São José dos Campos and Cachoeira Paulista, respectively. Nevertheless, the aforementioned parameter shows a very similar seasonal trend among the three sites, peaking to its maxima during the meridional summer - around 1.92 eV - and to its minima in meridional winter - down to 1.89 eV in São José dos Campos. Such seasonality is very similar to that exhibited by the

monthly *PW* (retrieved from AERONET) which means that water vapor may be an atmospheric factor driving solar spectrum variations in this Brazilian region. Depending on the period of the year (from approximately August to October – the dry season), these variations can also be due to biomass burning aerosols emitted by fires in Amazonia and Cerrado. More studies concerning pollution and its impacts on solar resource must be conducted for more precise information. It is worth mentioning that Cloud Enhancement effects were observed in few measurements performed in all sites. These results indicate that despite a higher *GHI*, the spectral shape seems to be very similar to the that of the solar spectrum collected under clear skies, causing similar impacts on PV in both cases. However, more research on this subject is yet to be carried out.

The effects caused on PV by blue biased spectra is somewhat pronounced depending on the properties of each PV material. Solar cells with larger band gap energies (i.e.: a-Si, CdTe, and Perovskite) are more likely to be affected by solar spectrum distribution regardless of the time scale considered, unlike photovoltaic materials with lower gap energies. On an instantaneous basis, devices with higher E_{GAP} may exhibit pronounced spectral gains under low light conditions, as for example a-Si which reaches almost 30% of gain under overcast skies. Gains also happen on a monthly basis analysis once the spectral mismatch factor stays above the unit for these technologies the entire year, with a similar trend to that of the APE_{MW}. In sequence, a-Si, Perovskite, and CdTe present higher monthly spectral gains in summer and lower gains during winter in all sites. Similar results were obtained on an annual basis, as gains of up to ~6%, ~5% and ~3% occur for a-Si, Perovskite and CdTe, respectively. These are significant results which highlight the importance of considering spectral effects on these devices if they are installed in the surroundings of the three sites investigated here regardless of the timescale considered. On the other hand, PV materials with smaller band gaps behave in the opposite way when compared with the technologies previously discussed. For these devices, the monthly mismatch factor values have a lower variation amplitude over the year. Indeed, spectral losses of around 1% are reached in January and December for CIGS, mc-Si, and sc-Si, while spectral effects are hardly noticeable from June to August. Considering that the

annual gains are in the vicinity of the unit for these PV materials, the influence of the spectrum on them might be ignored in practical terms.

The annual results concerning solar spectra and their impacts on the presented PV, reasonably agree with findings previously obtained in Florianópolis (BRAGA et al., 2020), Singapore (YE et al., 2014) and Lima (CONDE et al. 2021). Such agreements reveal that, in general, sites closer to the Equator have climates that lead to a beneficial solar resource for large band gap PV technologies such as a-Si, Perovskite, and CdTe from a spectral point of view. The annual findings presented here also agree with those obtained by synthetic spectra in Campo Grande (POLO et al., 2017) and Alta Floresta (FERNÁNDEZ et al., 2016). Furthermore, most of the monthly spectral gain results obtained in the latter site by means of simulation agree reasonably well with those presented in this work. The largest discrepancies seem to be caused by biomass burning in the Northern and Midwestern Brazil which takes place during the dry season. These fires may impact PV in Southeast Brazil as well, but to a lower extent, as revealed by the relationship between the daily average photon energy and the daily aerosol optical depth investigated in Cachoeira Paulista and São Paulo. Moreover, for the latter, local urban pollution may also cause effects on PV. The similarity between experimental and simulated results indicates that the synthetic spectra obtained with radiative transfer models may be a good approach to estimate PV spectral effects in low-latitude sites.

Besides, the correlation between *APE* and *MM* in tropical sites was also verified following the same procedure previously used by Ishii et al. (2013) and Dirnberger et al. (2015). Hence, scatterplots of monthly weighted *MM* vs monthly weighted *APE* were generated in conjunction with regression lines and their linear equations for all sites. A quasi-linear correlation between both parameters is observed for all PV technologies, in a way that the annual spectral impact on the PV materials may be derived from the annual weighted *APE* and from the mentioned equations. The computed annual spectral gains deviate at most by 2% from those obtained with the regression lines depending on the technology used. Additionally, the linear equations are very similar among the three sites, which indicates that maybe a single mathematical expression can be obtained for

each PV material in order to derive the spectral impacts on solar cells as a function of solar spectrum variations. Therefore, in low latitudes APE_{MW} may be used as input for the regression line equations to obtain the spectral impacts on monthly and annual timescales for each PV technology, which can be an easier procedure for solar engineers and project developers when estimating the spectral impact on PV performance.

The employment of two similar spectroradiometers in conjunction with a third device, calibrated indoors at INPE in locations relatively close to each other, in addition to the similarity of the results obtained here grant high accuracy to this work and indicate that the spectral impacts may have a regional behavior. The temporal and spatial limits of this behavior should be investigated in depth over wider areas and longer analysis intervals through terrestrial measurements and simulations. Studies on PV systems spectral impacts can help to design, improve, and validate PV yield prediction models, notably in tropical and subtropical countries where the lack of such studies is notorious. As the photovoltaic market grows rapidly in these regions, more research on photovoltaic systems spectral impacts have been gaining importance, especially in large-scale photovoltaic plant projects, because due to the greater investments and the greater power generated, small losses of photovoltaic yield can represent revenue losses.

7 PUBLICATIONS

i. NEVES, G. M., VILELA, W. A., PEREIRA, E. B., BERNI, L. A. Influência do espectro solar em módulos fotovoltaicos sob céu limpo, céu parcialmente nublado e céu nublado. In: **VII Congresso Brasileiro de Energia Solar-CBENS 2018**. 2018.

ii. NEVES, G., VILELA, W., PEREIRA, E., YAMASOE, M., & NOFUENTES, G. Spectral impact on PV in low-latitude sites: The case of southeastern Brazil. **Renewable Energy**, v. 164, p. 1306-1319, 2021.

iii. NOFUENTES, G., GUEYMARD, C. A., CABALLERO, J. A., MARQUES-NEVES, G., & AGUILERA, J. Experimental evaluation of a spectral index to characterize temporal variations in the direct normal irradiance spectrum. **Applied Sciences**, v. 11, n. 3, p. 897, 2021.

8 FUTURE LINES OF RESEARCH

   i.   To perform new experimental campaigns to investigate the variations of solar radiation spectral distribution and its impacts on PV in other Brazilian regions, such as North and Midwest Brazil.

  ii.   To develop experimental facilities and carry out an investigation on cloud enhancement events from a 'spectral' point-of-view to verify how parameters as the average photon energy and spectral mismatch factors behave in such situations.

 iii.   To investigate the effects caused by urban and biomass burning aerosols on solar spectrum and its impacts on PV.

 iv.   To extend the research described in this work to other PV technologies as those from the third and fourth solar cell generations.

REFERENCES

AJADI, T.; CUMING, V.; BOYLE, R.; STRAHAN, D.; KIMMEL, M.; LOGAN, M.; MCCRONE, A. **Global trends in renewable energy investment 2020**. Frankfurt am Main: Frankfurt School of Finance & Management, 2020.

ALBUQUERQUE, T.; ANDRADE, M.; YNOUE, R. Characterization of atmospheric aerosols in the city of São Paulo, Brazil: comparisons between polluted and unpolluted periods. **Environmental Monitoring and Assessment**, v. 184, n. 2, p. 969-984, 2012.

ALMEIDA, G. P.; BRITO, J.; MORALES, C. A.; ANDRADE, M. D. F.; ARTAXO, P. Measured and modelled Cloud Condensation} Nuclei (CCN) concentration in São Paulo, Brazil: the importance of aerosol size-resolved chemical composition on CCN concentration prediction. **Atmospheric Chemistry & Physics Discussions**, v. 13, n. 12, 2013.

ALMEIDA, G. P.; BRITO, J.; MORALES, C. A.; ANDRADE, M. D. F.; ARTAXO, P. Measured and modelled cloud condensation nuclei (CCN) concentration in São Paulo, Brazil: the importance of aerosol size-resolved chemical composition on CCN concentration prediction. **Atmospheric Chemistry and Physics**, v. 14, n. 14, p. 7559-7572, 2014.

ALMEIDA, M.; ZILLES, R.; LORENZO, E. Extreme overirradiance events in São Paulo, Brazil. **Solar Energy**, v. 110, p. 168-173, 2014.

ALONSO-ABELLA, M.; CHENLO, F.; NOFUENTES, G.; TORRES-RAMÍREZ, M. Analysis of spectral effects on the energy yield of different PV (photovoltaic) technologies: the case of four specific sites. **Energy**, v. 67, p. 435-443, 2014

ALVIM, D.; PENDHARKAR, J.; CAPISTRANO, V.; FRASSONI, A.; ENORÉ, D.; NETO, O.; GUTIERREZ, E.; CHOUDHURY, A.; KUBOTA, P.; SILVA, J.; CORREA, S.; NOBRE, P.; FIGUEROA, S. Aerosol distribution over Brazil with ECHAM-HAM and CAM5-MAM3 simulations and its comparison with ground-based and satellite data. **Atmospheric Pollution Research**, v. 8, n. 4, p. 718-728, 2017.

AMERICAN SOCIETY FOR TESTING AND MATERIALS. **ASTM E490-00a**: standard solar constant and zero air mass solar spectral irradiance tables. West Conshohocken, 2000.

AMERICAN SOCIETY FOR TESTING AND MATERIALS. **ASTM E772:** standard terminology of solar energy conversion. West Conshohocken, 2015.

AMERICAN SOCIETY FOR TESTING AND MATERIALS. **ASTM G173-03**: standard tables for reference solar spectral irradiances: direct normal and **h**emispherical on 37° tilted surface. West Conshohocken, 2012.

AMILLO, A.M.G.; HULD, T.; VOURLIOTI, P.; MÜLLER, R.; NORTON, M. Application of satellite-based spectrally-resolved solar radiation data to PV performance studies. **Energies**, v. 8*,* p. 3455-3488, 2015. Available from: https://doi.org/10.3390/en8053455.

ASSOCIAÇÃO BRASILEIRA DE ENERGIA SOLAR FOTOVOLTAICA (ABSOLAR). **Panorama of solar photovoltaic in Brazil and in the World**. Available from: <https://www.absolar.org.br/en/market/infographic/>. Assess on: 15 Aug. 2021.

ARTAXO, P.; MARTINS, J.; YAMASOE, M.; PROCÓPIO, A.; PAULIQUEVIS, T.; ANDREAE, M.; GUYON, P.; GATTI, L.; LEAL., A. M. Physical and chemical properties of aerosols in the wet and dry seasons in Rondônia, Amazonia. **Journal of Geophysical Research: Atmospheres**, v. 107, n. D20, 2002.

AVRUTIN, V.; IZYUMSKAYA, N.; MORKOÇ, H. Semiconductor solar cells: recent progress in terrestrial applications. **Superlattices and Microstructures**, v. 49, n. 4, p. 337-364, 2011.

BAEK, S. W.; JUN, S.; KIM, B.; PROPPE, A.; OUELLETTE, O.; VOZNYY, O.; KIM, C.; KIM, J.; WALTERS, G.; SONG, J.; JEONG, S.; BYUN, H.; SEOK, M.; HOOGLAND, S.; ARGUER, F.; KELLEY, S.; LEE, J.Y., SARGENT, E. Efficient hybrid colloidal quantum dot/organic solar cells mediated by near-infrared sensitizing small molecules. **Nature Energy**, v. 4, n. 11, p. 969-976, 2019.

BARRUCHO, L. **Brazil Drought stokes worries over energy shortages**. Available from: https://www.bbc.com/news/world-latin-america-21055803. Assess on: 20 June 2021.

BERGSTROM, R. W.; PILEWSKIE, P.; RUSSELL, P. B.; REDEMANN, J.; BOND, T. C.; QUINN, P. K.; SIERAU, B. Spectral absorption properties of atmospheric aerosols. **Atmospheric Chemistry and Physics**, v. 7, n. 23, p. 5937-5943, 2007.

BERGSTROM, R. W.; RUSSELL, P. B.; HIGNETT, P. Wavelength dependence of the absorption of black carbon particles: Predictions and results from the TARFOX experiment and implications for the aerosol single scattering albedo. **Journal of the Atmospheric Sciences**, v. 59, n. 3, p. 567-577, 2002.

BETTS, T. R. **Investigation of photovoltaic device operation under varying spectral conditions**. 2004. 129 p. Thesis (Philosophy Doctorate) - Loughborough University, Loughborough, 2004. Available from: https://repository.lboro.ac.uk/articles/thesis/Investigation_of_photovoltaic_devic

e_operation_under_varying_spectral_conditions/9525275. Assess on 15 Apr. 2021.

BRITISH PETROLEUM (BP). **Statistical review of world energy**. 2021. 71p. Available from: <https://www.bp.com/content/dam/bp/business-sites/en/global/corporate/pdfs/energy-economics/statistical-review/bp-stats-review-2021-full-report.pdf>. Assess on: 15 Apr. 2021.

BRAGA, M.; DO NASCIMENTO, L.; RÜTHER, R. Spectral modeling and spectral impacts on the performance of mc-Si and new generation CdTe photovoltaics in warm and sunny climates. **Solar Energy**, v. 188, p. 976-988, 2019.

BRASILIENSE, C. S.; DERECZYNSKI, C. P.; SATYAMURTY, P.; CHOU, S. C.; DA SILVA SANTOS, V. R.; CALADO, R. N. Synoptic analysis of an intense rainfall event in Paraíba do Sul river basin in southeast Brazil. **Meteorological Applications**, v. 25, n. 1, p. 66-77, 2018.

BUNEA, G. E.; WILSON, K. E.; MEYDBRAY, Y.; CAMPBELL, M. P.; DE CEUSTER, D. M. Low light performance of mono-crystalline silicon solar cells. In: IEEE WORLD CONFERENCE ON PHOTOVOLTAIC ENERGY CONFERENCE, 4., 2006, Waikoloa, USA. **Proceedings…** 2006. p. 1312-1314.

CABALLERO, J. A.; FERNÁNDEZ, E. F.; THERISTIS, M.; ALMONACID, F.; NOFUENTES, G. Spectral corrections based on air mass, aerosol optical depth, and precipitable water for PV performance modeling. **IEEE Journal of Photovoltaics**, v. 8, n. 2, p. 552-558, 2018.

CABALLERO, J. A.; FERNÁNDEZ, E. F.; THERISTIS, M.; ALMONACID, F.; NOFUENTES, G. Spectral corrections based on air mass, aerosol optical depth, and precipitable water for PV performance modeling. **IEEE Journal of Photovoltaics**, v. 8, n. 2, p. 552-558, 2018.

CASTANHO, A.; ARTAXO, P. Wintertime and summertime São Paulo aerosol source apportionment study. **Atmospheric Environment**, v. 35, n. 29, p. 4889-4902, 2001.

CASTANHO, A.; MARTINS, J.; ARTAXO, P. MODIS aerosol optical depth retrievals with high spatial resolution over an urban area using the critical reflectance. **Journal of Geophysical Research: Atmospheres**, v. 113, n. D2, 2008.

CASTRO, J.;SCHWEIGER, M.; MOSEK, D.; TANAHASHI, T.; KING, B.; FRIESEN, G.; HAITAO, L.; FRENCH, R.; BRUCKMAN, L.; MULLER, B.; REISE, C.; EDER, G.; VAN SARK, W.; SANGPONGSANON, Y.; VALENCIA, F.; STEIN, J. **Climatic rating of photovoltaic modules**: different technologies for various operating conditions. Paris: International Energy Agency (IEA-PVPs), 2020.

CHANTANA, J.; IMAI, Y.; KAWANO, Y.; HISHIKAWA, Y.; NISHIOKA, K.; MINEMOTO, T. Impact of average photon energy on spectral gain and loss of various-type PV technologies at different locations. **Renewable Energy**, v. 145, p. 1317-1324, 2020.

CHANTANA, J.; KAMEI, A.; MINEMOTO, T. Influences of environmental factors on Si-based photovoltaic modules after longtime outdoor exposure by multiple regression analysis. **Renewable Energy**, v. 101, p. 10-15, 2017.

CHEN, C. **Physics of solar energy**. New Jersey: John Wiley & Sons, 2011.

CONDE, L. A.; ANGULO, J. R.; SEVILLANO-BENDEZÚ, M. Á.; NOFUENTES, G.; TÖFFLINGER, J. A.; DE LA CASA, J. Spectral effects on the energy yield of various photovoltaic technologies in Lima (Peru). **Energy**, v. 223, e 120034, 2021.

CLIMATE AMBITION ALLIANCE 25 (COP25). **Objectives**. Available from: https://cop25.mma.gob.cl/en/home/. Assess on: 8 May 2021.

CORNARO, C.; ANDREOTTI, A. Influence of average photon energy index on solar irradiance characteristics and outdoor performance of photovoltaic modules. **Progress in Photovoltaics: Research and Applications**, v. 21, n. 5, p. 996-1003, 2013.

DE LIMA, G.; RUEDA, V. The urban growth of the metropolitan area of Sao Paulo and its impact on the climate. **Weather and Climate Extremes**, v. 21, p. 17-26, 2018.

DECKER, M.; BRUNKE, M. A.; WANG, Z.; SAKAGUCHI, K.; ZENG, X.; BOSILOVICH, M. G. Evaluation of the reanalysis products from GSFC, NCEP, and ECMWF using flux tower observations. **Journal of Climate**, v. 25, n. 6, p. 1916-1944, 2012.

DEUTSCHE GESELLSCHAFT FÜR SONNENENERGIE (DGS). **Planning and installing photovoltaic systems:** a guide for installers, architects and engineers. Routledge: DGS, 2013.

DEWITTE, S.; CLERBAUX, N. Measurement of the Earth radiation budget at the top of the atmosphere: a review. **Remote Sensing**, v. 9, n. 11, p. 1143, 2017.

DIRNBERGER, D.; BLACKBURN, G.; MÜLLER, B.; REISE, C. On the impact of solar spectral irradiance on the yield of different PV technologies. **Solar Energy Materials and Solar Cells**, v. 132, p. 431-442, 2015.

DIRNBERGER, D.; MÜLLER, B.; REISE, C.. PV module energy rating: opportunities and limitations. **Progress in Photovoltaics: Research and Applications**, v. 23, n. 12, p. 1754-1770, 2015.

DUBOVIK, O.; HOLBEN, B.; ECK, T. F.; SMIRNOV, A.; KAUFMAN, Y. J.; KING, M. D.; TANRÉ, D.; SLUTSKER, I. Variability of absorption and optical properties of key aerosol types observed in worldwide locations. **Journal of the atmospheric sciences**, v. 59, n. 3, p. 590-608, 2002.

DUCK, B.C.; FELL, C.J. Comparison of methods for estimating the impact of spectrum on PV output, in: IEEE PHOTOVOLTAIC SPECIALIST CONFERENCE (PVSC), 42., 2015, New Orleans, LA, USA. **Proceedings…** New Orleans: IEEE, 2015. p. 1-6. Available from: https://doi.org/10.1109/PVSC.2015.7356211. Accessed on: 9 Sept. 2020.

DURRANI, S. P.; BALLUFF, S.; WURZER, L.; KRAUTER, S. Photovoltaic yield prediction using an irradiance forecast model based on multiple neural networks. **Journal of Modern Power Systems and Clean Energy**, v. 6, n. 2, p. 255-267, 2018.

ELECTROOPTICS. **'Record-breaking' bifacial solar cells produced using laser doping.** Available from: https://www.electrooptics.com/news/record-breaking-bifacial-solar-cells-produced-using-laser-doping. Access on: 30 Oct. 2021.

EMERY, K. The rating of photovoltaic performance. **IEEE Transactions on Electron Devices**, v. 46, n. 10, p. 1928-1931, 1999.

EMPRESA DE ENERGIA ELÉTRICA (EPE). **Anuário estatístico**. Rio de Janeiro: EPE, 2011.

EMPRESA DE ENERGIA ELÉTRICA (EPE). **Leilão de energia de reserva de 2014**. Rio de Janeiro: EPE, 2014.

EMPRESA DE ENERGIA ELÉTRICA (EPE). **Anuário estatístico**. Rio de Janeiro: EPE, 2020

EMPRESA DE ENERGIA ELÉTRICA (EPE). **BEN summary report**. Rio de Janeiro: EPE, 2021

ESCOBEDO, J. F.; GOMES, E. N.; OLIVEIRA, A. P.; SOARES, J. Modeling hourly and daily fractions of UV, PAR and NIR to global solar radiation under various sky conditions at Botucatu, Brazil. **Applied Energy**, v. 86, n. 3, p. 299-309, 2009.

FERNÁNDEZ, E. F.; SORIA-MOYA, A.; ALMONACID, F.; AGUILERA, J. Comparative assessment of the spectral impact on the energy yield of high concentrator and conventional photovoltaic technology. **Solar Energy Materials and Solar Cells**, v. 147, p. 185-197, 2016.

FONASH, S. **Solar cell device physics**. Pennsylvania: Elsevier, 2012.

FOUAD, M. M.; SHIHATA, L. A.; MORGAN, S. I. An integrated review of factors influencing the perfomance of photovoltaic panels. **Renewable and Sustainable Energy Reviews**, v. 80, p. 1499-1511, 2017.

FRAUNHOFER INSTITUTE FOR SOLAR ENERGY SYSTEMS (ISE) **Photovoltaics report**. Available from: https://www.ise.fraunhofer.de/content/dam/ise/de/documents/publications/studie s/Photovoltaics-Report.pdf. Access on: 7 Jan. 2022.

FREITAS, S.; LONGO, K.; DIAS, M.; DIAS, P.; CHATFIELD, R.; PRINS, E.; ARTAXO, P.; GRELL, G.; RECUERO, F. Monitoring the transport of biomass burning emissions in South America. **Environmental Fluid Mechanics**, v. 5, n. 1, p. 135-167, 2005.

FUZZI, S.; ANDREAE, M. O.; HUEBERT, B. J.; KULMALA, M.; BOND, T. C.; BOY, M. S.; DOHERTY, J.; GUENTHER, A.; KANAKIDOU, M.; KAWAMURA, K.; KERMINEN, V.-M.; LOHMANN, U.; RUSSELL, L. M.; PÖSCHL, U. Critical assessment of the current state of scientific knowledge, terminology, and research needs concerning the role of organic aerosols in the atmosphere, climate, and global change. **Atmospheric Chemistry and Physics**, v. 6, n. 7, p. 2017-2038, 2006.

NOFUENTES, G.; GARCÍA-DOMINGO, B.; FUENTES, M.; MORENO, R.; CANETE, C.; SIDRACH-DE-CARDONA, M.; ALONSO, M.A.; CHENLO, F. Comparative analysis of the effects of spectrum and module temperature on the performance of thin film modules on different sites. In: EUROPEAN PHOTOVOLTAIC SOLAR ENERGY CONFERENCE, 26., 2012. **Proceedings…** 2012.

GARCÍA, R.; TORRES-RAMÍREZ, M.; MUÑOZ-CERÓN, E.; DE LA CASA, J.; AGUILERA, J. Spectral characterization of the solar resource of a sunny inland site for flat plate and concentrating PV systems. **Renewable Energy**, v. 101, p. 1169-1179, 2017.

GEISLER, W. S.; BANKS, M. S. **Handbook of optics**: fundamentals, techniques, and design. Second edition. California: McGraw-Hill, 1995. ISBN 0070479747.

GOOCH AND HOUSEGO. **Technical papers**. Available from < https://gandh.com/category/technical-papers/ >. Access on 15 Jan. 2022.

GOODY, R. M.; YUNG, Y. L. **Atmospheric radiation**: theoretical basis. New York: Oxford University Press, 1995.

GOTTSCHALG, R.; BETTS, T. R.; INFIELD, D. G.; KEARNEY, M. J. Experimental investigation of spectral effects on amorphous silicon solar cells in outdoor operation. In: IEEE Photovoltaic Specialists Conference, 29., 2002. **Proceedings…** IEEE, 2002. p. 1138-1141.

GOTTSCHALG, R.; BETTS, T. R.; INFIELD, D. G.; KEARNEY, M. J. The effect of spectral variations on the performance parameters of single and double junction amorphous silicon solar cells. **Solar Energy Materials and Solar Cells**, v. 85, n. 3, p. 415-428, 2005.

GOTTSCHALG, R.; BETTS, T. R.; INFIELD, D. G.; KEARNEY, M. J. The effect of spectral variations on the performance parameters of single and double junction amorphous silicon solar cells. **Solar Energy Materials and Solar Cells**, v. 85, n. 3, p. 415-428, 2005.

GOTTSCHALG, R.; INFIELD, D. G.; KEARNEY, M. J. Experimental study of variations of the solar spectrum of relevance to thin film solar cells. **Solar Energy Materials and Solar Cells**, v. 79, n. 4, p. 527-537, 2003.

GREEN, M.; DUNLOP, E.; HOHL-EBINGER, J.; YOSHITA, M.; KOPIDAKIS, N.; HAO, X. Solar cell efficiency tables (version 57). **Progress in Photovoltaics: Research and Applications**, v. 29, n. 1, p. 3-15, 2021.

GUEYMARD, C. A. Cloud and albedo enhancement impacts on solar irradiance using high-frequency measurements from thermopile and photodiode radiometers. Part 1: Impacts on global horizontal irradiance. **Solar Energy**, v. 153, p. 755-765, 2017.

GUEYMARD, C. A. Direct solar transmittance and irradiance predictions with broadband models. Part I: detailed theoretical performance assessment. **Solar Energy**, v. 74, n. 5, p. 355-379, 2003.

GUEYMARD, C. A. Parameterized transmittance model for direct beam and circumsolar spectral irradiance. **Solar Energy**, v. 71, n. 5, p. 325-346, 2001.

GUEYMARD, C. A. **SMARTS2**: a simple model of the atmospheric radiative transfer of sunshine: algorithms and performance assessment. Cocoa, FL: Florida Solar Energy Center, 1995.

GUEYMARD, C. A.; MYERS, D.; EMERY, K. Proposed reference irradiance spectra for solar energy systems testing. **Solar Energy**, v. 73, n. 6, p. 443-467, 2002.

GUEYMARD, C.; KAMBEZIDIS, H. D. Solar radiation and daylight models. **Solar Spectral Radiation**, p. 221-301, 1997.

HÄBERLIN, H. **Photovoltaics**: system design and practice. Chichester: John Wiley & Sons, 2012.

HATHAWAY, D. H. The solar cycle. **Living Reviews in Solar Physics**, v. 12, n. 1, p. 1-87, 2015.

HELD, G.; ALLEN, A. G.; LOPES, F. J.; GOMES, A. M.; CARDOSO, A. A.; LANDULFO, E. Review of aerosol observations by lidar and chemical analysis in the state of São Paulo, Brazil. In: ABDUL-RAZZAK, H. (Ed.). **Atmospheric**

aerosols-regional characteristics-chemistry and physics. [S.l.]: IntechOpen, 2012.

HERNÁNDEZ-CALLEJO, L.; GALLARDO-SAAVEDRA, S.; ALONSO-GÓMEZ, V. A review of photovoltaic systems: design, operation and maintenance. **Solar Energy**, v. 188, p. 426-440, 2019.

HOLBEN, B. N.; TANRÉ, D.; SMIRNOV, A.; ECK, T. F.; SLUTSKER, I.; ABUHASSAN, N.; NEWCOMB, W. W.; SCHAFER, J. S.; CHATENET, B.; LAVENU, F.; KAUFMAN, Y. J.; VANDE CASTLE, J.; SETZER, A.; MARKHAM, B.; CLARK, D.; FROUIN, R.; HALTHORE, R.; KARNELI, A.; O'NEILL, N. T.; PIETRAS, C.; PINKER, R. T.; VOSS, K.; ZIBORDI, G. An emerging ground-based aerosol climatology: aerosol optical depth from AERONET. **Journal of Geophysical Research: Atmospheres**, v. 106, n. D11, p. 12067-12097, 2001.

HOLBEN, B.N.; ECK, T.F.; SLUTSKER, I.; TANRÉ, D.; BUIS, J.P.; SETZER, A.; VERMOTE, E.; REAGAN, J.A.; KAUFMAN, Y.J.; NAKAJIMA, T.; LAVENU, F.; JANKOWIAK, I.; SMIRNOV, A. AERONET: a federated instrument network and data archive for aerosol characterization. **Remote Sensing of Environment**, v. 66, n. 1, p. 1-16, 1998.

HU, C.; WHITE, R. M. **Solar cells**: from basic to advanced systems. Cambridge: McGraw-Hill, 1983.

HUANG, G.; LI, Z.; LI, X.; LIANG, S.; YANG, K.; WANG, D.; ZHANG, Y. Estimating surface solar irradiance from satellites: past, present, and future perspectives. **Remote Sensing of Environment**, v. 233, e 111371, 2019.

HULD, T.; DUNLOP, E.; BEYER, H. G.; GOTTSCHALG, R. Data sets for energy rating of photovoltaic modules. **Solar Energy**, v. 93, p. 267-279, 2013.

INSTITUTO BRASILIERO DE GEOGRAFIA E ESTATÍSTICA (IBGE). **Organização do território**: biblioteca digital. 2021. Available from: https://www.ibge.gov.br/geociencias/downloads-geociencias.html. Assess on: 15 Sept. 2021.

INTERNATIONAL ENERGY AGENCY (IEA). **Global electricity generation mix, 2010-2020.** Paris: IEA, 2021a. Available from: https://www.iea.org/data-and-statistics/charts/global-electricity-generation-mix-2010-2020. Assess on: 12 May 2021.

INTERNATIONAL ENERGY AGENCY (IEA). **Net zero by 2050**. Paris: IEA, 2021b. Available from: https://www.iea.org/reports/net-zero-by-2050. Assess on: 8 May 2021.

INTERNATIONAL ENERGY AGENCY (IEA). **Electricity market report - July 2021**. Paris: IEA, 2021c. Available from: https://www.iea.org/reports/electricity-market-report-july-2021. Assess on: 13 May 2021.

INTERNATIONAL ENERGY AGENCY (IEA). **Global energy review 2021**. Paris: IEA, 2021d. Available from: https://www.iea.org/reports/global-energy-review-2021. Assess on: 8 May 2021.

INTERNATIONAL ENERGY AGENCY (IEA). **Global energy review 2021**. Paris: IEA, 2021e. Available from: https://www.iea.org/reports/global-energy-review-2021. Assess on: 8 May 2021.

INTERNATIONAL ENERGY AGENCY (IEA). **Renewable energy market update 2021**: outlook for 2021 and 2022. Paris: IEA, 2021e. Available from: https://www.iea.org/reports/renewable-energy-market-update-2021. Assess on: 8 May 2021.

INTERNATIONAL ENERGY AGENCY PHOTOVOLTAIC POWER SYSTEMS PROGRAMME (IEA-PVPs). **Snapshot of global PV markets 2021**. IEA-PVPs, 2021. Available from: https://iea-pvps.org/snapshot-reports/snapshot-2021/. Assess on: 8 May 2021.

INSTITUTO NACIONAL DE PESQUISAS ESPACIAIS (INPE). **Terra Brasilis**: biblioteca digital. 2021. Available from: http://terrabrasilis.dpi.inpe.br/downloads/. Assess on: 20 June 2021.

INTERNATIONAL ELECTROTECHNICAL COMMISSION. **IEC 60904-3**: photovoltaic devices - part 3: measurement principles for terrestrial Photovoltaic (PV) solar devices with reference spectral irradiance data. Geneva, Switzerland, 2019.

INTERNATIONAL ELECTROTECHNICAL COMMISSION. **IEC 60904-7**: Photovoltaic devices e part 7: computation of the spectral mismatch correction for measurements of photovoltaic devices. Geneva, Switzerland, 2008. Switzerland, 1992.

INTERNATIONAL PANEL FOR CLIMATE CHANGES (IPCC). **Climate change 2013**: the physical science basis. Cambridge: Cambridge University Press, 2013.

INTERNATIONAL PANEL FOR CLIMATE CHANGES (IPCC). **Climate change 2014**: mitigation of climate change. Cambridge: Cambridge University Press, 2014.

INTERNATIONAL PANEL FOR CLIMATE CHANGES (IPCC). **Global warming of 1.5°C**. Cambridge: Cambridge University Press, 2018.

INTERNATIONAL PANEL FOR CLIMATE CHANGES (IPCC). **Climate change 2021**: the physical science basis. Cambridge: Cambridge University Press, 2021.

IQBAL, M. **An introduction to solar radiation**. New York: Elsevier, 1983.

INTERNATIONAL RENEWABLE ENERGY AGENCY (IRENA). **Bracing for climate impacte:** renewables as a climate change adaptation strategy. Abu Dhabi: IRENA, 2021, 103 p. Available from: https://www.irena.org/publications/2021/Aug/Bracing-for-climate-impact-2021#:~:text=Bracing%20for%20Climate%20Impact%3A%20Renewables%20as%20a%20Climate%20Change%20Adaptation%20Strategy,-August%202021&text=Many%20climate%20change%20adaptation%20strategies,in%20policy%20making%20or%20practice. Assess on: 29 Apr. 2021.

INTERNATIONAL RENEWABLE ENERGY AGENCY (IRENA). **Renewable capacity statistics 2021**. Abu Dhabi: IRENA, 2021, 63 p. Available from: < https://www.irena.org/publications/2021/March/Renewable-Capacity-Statistics-2021>. Assessed on: 29 Apr. 2021.

INTERNATIONAL ORGANIZATION FOR STANDARDIZATION (ISO). **ISO 9845-1**: solar energy: reference solar spectral irradiance at the ground at different receiving conditions — Part 1: direct normal and hemispherical solar irradiance for air mass 1,5. Geneva, 1992.

ISHII, T.; OTANI, K.; TAKASHIMA, T. Effects of solar spectrum and module temperature on outdoor performance of photovoltaic modules in round-robin measurements in Japan. **Progress in Photovoltaics: Research and Applications**, v. 19, n. 2, p. 141-148, 2011.

ISHII, T.; OTANI, K.; TAKASHIMA, T.; XUE, Y. Solar spectral influence on the performance of photovoltaic (PV) modules under fine weather and cloudy weather conditions. **Progress in Photovoltaics: Research and Applications**, v. 21, n. 4, p. 481-489, 2013.

JACOB, D. The role of water vapour in the atmosphere: a short overview from a climate modeller's point of view. **Physics and Chemistry of the Earth, Part A: Solid Earth and Geodesy**, v. 26, n. 6-8, p. 523-527, 2001.

JAEGER-WALDAU, A. **PV status report 2019**. Luxembourg: Publications Office of the European Union, 2019. 79 p. Available from: **Erro! A referência de hiperlink não é válida.**. Access on: 8 Aug. 2020.

JARDINE, C. N.; BETTS, T. R.; GOTTSCHALG, R.; INFIELD, D. G.; LANE, K. Influence of spectral effects on the performance of multijunction amorphous silicon cells. In: PHOTOVOLTAIC IN EUROPE CONFERENCE, 2002. **Proceedings…** 2002.

JÄRVELÄ, M.; LAPPALAINEN, K.; VALKEALAHTI, S. Characteristics of the cloud enhancement phenomenon and PV power plants. **Solar Energy**, v. 196, p. 137-145, 2020.

KHATUN, S.; MAITI, A.; DAS, G.;PAL, A. J. Role of individual bands in the unusual temperature-dependent band gap of methylammonium lead iodide. **The Journal of Physical Chemistry C**, v. 124, n. 36, p. 19841-19848, 2020.

KIRCHSTETTER, T. W.; NOVAKOV, T.; HOBBS, P. V. Evidence that the spectral dependence of light absorption by aerosols is affected by organic carbon. **Journal of Geophysical Research: Atmospheres**, v. 109, n. D21, 2004.

KYLLING, A.; ALBOLD, A.; SECKMEYER, G. Transmittance of a cloud is wavelength-dependent in the UV-range: physical interpretation. **Geophysical Research Letters**, v. 24, n. 4, p. 397-400, 1997.

LASKIN, A.; LASKIN, J.; NIZKORODOV, S. A. Chemistry of atmospheric brown carbon. **Chemical Reviews**, v. 115, n. 10, p. 4335-4382, 2015.

LABORATORY FOR ATMOSPHERIC AND SPACE PHYSICS (LASP). **LASP interactive solar irradiance data center**. Colorado, 2021. Available from: <http://lasp.colorado.edu/lisird/sorce/sorce_tsi/>. Assess on: 7 July 2021.

LAZARD. **Levelized cost of energy, levelized cost of storage, and levelized cost of hydrogen 2020.** 2020. Available from: https://www.lazard.com/perspective/lcoe2020. Assess on: 7 July 2021.

LANDULFO, E.; PAPAYANNIS, A.; ARTAXO, P.; CASTANHO, A. D. A.; FREITAS, A. Z.; SOUZA, R. F.; VIEIRA JUNIOR, N. D.; JORGE, M. P.; SÁNCHEZ-CCOYLLO, O. R.; MOREIRA, D. S. Synergetic measurements of aerosols over São Paulo, Brazil using LIDAR, sunphotometer and satellite data during the dry season. **Atmospheric Chemistry and Physics**, v. 3, n. 5, p. 1523-1539, 2003.

LIANG, S.; WANG, D.; HE, T.; YU, Y. Remote sensing of earth's energy budget: Synthesis and review. **International Journal of Digital Earth**, v. 12, n. 7, p. 737-780, 2019.

LINDSAY, N.; LIBOIS, Q.; BADOSA, J.; MIGAN-DUBOIS, A.; BOURDIN, V. Errors in PV power modelling due to the lack of spectral and angular details of solar irradiance inputs. **Solar Energy**, v. 197, p. 266-278, 2020.

LIOU, K. N. **An introduction to atmospheric radiation**. 2.ed. Cambridge: Academic Press, 2002.

LIU, H.; NOBRE, A. M.; YANG, D.; YE, J. Y.; MARTINS, F. R.; RÜTHER, R.; REINDL, T.; ABERLE, A. G.; PETERS, I. M. The impact of haze on performance ratio and short-circuit current of PV systems in Singapore. **IEEE Journal of Photovoltaics**, v. 4, n. 6, p. 1585-1592, 2014.

LOPES, F. J. S.; MARIANO, G. L.; LANDULFO, E.; MARIANO, E. V. C. Impacts of biomass burning in the atmosphere of the southeastern region of Brazil using remote sensing systems. **Atmospheric Aerosols—Regional Characteristics—Chemistry and Physics**, p. 978-953, 2012.

LUCEÑO-SÁNCHEZ, J. A.; DÍEZ-PASCUAL, A. M.; PEÑA CAPILLA, R. Materials for photovoltaics: state of art and recent developments. **International Journal of Molecular Sciences**, v. 20, n. 4, p. 976, 2019.

LUNA, M. A. R.; CUNHA, F. B. F.; DE MIRANDA MOUSINHO, M. C. A.; TORRES, E. A. Solar photovoltaic distributed generation in Brazil: the case of resolution 482/2012. **Energy Procedia**, v. 159, p. 484-490, 2019.

LUQUE, A.; HEGEDUS, S., **Handbook of photovoltaic science and engineering**. England : John Wiley & Sons, 2003.

MAGARE, D.B.; SASTRY, O.S.; GUPTA, R.; BETTS, T.R.; GOTTSCHALG, R.; KUMAR, A.; BORA, B.; SINGH, Y.K. Effect of seasonal spectral variations on performance of three different photovoltaic technologies in India. **International Journal of Energy and Environmental Engineering**, v. 7, n. 1, p. 93-103, 2016.

MAHOWALD, N.; ALBANI, S.; KOK, J. F.; ENGELSTAEDER, S.; SCANZA, R.; WARD, D. S.; FLANNER, M. G. The size distribution of desert dust aerosols and its impact on the Earth system. **Aeolian Research**, v. 15, p. 53-71, 2014.

MARTIN, N.; RUIZ, J. M. A new method for the spectral characterization of PV modules. **Progress in Photovoltaics: Research and Applications**, v. 7, n. 4, p. 299-310, 1999.

MARTIN, S.; ANDREAE, M.; ARTAXO, P.; BAUMGARDNER, D.; CHEN, Q.; GOLDSTEIN, A.; GUENTHER, A.; HEALD, C.; MAYOL-BRACERO, O.; MCMURRY, P.; PAULIQUEVIS, T.; PÖSCHL, U.; PRATHER, K.; ROBERTS, G.; SALESKA, S.; SILVA DIAS, M. A.; SPRACKLEN, D.; SWIETLICKI, E.; TREBS, I. Sources and properties of Amazonian aerosol particles. **Reviews of Geophysics**, v. 48, n. 2, 2010.

MARTINS, L.; WIKUATS, C.; CAPUCIM, M.; ALMEIDA, D.; COSTA, S.; ALBUQUERQUE, T.; CARVALHO, V.; FREITAS, E.; ANDRADE, M.; MARTINS, J. Extreme value analysis of air pollution data and their comparison between two large urban regions of South America. **Weather and Climate Extremes**, v. 18, p. 44-54, 2017.

MCCLUNEY, W. **Introduction to radiometry and photometry**. [S.l.]: Artech House, 1983.

MCEVOY, A.; CASTANER, L.; MARKVART, T. **Solar cells:** materials, manufacture and operation. Oxford: Academic Press, 2012.

MINEMOTO, T.; FUKUSHIGE, S.; TAKAKURA, H. Difference in the outdoor performance of bulk and thin-film silicon-based photovoltaic modules. **Solar Energy Materials and Solar Cells**, v. 93, n. 6-7, p. 1062-1065, 2009.

MINEMOTO, T.; NAKADA, Y.; TAKAHASHI, H.; TAKAKURA, H. Uniqueness verification of solar spectrum index of average photon energy for evaluating

outdoor performance of photovoltaic modules. **Solar Energy**, v. 83, n. 8, p. 1294-1299, 2009.

MINEMOTO, T.; NAGAE, S.; TAKAKURA, H. Impact of spectral irradiance distribution and temperature on the outdoor performance of amorphous Si photovoltaic modules. **Solar Energy Materials and Solar Cells**, v. 91, n. 10, p. 919-923, 2007.

MASSACHUSSETS INSTITUTE OF TECHNOLOGY (MIT). **The future of solar energy**. Massachusetts: Massachusetts Institute of Technology, 2015. Available from: <https://energy.mit.edu/research/future-solar-energy/>. Assess on 28 Jan. 2021.

MOOSMÜLLER, H.; CHAKRABARTY, R. K.; ARNOTT, W. P. Aerosol light absorption and its measurement: a review. **Journal of Quantitative Spectroscopy and Radiative Transfer**, v. 110, n. 11, p. 844-878, 2009.

MÜLLER, B.; HARDT, L.; ARMBRUSTER, A.; KIEFER, K.; REISE, C. Yield predictions for photovoltaic power plants: empirical validation, recent advances and remaining uncertainties. **Progress in Photovoltaics: Research and Applications**, v. 24, n. 4, p. 570-583, 2016.

NAKADA, Y.; TAKAHASHI, H.; ICHIDA, K.; MINEMOTO, T.; TAKAKURA, H. Influence of clearness index and air mass on sunlight and outdoor performance of photovoltaic modules. **Current Applied Physics**, v. 10, n. 2, p. S261-S264, 2010.

YOON, H.; GIBSON, C. **NIST measurement services:** spectral irradiance calibrations. Gaithersburg: National Institute of Standards and Technology (NIST), 2011. Available from: https://nvlpubs.nist.gov/nistpubs/Legacy/SP/nistspecialpublication250-89.pdf. Assess on: 12 May 2021.

NATIONAL AERONAUTICS AND SPACE ADMINISTRATION (NOAA). **U. S. sStandard atmosphere.** Washington: National Aeronautics and Space Administration, 1976.

NOFUENTES, G.; DE LA CASA, J.; SOLÍS-ALEMÁN, E. M.; FERNÁNDEZ, E. F. Spectral impact on PV performance in mid-latitude sunny inland sites: experimental vs. modelled results. **Energy**, v. 141, p. 1857-1868, 2017b.

NOFUENTES, G.; ALMONACID, G. Design tools for the electrical conFiguretion of architecturally-integrated PV in buildings. **Progress in Photovoltaics: Research and Applications**, v. 7, n. 6, p. 475-488, 1999.

NOFUENTES, G.; DE LA CASA, J.; TORRES-RAMÍREZ, M.; ALONSO-ABELLA, M. Solar spectral and module temperature influence on the outdoor performance of thin film PV modules deployed on a sunny inland site. **International Journal of Photoenergy**, v. 2013, 2013a.

NOFUENTES, G.; GARCÍA-DOMINGO, B.; MUÑOZ, J. V.; CHENLO, F. Analysis of the dependence of the spectral factor of some PV technologies on the solar spectrum distribution. **Applied Energy**, v. 113, p. 302-309, 2014.

NOFUENTES, G.; GUEYMARD, C. A.; AGUILERA, J.; PÉREZ-GODOY, M. D.; CHARTE, F. Is the average photon energy a unique characteristic of the spectral distribution of global irradiance? **Solar Energy**, v. 149, p. 32-43, 2017b.

NATIONAL RENEWABLE ENERGY LABORATORY (NREL). **Best research-cell efficiency chart**. Available from: <https://www.nrel.gov/pv/cell-efficiency.html#:~:text=NREL%20maintains%20a%20chart%20of,our%20research%2Dcell%20efficiency%20data>. Assess on: 13 July 2021.

OLIVEIRA, P.; ARTAXO, P.; PIRES, C.; LUCCA, S.; PROCÓPIO, A.; HOLBEN, B.; SCHAFER, J.; CARDOSO, L.; WOFSY, S.; ROCHA, H. The effects of biomass burning aerosols and clouds on the CO2 flux in Amazonia. **Tellus B: Chemical and Physical Meteorology**, v. 59, n. 3, p. 338-349, 2007.

PARK, H.; CHANG, S.; ZHOU, X.; KONG, J.; PALACIOS, T.; GRADEČAK, S. Flexible graphene electrode-based organic photovoltaics with record-high efficiency. **Nano Letters**, v. 14, n. 9, p. 5148-5154, 2014.

PARK, S.; YU, G. Absorption properties and size distribution of aerosol particles during the fall season at an urban site of Gwangju, Korea. **Environmental Engineering Research**, v. 24, n. 1, p. 159-172, 2019.

PEARSALL, N. **The performance of photovoltaic (PV) systems:** modelling, measurement and assessment. Cambridge: Woodhead Publishing, 2017.

PEREIRA, E.; MARTINS, A.; GONÇALVES, R.; COSTA, F.; LIMA, R.; RÜTHER, S.; ABREU, G.; TIEPOLO, S.; PEREIRA, J. S. **Atlas brasileiro de energia solar**. São José dos Campos: INPE, 2017. Available from: http://urlib.net/rep/8JMKD3MGP3W34P/3PERDJE. Access on: 12 Aug. 2020.

PHOTOVOLTAIC GEOGRAPHICAL INFORMATION SYSTEM (PVGIS). **Solar radiation tool**. European commission science hub. Available from: https://ec.europa.eu/jrc/en/pvgis. Access on: 30 July 2020.

PIEDEHIERRO, A.; ANTON, M.; CAZORLA, A.; ALADOS-ARBOLEDAS, L.; OLMO, F. Evaluation of enhancement events of total solar irradiance during cloudy conditions at Granada (Southeastern Spain), **Atmospheric Research**, v. 135 – 136, p. 1-7, 2014.

POLO, J.; ALONSO-ABELLA, M.; MARTÍN-CHIVELET, N.; ALONSO-MONTESINOS, J.; LOPEZ, G.; MARZO, A.; NOFUENTES, G.; VELA-BARRIONUEVO, N. Typical meteorological year methodologies applied to solar spectral irradiance for PV applications. **Energy**, v. 190, e116453, 2020.

PÖSCHL, U. Atmospheric aerosols: composition, transformation, climate and health effects. **Angewandte Chemie International Edition**, v. 44, n. 46, p. 7520-7540, 2005.

PV EDUCATION. **Spectral response**. Available from: https://www.pveducation.org/pvcdrom/solar-cell-operation/spectral-response. Assess on: 20 Apr. 2021.

QUEIROZ, A. R.; FARIA, V. A.; LIMA, L. M.; LIMA, J. W. Hydropower revenues under the threat of climate change in Brazil. **Renewable Energy**, v. 133, p. 873-882, 2019.

RANABHAT, K.; PATRIKEEV, L.; ANTAL'EVNA-REVINA, A.; ANDRIANOV, K.; LAPSHINSKY, V.; SOFRONOVA, E. An introduction to solar cell technology. **Journal of Applied Engineering Science**, v. 14, n. 4, p. 481-491, 2016.

RENEWABLES 21 (REN21). **Renewables 21 global status report.** Paris: REN21 Secretariat, 2021. Available from: <https://www.ren21.net/reports/global-status-report/>. Assess on: 15 Aug. 2021.

RODRIGO, P. M.; FERNANDEZ, E. F.; ALMONACID, F. M.; PEREZ-HIGUERAS, P. J. Quantification of the spectral coupling of atmosphere and photovoltaic system performance: Indexes, methods and impact on energy harvesting. **Solar Energy Materials and Solar Cells**, v. 163, p. 73-90, 2017.

ROELOFS, G. J. Aerosol lifetime and climate change. **Atmospheric Chemistry & Physics Discussions**, v. 12, n. 7, 2012.

RUIZ-ARIAS, J. A.; GUEYMARD, C. A. Solar resource for high-concentrator photovoltaic applications. In: PÉREZ-HIGUERAS, P.; FERNANDEZ, E. F. (Ed.). **High concentrator photovoltaics**. Cham: Springer, 2015. p. 261-302.

SAMPAIO, P.; GONZÁLEZ, M. Photovoltaic solar energy: conceptual framework. **Renewable and Sustainable Energy Reviews**, v. 74, p. 590-601, 2017.

SAMSET, B. H.; STJERN, C. W.; ANDREWS, E.; KAHN, R. A.; MYHRE, G.; SCHULZ, M.; SCHUSTER, G. L. Aerosol absorption: progress towards global and regional constraints. **Current Climate Change Reports**, v. 4, n. 2, p. 65-83, 2018.

SCHNEIDER, T.; O'GORMAN, P.; LEVINE, X. Water vapor and the dynamics of climate changes. **Reviews of Geophysics**, v. 48, n. 3, 2010.

SECKMEYER, G.; ERB, R.; ALBOLD, A. Transmittance of a cloud is wavelength-dependent in the UV-range. **Geophysical Research Letters**, v. 23, n. 20, p. 2753-2755, 1996.

SHETTLE, E.; FENN, R. Models of the atmospheric aerosols and their optical properties. In: AGARD OPTIC (Ed). **Propagation in the atmosphere.** [S.l.: s.n.], 1976.

SILVA, G.; FONSECA, M. L. São Paulo, city-region: constitution and development dynamics of the São Paulo macrometropolis. **International Journal of Urban Sustainable Development**, v. 5, n. 1, p. 65-76, 2013.

SILVESTRE, S.; KICHOU, S.; GUGLIELMINOTTI, L.; NOFUENTES, G.; ALONSO-ABELLA, M. Degradation analysis of thin film photovoltaic modules under outdoor long-term exposure in Spanish continental climate conditions. **Solar Energy**, v. 139, p. 599-607, 2016.

SINKE, W. C. Development of photovoltaic technologies for global impact. **Renewable Energy**, v. 138, p. 911-914, 2019.

SIRISAMPHANWONG, C.; KETJOY, N. Impact of spectral irradiance distribution on the outdoor performance of photovoltaic system under Thai climatic conditions. **Renewable Energy**, v. 38, n. 1, p. 69-74, 2012.

SOLANKI, S. K. Sunspots: an overview. **The Astronomy and Astrophysics Review**, v. 11, n. 2, p. 153-286, 2003.

SOUZA, D. Z.; VASCONCELLOS, P. C.; LEE, H.; AURELA, M.; SAARNIO, K.; TEINILÄ, K.; HILLAMO, R. Composition of PM2. 5 and PM10 collected at urban sites in Brazil. **Aerosol and Air Quality Research**, v. 14, n. 1, p. 168-176, 2014.

SUTTERLUETI, J.; RANSOME, S.; KRAVETS, R.; SCHREIER, L. Characterizing PV modules under outdoor conditions: what's most important for energy yield. **Channels**, v. 48, n. 24, p. 24, 2008.

TANG, W.; QIN, J.; YANG, K.; LIU, S.; LU, N.; NIU, X. Retrieving high-resolution surface solar radiation with cloud parameters derived by combining MODIS and MTSAT data. **Atmospheric Chemistry and Physics**, v. 16, n. 4, p. 2543-2557, 2016.

TAYLOR, R. Interpretation of the correlation coefficient: a basic review. **Journal of Diagnostic Medical Sonography**, v. 6, n. 1, p. 35-39, 1990.

TORRES, P. H. C.; RAMOS, R. F.; POLLACHI, A. A macrometropolização em São Paulo: reterritorialização, reescalonamento e a cidade-região. **Cadernos Metrópole**, v. 22, p. 103-122, 2019.

TRAVASSOS, L. R. F. C.; ZIONI, S.; TORRES, P. H. C.; FERNANDES, B. D. S.; ARAUJO, G. Heterogeneity and spatial fragmentation in the Sao Paulo macrometropolis: the production of borders and holes. **Ambiente & Sociedade**, v. 23, 2020.

TSAI, B. K.; ALLEN, D. W.; HANSSEN, L. M.; WILTHAN, B.; ZENG, J. A comparison of optical properties between high density and low density sintered PTFE. In: HANSSEN, L. M. (Ed.). **Reflection, scattering, and diffraction from surfaces**. [S.l.]: International Society for Optics and Photonics, 2008. p. 70650Y.

KOMMALAPATI, R. R.; VALSARAJ, K. T. Atmospheric aerosols and their importance: in atmospheric aerosols characterization, chemistry, modeling and climate. In: LEE, S. (Ed.). **ACS symposium series**. [S.l.]: ACS, 2009. p. 199.

VIDYANANDAN, K. V. An overview of factors affecting the performance of solar PV systems. **Energy Scan**, v. 27, n. 28, p. 216, 2017.

VILELA, W. **Estudo, desenvolvimento e caracterização de radiômetros para medidas da radiação solar**. 2010. 177 p. Thesis (Doctorate in Spatial Engineering and Technologies program) – Brazilian National Institute for Space Research (INPE), São José dos Campos, 2010.

WALLACE, J. M.; HOBBS, P. V. **Atmospheric science**: an introductory survey. 2.ed. Washington: Elsevier, 2006.

XIE, J.; HUANG, K.; YU, X.; YANG, Z.; XIAO, K.; QIANG, Y.; ZHU, X.; XU, Z.; WANG, P.; CUI, C.; YANG, D. Enhanced electronic properties of SnO2 via electron transfer from graphene quantum dots for efficient perovskite solar cells. **Acs Nano**, v. 11, n. 9, p. 9176-9182, 2017.

XIE, S.; LI, X.; JIANG, Y.; YANG, R.; FU, M.; LI, W.; PAN, Y.; QIN, D.; XU, W.; HOU, L. Recent progress in hybrid solar cells based on solution-processed organic and semiconductor nanocrystal: perspectives on device design. **Applied Sciences**, v. 10, n. 12, p. 4285, 2020.

YAMASOE, M.; CORRÊA, M. **Processos radiativos na atmosfera**. São Paulo: Oficina de Textos, 2016.

YAMASOE, M.; ROSARIO, N. M. E.; BARROS, K. Downward solar global irradiance at the surface in São Paulo city: the climatological effects of aerosol and clouds. **Journal of Geophysical Research: Atmospheres**, v. 122, n. 1, p. 391-404, 2017.

YE, J. Y.; REINDL, T.; ABERLE, A. G.; WALSH, T. M. Effect of solar spectrum on the performance of various thin-film PV module technologies in tropical Singapore. **IEEE Journal of Photovoltaics**, v. 4, n. 5, p. 1268-1274, 2014.

YORDANOV, G. H.; MIDTGÅRD, O. M.; SAETRE, T. O.; NIELSEN, H. K.; NORUM, L. E. Overirradiance (cloud enhancement) events at high latitudes. In: IEEE PHOTOVOLTAIC SPECIALISTS CONFERENCE (PVSC), 38. 2012. **Proceedings…** IEEE, 2012. p. 1-7.

YORDANOV, G.; SAETRE, T.; MIDTGÅRD, O. M. 100-millisecond resolution for accurate overirradiance measurements. **IEEE Journal of Photovoltaics**, v. 3, n. 4, p. 1354-1360, 2013b.

ZILLI, M. T.; CARVALHO, L.; LINTNER, B. R. The poleward shift of South Atlantic Convergence Zone in recent decades. **Climate Dynamics**, v. 52, n. 5, p. 2545-2563, 2019.